A Semiclassical Approach to the Spin Dynamics in a Singly Charged Semiconductor Quantum Dot

by

Natalie Jäschke

A thesis submitted for the degree of

Doctor rerum naturalium (Dr. rer. nat.)

Technische Universität Dortmund
Fakultät Physik
Lehrstuhl für Theoretische Physik II

August 2019

First Reviewer : Prof. Dr. Frithjof B. Anders

Second Reviewer : Prof. Dr. Mikhail M. Glazov

Abstract

The prospect of utilizing the highly localized electron spin of singly charged semiconductor quantum dots as building blocks for quantum information processing sparked interest in the behavior of the spins in such a system. In this thesis we focus on the theoretical modeling of pump-probe experiments which provide an experimental approach to investigate the spin dynamics. We derive a semiclassical description of the spin dynamics in the periodically pulsed quantum dot including not only the hyperfine interaction of the electron spin with the nuclear spins but also the probabilistic nature of the photon absorption. The periodic pulses lead to a focusing of the electron frequencies onto a few modes which goes hand in hand with a re-alignment of the nuclear spins. In an analytical approach we find two classes of resonance conditions for the coherent electron spin dynamics. We show that the non-equilibrium distribution of the nuclear spins is mirrored in the spin noise of the electron and therefore accessible in experiment via spin-noise spectroscopy. Another application of the spin-spectroscopy is the measurement of higher-order correlation functions. Those can reveal information about physical effects beyond the macroscopic linear effects. We exploit the fourth-order spin-noise spectrum to gain an understanding of the influence of the quadrupolar interaction on the spin dynamics in the presence of a strong external magnetic field.

Kurzfassung

Der Spin eines stark lokalisierten Elektrons in einem einfach geladenen Halbleiterquantenpunkt ist ein möglicher Kandidat für den Grundbaustein in der Quanteninformationsverarbeitung. Daher ist es von besonderem Interesse, die Dynamik des Spins in einem solchen System zu verstehen. Anrege-Abfrage Experimente sind eine Möglichkeit dieses Problem zu untersuchen. Wir wollen die theoretische Modellierung zu diesen Experimenten liefern. Dazu leiten wir eine semiklassische Beschreibung der Spindynamik in einem periodisch gepulsten Quantenpunkt her. Diese beinhaltet sowohl die Hyperfeinwechselwirkung zwischen Elektronen- und Kernspins als auch die probabilistische Natur der Photoabsorption. Unter dem Einfluss der periodische Pumppulse werden die Frequenzen der Elektronenspinpräzession auf einige wenige reduziert. Die Ursache dafür ist die Neuausrichtung der Kernspins untereinander. Wir leiten zwei Klassen von Resonanzbedingungen her, welche die Frequenzen der kohärenten Elektronenspinpräzession vorhersagen und auch die Nicht-Gleichgewichtsverteilung der Kernspins beeinflussen. Wir zeigen, dass diese Nicht-Gleichgewichtsverteilung im elektronischen Spinrauschen, messbar durch Spinrauschspektroskopie, wiedergefunden werden kann. Eine andere Anwendungsmöglichkeit für Spinrauschspektroskopie besteht in Messung von höheren Korrelationsfunktionen. Diese können dazu verwendet werden, um Physik, die über makroskopische, lineare Effekte hinaus geht, offen zu legen. Wir benutzen die Korrelationsfunktion vierter Ordnung, um den Einfluss der quadrupolaren Wechselwirkung auf die Spindnyamik in einem starken Magnetfeld zu verstehen.

Contents

Publication list

- Jäschke, Natalie and Fischer, Andreas and Evers, Eiko and Belykh, Vasilii V. and Greilich, Alex and Bayer, Manfred and Anders, Frithjof B., Nonequilibrium nuclear spin distribution function in quantum dots subject to periodic pulses. *Phys. Rev. B* 96 (2017) 205419
- Jäschke, Natalie and Anders, Frithjof B. and Glazov, Mikhail M., Electron spin noise under the conditions of nuclei-induced frequency focusing. *Phys. Rev. B* 98 (2018), 045307
- Fröhling, Nina and Jäschke, Natalie and Anders, Frithjof B., Fourth-order spin correlation function in the extended central spin model. *Phys. Rev. B* 99 (2019), 155305

List of acronyms

CET	Chebychev expansion technique
CSM	Central spin model
ED	Exact diagonalization
FOA	Frozen Overhauser field approximation
QD	Quantum dot
RK4	Runge-Kutta fourth-order method
SCA	Semiclassical approach

Chapter 1

Introduction

Quantum computing is still in its infancy and pivotal elements are not yet mature. Since its inception about half a century ago [1–3], quantum computing has become a topic of vivid interest not only in the physics community [4–7] but also in other fields such as chemistry [8, 9] or machine learning [10, 11]. Like a classical computer, a quantum computer has to possess the ability to store and manipulate information. However, for this task the classical bit is replaced by a quantum bit or qubit. While a classical bit only assumes either the state $|0\rangle$ or $|1\rangle$, a qubit can also be in a superposition of both states. Still, the measurement of a single qubit provides one bit of information since the superposition state collapses to an eigenstate. The advantage of quantum computers lies in performing certain operations on multiple values in one stroke instead of sequentially [12] using the unitary time evolution in a closed quantum system. Therefore, quantum computers perform better at some tasks than their classical counterparts. A famous example is the prime decomposition via the Shor algorithm [13, 14] or Grover's algorithm [15, 16] for searches in disordered lists. Also, the simulation of inherently quantum mechanical systems could be more efficient, as Feynman and Manin suggested [17, 18]. The requirements for a quantum computer are characterized by the DiVincenzo criteria [19, 20]. They include but are not limited to the ability to initialize and read a qubit. DiVincenzo identifies the decoherence in a qubit as one of the biggest problems encountered. Coherence times, exceeding the gate operation time, are necessary to compute data. The first hurdle that has to be overcome on the way to a working quantum computer is finding a qubit meeting all those requirements. Multiple candidates [4] were proposed for this essential building block which consists of a quantum mechanical two-level system. Proposals for the realization of qubits include the polarization state of a photon [21–24], superconducting circuits [25–28] or trapped atoms [29–31]. The candidate that constitutes the basis of this thesis is the highly localized electron spin in a semiconductor quantum dot [6, 20, 32]. While quantum-dot qubits have the edge over the other proposals concerning the integrability into existing semiconductor-based information technology, the main obstacle to their usage turns out to be their coherence time. The decay of the electron spin coherence is dominated by the Fermi contact hyperfine interaction with a fluctuating nuclear spin bath. However, Greilich et al. [33–35] showed that the influence of the hyperfine interaction does not have to be detrimental to the conservation of quantum information. Periodic pulsing of the quantum dot ensemble leads to a focusing of the electron precession frequencies onto few modes via spin-flip processes with the nuclear spins. The electron spin dynam-

ics shows an integer multiple of spin revolutions during a pulse interval, while settings of the nuclear spin ensemble, that generate a non-resonant electron spin dynamics, become less probable. This effect is referred to as nuclear focusing. Since the nuclear spins couple only weakly to the environment, their collective influence stabilizes the coherent electron spin dynamics and the coherence time is prolonged [36].

A model tailored to the spin dynamics in a singly charged quantum dot is the central spin model first proposed by Gaudin in 1976 [37]. The theoretical description comprises the electron and the nuclear spins. The nuclear spins are assumed to not be coupled to each other and only interact indirectly via the central electron spin. The central spin model is integrable [37] and an analytic [38–40] and stochastic [41, 42] solution is e. g. given by the Bethe ansatz. Most analytical approaches require certain assumptions such as homogeneous hyperfine coupling constants [43–46] or a pre-set nuclear spin polarization [47, 48]. Numerical approaches to the central spin model provide an often more efficient alternative. Examples include, but are not limited to, Chebyshev polynomial expansion techniques [49], cluster expansion [50, 51] or time-dependent density matrix renormalization group [52, 53]. Semiclassical approaches [54–58], as employed in this thesis, are conspicuous by the fact that they allow for the treatment of large nuclear spin baths and simultaneously give access to long time scales.

Equipped with this knowledge about the central spin model, theoretical descriptions for the dynamics in a periodically pulsed quantum dot were developed. As early as 2007, Uhrig [59] showed that an optimized sequence of π-pulses leads to an increase in coherence time. Subsequent quantum mechanical investigations delved deeper into spin dynamics in a pulsed quantum dot [60–63]. While a quantum mechanical approach allows for the treatment of very long pulse sequences with millions of pulses, it suffers from a severe restriction of the number of nuclear spins [63]. The calculation of the time evolution operator, which makes it possible to calculate the dynamics between two pulses in just one step, is now its downfall, since the Hilbert space grows exponentially with the bath size. The inverse is true for a semiclassical approximation: While the dynamics, that bridges the time between two pulses, cannot be reduced to a single step, the computation time only grows linearly with the number of nuclear spins. A further improvement in computational effort is possible for the case of homogeneous coupling constants [60, 64] or with more sophisticated methods like a spectral density approach [65].

Another way to investigate the spin dynamics in singly charged semiconductor quantum dots experimentally is through optical spin-noise spectroscopy which was originally proposed by Aleksandrov and Zapasskii [66, 67] in 1981. A non-resonant laser beam changes its polarization plane after propagating through the sample. The Faraday rotation measurement provides a way to study the electron spin noise nearly perturbation-free. Since 1981 this minimally invasive method has found many applications [68], e. g. measuring spin noise in an ensemble of alkali atoms [69] or in bulk semiconductors [70–72]. In semiconductor quantum dots spin-noise spectroscopy serves as an experimental tool to study the second-order spin noise [69, 70, 72–75]. These experimental studies were complemented by extensive theoretical investigations [49, 75–77]. The influence of the electrical-nuclear quadrupolar interactions on the long-time decay of the electron spin correlation function [78, 79] and the spin-noise power spectrum [49, 73, 75, 80–83] were ascertained in the absence of an external magnetic field. However, in order to obtain information beyond linear effects, non-equilibrium conditions have to be util-

ized. In an experimental setup they are realized by applying radio-frequency magnetic fields [84–86] or through periodic laser pulses [35, 87–90]. The limitations, that the fluctuation-dissipation theorem imposes on the second-order spin correlations, do not hold for higher-order correlation functions. The nuclear-electric quadrupolar interaction in a finite external magnetic field serves as a prime example for the advantage of higher-order noise investigations. In the presence of a large magnetic field the information about weak interactions, such as the quadrupolar interaction, is inaccessible in the second-order correlation function due to the fast dephasing time of the electron spin. When fourth-order spin response functions were experimentally investigated [91, 92] at magnetic fields above 1 T, it was shown by Fröhling et al. [93] that the quadrupolar interaction is necessary to understand their long-time decay. The same information can be extracted from the fourth-order spin-noise spectrum [94]. An extension of the spin-noise spectroscopy to fourth order [95, 96] would allow for a measurement of this quantity.

The central goal of this thesis is gaining an understanding of the spin dynamics in singly charged semiconductor quantum dots. We aim at the description of two types of measurements: pump-probe experiments and spin-noise spectroscopy measurements. Hereby, emphasis is put on the pump-probe experiments [33–35]. A semiclassical approach describing the periodic excitation in quantum dots is devised in this thesis.
In Chap. 2 a short introduction to the experimental background is given. We discuss the properties and the production process of self-assembled semiconductor quantum dots. Special focus is placed on their behavior under optical excitations since it is a precursor to understanding pump-probe experiments and spin-noise spectroscopy. Both types of measurements are outlined. Additionally, we review exemplary results of pump-probe experiments [33–35]. The theoretical model of the spin dynamics in a singly charged semiconductor quantum dot is the topic of Chap. 3. The central spin model, which comprises the hyperfine Fermi contact interaction between nuclear and electron spins as well as the nuclear and electron Zeeman interaction, is introduced. It is supplemented by the theoretical description of the nuclear-electric quadrupolar interaction. The hyperfine coupling constant distribution [49] as well as its implications for the electron spin dynamics are discussed. The definitions of correlation functions up to the fourth order are introduced in Chap. 4. In Chap. 5 the semiclassical approximation is derived by expanding the path-integral representation around its saddle-point. The resulting set of classical Euler-Lagrange equations of motion are the essential building-block to all further investigations in this thesis. The parameters of the semiclassical simulation are discussed. The spin dynamics gained by the application of the semiclassical approximation are benchmarked against results of quantum mechanical methods like the Lanczos approach or an exact diagonalization.
The chapters 6 to 8 present the results of this thesis on three different topics: the classical treatment of fourth-order spin correlation functions, a semiclassical description of the mode locking in a pulsed quantum dot and the subsequent spin dynamics in a mode-locked system. The calculations in Chap. 6 are based on the definitions introduced in Chap. 4. The spin correlation functions of second and fourth order are calculated in the semiclassical approach and compared with the results of a quantum mechanical approach. The influence of the quadrupolar interaction on the fourth-order spectrum is investigated in detail. Chapter 7 is dedicated to the modeling of a periodic laser pulse sequence on a semiconductor quantum dot. The equations of motion are expanded upon by a semiclassical description for the laser pump pulse and the subsequent decay of the

excited state. Under the assumption of frozen nuclear spins [55], an analytical solution is found. The core part of the chapter are numerical simulations. The influence of individual parameters on the spin dynamics and the development of a non-equilibrium steady state is discussed. Chapter 8 is directly linked to the results of Chap. 7. After periodic pulses have driven the spin system into a non-equilibrium steady state, the train of optical pulses stops. The electron and nuclear spin relaxation are discussed. Furthermore, we analyze the correspondence of the electron spin-noise spectra to the time evolution of nuclear spin distributions in this non-equilibrium case.
The thesis ends with a conclusion and a short outlook.

Chapter 2

Experimental background

Since the theoretical investigations in this work are closely related to pump-probe experiments, especially those conducted on singly charged quantum dots [33, 88, 97], they shall briefly be introduced here. The materials analyzed in those experiments are semiconductor quantum dots. In pump-probe experiments transitions in the quantum dot are periodically excited. The sample response is measured with the probe pulse which reveals physical properties of the spin dynamics. Both, the setup and results of those experiments, are discussed in this chapter.

2.1 Semiconductor quantum dots

Quantum dots (QDs) are solid state structures that provide confinement in three dimensions for electrons or holes and feature a discrete energy spectrum. While there are many different types of QDs like natural QDs which occur due to potential fluctuations [98–100] or QDs which result from electron beam lithography and wet chemical etching [101, 102], we restrict ourselves to self-assembled In(As)Ga QDs which are a product of molecular beam epitaxy.

In vacuum at $\sim$ 600°C monolayers of InAs are deposited on a substrate of GaAs [103–105]. Due to the very slow application, the InAs adopts the lattice structure of the host at first. This layer is called the wetting layer. But the difference of approximately 7% in lattice constants between 5.65 Å for GaAs and 6.06 Å for InAs [106] leads to lattice strain in subsequent InAs layers. The strain increases with additionally applied monolayers until the islands "bulge up" on the wetting layer which is called Stranski–Krastanov growth [107]. Those QD islands lead to partial strain relaxation, see Fig. 2.1 on the left. The strain due to the difference in lattice constants through the layers is depicted in Fig. 2.1 in the left panel. Since this occurs spontaneously, the QDs are called self-assembled. The QDs are usually tens of nanometers in diameter and a few nanometers high [104]. A QD ensemble at this stage in its production is depicted in Fig. 2.1 on the right.

The QD can be charged with a carrier by including a doping layer below the substrate. Here, n-doped QD are the focus of investigation. An electron tunneling from e. g. a Si layer to the QD leads to a singly negatively charged QD [109].

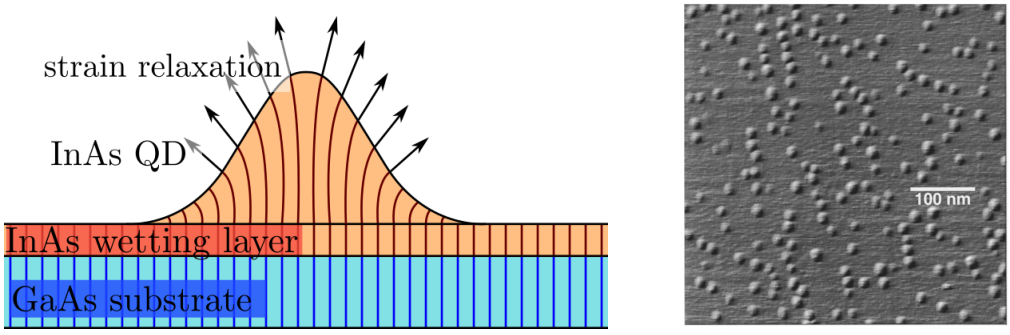

Figure 2.1: Left panel: Schematics of the growth of a InAs QD on an GaAs substrate. The lattice constant mismatch (blue lines - GaAs, red lines -InAs) leads to a strained InAs wetting layer. The formation of the InAs QD relaxes the strain partially. Right panel: Atomic force microscopy image of an uncapped InAs QD ensemble [108].

The resultant QD ensemble is overgrown with an additional layer of GaAs. The smaller band gap of the InAs is now sandwiched between the larger ones of the GaAs and carriers are locally confined in all three dimensions. The potential well is of a size comparable to their de-Broglie wavelength. This reduces the interaction of the trapped electron or hole spin with the substrate but enhances the hyperfine interaction with the nuclear spins in the QD.

The last step is the annealing process [110]. Here, the QD ensemble is heated to $\sim 900°\mathrm{C}$ which leads to diffusion between the GaAs and InAs layers. It reduces the lattice defects and harmonize the geometry of the QDs [111–113]. The temperature and the duration of the process is also used to tune the band gap which affects various, optical properties of the QD ensemble.

2.2 Optical excitations in a quantum dot

Both InAs and GaAs are direct semiconductors, meaning that the minimum of the lowest conduction band and the maximum of the highest valence band coincide at the same k-value. A schematic representation of the band structure of a direct semiconductor is shown in Fig. 2.2 in the left panel. The Fermi level E_F, also known as the chemical potential, is located between the bands. E_g is the minimum required energy that allows for the excitation of an electron from the completely filled valence band to the completely empty conduction band at $T = 0\,\mathrm{K}$. In contrast to an insulator, the band gap E_g is small enough to allow for the excitation of a carrier from the valence to the conduction band. For InAs the band gap is $0.354\,\mathrm{eV}$ and for GaAs it is $1.424\,\mathrm{eV}$ [106]. Near the Γ-point at $k = 0$, the center of the Brillouin zone, the bands are assumed to be parabolic.

The difference in band gap energy of the two materials leads to the formation of a quantum well which traps electrons and holes in all spatial directions. Since the confining well is of the order of magnitude of the de-Broglie wavelength, the energy spectrum becomes discrete [114–116]. The energy levels spacing depends on shape and size of the QD. Due to its discrete spectrum a QD is often called an artificial atom.

In a semiconductor material the spin-orbit coupling leads to the particle's spin angular momentum $\vec{S}$ and its orbital angular momentum $\vec{L}$ no longer being conserved separately.

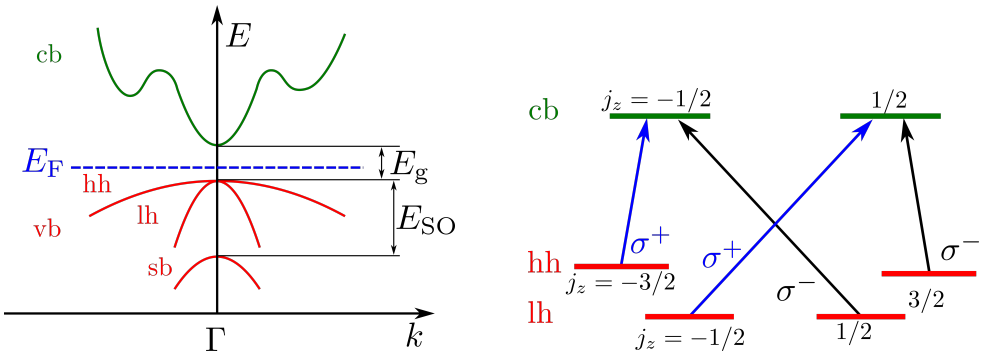

Figure 2.2: cb and vb label the conduction and the valence band. The heavy holes, light holes and the split-off band are hh, lh and sb. Left panel: Schematic of the band structure of a direct semiconductor near the Γ point. E_F is the Fermi level, E_g the energy of the band gap and E_SO the energy difference between the sb and the other two valence bands. Right panel: optical transitions between electron states in an n-doped QD enabled by circularly polarized light $\sigma^\pm$. Schematic inspired by [114, 115].

Instead the total angular momentum $\vec{J} = \vec{L} + \vec{S}$ acts as the conserved quantity with the quantum number $|l - s| \leq j \leq l + s$. For the s-like conduction band this leads to $j = s = 1/2$ which is doubly degenerate while the p-like valence band with $l = 1$ is degenerate twice for $j = 1/2$ and four times degenerate for $j = 3/2$ at $k = 0$ [117]. The $j = 1/2$ band is split off by the energy E_SO which is in the order of magnitude of the band gap [106] and is neglected in this work. The states $j = 3/2$ with $j_z = -3/2, -1/2, 1/2$ and $3/2$ correspond to the light holes for $|j_z| = 1/2$ and to the heavy holes for $|j_z| = 3/2$. The term heavy and light holes is connected to their effective mass which is derived from the curvature of their respective valence bands.

Photons carry the angular momentum of ± 1 depending on their helicity. This enables the transitions between the valence and the conduction band presented in Fig. 2.2 in the right panel. For right circularly polarized light σ^+ which increases the angular momentum of a state in an absorption process by 1, two excitations are possible: One from the heavy hole band with $j_z = -3/2$ to the conduction band with $j_z = -1/2$ under the absorption of the polarized photon and the other from the light hole band with $j_z = -1/2$ to the valence band state with $j_z = 1/2$. The transitions between the band due to excitation with σ^--polarized light behaves analog to that. Excitations of electrons to the conduction band leave behind a hole in the valence band. If the conduction band is empty prior to the photo-excitation, the resulting particle is called an exciton. If the QD is already charged with a single electron, then the excited electron features a spin aligned opposing to those of the resident electron. The electron singlet and the hole in the valence band are referred to as a trion.

The excited carriers have a life time of $\tau \sim 400\,\mathrm{ps}$ for direct semiconductors before they recombine [88]. The decay is accompanied by photo-emission. Since the light hole band is usually energetically lower than the heavy hole band, it can be neglected. Only the smallest band gap between the conduction band and the heavy hole band is taken into account.

2.3 Pump-probe experiments

Pump-probe experiments have proven to be a valuable tool to study the time-resolved dynamics of the electron in a semiconductor QD [35, 118, 119]. The system periodically experiences optical excitations via pump pulses and the spin polarization is detected by a second pulse, the probe pulse. The experiments are conducted in Voigts geometry, meaning an external magnetic field of 1-6 T magnitude is applied orthogonal to the pump beam [33]. The high magnetic fields require the use of a cryostat in which the sample is cooled to $\sim 6\,\mathrm{K}$. The sample is an ensemble of In(Ga)As QDs which are single negatively charged.

In Fig. 2.3 a simple blueprint[1] for such experiments is shown. The laser provides a train of linear polarized light pulses with a time delay of $T_\mathrm{R} \approx 13\,\mathrm{ns}$. The initial beam is divided in a pump and a probe beam. If pump and probe arrive at the sample at the same time, the electron polarization at $t = 0$ is measured. To gain further information about the spin polarization in time a delay line is introduced. The length of the delay line is proportional to the time Δt after a pump pulse. Each data point in time is averaged over multiple consecutive pulses. The measurement relies on Faraday rotation or ellipticity [120, 121] to gain insight into the electron spin polarization.

After the delay line the pump pulse is circularly polarized by the combination of a Glan-Thompson prism (GT) and a $\lambda/4$-waveplate. When the pump power is optimized maximizing the signal amplitude, then this pump pulse is assumed to be a π-pulse. The polarized light excites a trion state. Since the pump pulse only excites one electron spin state to a trion state depending on its polarization, the other electron state is unaffected by the laser. During process of the trion decay, the unpumped state precesses in the external magnetic field. If a strong external magnetic field results in a Larmor precession period larger or of the order of magnitude of the decay time, the decaying spin component averages to zero and the excitation leads to a build-up of polarization in the system.

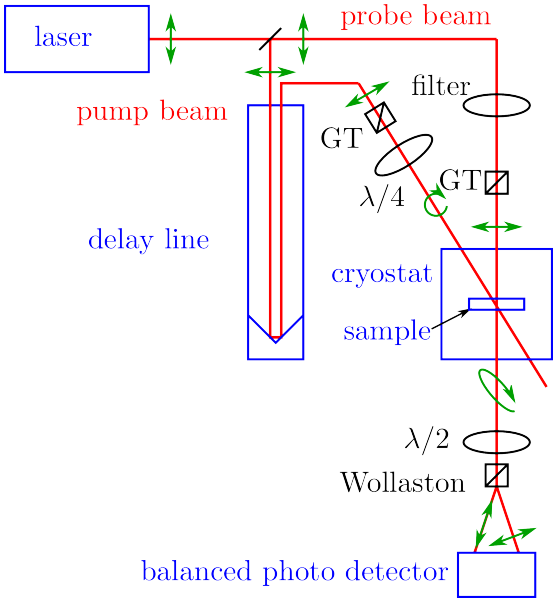

Figure 2.3: Schematic setup of a pump–probe experiment with Faraday rotation measurement. GT is a Glan-Thompson prism. $\lambda/4$ is a $\lambda/4$-waveplate and $\lambda/2$ is a $\lambda/2$-waveplate.

To avoid any strong perturbation of the system, the power of the probe beam is reduced before it arrives at the sample. Since a trion is excited in the QD, one circular polarization state is damped. This leads to two circular polarization states with different amplitudes. The probe beam experiences a rotation of the polarization frame and gets elliptically polarized after the transmission through the sample. The Wollaston prism

[1] Private communication by E. Evers

separates the beam in two parts with orthogonal polarization. The generated spin polarization in the sample is proportional to the difference of the amplitudes of both linearly polarized beams measured via a balanced photon detector. In Fig. 2.3 a Faraday rotation measurement is presented. The tilt of the polarization axis of linearly polarized light after the transition through a medium is proportional to the spin polarization. For the measurement of the ellipticity the second $\lambda/2$ waveplate is replaced by a $\lambda/4$-waveplate.

2.4 Experimental results a of pump-probe experiment

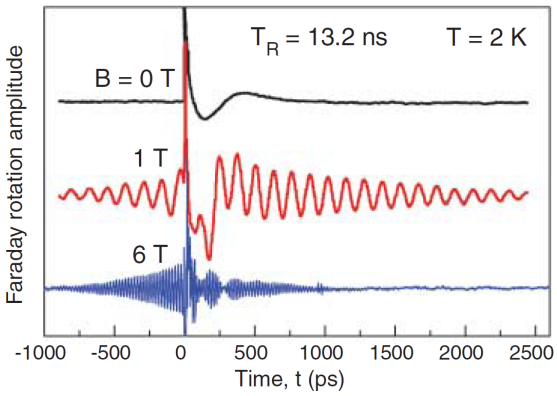

Figure 2.4: The Faraday rotation signal measured at different external magnetic field strengths $|\vec{B}_{\text{ext}}| = 0\,\text{T}$, $|\vec{B}_{\text{ext}}| = 1\,\text{T}$, and $|\vec{B}_{\text{ext}}| = 6\,\text{T}$. The pump pulse repetition time is $T_{\text{R}} = 13.2\,\text{ns}$. The Faraday rotation signal is proportional to the electron spin dynamics. The plot is taken from Ref. [88]

A typical pump-probe measurement on a semiconductor QD ensemble is presented in this section. Figure 2.4 is taken from Ref. [88]. It shows the time evolution of the Faraday rotation amplitude recorded by the experimental scheme presented above. Similar pump-probe experiments have been conducted in Refs. [33, 35]. The electron spin component along the optical axis, which is proportional to the Faraday rotation signal, is shown immediately before the pulse at $t = 0$ and directly after. The pump pulse is applied every $T_{\text{R}} = 13.2\,\text{ns}$. The spin dynamics is subject to an external magnetic field of strength $|\vec{B}_{\text{ext}}| = 0$, $|\vec{B}_{\text{ext}}| = 1\,\text{T}$ or $|\vec{B}_{\text{ext}}| = 6\,\text{T}$.

At $|\vec{B}_{\text{ext}}| = 0$ the Faraday rotation signal shows a single minimum for $t < 500\,\text{ps}$. After $t > 500\,\text{ps}$ the signal approaches a constant value. Due to the missing external magnetic field, no electron spin precessions is observed and no signal is detected immediately before the pulse. For $|\vec{B}_{\text{ext}}| = 1\,\text{T}$ the Faraday rotation signal reveals a decaying electron spin precession around the external magnetic field after the pulse. The time scale of the decay is approximately $\sim 2\,\text{ns}$. For negative times, directly before the next pulse, the Faraday rotation signal increases towards the pulse. This electron spin revival before the pulse is also observed for the measurement at $|\vec{B}_{\text{ext}}| = 6\,\text{T}$. The spin precession can no longer be resolved on the depicted time scale for $|\vec{B}_{\text{ext}}| = 6\,\text{T}$.

The electron spin revival hints at a synchronization of the electron spin precession modes to the pulse repetition time T_{R}. Those modes, which are defined by a single frequency, superimpose constructively at integer multiples of T_{R}. This effect is called

mode locking. The focusing on a few select frequencies is induced by a re-alignment of the nuclear spins [33].

We strive to explain the electron spin dynamics and the not-directly measurable nuclear spin dynamics during a pump pulse sequence in more detail in Chap. 7. After the pump pulses stop, the experimental measurement is conducted. Therefore, we bridge the divide between theoretical description and experiment in Chap. 8 by discussing the electron spin dynamics in time and frequency domain in an already mode-locked system. The electron spin dynamics in the frequency domain can be experimentally accessed through spin-noise spectroscopy.

2.5 Spin-noise spectroscopy

Spin-noise spectroscopy is a minimally invasive method to measure the spin dynamics of doped semiconductor QDs. In contrast to the pump-probe technique it relies only on non-resonant, continuous probe beams and avoids exposing the system to unnecessary excitations. The studied system stays in thermal equilibrium [117]. The setup is comparable to that of the pump-probe experiment in Sec. 2.3. However, the pump pulses are omitted and only the linearly polarized probe beam is applied to the sample instead. Upon contact with the sample the plane of the laser beam polarization is rotated. The measurement relies on Faraday rotation or Kerr effect, depending on whether the beam is transmitted through the sample or reflected. Spin fluctuations only lead to a weak magnetization in the sample. Combined with a weak probe beam intensity, the measured signal is smaller compared to that of a pump-probe experiment. The measured signal is noisy in the time domain. As a last step, a Fourier transformation is applied to the data recorded in time. The obtained spin-noise spectrum reveals the frequency composition of the spin dynamics.

Chapter 3

Model

In this chapter we lay the foundation for all theoretical investigations in this thesis. We derive a Hamiltonian that incorporates all important interactions in a single semiconductor QD. The localization of the electron in a QD pushes the hyperfine interaction to the fore [114, 117]. We also include the interaction of the spins in the QD with an external magnetic field as well as the nuclear-electric quadrupolar interaction. Hyperfine and quadrupolar coupling constants are discussed. Other interactions like e. g. the dipole-dipole interactions, which are important when holes come into play, are neglected.

From that point on we use $\hbar = 1$, measuring the time $t \to t/\hbar$ in units of inverse energy.

3.1 Central spin model

Neglecting charge fluctuations, the description of the spin dynamics in a singly charged semiconductor QD is given by the total Hamiltonian

$$H_{\text{tot}} = H_{\text{CSM}} + H_{\text{Q}}. \tag{3.1.1}$$

The first part H_{CSM} contains the central spin model (CSM) including the hyperfine interaction and the Zeeman interaction of the nuclear and electron spin with the external magnetic field. The other Hamiltonian H_{Q} comprises the nuclear-electric quadrupolar interaction. We also introduce a characteristic time scale T^* which is related to the fluctuations of the effective magnetic field acting on the electron spin.

3.1.1 The Gaudin model

The CSM in its simplest form was presented by Gaudin in 1976 [37]. It only incorporates the interaction between a central spin and a spin bath. We identify this interaction as the Fermi contact hyperfine interaction, which was derived in a perturbative approach in Refs. [122, 123].

The wave function of the strongly localized electron spin envelopes multiple nuclear spins. Each nuclear spin can be described by the magnetic moment $\vec{\mu}_{\text{I}} = \mu_{\text{I}}\vec{I}/I$. The

interaction of the electron spin with a single nuclear spin is modeled by the magnetic field

$$\vec{B}_{\mathrm{I}}(\vec{r}) = \nabla \times \frac{\vec{\mu}_{\mathrm{I}} \times \vec{r}}{r^3} = \nabla \times \vec{A} \tag{3.1.2}$$

with the distance $|\vec{r}_{\mathrm{S}} - \vec{r}_I| = |\vec{r}| = r$ between the electronic dipole moment at $\vec{r}_{\mathrm{S}}$ and the nuclear magnetic moment at $\vec{r}_{\mathrm{I}}$. The vector potential belonging to $\vec{B}_{\mathrm{I}}(\vec{r})$ is

$$\vec{A} = \nabla \times \frac{\vec{\mu}_{\mathrm{I}}}{r}. \tag{3.1.3}$$

The Hamiltonian of an electron in the presence of an electromagnetic field with a vector potential $\vec{A}$ is given by the Pauli Hamiltonian

$$H_{\mathrm{I}} = \frac{1}{2m_{\mathrm{e}}} \left(\vec{p} - e\vec{A}\right)^2 + g_0 \mu_{\mathrm{B}} \vec{S} \vec{B}_{\mathrm{I}} \tag{3.1.4}$$

where m_{e} is the mass of the free electron, e its charge and $g_0 = 2$ its g-factor. $\vec{S}$ denotes the electron spin operator and $\vec{p}$ the electron momentum operator. Neglecting the quadratic terms of $\vec{A}$ in a first-order perturbation calculation, the Hamiltonian H_{I} is rewritten as

$$H_{\mathrm{I}} = H_0 + H_{\mathrm{hf}}, \tag{3.1.5}$$

where H_0 is the Hamiltonian of a free electron and H_{hf} that of the perturbation linear in $\vec{A}$. The definition of the electron angular momentum $\vec{l} = \vec{r} \times \vec{p}$ enables us to combine the first two terms as $\vec{p}\vec{A} + \vec{A}\vec{p} = 2\mu_{\mathrm{I}}/r^3 I(\vec{I}\vec{l})$ using the Coulomb gauge $\nabla \vec{A} = 0$. The last term accounting for the Zeeman effect generated by the nuclear magnetic field, is recast as

$$\begin{aligned} \vec{S}\vec{B}_{\mathrm{I}} &= \vec{S}\left(\nabla \times \left(\nabla \times \frac{\vec{\mu}_{\mathrm{I}}}{r}\right)\right) \\ &= \left[\left(\vec{S}\nabla\right)\left(\vec{\mu}_{\mathrm{I}}\nabla\right) - \frac{1}{3}\left(\vec{S}\vec{\mu}_{\mathrm{I}}\right)\Delta\right]\frac{1}{r} - \frac{2}{3}\left(\vec{S}\vec{\mu}_{\mathrm{I}}\right)\Delta\frac{1}{r}. \end{aligned} \tag{3.1.6}$$

The first summand provides terms for $r \neq 0$. The second one only contributes for $r = 0$. Evaluating the derivatives leads to

$$H_{\mathrm{hf}} = \frac{2\mu_{\mathrm{B}}\mu_{\mathrm{I}}}{I}\vec{I}\left[\frac{\vec{l}}{r^3} - \frac{\vec{S}}{r^3} + 3\frac{\vec{r}(\vec{S}\vec{r})}{r^5} + \frac{8\pi}{3}\vec{S}\delta(\vec{r})\right]. \tag{3.1.7}$$

The first term describes the interaction of the nuclear magnetic moment $\vec{I}$ with a current carrying the electron angular momentum $\vec{l}$. The dipole-dipole interaction is represented by the second and third term. The last term can be identified as the contact interaction which was first derived by Fermi [124]. Opposite to the dipole-dipole interaction, the Fermi contact interaction only contributes if the electron is found at the position of the nucleus with a finite probability. This is true for s-type wave functions and, therefore, the contact hyperfine interaction is the only dominant interaction in this case. The opposite is holds for $l \neq 0$. For those orbital configurations of the wave function the dipole-dipole interaction becomes significant and the Fermi contact interaction does not contribute.

The anisotropy induced by the hyperfine interaction of a hole trapped in a QD with the nuclear spins is not investigated here [125]. Instead we focus on the electron-nuclear hyperfine interaction since electrons confined in semiconductor QDs can be described by s-type wave functions. In this spherical symmetry only the Fermi contact interaction remains and because the electron spin interacts with multiple nuclear spins, the new Hamiltonian is

$$H_{\mathrm{G}} = \sum_{k=1}^{N} A_k \vec{I}_k \vec{S}. \tag{3.1.8}$$

The spin operators $\vec{S}$ for the electron spin is coupled to each of the N nuclear spin vectors $\vec{I}_k$ via the coupling constant A_k. The electron spin interacts with the nuclear spin bath via the Overhauser field $\vec{B}_{\mathrm{N}}$

$$\vec{B}_{\mathrm{N}} = \sum_{k} A_k \vec{I}_k \tag{3.1.9}$$

and the feedback onto k-th nuclear spin is given by the Knight field $\vec{B}_k = A_k \vec{S}$. The Gaudin model is schematically depicted in Fig. 3.1. The hyperfine coupling constants

$$A_k = \frac{16}{3} \pi \mu_{\mathrm{B}} \frac{\mu_{\mathrm{I}}}{I} |\psi_{\mathrm{e}}(\vec{R}_k)|^2 \tag{3.1.10}$$

depend on the probability of an electron [32, 55] being present at the position of the k-th nucleus $|\psi_{\mathrm{e}}(\vec{R}_k)|^2$ and on the nuclear spin length I. In a real In(Ga)As QD, μ_{I} and I vary, e. g. for Gallium and Arsenic $I = 3/2$ while for Indium $I = 9/2$ holds. Note that we use the approximation of identical nuclei in the following.

The electron wave function can be divided in two parts $\psi_{\mathrm{e}}(\vec{R}) = u(\vec{R})\psi(\vec{R})$: the Bloch amplitude $u(\vec{R})$ and the envelope $\psi(\vec{R})$. The Bloch amplitude describes the periodic behavior of the wave function which repeats in each unit cell. For free electrons the Bloch function is constant $\eta_{\mathrm{e}} = |u(\vec{R})|^2 = 1$ while in semiconductors η_{e} varies between 10^3 and 10^4 [48]. The material dependence of η_{e} can be disregarded here since we are only interested in the distribution of A_k and η_{e} is set as constant, $\eta_{\mathrm{e}} = \mathrm{const.}$. The modulating envelope function $\psi(\vec{R})$ suffices to describe the behavior of ψ_{e} depending on the position of the electron. It determines the distribution function $p(A)$ of the coupling constants A_k. Equation (3.1.10) is often rewritten as

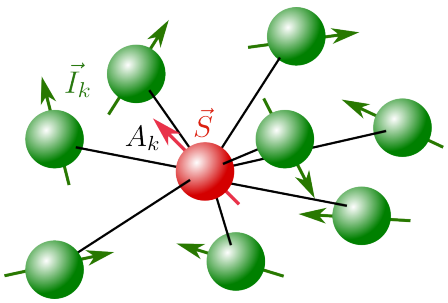

Figure 3.1: In the central spin model the central electron spin $\vec{S}$ interacts with the nuclear spins $\vec{I}_k$ via the coupling constant A_k.

$$A_k = A_{\mathrm{s}} \Omega |\psi(\vec{R}_k)|^2 \tag{3.1.11}$$

where A_{S} is a prefactor and Ω is the volume of the unit cell. Ω is assumed to be small compared to the QD and ψ nearly constant within a single unit cell. Since the probability density function ψ is normalized,

$$1 = \int |\psi(\vec{r})|^2 \mathrm{d}\vec{r} \approx \sum_{k} \Omega |\psi(\vec{R}_k)|^2 \tag{3.1.12}$$

holds and the prefactor A_S is identified as the sum over all coupling constants $A_\mathrm{S} = \sum_k A_k$. A_S can be seen as an indicator for the hyperfine interaction strength and is a material constant, e. g. for GaAs $A_\mathrm{S} \sim 10 - 100\,\mu\mathrm{eV}$ [48, 55, 126]. A more in-depth investigation of A_S related to the chosen distribution of the coupling constants and the number of nuclear spins is found in Sec. 3.1.3.

Usually an external magnetic field is applied in experiments. The Gaudin model (3.1.8) is easily extended to

$$H_\mathrm{CSM} = g_\mathrm{e}\mu_\mathrm{B}\vec{B}_\mathrm{ext}\vec{S} + \mu_\mathrm{N}\vec{B}_\mathrm{ext}\sum_k g_k\vec{I}_k + \sum_{k=1}^{N} A_k\vec{I}_k\vec{S} \tag{3.1.13}$$

where g_e is the electron g-factor and $\mu_\mathrm{B} = 9.27 \times 10^{-24}\,\mathrm{J/T}$ is the Bohr magneton. The electron g-factor of a free electron is $g_\mathrm{e} = 2$, in a QD this value is reduced to $g_\mathrm{e} = 0.555$ [33]. The precession of the nuclear spins is much slower. The nuclear magneton is $\mu_\mathrm{N} = 5.05 \times 10^{-27}\,\mathrm{J/T}$ and therefore approximately ~ 1800 times smaller than the Bohr magneton [117]. The ratio between the electron and nuclear Zeeman splitting can be quantified by the parameter

$$\zeta = \frac{g_\mathrm{N}\mu_\mathrm{N}}{g_\mathrm{e}\mu_\mathrm{B}}. \tag{3.1.14}$$

The electron spins precess with the Larmor frequency $\omega_\mathrm{e} = g_\mathrm{e}\mu_\mathrm{B}|\vec{B}_\mathrm{ext}|$ and the k-th nuclear spin with the frequency $\omega_{\mathrm{N},k} = g_k\mu_\mathrm{N}|\vec{B}_\mathrm{ext}|$ around the external magnetic field. For simplicity, we assume that all nuclear spins have the same g-factor, $g_k = g_\mathrm{N}\forall k$.

In its simplest form Eq. (3.1.8), the CSM can be solved analytically, for example by a sophisticated Bethe ansatz [37, 38]. This approach limits the number of nuclear spins to $N < 50$ [41, 42]. But an exact analytical solution is also possible with a pre-set nuclear spin polarization [47] or the simplification of equal coupling constants [45, 77]. Other analytical methods include a cluster expansion approach [50], a Born approximation for the non-Markovian dynamics [127] or perturbative approaches [47, 128]. This list is by no way exhaustive and neglects all the numerical approaches ranging from classical approaches [55, 129, 130] to Chebychev expansion techniques [49].

3.1.2 Quadrupolar interaction

The growth process of self-assembled QDs relies on different lattice constants between growth layers. The mismatch which is up to 7 % for InAs/GaAs [114], leads to lattice strain under which the nuclei can be deformed to a non-spherical shape. The new charge distribution in the nucleus gives rise to an electric field gradient in the QD. The quadrupolar moment of the nucleus now reacts with this strain field and a quadrupolar interaction [131, 132] can be observed.

Starting from classical description, the Hamiltonian for the interaction between a single nucleus and the electron cloud is derived [122, 133]. The interaction energy E of the charge distribution of the nucleus of density ρ with the potential V is calculated by

$$E = \int \rho(\vec{r})V(\vec{r})\mathrm{d}\vec{r}. \tag{3.1.15}$$

The potential V is generated by the electron at $\vec{r}$ where $\vec{r} = 0$ describes the mass center of the nucleus. In a Taylor expansion of V around the origin, the energy is rewritten as

$$E = V(0) \int \rho \mathrm{d}\vec{r} + \sum_{\alpha} V_{\alpha} \int r_{\alpha} \rho \mathrm{d}\vec{r} + \frac{1}{2} \sum_{\alpha,\beta} V_{\alpha\beta} \int r_{\alpha} r_{\beta} \rho \mathrm{d}\vec{r} \tag{3.1.16}$$

where r_{α}, r_{β} denote the spatial directions x, y, z and

$$V_{\alpha} = \left. \frac{\partial V}{\partial r_{\alpha}} \right|_{r=0} \quad \text{and} \quad V_{\alpha\beta} = \left. \frac{\partial^2 V}{\partial r_{\alpha} \partial r_{\beta}} \right|_{r=0} \tag{3.1.17}$$

are the derivatives of the potential. The first derivative gives the electric field components and $\partial^2 V / \partial r_{\alpha} \partial r_{\beta}$ are the tensor components of the electric field gradient.

The first term of Eq. (3.1.16) describes a point charge. The second summand is the electric dipole moment of the nucleus. It usually vanishes due to parity when the center of mass is at the center of charge. The third term is the quadrupolar energy $E^{(2)}$. Since V must satisfy the Laplace equation $\nabla^2 V = 0$ this contribution vanishes in bulk material where $V_{xx} = V_{yy} = V_{zz} = 0$. However, it contributes to the dynamics in a QD, where the symmetry is broken.

An entry of the quadrupole moment tensor Q is given by

$$Q_{\alpha\beta} = \int \left(3 r_{\alpha} r_{\beta} - \delta_{\alpha\beta} r^2\right) \rho \mathrm{d}\vec{r}. \tag{3.1.18}$$

It is used to rewrite the quadrupolar energy $E^{(2)}$ as

$$E^{(2)} = \frac{1}{6} \sum_{\alpha\beta} V_{\alpha\beta} Q_{\alpha\beta}. \tag{3.1.19}$$

For a transition to a quantum mechanical picture the classical density has to be substituted by the operator $\rho = e \sum_k^{\text{protons}} \delta(\vec{r} - \vec{r}_k)$ with k nuclear particles with charge e.

The Hamiltonian of the quadrupolar interaction is

$$\mathcal{H}_{\mathrm{Q}} = \frac{1}{6} \sum_{\alpha\beta} V_{\alpha\beta} Q_{\alpha\beta}. \tag{3.1.20}$$

The Wigner-Eckart theorem allows to calculate the tensor elements of the quadrupolar operator via the Clebsch-Gordon coefficients and express (3.1.20) in spin coordinates. The entries of the quadrupole tensor are given by

$$\left\langle Im\tilde{\eta} \left| e \sum_{k}^{\text{protons}} (3 r_{\alpha,k} r_{\beta,k} - \delta_{\alpha\beta} r_k^2) \right| Im'\tilde{\eta} \right\rangle = C \left\langle Im\tilde{\eta} \left| 3 \frac{I_{\alpha} I_{\beta} + I_{\beta} I_{\alpha}}{2} - \delta_{\alpha\beta} I^2 \right| Im'\tilde{\eta} \right\rangle, \tag{3.1.21}$$

where I is the total angular momentum and m the secondary total angular momentum quantum number and $\tilde{\eta}$ a set of quantum numbers. The constant C can be identified as

$$C = \frac{eQ}{I(2I-1)} \tag{3.1.22}$$

with the quadrupole moment of the nucleus Q, which is independent of the quantum numbers m, m' or the spatial directions r_α, r_β.

The electric field gradient is diagonalized. Plugging the tensor entries Eq. (3.1.21) into the Hamiltonian (3.1.20), we arrive at

$$\mathcal{H}_\mathrm{Q} = \frac{e^2\tilde{d}Q}{4I(2I-1)}\left[3I_z^2 - I(I+1) + \eta_\mathrm{Q}(I_x^2 - I_y^2)\right]. \tag{3.1.23}$$

The electric field gradient in z-direction is replaced by $e\tilde{d} = V_{zz}$ and the asymmetry parameter $\eta_\mathrm{Q} = (V_{xx} - V_{yy})/V_{zz}$ is introduced. In the following, we apply the assumption [83] of axial symmetry $\eta_\mathrm{Q} = 0$, meaning that the quadrupolar interaction strength does not depend on an angle perpendicular to the growth axis z.

To include the whole nuclear spin bath, we sum over all individual nuclear spin Hamiltonian operators. Each has its own symmetry axis defined by the eigenvector of the largest eigenvalue of the electric field gradient, which is called the quadrupole orientation $\vec{n}_k$. The influence of the quadrupolar interaction [83, 134, 135] on all nuclear spins is given by

$$H_\mathrm{Q} = \sum_k \mathcal{H}_\mathrm{Q}^k = \sum_k \frac{e^2\tilde{d}Q}{4I(2I-1)}\left(3(\vec{I}_k\vec{n}_k)^2 - I(I+1)\right). \tag{3.1.24}$$

The prefactor is encapsulated in the parameter

$$\overline{q}_k = \frac{3e^2\tilde{d}_k Q}{4I(2I-1)} \tag{3.1.25}$$

for each nuclear spin.

The quadrupole orientation vector $\vec{n}_k$ is a unit vector defined by its deviation angle θ from the growth axis which is aligned in z-direction. The variation of the angle θ depends on the isotope. Since in future investigations in this work all nuclear spins are considered to be of the same kind, an average angle $\overline{\theta} = 23.78°$ is introduced. Then the quadrupole orientation vector $\vec{n}_k$ is restricted to a sphere segment around the z-axis defined by the angle $\theta_\mathrm{max} = 35°$ which reproduces the the mean deviation angle of $\overline{\theta}$ for $In_{0.4}Ga_{0.6}As$ [135]. The random unit vectors $\vec{n}_k$ are generated uniformly within this sphere segment [81], see Fig. 3.2. The second quadrupolar parameter $\overline{q}_k$ defines the interaction strength. With $\overline{q}_k/(2\pi) \sim 1.677\,\mathrm{MHz}$ for As and 2.346 MHz for In in $In_{0.4}Ga_{0.6}As$ QD [134, 135], the quadrupolar interaction is of the order of magnitude of the nuclear Zeeman interaction for an external magnetic field of $|\vec{B}_\mathrm{ext}| = 1\,\mathrm{T}$. In this model the strength of the quadrupolar coupling $\overline{q}_k$ is defined in relation to the hyperfine coupling constants [81] via the ratio

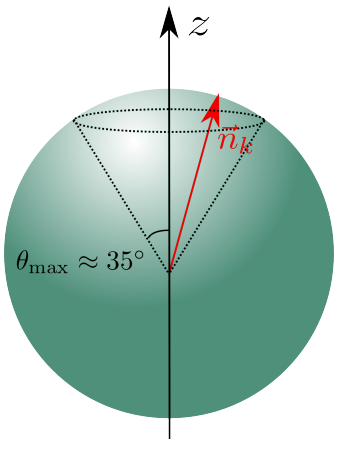

Figure 3.2: A random quadrupole orientation vector $\vec{n}_k$ inside the cone given by θ_max in dotted lines.

$$Q_\mathrm{r} = \frac{A_\mathrm{q}}{A_\mathrm{S}} \tag{3.1.26}$$

with $A_\mathrm{q} = \sum_k \overline{q}_k$ where the $\overline{q}_k$ are assumed to be uniformly distributed. This simplification neglects any potential correlation to the hyperfine coupling constant due to position in the QD [136]. Each quadrupole coupling is generated via

$$\overline{q}_k = Q_\mathrm{r} x_k \frac{\sum_k A_k}{\sum_k x_k}. \tag{3.1.27}$$

The random variable x_k is uniformly distributed in $x_k \in [0.5, 1]$.

The quadrupolar interaction only contributes to the dynamics for $I > 1/2$ which can lead to a severe restriction concerning the nuclear spin bath size [81, 93, 137]. To simplify the model it was suggested to map the problem on an effective spin $I = 1/2$ model [83]. However, we take another path by deriving a classical analogon to the quantum mechanical Hamiltonian in Sec. 5.2.2.

In an In(Ga)As QD the frequency induced by the Knight field is reported to be of the order of a few MHz [134, 138–140], the same holds for the prefactor $\overline{q}_k$ [134, 135]. However, while all $\vec{I}_k$ are influenced by the same Knight field, the quadrupolar interaction varies from nuclear spin to nuclear spin. This way the influence of the overall quadrupolar interaction on the nuclear spin is often weaker than that of the hyperfine interaction.

3.1.3 Characteristic time scale

The characteristic time scale T^* governs the short time dynamics given by the dephasing time of the electron spin dynamics. A similar time scale was also introduced by Merkulov et al. [55] and its systematic derivation of the constant is presented in Ref. [141]. Via the fluctuations of the Overhauser field $\langle \vec{B}_\mathrm{N}^2 \rangle$ the characteristic time scale

$$T^* = \sqrt{\frac{3}{4} \frac{1}{\langle \vec{I}^2 \rangle \sum_{k=1}^{N} A_k^2}} \tag{3.1.28}$$

is defined, and it retains the dependence of $\vec{B}_\mathrm{N}$ on the spin length of the nuclear spins, see Eq. (3.1.9). For a quantum mechanical approach $\langle \vec{I}^2 \rangle = I(I+1)$, while for a classical one it is I^2. For large nuclear spins ($I \to \infty$) both approaches become identical. The fluctuation frequency $\omega_\mathrm{fluc} = 1/T^*$ defines a characteristic energy scale. The dephasing time T^* was experimentally determined to be of the order of magnitude of 100 ps to a few nanoseconds [78, 81, 142–144] depending on the size of the QD. Hackmann et al. [49] linked $T^* \sim \sqrt{N(L_0)}$ to the number of nuclei in a sphere of radius L_0 where L_0 is the length scale of the envelope function.

The total Hamiltonian is composed of the hyperfine coupling of electron and nuclear spins with their Zeeman interaction Eqs.(3.1.13) and the nuclear-electric quadrupolar interaction (3.1.24)

$$H_\mathrm{tot} = H_\mathrm{CSM} + H_\mathrm{Q}. \tag{3.1.29}$$

The characteristic time scale can be used to define a dimensionless Hamiltonian

$$H = H_\mathrm{tot} T^* = \vec{b}_\mathrm{ext} \vec{S} + \zeta \vec{b}_\mathrm{ext} \sum_{k=1}^{N} \vec{I}_k + \sum_{k=1}^{N} a_k \vec{I}_k \vec{S} + \sum_{k=1}^{N} q_k \left(\vec{I}_k \vec{n}_k \right)^2 \tag{3.1.30}$$

with the external magnetic field $\vec{b}_{\text{ext}} = g_{\text{e}}\mu_{\text{B}}T^*\vec{B}_{\text{ext}}$ and the ratio ζ given by Eq. (3.1.14). The coupling constants of the hyperfine interaction are

$$a_k = T^* A_k. \tag{3.1.31}$$

Note that only the rescaled time t/T^* and the frequency $\omega/\omega_{\text{fluc}}$ are dimensionless. Since the short time dynamics is only governed by the fluctuations of the Overhauser field, it becomes invariant in the time frame of T^*. The quadrupolar couplings q_k can also be expressed dependent on a_k and Eq. (3.1.27) is rewritten as

$$q_k = T^*\overline{q}_k = Q_{\text{r}} x_k \frac{\sum_k a_k}{\sum_k x_k}. \tag{3.1.32}$$

3.2 Distribution of the hyperfine coupling constants

We found that the coupling constants a_k are closely related to the time scale of the system T^*, see Eq. (3.1.28). Up until now no assumption about their distribution $p(a)$ was included in the model. A few of the different distributions reoccurring in the literature [49, 52, 127, 145, 146] shall be presented here.

The possibly easiest distribution features equal coupling constants $A_k = A = 1/\sqrt{N}\,\forall\, k$. A CSM with this kind of A_k is referred to as the box model. While seemingly simplistic the box model allows for an analytical treatment of the CSM in some cases [39, 60, 77] or at least a reduction in complexity which proves advantageous concering computation time.

A starting point for the derivation of a distribution which more realistically represents the hyperfine coupling constants of a model bath with $N \ll 10^5$ is given by Eq. (3.1.11). It links the coupling constant to the squared modulus of the envelope of the electron wave function $|\psi(\vec{R})|^2$. The wave function assumes the form

$$\psi(\vec{R}_k) \propto L_0^{-\xi/m} \exp\left[-\frac{1}{2}\left(\frac{r}{L_0}\right)^m\right]\Bigg|_{r=|\vec{R}_k|} \tag{3.2.1}$$

where $L_0 \approx 5\,\text{nm}$ is the characteristic length scale of the QD [141] and $\vec{R}_k$ the location of the k-th nucleus. For $m = 1$ the envelope of the wave function is hydrogen like; for $m = 2$ it is Gaussian [127]. In the following we restrict ourselves to $m = 2$. The parameter ξ is determined by the dimension of the QD. An isotropic QD corresponds to $\xi = 3$. If the quantization of the QD along the growth axis exceeds that in the QD plane then $\xi = 2$.

The probability to find a large coupling constant increases with larger r in Eq. (3.2.1). Therefore, the cut-off radius R_0 is introduced. For a QD of spherical shape in ξ dimensions the probability to find a nuclear spin with distance r is given by $\xi r^{\xi-1}/R_0^\xi$. Via the normalization condition $p(A)\mathrm{d}A = p(r)\mathrm{d}r$ the coupling constant distribution is determined

$$p_{r_0}(A) = -\frac{\xi}{2r_0^\xi}\frac{1}{A}\left[\ln\left(\frac{A_{\max}}{A}\right)\right]^{\frac{\xi-2}{2}}. \tag{3.2.2}$$

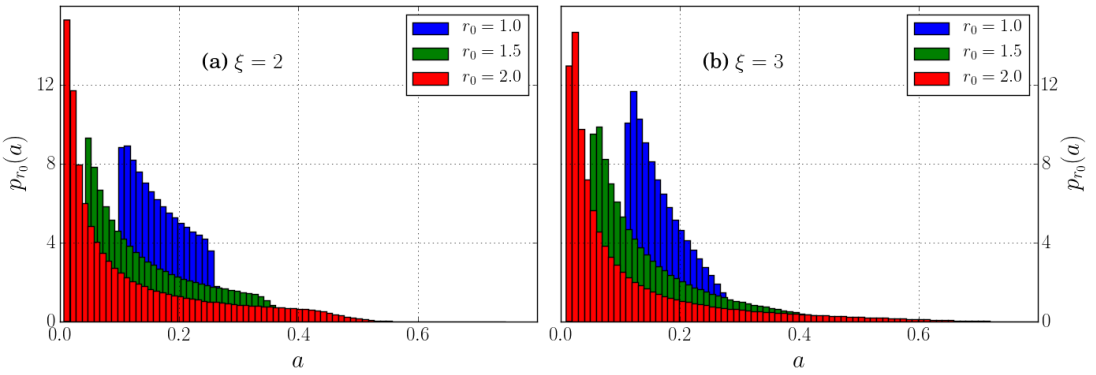

Figure 3.3: Histogram of the hyperfine coupling constant distribution for $N = 100$ for different r_0. Panel (a) $\xi = 2$ and panel (b) $\xi = 3$. Each histogram uses 10^7 data points.

It describes the probability to pick a nuclear spin with the coupling constant A for a given r_0. The ratio $r_0 = R_0/L_0$ determines how far the wave function is taken into account outside the QD. The maximum coupling constant is given at the center of the QD $A_{\max} = A(0)$. The smallest coupling constant is predetermined by the cut-off r_0 as $A_{\min} = A_{\max} \exp(-{r_0}^2)$. This distribution was first used by Hackmann [49, 75, 81, 82].

To generate the distribution, inverse transformation sampling is used, where $p(A)\mathrm{d}A = p(u)\mathrm{d}u$ with a random number u which is uniformly distributed on $[0, 1]$. By integrating over both sides we arrive at

$$u(A) = \frac{1}{r_0^\xi} \left[\ln\left(\frac{A_{\max}}{A} \right) \right]^{\xi/2}. \tag{3.2.3}$$

From there on the inversion function provides the desired result

$$A = A_{\max} \exp\left(-r_0^2 u^{2/\xi} \right), \tag{3.2.4}$$

which is utilized to generate the hyperfine coupling constants. For $\xi = 2$ the coupling constants are exponential which is found in literature [41, 48, 58, 93, 129].

Exemplary histograms of the distributions for different r_0 for $\xi = 2$ and $\xi = 3$ are found in Fig. 3.3 in panel (a) and (b), respectively. For $\xi = 2$ the probability to find coupling constants of the same order of magnitude is enhanced compared to $\xi = 3$. This fact is most obvious for $r_0 = 1.0$ where the probability to find smaller coupling constants is noticeably higher for $\xi = 3$ than for $\xi = 2$. The same trend is observed for larger r_0 where finding small coupling constants is more likely the larger the cut-off ratio r_0. This coincides with the fact that when more nuclear spins are allowed in a larger radius R_0 around the electron spin, most of those nuclear spins only interact weakly with $\vec{S}$. Only a few nuclear spins are left to contribute significantly to the dynamics. This necessitates an increasing number of nuclear spins N in the model if r_0 is large enough to represent the distribution adequately. For $N = 100$ the cut of $r_0 = 1.5$ has proven to be sufficient.

While the short time dynamics is governed by T^* defined in the previous section, the additional moments of the probability density function $p_{r_0}(a_k)$ also influence the long-time limit of the system [55, 79, 127]. Merkulov et al. [55] proposed the correlation function of the Overhauser field, which is proportional to $a_S = \sum_k a_k$, as a quantity to

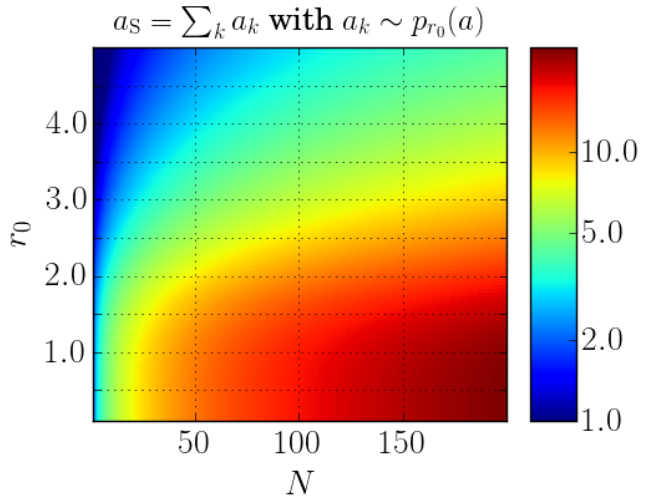

Figure 3.4: The sum over all coupling constants a_S for $\xi = 3$ as a function of the number of nuclear spins N and the cut-off ratio r_0. The coupling constants follow $a_k \sim p_{r_0}(a)$.

measure the influence on the long-time behavior

$$\tilde{\gamma}^{-1} \propto \frac{\langle A \rangle^2}{\langle A^2 \rangle} = \frac{a_S^2}{N}. \tag{3.2.5}$$

The analytical result of a_S is depicted in Fig. 3.4 as a function of r_0 and N for $\xi = 3$. The expectation value of the sum over all a_k is

$$a_S = \sqrt{3N} \frac{\int_{A_{\min}}^{A_{\max}} p(A) A \mathrm{d}A}{\sqrt{\int_{A_{\min}}^{A_{\max}} p(A) A^2 \mathrm{d}A}} = \frac{3\sqrt{N}}{\sqrt{r_0^3}} \frac{\sqrt{\pi}\mathrm{erf}(r_0) - 2\mathrm{e}^{-r_0^2}}{\sqrt{\sqrt{2\pi}\mathrm{erf}(\sqrt{2}r_0) - 4r_0\mathrm{e}^{-2r_0^2}}}. \tag{3.2.6}$$

For small r_0 the sum a_S assumes its maximum value $\max(a_S) = \sqrt{3N}$ which is equivalent to the box model and the effective number of nuclear spins contributing to the central spin dynamics is $a_S^2 \sim N$. Each nuclear spin contributes equally. For a large cut-off sphere around the electron spin the sum over all a_k is given by $\min(a_S) = \sqrt{3}$. Then all nuclear spins are $a_k = 0$ except for one which assumes the maximal possible coupling constant of $\sqrt{3}$. The number of nuclear spins which couple significantly to the central spin is 1. This shall be discussed a bit more in-depth later in Sec. 5.3.3.

Also, other distributions are imaginable like a uniform distribution [38] or a distribution with equidistant coupling constants [52, 53]. A similar scheme was also applied for exponential coupling constants where the random parameter u in (3.2.4) is replaced with a set of evenly spaced values in a given interval [58, 127].

Chapter 4

Correlation functions in the central spin model

Correlation functions are a useful tool to reveal correlations between measurands. Its order is determined by the number of operators involved. Here, we have to distinguish between correlation functions of operators which stand in for different physical measurement parameters and auto-correlation functions. Auto-correlation functions describe the correlation of a measurand with itself at different times. The auto-correlation function of spins in the frequency space is called spin noise.

We discuss the general definition of cumulants and how they pertain to correlation functions. In the following, we restrict ourselves to the second and fourth-order correlation functions since in systems with time reversal symmetry the third-order spin correlation is imaginary and therefore not an observable [147].

4.1 Correlation functions

Cumulants are used to reveal interactions and correlations in system. Only if correlation exists the cumulant displays a non-zero value. Therefore, Kubo's generalized cumulant expansion provides an important statistical tool for solving many physical problems ranging from thermodynamics to solid state physics [148–152]. The cumulant generating functional for a random variable X is

$$K_X(\xi) = \ln\Big(\langle e^{\xi X}\rangle\Big) = \ln\left(\sum_{n=0}^{\infty}\frac{\xi^n}{n!}m_n\right) = \sum_{\nu=1}^{\infty}(-1)^{\nu+1}\frac{\big(\langle e^{\xi X}\rangle - 1\big)^{\nu}}{\nu} = \sum_{n=1}^{\infty}\frac{\xi^n}{n!}\kappa_n. \tag{4.1.1}$$

The bracket $\langle X\rangle$ denotes the expectation value of a random variable X. In many-particle systems X pertains to particles or excitations. The cumulant generating function is linked to the characteristic function $\langle e^{\xi X}\rangle$ via the natural logarithm. The parameter $m_n = \langle X^n\rangle$ is the n-th moment and κ_n the n-th cumulant of the random variable X. The cumulant can be calculated via the derivative

$$\kappa_n = \left.\frac{\partial^n K_X(\xi)}{\partial \xi^n}\right|_{\xi=0}. \tag{4.1.2}$$

The same concept is applicable for multiple random variables. The first cumulant of X is identical to its first moment: the mean value $\langle X\rangle_c = \langle X\rangle$. The subscript c refers to the cumulant average. But already for the second-order cumulant and moment deviate. The covariance of X_1 and X_2 is given by

$$\langle X_1 X_2\rangle_c = \langle X_1 X_2\rangle - \langle X_1\rangle\langle X_2\rangle \tag{4.1.3}$$

and vanishes for two independent random variables. Higher orders of moments can be expressed via a sum of cumulants of the same and combinations of lower-order cumulants by rewriting Eq. (4.1.1). All contributions involving cumulants with two or more independent variables vanish. Vice versa κ_n is composed of the moment m_n minus all combinations of lower moments that represent lower-order correlations. If X is a random variable that follows a Gaussian probability distribution, all cumulants with $n > 2$ vanish.

Therefore, higher-order cumulants present a way to access true correlations beyond that of Gaussian noise [92, 95, 153]. In the quantum mechanical calculations, the random variables are replaced by operators [154] and the average by traces.

4.2 Second-order correlation function and spin noise

Spin-noise experiments on singly charged semiconductor QDs are typically conducted at temperatures of $T = 4 - 6\,\mathrm{K}$, which can be considered as a high-temperature limit, since its thermal energy of $\sim 350 - 520\,\mu\mathrm{eV}$ is very large compared to the energy scale of the Overhauser field with $A_\mathrm{S} \approx 90\,\mu\mathrm{eV}$ [55, 126]. If, additionally, the external magnetic field is low ($|\vec{B}_\mathrm{ext}| < 4\,\mathrm{T}$), the equilibrium spin polarization can be neglected and the second-order moment, the auto-correlation function, is identified as the cumulant. In the time domain the second-order correlation function is

$$\tilde{C}_2(t_1, t_2) = \langle S_z(t_1) S_z(t_2)\rangle, \tag{4.2.1}$$

which is a measure of the joint variability of the z-component of the spin at the start time of the measurement t_1 and a second time t_2. Since we assume equilibrium, the time dependency of $\tilde{C}_2$ is reduced to the relative time $\tau = t_2 - t_1$ by exploiting the commutability the Hamiltonian and the density operator. The auto-correlation function

$$C_2(\tau) = \langle S_z(\tau) S_z(0)\rangle \tag{4.2.2}$$

is translationally invariant in time. This scheme extends to higher-order auto-correlation functions. If the time invariance is given, the number of arguments of C_n can be lowered from n to $n-1$. The Fourier transform of $C_2(\tau)$ is called the spin-noise spectrum

$$C_2(\omega) = \int_{-\infty}^{\infty} d\tau \langle S_z(\tau) S_z(0)\rangle e^{-i\omega\tau}. \tag{4.2.3}$$

A useful function [147] for the transition from time domain to frequency space for spin correlation functions of arbitrary order is the Fourier transform of the Heisenberg operator $S_z(t)$

$$a(\omega) = \frac{1}{\sqrt{T_m}} \int_{-T_m/2}^{T_m/2} \mathrm{d}t\, e^{-\mathrm{i}\omega t} S_z(t). \tag{4.2.4}$$

The Fourier transform is applied for the duration of the measurement T_m. For symmetry reasons the measurement time starts at $t_0 = -T_m/2$. The prefactor $1/\sqrt{T_m}$ ensures the convergence of $\tilde{C}_2(\omega_1, \omega_2)$.

The Wiener-Chintchin theorem [68, 155, 156] connects the steady-state spin autocorrelation function $\tilde{C}_2(\omega_1, \omega_2) = \langle a(\omega_1)a(\omega_2)\rangle$ to the spin-noise spectrum. A prerequisite for the theorem is that the limit $T_m \to \infty$ can be applied. Albeit the measurement time is finite in an experiment, it is assumed large compared to the time scale of the spin decay T^* [68, 147]. Employing the Fourier transformation (4.2.4) and using the translational invariance in time, the second-order spin correlation function is obtained

$$\begin{aligned}\tilde{C}_2(\omega_1, \omega_2) &= \lim_{T_m\to\infty} \langle a(\omega_1)a(\omega_2)\rangle \\ &= \lim_{T_m\to\infty} \frac{1}{T_m} \int_{-\frac{T_m}{2}}^{\frac{T_m}{2}} dt_1\, e^{-\mathrm{i}\omega_1 t_1} \int_{-\frac{T_m}{2}}^{\frac{T_m}{2}} dt_2\, e^{-\mathrm{i}\omega_2 t_2} \langle S_z(t_1)S_z(t_2)\rangle \\ &= \delta_{\omega_1,-\omega_2} C_2(\omega).\end{aligned} \tag{4.2.5}$$

The spin-noise spectrum $C_2(\omega)$ satisfies the sum rule

$$\int_{-\infty}^{\infty} d\omega C_2(\omega) = \frac{\pi}{2}. \tag{4.2.6}$$

4.3 Fourth-order spin noise

Unlike the second-order spin noise which has been extensively studied both in frequency and time domain [69, 75, 78], the investigation of higher-order spin noise is a recent development [96].

As already briefly discussed in Sec. 4.1, a cumulant of fourth order separates the true higher-order correlations from factorization by subtracting all combinations of moments which represent lower correlations [154]. The fourth-order cumulant of $a(\omega)$ is defined as

$$\begin{aligned}\tilde{S}_4(\omega_1, \omega_2, \omega_3, \omega_4) =& \tilde{C}_4(\omega_1, \omega_2, \omega_3, \omega_4) \\ &- \tilde{C}_2(\omega_1, \omega_2)\tilde{C}_2(\omega_3, \omega_4) \\ &- \tilde{C}_2(\omega_1, \omega_3)\tilde{C}_2(\omega_2, \omega_4) \\ &- \tilde{C}_2(\omega_1, \omega_4)\tilde{C}_2(\omega_2, \omega_3).\end{aligned} \tag{4.3.1}$$

The high-temperature limit eliminates all contributions of first order in a finite magnetic field. The same assumption of invariance in time applied in $\tilde{C}_2$ also holds for $\tilde{C}_4$ and allows for the elimination of one variable. In the limit $T_m \gg T^*$ the correlation function $\tilde{C}_4$ yields

$$\tilde{C}_4(\omega_1, \omega_2, \omega_3, \omega_4) = \delta_{\omega_1+\omega_2+\omega_3+\omega_4,0} C_4(\omega_1, \omega_2, \omega_3, -(\omega_1 + \omega_2 + \omega_3)). \tag{4.3.2}$$

The cut $S_4(\omega_1, \omega_2) = \tilde{S}_4(\omega_1, -\omega_1, \omega_2, -\omega_2)$ through the $\tilde{S}_4$-spectrum correlates two spin-noise power spectrum component $|a(\omega)|^2$ at different frequencies with each other.

Expressing this bispectrum $S_4(\omega_1, \omega_2)$ as

$$\begin{aligned} S_4(\omega_1, \omega_2) =& \tilde{S}_4(\omega_1, -\omega_1, \omega_2, -\omega_2) \\ =& C_4(\omega_1, \omega_2) - C_2(\omega_1) C_2(\omega_2) \\ & \times (1 + \delta_{\omega_1, \omega_2} + \delta_{\omega_1, -\omega_2}) \end{aligned} \tag{4.3.3}$$

with $C_4(\omega_1, \omega_2) = \tilde{C}_4(\omega_1, -\omega_1, \omega_2, -\omega_2)$ is possible since $a(-\omega) = a^*(\omega)$. A positive bispectrum indicates that a spin component with the frequency ω_1 increases the likelihood of finding a spin precession with ω_2 at the same time. Vice versa if $S_4(\omega_1, \omega_2)$ features anti-correlation, the probability for observing spin precessions with ω_1 and ω_2 simultaneously declines. For uncorrelated frequency components the cumulant vanishes. In the limit $T_m \to \infty$, the last two components of Eq. (4.3.3) only contribute for $\omega_1 = \pm\omega_2$.

The auto-correlation function C_4 obeys the sum rule

$$\int_{-\infty}^{\infty} d\omega_1 \int_{-\infty}^{\infty} d\omega_2 C_4(\omega_1, \omega_2) = \frac{\pi^2}{4}. \tag{4.3.4}$$

Combining the sum rules of C_2 and C_4 yields the sum rule for $S_4(\omega_1, \omega_2)$. The $\delta_{\omega_1, \pm\omega_2}$ are infinitesimally narrow and can be discarded when calculating the integral. The integral of $S_4(\omega_1, \omega_2)$ over the $\omega_1 - \omega_2$-plane vanishes indicating that the bispectrum contains as much spectral weight in the correlations as in the anti-correlations.

For the long measurement limit the Fourier transform of $C_4(\omega_1, \omega_2)$

$$\begin{aligned} \mathcal{F}C_4(\omega_1, \omega_2) = C_4(t_1, t_2) &= \frac{1}{T_m} \int_{-T_m/2}^{T_m/2} d\tau \langle S_z(t_1 + \tau) S_z(\tau) S_z(t_2) S_z \rangle \\ &= \frac{1}{T_m} \int_{-T_m/2}^{T_m/2} d\tau \langle \tilde{C}_2(t_1, \tau) \tilde{C}_2(t_2, 0) \rangle. \end{aligned} \tag{4.3.5}$$

connects the fourth-order correlation function in time with two measurements of $C_2(t_{1/2})$. One measurement starts at $t = 0$ and the other after a delay of τ. To get the correlation between the two measurements the average over the time delay is calculated. This shows that by measuring a higher-order correlation functions [92, 93] in the time domain, the bispectrum $S_4(\omega_1, \omega_2)$ becomes accessible in experiment.

Chapter 5

Electron spin dynamics in the central spin model

The purpose of this chapter is manifold: (1) The most intuitive approach for the Hamiltonian presented in Eq. (3.1.30) is the exact diagonalization. However, the nuclear spin bath size is limited for this approach due to exponential growth of the Hilbert space with the number of nuclear spins. (2) We derive the semiclassical approximation that is the main building block for all later investigations in this thesis. The semiclassical equations of motion should be able to represent all interactions of the Hamiltonian. (3) We present various approaches to solve the electron spin dynamics in a semiconductor QD, ranging from analytic solutions – especially the frozen Overhauser field approximation by Merkulov et al. [55] – to numerical solutions. (4) The standard set of parameters which is reused in later chapters shall be discussed. Those are utilized to benchmark the semiclassical approximation against other approaches and validate its use in following chapters. We also look into the variation of a few of those parameters and how they affect the dynamics.

5.1 Exact diagonalization

The Hamiltonian is constructed using the Kronecker product given by $C = A \otimes B$ where A is a $v \times m$ matrix and B a $p \times q$ matrix resulting in a $(vp) \times (mq)$ matrix C. For the hermitian spin matrices one index suffices. The spin operators S_i and $I_{k,i}$ with $i = x, y, z$ in the two or $n = (2I + 1)$ dimensional vector space are given by the matrix representation $S_{2,i} = (1/2)\sigma_{2,i}$ and $I_{n,k,i}$, respectively. In the case of the electron spin or $I = 1/2$, the spin operator $I_{2,k,i} = (1/2)\sigma_{2,i}$ is defined by the Pauli spin matrices $\sigma_{2,i}$.

For the n- and m-dimensional identity matrix $\mathbb{1}_n \otimes \mathbb{1}_m = \mathbb{1}_{nm}$ holds. Therefore, the spin matrices can be written as

$$S_{D,i} = \frac{1}{2}\sigma_{2,i} \otimes \mathbb{1}_{n^N} \tag{5.1.1a}$$

$$I_{D,k,i} = \mathbb{1}_{2n^{k-1}} \otimes I_{n,k,i} \otimes \mathbb{1}_{n^{N-k}} \tag{5.1.1b}$$

where N is the size of the nuclear spin bath and the dimension of the Hilbert space is given by $D = \dim(\mathcal{H}) = 2(n^N)$. Inserting the spin matrices into Eq. (3.1.30), the Hamiltonian is given in the eigenbasis of S_z and $I_{k,z}$.

For the time evolution of the autocorrelation function $\langle S_z(t)S_z(0)\rangle$ the orthonormal basis of eigenvectors $|\nu\rangle$ are used

$$\langle S_z(t)S_z(0)\rangle = \frac{1}{D}\sum_n \langle\nu|\mathrm{e}^{\mathrm{i}Ht}S_z\mathrm{e}^{-\mathrm{i}Ht}S_z|\nu\rangle. \tag{5.1.2}$$

The prefactor $1/D$ is due to the high-temperature limit where

$$\rho = \frac{1}{D}\mathbb{1}. \tag{5.1.3}$$

Inserting the identity, leads to the Lehmann representation

$$\begin{aligned}\langle S_z(t)S_z(0)\rangle &= \frac{1}{D}\sum_{\nu\mu}\langle\nu|\mathrm{e}^{\mathrm{i}E_\nu t}S_z\mathrm{e}^{-\mathrm{i}Ht}|\mu\rangle\langle\mu|S_z|\nu\rangle \\ &= \frac{1}{D}\sum_{\nu\mu}\mathrm{e}^{\mathrm{i}(E_\nu-E_\mu)t}|\langle\nu|S_z|\mu\rangle|^2\end{aligned} \tag{5.1.4}$$

where $\langle\nu|S_z|\mu\rangle = (U^\dagger S_z U)_{\nu\mu}$ is the matrix element of S_z in the eigenspace of H. The transformation matrix U is given by the eigenvectors $U = (\vec{\nu}_1, ...\vec{\nu}_D)$. At $t = 0$ the correlation function assumes $\langle S_z(t=0)S_z(0)\rangle = 1/4$ since the square of the spin vector is $\langle\vec{S}(t=0)\vec{S}(0)\rangle = \langle S_x(0)^2 + S_y(0)^2 + S_z(0)^2\rangle = S(S+1) = 3/4$.

The explicit construction of the Hamiltonian is not viable for a larger nuclear spin bath where more elaborate methods that do not require this step have to be applied for a quantum mechanical treatment. Examples for those methods include the Chebyshev polynomial expansion technique [49], a Lanczos approach [93] or a time-dependent density matrix renormalization group approach [52]. Also, decompositions of the hyperfine Hamiltonian in multiple, box-model like sub-Hamiltonians can be used as an approach [157].

5.2 Semiclassical approximation

While quantum mechanical approaches are feasible to extract the electron spin dynamics, we go another route and instead use a semiclassical approach (SCA). The SCA is a common approach which was employed by Merkulov et al. [55] to solve the dynamics for a frozen Overhauser field and was expanded upon by various others to investigate many aspects of the dynamics in QDs like the dephasing mechanisms or spin noise [53, 57, 58, 60, 120].

We derive equations of motion via a path integral formalism and discuss their intricacies like the dependence on spin length or the configuration averaging. This work was done in collaboration with Andreas Fischer. We then present the analytical solution by Merkulov and cover the numerical approach used in this work briefly.

5.2.1 Derivation of a scheme for the classical equations of motion

The path integral representation [158–160] of the partition function Z of a spin in an external magnetic field shall be derived. Subsequently, a saddle point approximation leads to a formalism which enables us to find classical equations of motion for arbitrary Hamiltonians.

We use spin coherent states [159, 161, 162] as a representation of a spin s where

$$|\uparrow_0\rangle = |s, m = s\rangle \tag{5.2.1}$$

is the maximum weight state. $|\uparrow_0\rangle$ is also the eigenstate of s_z as well as of $\vec{s}^{\,2}$

$$s_z|\uparrow_0\rangle = s|\uparrow_0\rangle \tag{5.2.2a}$$
$$\vec{s}^{\,2}|\uparrow_0\rangle = s(s+1)|\uparrow_0\rangle. \tag{5.2.2b}$$

We later identify the arbitrary spin $\vec{s}$ with either the electron spin $\vec{S}$ or a nuclear spin $\vec{I}_k$. The spin coherent states $|n\rangle$ are gained by the rotation of $|\uparrow_0\rangle$ on the Bloch sphere from the quantization axis in z-direction to a new direction. These rotations can be defined by the Euler angles $\{\phi, \psi \in [0, 2\pi), \theta \in [0, \pi)\}$

$$|n\rangle = \mathrm{e}^{-\mathrm{i}\phi s_z}\mathrm{e}^{-\mathrm{i}\theta s_x}\mathrm{e}^{-\mathrm{i}\psi s_z}|\uparrow_0\rangle = \mathrm{e}^{-\mathrm{i}\phi s_z}\mathrm{e}^{-\mathrm{i}\theta s_x}|\uparrow_0\rangle\mathrm{e}^{-\mathrm{i}\psi s} = \mathcal{R}(\phi,\theta)|\uparrow_0\rangle\mathrm{e}^{-\mathrm{i}\psi s}. \tag{5.2.3}$$

Since $|\uparrow_0\rangle$ is an eigenstate of s_z the rotation around ψ only enters as a phase factor and is neglected [160, 163]. The resolution of identity in this overcomplete basis is

$$\frac{2s+1}{4\pi}\int \mathrm{d}n|n\rangle\langle n| = 1. \tag{5.2.4}$$

The expectation value of the spin operator for the state $|n\rangle$ is $s\vec{n} = \langle n|\vec{s}|n\rangle$.

The representation via a partition function replaces the sum over all possible paths from n_{start} to n_{end} with a sum over all closed loops. The imaginary time interval is then split in N parts of length $\mathrm{i}\delta t$

$$Z = \lim_{N\to\infty} \mathrm{tr}\left(\mathrm{e}^{-\beta H}\right) = \lim_{N\to\infty} \mathrm{tr}\left(\mathrm{e}^{-\mathrm{i}\delta t H}\right)^N \tag{5.2.5}$$

with $\mathrm{i}\delta t = \beta/N$. In between each interval we insert a resolution of identity

$$Z = \lim_{N\to\infty}\left(\prod_{i=0}^{N-1}\mathrm{d}n_i\right)\int_{n_N=n_0}\prod_{i=0}^{N-1}\langle n_{i+1}|\mathrm{e}^{-\mathrm{i}\delta t H}|n_i\rangle. \tag{5.2.6}$$

Applying a first-order Taylor series approximation, we arrive at

$$Z = \lim_{N\to\infty}\prod_{i=0}^{N-1}\mathrm{d}n_i \exp\left[-\mathrm{i}\delta t\sum_{i=0}^{N-1}\left(\langle n_{i+1}|H|n_i\rangle + \frac{1}{\mathrm{i}\delta t}\left(\langle n_i|n_i\rangle - \langle n_{i+1}|n_i\rangle\right)\right)\right]. \tag{5.2.7}$$

In the continuum limit for $N \to \infty$ and $\delta t \to 0$ the second term can be identified as a first derivative in time

$$Z = \int \mathcal{D}[n]\exp\left[-\int_0^T \mathrm{d}t\left(\mathrm{i}\langle n|H|n\rangle - \langle\partial_t n|n\rangle\right)\right]. \tag{5.2.8}$$

The upper bound of the integral is $T = N\delta t = \beta$.

For the kinetic term $\int \mathrm{d}t\langle\partial_t n|n\rangle$, we obtain

$$\mathrm{i}s\int_0^T \mathrm{d}t\dot{\phi}\cos\theta \tag{5.2.9}$$

applying the periodic boundary conditions. We also define $\langle n|H|n\rangle$ as a classical Hamiltonian function $\langle n|H|n\rangle = H(\vec{n})$. The partition function now takes the form

$$Z = \int \mathcal{D}[n]\exp\left[-\mathrm{i}\int_0^T \mathrm{d}t(H(\vec{n}) - s\dot{\phi}\cos\theta)\right] \tag{5.2.10}$$

where the action $S_\mathrm{A}[\vec{n}]$ is easily identifiable as

$$S_\mathrm{A}[\vec{n}] = \int_0^T \mathrm{d}t(H(\vec{n}) - s\dot{\phi}\cos\theta). \tag{5.2.11}$$

The term $\int_0^T \mathrm{d}ts\dot{\phi}\cos\theta$ is called the Berry phase S_B and is induced by the overlap between coherent states.

We rescale the quantum mechanical operators of the Hamiltonian with their spin length. For large s this is equivalent to the classical limit where spins freely commutate

$$[s_i/s, s_j/s] = \epsilon_{ijk}s_k/s^2 \propto \mathcal{O}(1/s). \tag{5.2.12}$$

Furthermore, this limit $s \gg 1$ leads to a rapidly oscillating behavior of $\mathrm{e}^{-\mathrm{i}S_\mathrm{A}[\vec{n}]}$. While a quantum object takes every possible path, a large variation of the complex phase which weights each path leads to destructive interference. This suppresses all but the classical case given by the saddle point approximation $\delta S_\mathrm{A} = 0$.

As a constraint the length of $\vec{n}$ is fixed to $\vec{n}^2 = 1$. Therefore, the Lagrange function $\mathcal{L}$ is

$$\mathcal{L}(\vec{n}, \dot{\vec{n}}, \lambda) = S_\mathrm{B} - H(\vec{n}) - \frac{\lambda}{2}(\vec{n}^2 - 1) \tag{5.2.13}$$

with λ the Lagrange multiplier. The total functional derivative

$$\delta\mathcal{L} = \left(\frac{\mathrm{d}}{\mathrm{d}t}\nabla_{\dot{\vec{n}}}\mathcal{L} - \nabla_{\vec{n}}\mathcal{L}\right)\delta\vec{n} = 0 \tag{5.2.14}$$

includes the variation of the Berry phase term which can be calculated separately and is given in Ref. [158]

$$\frac{\mathrm{d}}{\mathrm{d}t}\nabla_{\dot{\vec{n}}}S_\mathrm{B} - \nabla_{\vec{n}}S_\mathrm{B} = s\vec{n}\times\dot{\vec{n}}. \tag{5.2.15}$$

Since the appearing cross product $\vec{n}\times\dot{\vec{n}} = [n]_x\dot{\vec{n}}$ provides a non-regular matrix, it is extended to an invertible rotation matrix $\mathcal{R}_{\vec{n}}$ around the angle $\pi/2$ with an additional zero from the rewritten second-order condition $(\vec{n}\otimes\vec{n})\dot{\vec{n}} = 0$. This leads to

$$s\left([n]_x + \vec{n}\otimes\vec{n}\right)\dot{\vec{n}} - \nabla_{\vec{n}}H(\vec{n}) - \lambda\vec{n} = s\mathcal{R}_n(\alpha = \pi/2)\dot{\vec{n}} - \nabla_{\vec{n}}H(\vec{n}) - \lambda\vec{n} = 0. \tag{5.2.16}$$

This equation is easily solved for $\dot{\vec{n}}$

$$\dot{\vec{n}} = \frac{1}{s}\left[\left(\vec{n}\nabla_{\vec{n}}H(\vec{n}) + \lambda\right)\vec{n} + \nabla_{\vec{n}}H(\vec{n}) \times \vec{n}\right]. \tag{5.2.17}$$

The Lagrange multiplicator takes the role of a generalized force along the direction of the spin and can be chosen as $\lambda = -\vec{n}\nabla_{\vec{n}}H(\vec{n})$. Only the cross product term remains on the right-hand side for the derivative of $\vec{n}$ with respect to time. Multiplication with the spin length s yields

$$\dot{\vec{s}} = \nabla_{\vec{s}}H(\vec{n}) \times \vec{s}. \tag{5.2.18}$$

A set of often coupled classical equations of motion is derived from this general equation by deriving the appropriate Hamilton function for more than one spin. The time evolution of a spin vector $\vec{s} = s\vec{n}$ is always defined by its precession in an effective field given by $\vec{b}_{\text{eff}} = \nabla_{\vec{s}}H(\vec{n})$.

5.2.2 Equations of motion for the central spin model Hamiltonian

The previously discussed interactions in a singly charged QD, see Chap. 3, can be divided in two categories, one in which a spin operator occurs linearly in the Hamiltonian and the quadrupolar interaction which features a quadratic term of $I_{k,i}I_{k,j}$ for $i, j = x, y, z$. The derivation of the classical equations of motion for the first case shall be discussed using the example of the hyperfine interaction. A similar approach is found in Chen et al. [54] and Al-Hassanieh et al. [57], who transferred the quantum mechanical dynamics of the CSM containing only the hyperfine and Zeeman interaction into a set of classical Euler-Lagrange equations of motion using the path integral method outlined in the previous section.

The derivation of the equation of motion for the electron spin is straight forward since $\vec{S}$ contributes only linearly to the Hamiltonian. We observe

$$S\vec{n}_S = \langle n_S|\vec{S}|n_S\rangle \tag{5.2.19}$$

where the expectation value $S\vec{n}_S$ are computed using the identity related to the Baker-Campbell-Hausdorff formula [160]

$$\mathrm{e}^{\mathrm{i}\phi S_i} S_j \mathrm{e}^{-\mathrm{i}\phi S_i} = S_j\delta_{ij} + (1-\delta_{ij})\cos(\pi)S_j - \epsilon_{ijk}S_k. \tag{5.2.20}$$

The vector $\vec{n}_S = \vec{\mathrm{e}}_r$ is identified with the unit vector $\vec{\mathrm{e}}_r = (\sin\theta\cos\phi, \sin\theta\sin\phi, \cos\theta)^{\mathrm{T}}$ in spherical coordinates. The vectors given by the spin coherent states $|n_S\rangle$ can be interpreted as a classical analogue to the quantum mechanical angular momentum states. The same scheme may be applied to the nuclear spins. With Eq. (5.2.18) the $(N+1)$ dimensionless effective fields of the linear terms for the central spin $\vec{S}$ and the N bath spins $\vec{I}_k$ are found:

$$\vec{b}^{S}_{\text{eff}} = \vec{b}_{\text{N}} + \vec{b}_{\text{ext}}\,, \tag{5.2.21a}$$

$$\vec{b}^{I_k}_{\text{eff}} = a_k\vec{S} + \zeta\vec{b}_{\text{ext}} \tag{5.2.21b}$$

where $\vec{b}_{\text{N}} = \sum_k a_k\vec{I}_k$ is the classical Overhauser field. Various approaches can be applied to solve these $(N+1)$ coupled Euler-Lagrange equations approximately. The

include a frozen Overhauser field approximation proposed by Merkulov [55] and elaborate approaches [58, 129] which make it possible to use large bath sizes while allowing a variation of the hyperfine coupling constants. After solving the equations of motion for an individual initial condition, averaging over spin vectors on the Bloch sphere remains to be done.

The derivation of the effective field $\nabla_{\vec{I}_k} H(\vec{n}_I) = \nabla_{\vec{I}_k} \langle n_I|H|n_I\rangle$ with $I\vec{n}_I = \langle n_I|\vec{I}|n_I\rangle$ for the quadrupolar action, see Eq. (3.1.24), requires a bit more effort. To calculate the classical $H(\vec{n}_I)$ an additional identity $\mathcal{R}(\phi,\theta)\mathcal{R}^{-1}(\phi,\theta)$ is introduced

$$\langle n_I|H|n_I\rangle \sim \left\langle n_I \left| \left(\vec{I}_k\vec{n}_k\right)^2 \right| n_I \right\rangle = \left\langle \uparrow_0 \left| \left(\mathcal{R}^{-1}(\phi,\theta)\vec{I}_k\vec{n}_k\mathcal{R}(\phi,\theta)\right)^2 \right| \uparrow_0 \right\rangle, \tag{5.2.22}$$

to replace $|n_I\rangle \to |\uparrow_0\rangle$. Again Eq. (5.2.20) is utilized to simplify this equation and we arrive at

$$\left\langle n_I \left| \left(\vec{I}_k\vec{n}_k\right)^2 \right| n_I \right\rangle = \left\langle \uparrow_0 \left| \left(\vec{I}_k\vec{n}'_k\right)^2 \right| \uparrow_0 \right\rangle \tag{5.2.23}$$

where $\vec{n}'_k = \mathcal{R}_y^{-1}(\theta)\mathcal{R}_z^{-1}(\phi)\vec{n}_k$ is the local easy axis $\vec{n}_k$ rotated by the angle θ about the y-axis and by ϕ about the z-axis. Since all features of $\vec{n}_k$, such as the spin length $|\vec{n}_k|^2 = 1$, are transferred to the rotated easy axis, the expectation value $\langle n_I|(\vec{I}_k\vec{n}_k)^2|n_I\rangle$ is rewritten as

$$\left\langle n_I \left| \left(\vec{I}_k\vec{n}_k\right)^2 \right| n_I \right\rangle = \left(\vec{n}'_k\vec{e}_z\right)^2 \left(I^2 - \frac{I}{2}\right) + \frac{I}{2}. \tag{5.2.24}$$

The rotation from $\vec{n}'_k$ is also applied to $\vec{e}_z$ which therefore is a unit vector parameterized in terms of spherical coordinates. $\vec{n}'_k\vec{e}_z$ becomes $\vec{n}_k\vec{I}_k/I$. The effective quadrupolar field is then

$$\nabla_{\vec{I}_k}(T^* H_{\mathrm{QPI}}) = 2\tilde{q}_k \left(\vec{n}_k\vec{I}_k\right)\vec{n}_k \tag{5.2.25}$$

with an adjusted quadrupolar interaction constant[1]

$$\tilde{q}_k = \left(1 - \frac{1}{2I}\right) q_k. \tag{5.2.26}$$

This coincides with the quantum mechanical result that quadrupolar interaction only occurs for $I > 1/2$. It also provides a scaling behavior for the quadrupolar coupling strength depending on simulated spin length I. Larger nuclear spins lead to a stronger quadrupolar interaction strength. In the limit $I \to \infty$, the corrective factor leads to $\tilde{q}_k = q_k$. For this case the effective field of the quadrupolar interaction can also be derived by applying a Heisenberg equation on Eq. (3.1.24) while assuming classical, commuting variables [137, 164].

Combining Eqs. (5.2.21) and (5.2.25) yield the following system of dimensionless, coupled differential equations for the electron spin $\vec{S}$ and the N nuclear spins $\vec{I}_k$:

$$T^* \frac{\mathrm{d}}{\mathrm{d}t}\vec{S} = \left(\vec{b}_{\mathrm{ext}} + \vec{b}_{\mathrm{N}}\right) \times \vec{S} \tag{5.2.27a}$$

$$T^* \frac{\mathrm{d}}{\mathrm{d}t}\vec{I}_k = \left[a_k\vec{S} + \zeta\vec{b}_{\mathrm{ext}} + 2\tilde{q}_k \left(\vec{n}_k\vec{I}_k\right)\vec{n}_k\right] \times \vec{I}_k. \tag{5.2.27b}$$

[1] This constant was derived in collaboration with A. Fischer

The effective field of the electron spin is given by the constant external magnetic field and the Overhauser field $\vec{b}_\mathrm{N}$ stemming from the hyperfine interaction with the nuclear spins. Since the hyperfine interaction is bidirectional, each nuclear spin is influenced by the central spin via the Knight field $a_k\vec{S}$. The effect of the Zeeman term on the nuclear spins is usually much weaker than the electronic one, since $\zeta \ll 1$. $\vec{b}^j_\mathrm{eff}/T^*$ with $j = S, I_k$ are the precession frequencies in the effective fields.

The classical formalism extended by the quadrupolar interaction also includes the scalar projection of the nuclear spin $\vec{I}_k$ onto the local easy axis $\vec{n}_k$. Together with $\tilde{q}_k$ this projection gives the angular velocity of the precession of an individual nuclear spin around a constant axis $\vec{n}_k$.

5.2.3 Explanatory notes about the classical spin length

Since the saddle point approximation is used in the derivation, the classical equations of motion only hold for the limit of large spins. For this approximation the restriction of discrete eigenenergies is lifted and the energy spectrum becomes continuous. Therefore, no quantum mechanical spin length can consistently be assigned to a classical spin vector. In the classical approximation a given spin length pertains to the overall scaling behavior of the spin dynamics rather than to physical effect that emerge due to a discrete eigenenergy spectrum. Those quantum mechanical effects cannot be captured by the SCA. Since the classical equations of motions are norm conserving for all spin lengths, the classical spin length in the simulation can be arbitrarily rescaled. In the following, we choose spin vector length unity $|\vec{S}'| = 1$ and $|\vec{I}'_k| = 1$ for the numerical simulations to represent the electron spin $S = 1/2$ and a nuclear spin of $I \geq 1/2$.

While the dynamics described by Eq. (5.2.27) does not change qualitatively, the time dependence of the solution changes with the spin length. For the normed spin vectors $\vec{S} \to \vec{S}' = \vec{S}/S$ and $\vec{I}_k \to \vec{I}'_k = \vec{I}_k/I$ the coupled differential equations change to

$$T^* \frac{\mathrm{d}\vec{S}'}{\mathrm{d}t} = \left(\vec{b}_\mathrm{ext} + \frac{I}{S}\sum_k a'_k \vec{I}'_k\right) \times \vec{S}' \,, \tag{5.2.28a}$$

$$T^* \frac{\mathrm{d}\vec{I}'_k}{\mathrm{d}t} = \left(\zeta\vec{b}_\mathrm{ext} + a'_k\vec{S}' + 2q'_k(\vec{n}_k\vec{I}'_k)\vec{n}_k\right) \times \vec{I}'_k \,. \tag{5.2.28b}$$

It is possible to absorb the spin length into coupling constants and quadrupolar interaction strength, like we did in Eq. (3.1.28) for the quantum mechanical difference of $I(I+1)$ to I^2 in the time constant T^*. This results in an adjusted coupling constant $a_k \to a'_k = Sa_k$ and $\tilde{q}_k \to q'_k = I\tilde{q}_k$. Furthermore, the Overhauser field is rewritten as $\vec{b}'_\mathrm{N} = \frac{I}{S}\sum_k a'_k\vec{I}'_k = \vec{b}_\mathrm{N}$ in the context of the normed spin vectors. Since the Overhauser field $\vec{b}_\mathrm{N}$ is invariant of the spin vector length, this modification does not alter the electron spin Larmor precession frequency $\omega_\mathrm{L}T^* = |\vec{b}_\mathrm{ext} + \vec{b}_\mathrm{N}|$.

The transformed constants a'_k and q'_k are generated by

$$a'_k = \frac{S}{I}\sqrt{\frac{3}{4}}\frac{A_k}{\sqrt{\sum_k A_k^2}} \,, \tag{5.2.29a}$$

$$q'_k = I\left(1 - \frac{1}{2I}\right) q_k = \frac{I - 1/2}{S}\frac{\sum_k a'_k}{\sum_k \overline{q}_k}\, Q_\mathrm{r}\, \overline{q}_k \tag{5.2.29b}$$

with $\overline{q}_k \sim \mathcal{U}(0.5, 1.0)$. For $I = 1/2$ the quadrupolar interaction q'_k vanishes. Since $I = S$ the coupling constants a'_k as well as the Overhauser field become independent of the spin length.

5.2.4 Classical configuration averaging

In order to obtain an expectation value in the semiclassical approach, we perform an averaging over multiple initial configurations. There are two possible interpretations for this process: The first is purely classical. This assumes that one QD is represented by a single classical trajectory which is only defined by its initial condition. The averaging then leads to the description of a QD ensemble with identical QDs [64]. This leaves out the different time scales T^* that can occur in an ensemble. The second advocates an interpretation based on the assumption of repetitive measurements on the same QD. This agrees well with the measurement method used in Ref. [33] where each captured electron spin dynamics already consists of multiple measurements.

A general form of the density operator reads

$$\rho = \sum_{\sigma,\{m\}} p_i |\sigma, \{m\}\rangle\langle\sigma, \{m\}|. \tag{5.2.30}$$

The nuclear bath spins are encoded in $|\{m\}\rangle = |m_1, ...m_N\rangle$ where each m_k denotes the eigenvalue of I_x along the external magnetic field. $|\sigma\rangle$, the eigenstates of σ_z, represent the electron spin. p_i is the probability of a state $|\sigma, \{m\}\rangle$. The density matrix is rewritten in spin coherent states $|\{\vec{n}\}\rangle$, cf. Eq. (5.2.3),

$$\rho = \left(\frac{2s+1}{4\pi}\right)^{N+1} \int \mathrm{d}\{\vec{n}\} |\{\vec{n}\}\rangle\langle\{\vec{n}\}|. \tag{5.2.31}$$

The measuring temperature range of about $6\,K$ [33] leads to much higher energies than those given by the fluctuations of the Overhauser field. This results in a disordered spin bath and renders the density matrix isotropic. A Monte Carlo integration is used to reduce the number of configurations to M while still adequately representing the entirety of the sample space of the spins

$$\rho \approx \frac{1}{M} \sum_{\alpha=1}^{M} |\{\vec{n}\}\rangle_\alpha \langle\{\vec{n}\}|_\alpha. \tag{5.2.32}$$

$|\{\vec{n}\}\rangle_\alpha$ denotes a random coherent state. Since the spin coherent states are pure, their time evolution can be calculated via a Schrödinger equation.

The coherent states integral over the entire Hilbert space is equivalent to the integral over all initial classical spin configurations [53–55]. The average over the subset of initial conditions for nuclear and electron spin leads to a discretized representation

$$\langle \vec{S}(t) \rangle = \frac{1}{N_\mathrm{C}} \sum_{\mu}^{N_\mathrm{C}} \vec{S}_\mu(t) \tag{5.2.33}$$

with N_C the number of classical configurations using the approximation (5.2.30). For the classical simulation the Schrödinger equation is replaced by the classical equations of motion Eq. (5.2.27). The solution to these differential equations of one configuration μ is $\vec{S}_\mu(t)$.

5.2.5 Frozen Overhauser field approximation

Merkulov et al. [55] first used a frozen Overhauser field approximation (FOA) to solve the semiclassical equations of motion, cf. Eqs. (5.2.27). As the name of the approximation implies, the nuclear spin dynamics is considered as frozen, $\frac{\mathrm{d}}{\mathrm{d}t}\vec{I}_k = 0 \,\forall k$. This assumption holds especially for the short time dynamics, where the spread of all hyperfine coupling constants has not yet come into play.

For a constant effective field $\vec{b} = \vec{b}_{\mathrm{ext}} + \vec{b}_{\mathrm{N}}$ the differential equation (5.2.27a) is solved exactly by

$$\vec{S}(t) = (\vec{S}_0\vec{n})\vec{n} + [\vec{S}_0 - (\vec{S}_0\vec{n})\vec{n}]\cos(\omega_{\mathrm{L}}t) + [\vec{S}_0 - (\vec{S}_0\vec{n})\vec{n}] \times \vec{n}\sin(\omega_{\mathrm{L}}t) \tag{5.2.34}$$

where the Larmor precession frequency $\omega_{\mathrm{L}}T^* = |\vec{b}|$ is connected to the absolute value of the effective field and the vector $\vec{n} = \vec{b}/|\vec{b}|$ is defined by its direction. The vector $\vec{S}_0$ denotes the initial spin vector at $t = 0$. This result is of special importance for later analytical calculations in a pulsed QD. For benchmarking purposes the expectation value of the electron spin dynamics is calculated. The Overhauser field distribution follows a Gaussian distribution

$$p_i(b_{\mathrm{N},i}) = \frac{1}{\sqrt{2\pi\sigma^2}}\exp\left(-\frac{b_{\mathrm{N},i}^2}{2\sigma^2}\right) \tag{5.2.35}$$

in all spatial directions i for the limit of an infinitely large nuclear spin bath due to the central limit theorem. The variance is $\sigma^2 = 1/4$. The probability density of an Overhauser field vector is

$$p\left(\vec{b}_{\mathrm{N}}\right) = \prod_{i=x,y,z} p_i\left(b_{\mathrm{N},i}\right) \tag{5.2.36}$$

with $\vec{b}_{\mathrm{N}} \sim \mathcal{N}\left(\vec{\mu} = 0, \underline{\underline{\Sigma}} = \frac{1}{4}\mathbb{1}\right)$ and $\sigma^2_{|\vec{b}_{\mathrm{N}}|} = 3/4$. The expectation value is easily calculated for the case of zero-magnetic field

$$\langle\vec{S}(t)\rangle = \frac{\vec{S}_0}{3}\left\{1 + 2\left[1 - \left(\frac{t}{2T^*}\right)^2\right]\exp\left[-\frac{1}{2}\left(\frac{t}{2T^*}\right)^2\right]\right\}. \tag{5.2.37}$$

The time evolution becomes universal in (t/T^*) with the characteristic time scale T^* given by the material properties of the quantum dot. For the long-time limit the spin expectation value approaches $\lim_{t\to\infty}\langle\vec{S}(t)\rangle = \vec{S}_0/3$.

The box model solution $a_k = a\,\forall\, k$ and the FOA yield the same result for a central spin model without an additional external magnetic field and without quadrupolar interaction. Transformation to relative $\vec{c} = \vec{S} - \sum_k \vec{I}_k$ and center-of-mass coordinates $\vec{C} = \vec{S} + \sum_k \vec{I}_k$ yields a set of differential equations

$$T^*\frac{\mathrm{d}\vec{C}}{\mathrm{d}t} = 0 \tag{5.2.38a}$$

$$T^*\frac{\mathrm{d}\vec{c}}{\mathrm{d}t} = a\vec{C} \times \vec{c} \tag{5.2.38b}$$

whose solution exhibits the same dynamics for $\vec{c}$ as the FOA does for the central spin. Since the nuclear spins cannot deviate from their initial alignment to each other in

the box model, the long-time limit of the FOA $\vec{S}_0/3$ is recovered. This finite value is the upper bound of the long-time electron spin expectation value in the absence of an external magnetic field. The distribution of coupling constants a_k and the subsequent change of alignment of nuclear spins to each other induce a long-time decay [79, 127].

For the case of an arbitrary non-zero external magnetic field the analytical calculation of the expectation value of the central spin becomes more complicated. Therefore, Eq. (5.2.34) is averaged over all initial conditions to obtain the FOA benchmarks.

5.2.6 Numerical solution in the semiclassical approximation

In each of the M classical configurations the central spin dynamics $\vec{S}_\mu(t)$ for a given Overhauser field realization $b_{\mathrm{N},\mu} = \sum_k a_k \vec{I}_{k,\mu}$ is calculated. For an unpolarized system the sphere point picking algorithm [165] is used to get random spin vectors on the Bloch sphere. The coupling constants a_k and q_k are initially generated and are equal for all configurations.

The fourth-order Runge-Kutta method (RK4) has proven to be a reliable tool to solve first-order differential equations $\dot{\vec{y}} = \vec{f}(t, y(t))$ with the initial value $\vec{y}(t_0) = \vec{y}_0$. $\vec{y}$ is the unknown time evolution of the nuclear or electron spin vector and $\vec{f}(t, \vec{y}(t))$ the vector product with the effective field Eq. (5.2.28).

Although simpler methods, like the Euler integration, are computationally less expensive, the additional accuracy makes the RK4 worthwhile. The increased precision stems from the higher-order terms of the Taylor series [166, 167] compared to the Euler method which is derived from only incorporating the first term of the Taylor series. This means that a single time step of RK4 consists of the $\vec{y}_i$ and the weighted average of four evaluations of the function: one at the start, one at the end of the time step and two in the middle. The time step width is denoted h. A time step from t_n to $t_{n+1} = t_n + h$ is calculated by

$$\vec{y}_{n+1} = \vec{y}_n + \frac{1}{6}\left(\vec{k_1} + 2\vec{k_2} + 2\vec{k_3} + \vec{k_4}\right) + \mathcal{O}(h^5) \tag{5.2.39}$$

with

$$\vec{k}_1 = h\vec{f}\,(t_n, \vec{y}_n) \tag{5.2.40a}$$

$$\vec{k}_2 = h\vec{f}\left(t_n + \frac{h}{2}, \vec{y}_n + \frac{1}{2}\vec{k}_1\right) \tag{5.2.40b}$$

$$\vec{k}_3 = h\vec{f}\left(t_n + \frac{h}{2}, \vec{y}_n + \frac{1}{2}\vec{k}_2\right) \tag{5.2.40c}$$

$$\vec{k}_4 = h\vec{f}\left(t_n + h, \vec{y}_n + \vec{k}_3\right). \tag{5.2.40d}$$

The increments $\vec{k}_i$ represent the slope at the evaluation points which are depicted in Fig. 5.1. If only $\vec{k}_1$ is taken into account, the Euler method is obtained. If, additionally, $\vec{k}_2$ is included, the resulting scheme is called the second-order Runge-Kutta method. Through the weighted combination of the k_i, the error terms up to the third order are eliminated. The local truncation error is therefore of the order $\mathcal{O}(h^5)$ and the total accumulated error is of the order $\mathcal{O}(h^4)$.

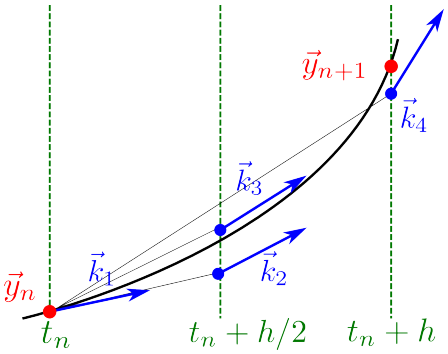

Figure 5.1: Schematics of the RK4 method. The black line represents the function to be approximated. The evaluation of the four derivatives are given by $\vec{k}_i$. The result after one RK4 step is $\vec{y}_{n+1}$.

Since the CSM is described by a system of coupled equations of motion, the time integration step has to be performed for each spin vector. As the information from the other spin vectors is kept constant during h, the time step width has to be adapted to match the fastest time scale. It is usually given by the electron spin precession in an external magnetic field. It is averaged over the RK4 result of N_C configurations to obtain the expectation value $\langle \vec{S}(t) \rangle$, cf. Eq. (5.2.33).

5.3 Benchmarks

The numerical solution to the coupled semiclassical equations of motion (5.2.27) is an integral part of this work. The equality between the autocorrelation function $C_2(t) = \langle S_z(t) S_z \rangle$ and the expectation value $\langle S_z(t) \rangle$ sets the stage for the benchmark of the approaches, cf. Sec. 5.3.1. The parameters are discussed in Sec. 5.3.2. Especially, the many parameters for the SCA are of importance, since this relatively simple simulation reappears as a building block for more intricate problems in later chapters. The benchmarks for $C_2(t)$ in Sec. 5.3.3 with quantum mechanical approaches assert the validity of the SCA with and without an external magnetic field. A good agreement can also be found if the quadrupolar interaction is included, see Sec. 5.3.4.

5.3.1 Spin correlation function and spin expectation value

Here, we show that the information contained in $\langle S_z(t) S_z(0) \rangle_{\rho_0}$ with the equilibrium density operator ρ_0 is equivalent to $\langle S_z(t) \rangle_{\rho_\uparrow}$ with a completely polarized electron spin at $t = 0$ [49].

In the high-temperature limit the autocorrelation function for an unpolarized electron spin is given by Eq. (5.1.2)

$$\langle S_z(t) S_z \rangle_{\rho_0} = \mathrm{Tr}\left(\rho_0 S_z(t) S_z\right) = \frac{1}{D} \mathrm{Tr}\left(S_z(t) S_z\right). \tag{5.3.1}$$

While $\langle S_z(t) \rangle_{\rho_0}$ vanishes for an unpolarized electron spin, a dynamics can be observed if a polarization at the time $t = 0$ is taken into account. Starting from an electron spin in the state $|\uparrow\rangle$:

$$\rho_\uparrow = \begin{pmatrix} 1 & 0 \\ 0 & 0 \end{pmatrix} \otimes \frac{2}{D} \mathbb{1} = \frac{2}{D} \left(\frac{1}{2} \mathbb{1} + S_z \right), \tag{5.3.2}$$

Isotope	μ/μ_N	I	g_N	$g_\mathrm{N}\mu_\mathrm{N}$ [MHz/T]	ζ_iso^{-1}
^{69}Ga	2.0166	3/2	1.3444	10.25	758
^{71}Ga	2.5623	3/2	1.7082	13.02	597
^{75}As	1.4395	3/2	0.9597	7.32	1062
^{115}In	5.5289	9/2	1.2286	9.37	829

Table 5.1: $\zeta_\mathrm{iso} = \frac{g_\mathrm{N}\mu_\mathrm{N}}{g_\mathrm{e}\mu_\mathrm{B}}$ of a single isotope. The magnetic moment μ, the nuclear spin length I and the g-factors are also given. The resonant frequency $g_\mathrm{N}\mu_\mathrm{N}$ of the nuclei of an isotope at 1 T can be compared to the electron Larmor frequency of 7.77 GHz.

the expectation value of the central spin dynamics is given by

$$\langle S_z(t)\rangle_{\rho_\uparrow} = \mathrm{Tr}\left(\rho_\uparrow S_z(t)\right) = \frac{2}{D}\mathrm{Tr}\left(S_z(t)S_z\right) = 2\langle S_z(t)S_z\rangle_{\rho_0}. \tag{5.3.3}$$

Therefore, we rescale the result for the autocorrelation function by a factor two and arrive at the same result as for an initially polarized expectation value.

5.3.2 Parameters

The SCA is benchmarked against the classical FOA as well as quantum mechanical methods: the exact diagonalization, the Chebyshev expansion technique and the Lanczos method. The parameters of the simulations are discussed in this section.

The z-component of the electron spin is simulated up to $T_\mathrm{max} = 400T^*$. The spin dynamics is investigated at an external magnetic field of $|\vec{b}_\mathrm{ext}| = 0$ and $|\vec{b}_\mathrm{ext}| = 10$. The external magnetic field is applied in x-direction. For all simulations the following parameters are chosen: The ratio $\zeta = \frac{g_k\mu_\mathrm{N}}{g_\mathrm{e}\mu_\mathrm{B}}$ of g-factors that governs nuclear Zeeman interaction is $\zeta = 1/800$. This value is an averaged quantity taking into account the different nuclear g-factors of the nuclear isotopes in InGaAs [168–170]. The electron has an effective g-factor of $|g_\mathrm{e}| = 0.555$ [171] in a GaAs quantum dot. The Larmor frequency for 1 T of both electron spin and nuclear spins is given by the product $\mu g/(2\pi)$ with μ being the magnetic moment, see Tab 5.1. Since the mass off the nuclei exceeds that of the electron by far, the Larmor frequency of the electron of 7.77 GHz is much larger than that of the average nucleus with 9.35 MHz [62]. All elements are assumed to contribute equally. Of the stable Gallium isotopes ^{69}Ga has a isotope abundance of $\sim 60\,\%$ and ^{71}Ga of $\sim 40\,\%$ [172]. Note that the Chebyshev data does not include the nuclear Zeeman splitting.

The bath size varies greatly between the different approaches. While an infinite bath size is assumed in the FOA, a bath size of $N = 100$ is used in the semiclassical simulation. The two quantum mechanical approaches are limited by the Hilbert space dimension and therefore by the available active memory. The number of nuclear spins for the exact diagonalization is $N = 10$. This number can be pushed to ~ 20 nuclear spins [48, 173] by partitioning the Hilbert space through conserved quantum numbers. The Lanczos method and the Chebyshev expansion technique can incorporate more spins with $N = 18$ and $N = 20$, respectively.

The coupling constants a_k follow the distribution $p_{r_0}(a)$ defined by Eq. (3.2.2) in a three-dimensional QD $\xi = 3$. $r_0 = 1.5$ has been chosen in accordance with [49]. The nuclear spin bath is unpolarized.

The quadrupolar interaction is neglected in the first part of the benchmark $Q_\mathrm{r} = 0$. In the second part the quadrupolar interaction strength is chosen to match the semiclassical and the Lanczos method [137]. The angle θ_max which restricts the easy axis $\vec{n}_k$ to a cone around the z-axis is 35°.

The number of classical configurations is $N_\mathrm{C} = 10^5$. Since the nuclear spin bath is unpolarized at $t = 0$, the nuclear spin vectors are distributed equally on the Bloch sphere. The electron spin vector is initially aligned in z-direction. The nuclear spin length is $I = 1/2$ for $Q_\mathrm{r} = 0$ and $I = 3/2$ for $Q_\mathrm{r} \neq 0$. The rescaling scheme presented in Sec. 5.2.3 is used in the simulation to account for the different spin lengths. The step width in the classical simulation is adapted depending on the external magnetic field. For $|\vec{b}_\mathrm{ext}| = 0$, the step width of $h = 0.01\,T^*$ is chosen in the RK4 in Eq. (5.2.39). The same step width has proven to be sufficient to trace the electron spin precession for the magnetic field of $|\vec{b}_\mathrm{ext}| = 10$. In the absence of a magnetic field C_2 is calculated analytically as the average over $N_\mathrm{C} = 10^5$ initial conditions of the Overhauser field.

To smooth the curves the Lanczos method averages over $N_\mathrm{C} = 32$ configurations of different a_k. The statistical noise of the exact diagonalization is reduced by averaging over $N_\mathrm{C} = 50$ configurations. The spin correlation function calculated via the Chebyshev method is also averaged over $N_\mathrm{C} = 50$ realizations of the hyperfine coupling constants.

5.3.3 Comparison without quadrupolar interaction

Figure 5.2 shows the comparison of the semiclassical approximation (SCA) to several other methods such as the exact diagonalization (ED), the Lanczos method, the Chebyshev expansion technique (CET) and the frozen Overhauser field approximation (FOA) in the absence of an external magnetic field on the left side as well as a finite magnetic field $|\vec{b}_\mathrm{ext}| = 10$ on the right-hand side. The data from the ED and the CET is taken from Hackmann et al. [49]. The data for the Lanczos method was provided by Nina Fröhling.

In absence of a magnetic field all methods agree very well in the short-time dynamics up to $t/T^* \approx 3$. Due to the precession of the central spin in a frozen or nearly constant Overhauser field, the FOA and the SCA coincide in the short-time dynamics even after the minimum of $C_2(t)$ at $t/T^* \approx 3.5$. They begin to differ after approximately $6\,T^*$ when spin dynamics obtained with the FOA reaches the plateau given by $S_0/3$, and $C_2(t)$ begins to decrease to a reduced value. The basis assumption for the FOA, the constant Overhauser field, is no longer valid for large times and, therefore, cannot capture any features of the long-time decay of $C_2(t)$ after $t/T^* \approx 10$. The box model faces the same problems due to its equivalence to the FOA. This leads to the insight that the long-time dephasing is attributed to the spread of the hyperfine coupling constants [55].

The deviation between classical and quantum mechanical calculation shortly after the minimum can be explained by the smaller number of nuclear spin in the quantum mechanical approach. Hackmann et al. [49] have shown that large r_0 as a parameter of the distribution p_{r_0} lead to damped oscillation of $C_2(t)$: The $p_{r_0}(a)$ favors a few large coupling constants and an increasing proportion of weak coupling constants the larger the r_0 becomes, cf. Sec. 3.2. For a small number of nuclear spins only the few spins with large a_k act as an effective field in which the electron spin precesses. As Stanek et al. [53] have shown this behavior also occurs for the classical simulation and for the

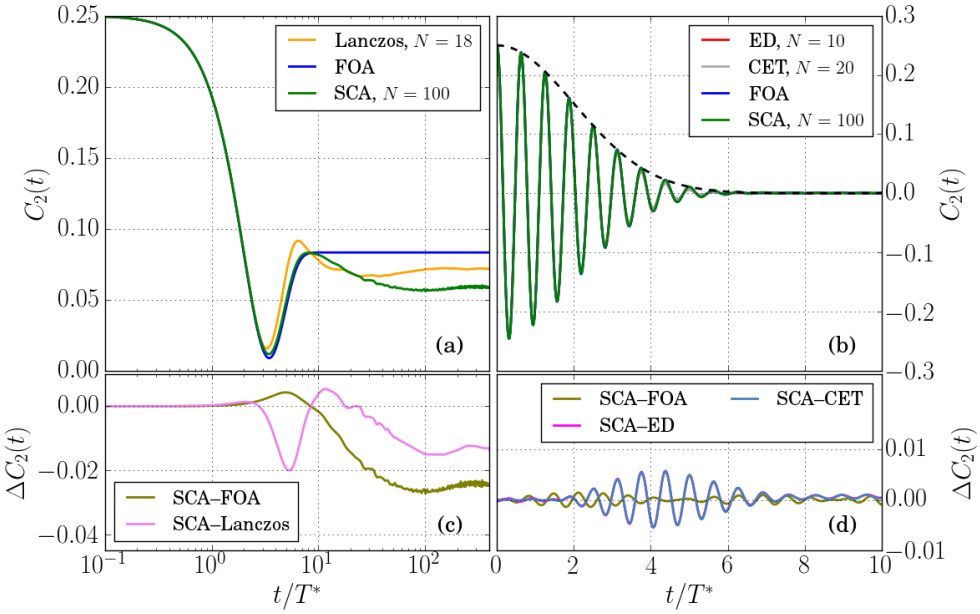

Figure 5.2: Comparison of spin correlation functions $C_2(t) = \langle S_z(t)S_z \rangle$ in absence of a magnetic field (a) and in a finite magnetic field $|\vec{b}_{\text{ext}}| = 10$ (b) calculated using different approaches. Quantum mechanical methods used are: Lanczos with $N = 18$, Chebyshev expansion technique (CET) with $N = 20$ and exact diagonalization (ED) with $N = 10$, and the two classical approaches are: the semiclassical approximation (SCA) and the frozen Overhauser field approximation (FOA), with $N = 100$ spins and $N_C = 100,000$. The CET data have been taken from Fig. 7 in Ref. [49]. The ED is taken from Ref. [89]. The Lanczos data is provided by Nina Fröhling. The dashed black line in (b) is the envelope function given by Eq. (5.3.5). All curves are congruent. (c) and (d) show the difference between SCA data and the data gained by other methods for both magnetic fields.

quantum mechanical tDMRG result for a small number of spins and is suppressed for a larger number of spins. The remaining weakly coupled nuclear spins induce the slower dephasing over time which is observed with both methods. The deviation between the long-time limits shall be discussed briefly in the following. The goal is not to make quantitative predictions for the constant value of the long-time limit $C_2(t \to \infty)$ but instead to explain the qualitative behavior of the plateau dependent on N and r_0. Exact predictions for different distributions are discussed in-depth in Refs. [54, 79, 127].

Figure 5.3 shows the Lanczos and the SCA result for different bath sizes N and cut-off parameters r_0. Panel (a) displays the dependence of the electron spin dynamics on the nuclear spin bath size. The autocorrelation function calculated with the Lanczos method shows a more pronounced maximum at $t/T^* \approx 6$ compared to the other curves. This effect can be attributed to the limited number of nuclear spins in the simulation. The long-time behavior of C_2 in the semiclassical simulation can be fitted to the quantum mechanical result if the bath size is reduced $N = 50$. With an increasing number of nuclear spins, the non-decaying fractions of the autocorrelation function calculated by the SCA converge [53]. Already for C_2 with $N = 100$ we observe a good agreement with the spin dynamics including $N = 200$.

Different coupling constants change the Overhauser field in a single classical configuration by allowing individual nuclear spins to align with each other differently over time.

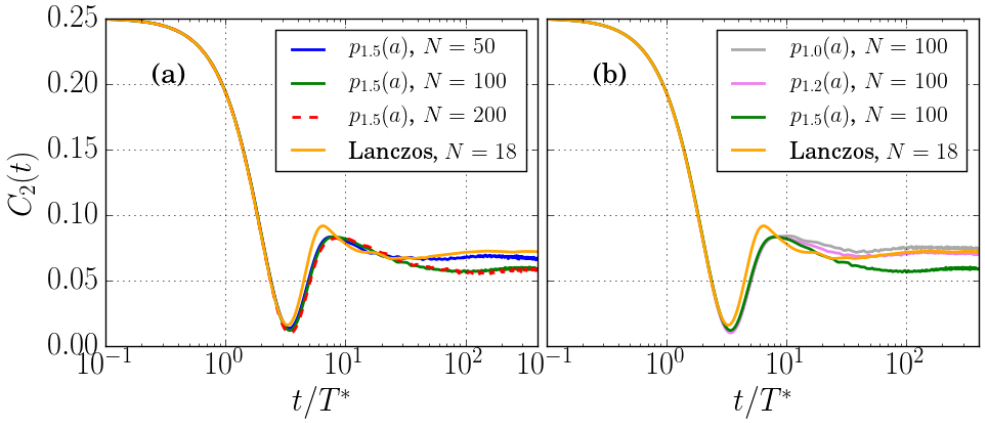

Figure 5.3: Electron spin correlation function for $|\vec{b}_{\text{ext}}| = 0$ for the quantum mechanical Lanczos method and SCA with different bath sizes in panel (a) and different cut-off parameters for the a_k distribution in panel (b). The dimension is $\xi = 3$. The hyperfine distribution for the Lanczos method is $p_{r_0}(a)$ with $r_0 = 1.5$. The data for the Lanczos method was provided by Nina Fröhling.

This leads to a long-time dephasing depending on the distribution of the hyperfine coupling constants [55]. Figure 5.3 (b) depicts $C_2(t)$ for different cut-off parameters r_0 and $N = 100$.
The non-decaying fraction of $C_2(t)$ decreases with increasing r_0. Merkulov et al. [55] connect the long-time asymptotic value to

$$\vec{S}(t) = \langle \vec{n}\vec{n}_0 \rangle \frac{\vec{S}_0}{3} = \tilde{\gamma}\frac{\vec{S}_0}{3} \tag{5.3.4}$$

with $\vec{n}_0 = \vec{b}_{\text{N}}(0)/|\vec{b}_{\text{N}}(0)|$ and $\vec{n} = \vec{b}_{\text{N}}(t)/|\vec{b}_{\text{N}}(0)|$. The parameter $\tilde{\gamma}$ is a monotonically decreasing function $\tilde{\gamma} : \mathbb{R}^+ \to (0, 1]$ of $\langle A_k^2 \rangle / \langle A_k \rangle^2$. This ratio can be used as a measure of the spread of the coupling constants, cf. Eq. (3.2.5), and is rewritten as N/a_{S}^2 with sum over all renormalized hyperfine coupling constants $a_{\text{S}} = \sum_k a_k$. N/a_{S}^2 is depicted in Fig. 5.4. The data is extracted from Fig. 3.4 as the inverse square of a cut at an arbitrary spin bath size $N > 1$. The cut is multiplied with the number of nuclear spin N. Since N/a_{S}^2 also is monotonous, the cut-off r_0 can be directly linked to the non-decaying fraction of the autocorrelation function. For an increasing r_0 a decreasing $\tilde{\gamma}$ follows and, therefore, also a smaller non-decaying fraction of $C_2(t)$.

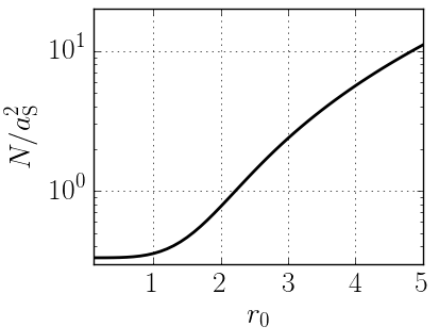

Figure 5.4: The parameter $\langle a^2 \rangle / \langle a \rangle^2 = N/a_{\text{S}}^2$ depending on r_0 which serves as a measure for the effectively contributing nuclear spins [55].

The long-time limit of the quantum mechanical Lanczos approach features a greater non-decaying fraction than the classical calculation of the same r_0. But the same long-

time behavior can be ensured by adjusting the parameter choice to smaller cut-offs for the SCA. In this case $r_0 = 1.2$ reproduces the quantum mechanical $C_2(t \to \infty)$ result.

The electron spin dynamics for a finite magnetic field of $|\vec{b}_{\text{ext}}| = 10$ is shown in Fig. 5.2 panel (b). On a short time, it is independent of the a_k distribution. The short-time dynamics is governed by the Larmor precession with the frequency $\omega_{\text{L}} T^* = |\vec{b}_{\text{ext}}|$. The envelope function is determined by the Overhauser field distribution and the time constant T^*. They determine its shape

$$S_{\text{env}}(t) = \frac{1}{4} \exp\left(-\frac{1}{2}\frac{t^2}{(2T^*)^2}\right). \tag{5.3.5}$$

Since the Overhauser field can be assumed constant for the dephasing time, the SCA and the FOA yield very similar results for the simulations of $C_2(t)$ in the presence of a large magnetic field.
The difference between the methods is presented in Fig. 5.2 (d). The agreement between all methods is considerably better than in the absence of the magnetic field. Even the largest discrepancy between SCA and CET never exceeds 0.01. The small differences observed between classical and quantum mechanical methods disappear with increasing bath size N [53]. The good agreement between the methods is important for later calculations with finite external magnetic field, e. g. pulsed systems but also higher-order correlation functions. Both investigations also include long-time effects which makes a good quality of the SCA all the more necessary and the long-time calculations less prone to large propagated errors.

5.3.4 Comparison including quadrupolar interaction

Not only the hyperfine interaction influences the long-time dynamics of the CSM but also the quadrupolar coupling plays a role in this regime. Three parameters govern the effect of the quadrupolar interaction, see Sec. 3.1.2: the coupling strength Q_{r}, the nuclear spin length I and the number of nuclear spin N. The easy axis $\vec{n}_k$ are randomly drawn from a cone around the z-axis with an apex angle of $2\theta_{\max} = 70°$, cf. Sec. 5.3.2. The differences between the classical simulation and quantum mechanical Lanczos approach are investigated.

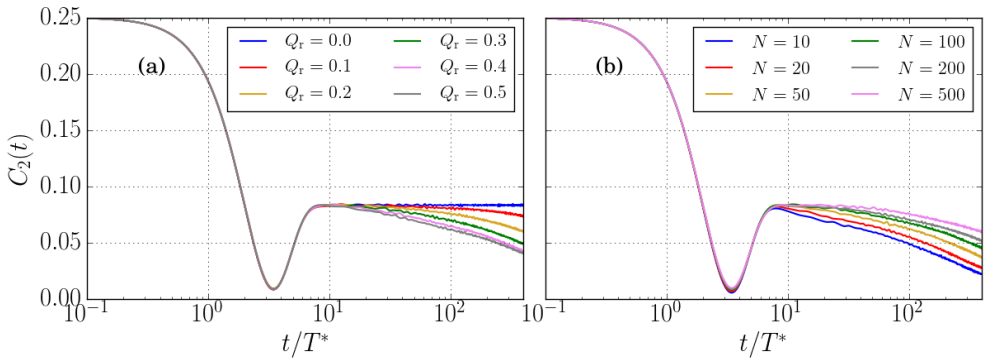

Figure 5.5: Classical simulation with equal hyperfine coupling constants and increasing Q_{r} for $N = 100$ nuclear spins in panel (a) and fixed $Q_{\text{r}} = 0.35$ and varying N in (b).

Figure 5.5 (a) shows the classical simulation results for different Q_r. The hyperfine coupling constants are set to be homogeneous, $A_k = \mathrm{const}$, to exclude their influence on the long-time dephasing for $t \gg T^*$. As discussed above, such a system is equivalent to the FOA for $Q_\mathrm{r} = 0$ and $|\vec{b}_\mathrm{ext}| = 0$ and features no long-time decay. The blue curve ($Q_\mathrm{r} = 0$) gives the plateau at $S(0)/3$, which is the upper bound for the long-time limit. If a non-zero Q_r is applied, $C_2(t)$ decays to zero. For increasing Q_r, the autocorrelation function decays faster. The scalar $\tilde{q}_k(\vec{n}_k\vec{I}_k)$, cf. Eq. (5.2.27b), multiplied with the unit vector $\vec{n}_k$ acts as an effective field. Since $\vec{n}_k\vec{I}_k \in [-I, I]$ is limited, the coupling constant $\tilde{q}_k$ defined by Eq. (5.2.26) determines the spread of the effective coupling constants to $\vec{n}_k$. An inverse behavior between spread of the coupling constants and long-time decay time can be found.

In experiments [81, 92] the decay attributed to the quadrupolar interaction occurs on a time scale of $200 - 600\,\mathrm{ns}$ depending on the growth conditions of the quantum dot ensemble. In Fig. 5.5 (b) the parameter Q_r is chosen as 0.35 to fit the experiments for $N = 100$. The parameter N is varied from small bath of $N = 10$ to $N = 1000$. The long-time decay reveals its dependence on N. The quadrupolar coupling constants q_k for equal hyperfine coupling constants are $q_k \sim Q_\mathrm{r}/\sqrt{N}$. Therefore, the spread of the quadrupolar coupling constants also depends on the bath size. The decay is slower the more nuclear spins are included.

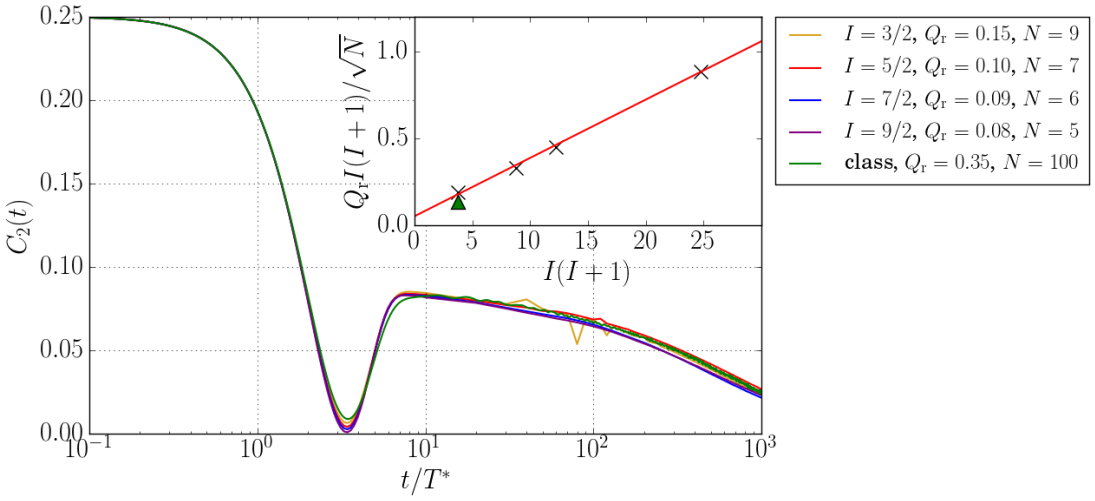

Figure 5.6: Electron spin dynamics for $|\vec{b}_\mathrm{ext}| = 0$ for a semiclassical calculation and a Lanczos method. The inset shows the dependence of $Q_\mathrm{r}I(I+1)/\sqrt{N}$ on $I(I+1)$. The quantum mechanical data is taken from [137].

Now that the two mechanisms determining the long-time decay of the autocorrelation function, the hyperfine and the quadrupolar interaction, are discussed, we compare the results of the classical simulation and the quantum mechanical Lanczos method [137]. We aim to tune the parameter Q_r in such a way that $C_2(t)$ stays invariant for both methods. For the quantum mechanical calculations, different nuclear spin lengths I are utilized and the Hilbert space dimension is kept approximately constant. The Hilbert space dimension limits the number of nuclear spins to 9 for $I = 3/2$ and $N = 5$ for $I = 9/2$. The autocorrelation functions are depicted in Fig. 5.6.

For $I = 3/2$ a coupling strength of $Q_\mathrm{r} = 0.15$ is chosen referring to previous investiga-

tions [81, 93] based on experimental data. In the quantum mechanical simulations for other spin lengths, Q_r is adjusted to reproduce the long-time decay of $I = 3/2$. For the Lanczos data we can linearly connect the $I(I+1)$ and $Q_\mathrm{r} I(I+1)/\sqrt{N}$ via the relation

$$\frac{Q_\mathrm{r}}{\sqrt{N}} I(I+1) = aI(I+1) + b, \tag{5.3.6}$$

with $a = 0.0336 \pm 0.0008$ and $b = 0.05 \pm 0.01$. The values for a and b are obtained via linear regression. This relation is depicted in the inset of Fig. 5.6 using the data labeled by the 'x' markers. The SCA result is included as a green triangle and does fit well into the scheme of the linear relation.

Here, we have to pay heed to the significantly different bath sizes used in the SCA and the Lanczos calculations. To compensate for the larger number of nuclear spins, the classical simulation has to feature a higher Q_r to produce matching curves. This fact is depicted in the inset plot of Fig. 5.6. And although Q_r was originally defined in Ref. [81] to minimize the dependency on N, the nuclear bath size still influences the long-time decay as is evident from the dependency $q_k \sim Q_\mathrm{r}/\sqrt{N}$.

Chapter 6

Fourth-order spin noise in a semiconductor quantum dot

Besides pump-probe experiments, higher-order spectroscopy provides access to additional information about interactions in QDs [68]. In contrast to the former, spin-noise spectroscopy is a non-invasive measurement [70]. Instead of using the probe beams in tandem with pump pulses, that affect the state of the system, only the weaker probe beams are applied. The resulting signal is noisy in the time domain. The information about its spectral composition is extracted by a Fourier transformation. Higher-order correlation functions show the interplay of two or more frequencies [174] and can therefore reveal dynamics beyond the Gaussian noise [175].

In this chapter we use the full Hamiltonian (3.1.30) also including the quadrupolar interaction [94, 119, 176]. We compare the classical and quantum mechanical results for the fourth-order spectrum $S_4(\omega_1, \omega_2)$ defined in Eq. (4.3.3) with and without quadrupolar interaction. Most of the data presented here is part of Ref. [137]. All results of the quantum mechanical simulation for higher-order correlation functions are the work of Nina Fröhling.

6.1 Classical treatment

In the SCA the mean value over all configurations with different initial conditions [54, 89] is calculated. The time evolution of the spin dynamics is dictated by Eqs. (5.2.27a) and (5.2.27b). The intricacies of the SCA are the topic of Sec. 5.2.
The fourth-order cumulant is composed of fourth and second-order correlation functions. For the special case of $\omega_1 = -\omega_2$ and $\omega_4 = -\omega_3$ its individual parts are given by

$$C_4(\omega_1, \omega_2) = \frac{1}{N_C} \sum_{\mu \in \text{config}} \mathcal{F}C_{2,\mu}(\omega_1) \mathcal{F}C_{2,\mu}(\omega_2) \tag{6.1.1}$$

and

$$C_2(\omega_1) = \frac{1}{N_C} \sum_{\mu \in \text{config}} \mathcal{F}C_{2,\mu}(\omega_1). \tag{6.1.2}$$

The correlation function $\mathcal{F}C_{2,\mu}(\omega)$ [55, 76] is the Fourier transformation of the electron spin correlation $C_{2,\mu}(t) = S_{z,\mu}(0)S_{z,\mu}(t)$ in a single classical configuration μ. It is the building block for both C_4 and C_2. Since the spin expectation value for a polarized initial condition can be translated to the spin correlation function of second order for an unpolarized electron at $t = 0$, see Sec. 5.3.1, the expectation value $S_{z,\mu}(t)$ is transformed instead.

The bispectrum $S_4(\omega_1, \omega_2)$ is then assembled by the recipe given in Eq. (4.3.3).

6.2 Spin-noise power spectrum $C_2(\omega)$

The spin correlation function of second order was already the subject of several investigations [49, 75, 76]. However, it plays an important role in the understanding of higher-order cumulants, see Chap. 4.1. After the time domain was revisited in Chap. 5, the spin noise $C_2(\omega)$ shall be the focus here.

A first step for understanding spin noise is taken by Fourier transforming the electron spin dynamics (5.2.37) in a FOA [55]. For $|\vec{b}_{\text{ext}}| = 0$ the analytical solution is readily available:

$$C_2(\omega) = \frac{1}{12}\left\{2\pi\delta(\omega) + \sqrt{8\pi}(2T^*)\,(2T^*\omega)^2 \exp\left[-\frac{1}{2}\,(2T^*\omega)^2\right]\right\}. \tag{6.2.1}$$

Integration over all frequencies shows that one third of the spectral weight can be attributed to the δ-peak at $\omega = 0$ [49, 55, 81]. Its weight amounts to $\pi/6$ in accordance with the sum rule (4.2.6). For non-zero magnetic fields the FOA solution has to be calculated numerically [49, 75, 79, 81]. This simple method is compared to two more sophisticated approaches in Fig. 6.1: the SCA and quantum mechanical calculation. In the SCA $C_2(\omega)$ is given by Eq. (6.1.2) but can also be simplified to

$$C_2(\omega) = \mathcal{F}\left(\frac{1}{2N_C}\sum_{\mu\in\text{config}} S_{z,\mu}(t)\right). \tag{6.2.2}$$

The initial condition is $\vec{S}_\mu(t = 0) = (1/2)\vec{e}_z\,\forall\,\mu$ due to the relation of the correlation function of the electron and the expectation value (5.3.3). The parameters for the classical calculation are the same as in Sec. 5.3.2 unless stated otherwise. For investigations in the frequency space we use $T^* = 1/\omega_{\text{fluc}}$ as defined in Sec. 3.1.3.

The spin noise is presented in Fig. 6.1 for the external magnetic fields $|\vec{b}_{\text{ext}}| = 0$ and $|\vec{b}_{\text{ext}}| = 5$. The plot is augmented by an additional plot which shows the low-frequency range in panel (b). The results for the FOA and the quantum mechanical calculations were provided by Nina Fröhling and are taken from Ref. [137]. The quantum mechanical calculation is averaged over $N_a = 32$ configurations for different sets of coupling constants $\{a_k\}$ and uses $N = 3$ nuclear spins of length $I = 9/2$. A smaller cut-off radius is used for the distribution of the hyperfine coupling constant distribution to compensate for the smaller nuclear bath size $r_0 = 0.8$.

All methods show good agreement for $|\vec{b}_{\text{ext}}| = 5$. The spin noise is represented by a Gaussian with a mean of

$$\mu(|\vec{b}_{\text{ext}}|) = \omega_{\text{fluc}}\sqrt{|\vec{b}_{\text{ext}}|^2 + 1/2} \tag{6.2.3}$$

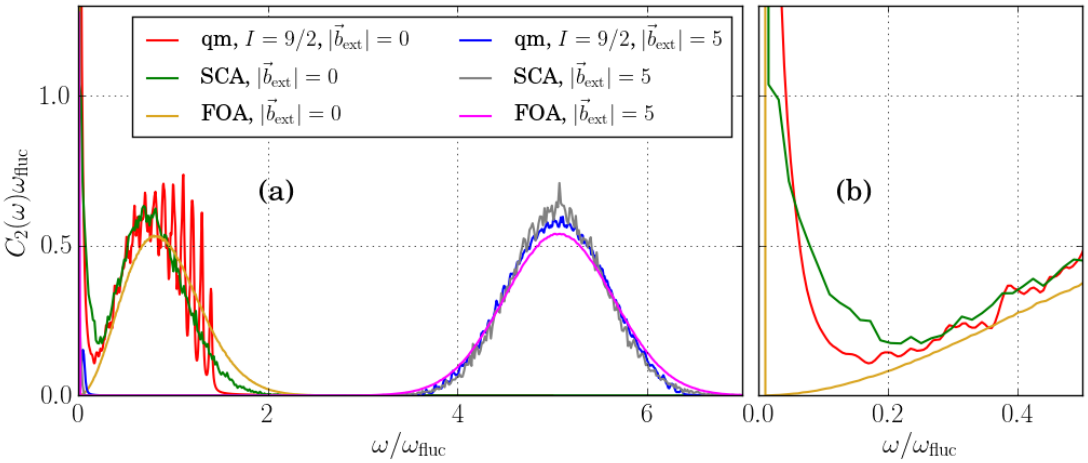

Figure 6.1: Spin noise $C_2(\omega)$ for $|\vec{b}_{\text{ext}}| = 0$ and $|\vec{b}_{\text{ext}}| = 5$ for different approaches: the quantum mechanical simulation (qm) with three $I = 9/2$ nuclear spins, the semiclassical approximation (SCA) and the frozen Overhauser field approximation (FOA). This data has previously been published in Ref. [137]. Panel (b) detail of $C_2(\omega)$ at $|\vec{b}_{\text{ext}}| = 0$ for low frequencies.

and a variance of $\sigma^2 = (\omega_{\text{fluc}}/2)^2$ [49]. Small deviations can be attributed to the small bath size in the quantum mechanical simulation or numerical noise due to the finite maximum time T_m in the classical simulation. For $|\vec{b}_{\text{ext}}| = 0$ the differences become more apparent. The spin-noise spectrum consists of peaked contribution at $\omega = 0$ and a Gaussian distribution at $\mu(|\vec{b}_{\text{ext}}| = 0) = \omega_{\text{fluc}}\sqrt{1/2}$. For low magnetic fields the distribution of the coupling constants $p(a)$ governs the long-time decay. The result of the FOA is equivalent to that of the box model for $|\vec{b}_{\text{ext}}| = 0$, cf. Sec. 5.2.5. The a_k-distribution of the box model is collapsed to a single δ-peak $p(a) = \delta(a - \overline{a})$ and, therefore, $C_2(t)$ in the FOA shows no long-time decay. This translates to a $\delta(\omega)$-peak of weight $\pi/6$ in the spin-noise spectrum. The long-time, decaying behavior for $p(a) = p_{r_0}(a)$ causes a shift of spectral weight from the $\delta(\omega)$-peak to non-zero frequencies, see Fig. 6.1 (b). The spectral weight of the $\delta(\omega)$-peak is proportional to the remaining non-decaying fraction of $C_2(t)$. The classical result traces the envelope of the quantum mechanical spectrum. For zero-magnetic field the degeneracies in the eigenenergies cannot be lifted by Zeeman splitting. In this restricted spectrum the excitations become visible as peaks. To smooth the spectrum a different choice of coupling constants or averaging over more than $N_a = 32$ different sets of hyperfine coupling constants are possible solutions.

6.3 Fourth-order spin noise

A few fundamental features of the fourth-order spectrum shall be investigated. First, we discuss the shape of the cumulant S_4-spectrum defined in Eq. (4.3.1) in terms of its components C_2 and C_4. Then the spectrum calculated via SCA is investigated as a limiting case of the quantum mechanical result. The last part is dedicated to the change of the classical spectrum under the influence of $|\vec{b}_{\text{ext}}|$.

For the classical simulation we mostly use the parameters presented in Sec. 5.3.2. We restrict ourselves to the dynamics given by H_{CSM} and leave the effect of the quadrupolar

interaction H_{Q} to Sec. 6.4. The size of the nuclear spin bath is $N = 100$ and the number of configurations $N_{\mathrm{C}} = 10^5$. The distribution of the hyperfine coupling constants is given by $p_{r_0}(a)$ with $r_0 = 1.5$ and $\xi = 3$. The strength of the nuclear Zeeman interaction is defined by $\zeta = 0.00125$. The measurement time is $T_m = 400\,T^*$.

6.3.1 Components of S_4

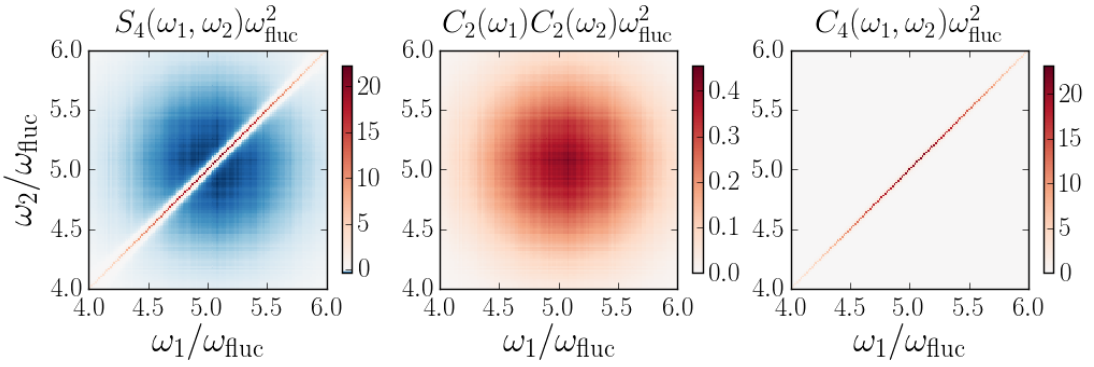

Figure 6.2: $S_4(\omega_1,\omega_2)$, $C_2(\omega_1)C_2(\omega_2)$ and $C_4(\omega_1,\omega_2)$ with an external magnetic field of $|\vec{b}_{\mathrm{ext}}| = 5$ obtained by the SCA. Data taken from Ref. [137].

As Eq. (4.3.3) shows, the spectrum of $S_4(\omega_1,\omega_2)$ consists of two parts: the correlation function $C_4(\omega_1,\omega_2)$ and the product of second-order correlations at different frequencies $C_2(\omega_1)C_2(\omega_2)$. The resulting S_4-spectrum as well as its components are depicted in Fig. 6.2 for an external magnetic field of $|\vec{b}_{\mathrm{ext}}| = 5$. $S_4(\omega_1,\omega_2)$ features a broad distribution of weak anti-correlations. Its strong correlations are concentrated on the diagonal $\omega_1 = \omega_2$. Since both parts are composed only of positive terms, the correlations of $S_4(\omega_1,\omega_2)$ can be attributed to $C_4(\omega_1,\omega_2)$ and its anti-correlations to $C_2(\omega_1)C_2(\omega_2)$. Positive and negative contributions cancel each other out for the frequency integral over the spectrum.

In a finite magnetic field $C_2(\omega)$ is a Gaussian distribution with mean $\mu(|\vec{b}_{\mathrm{ext}}|)$, cf. Eq. (6.2.3), and variance $\sigma^2 = (\omega_{\mathrm{fluc}}/2)^2$ related to the dephasing time of $S_z(t)$ for large magnetic fields [55]. This Gaussian can be extracted from the envelope of the electron spin dynamics via Fourier transformation. Since ω_1 and ω_2 are uncorrelated, the second-order contributions combined follow a multivariate Gaussian whose covariance matrix is diagonal with identical entries of $\sigma^2 = (\omega_{\mathrm{fluc}}/2)^2$. The two-dimensional Gaussian is depicted in the middle panel of Fig. 6.2.

The right-hand panel of Fig. 6.2 shows $C_4(\omega_1,\omega_2)$. Its contribution is restricted to the diagonal $\omega_1 = \omega_2$. In each classical configuration the electron spin frequency is given by the external magnetic field and an Overhauser field related perturbation. The Overhauser field, only influenced by the hyperfine interaction and a weak nuclear Zeeman term, is almost constant over the measurement time T_m. The Fourier transform in an individual configuration $C_{2,\mu}(\omega)$ is therefore given by a single, narrow peak. The product of $C_{2,\mu}(\omega_1)C_{2,\mu}(\omega_2)$ only contributes to $C_4(\omega_1,\omega_2)$ at the overlap at $\omega_1 \approx \omega_2$. The projection of the diagonal contribution on the ω_1-axis or the ω_2-axis can be approximated by the Gaussian distribution of the second-order correlation function $\mathcal{N}(\mu(|\vec{b}_{\mathrm{ext}}|), (\omega_{\mathrm{fluc}}/2)^2)$.

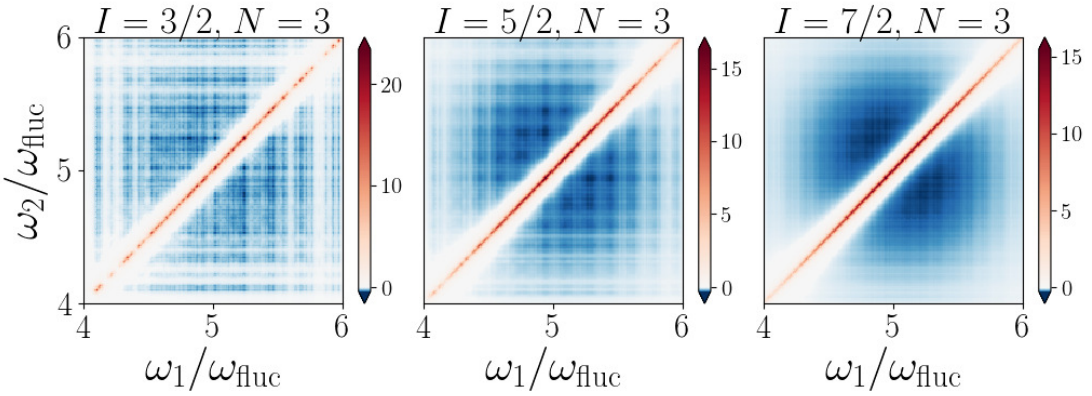

Figure 6.3: $S_4(\omega_1, \omega_2)$ calculated quantum mechanically for the bath size $N = 3$ and spin length $I = 3/2$, $I = 5/2$ and $I = 7/2$. $|\vec{b}_{\text{ext}}| = 5$. Hyperfine coupling is given by $r_0 = 0.8$ and quadrupolar coupling is switched off $Q_r = 0$. Plot taken from Ref. [137].

6.3.2 Classical limit to quantum mechanical simulations

The quantum mechanical S_4-spectrum can - at first glance - deviate greatly from the semiclassically computed one [94]. However, we show that the SCA provides a valid approach in certain limits.

In Fig. 6.3 the results of a quantum mechanical exact diagonalization[1] are shown for different nuclear spin lengths ($I = 3/2$, $5/2$, $7/2$). The bath size is restricted to $N = 3$. The hyperfine coupling constants are $p_{r_0}(a)$-distributed with a cut-off $r_0 = 0.8$ and averaged over $N_a = 32$ configurations. A transversal magnetic field of $|\vec{b}_{\text{ext}}| = 5$ is applied. For the quantum mechanical spectra a Lorentzian broadening with $\omega/\omega_{\text{fluc}} = 0.01$ is used to make discrete results visible.

For $I = 3/2$ the discrete nature of the second-order spectrum $C_2(\omega)$ is found in the anti-correlations. The contributions to S_4 are limited to a sparse number of (ω_1, ω_2) frequency pairs which are artificially broadened. More general features like the correlations along the diagonal or the centering of the spectrum with respect to the external magnetic field strength remain the same as for the SCA results. The spectrum becomes more continuous with an increasing nuclear spin length. For $I = 7/2$ it strongly resembles that of the classical calculation presented in Fig. 6.2. Larger spins necessitate a larger Hilbert space to describe and have more non-degenerate eigenenergies. For $I \to \infty$ the quantum mechanical spectrum is no longer discrete and a classical limit could be reached.

The other candidate for a quantum mechanical calculation approaching the classical result is found in the nuclear spin bath size. In Fig. 6.4 the fourth-order cumulant spectrum is presented with a different number of nuclear spins. The spin length is fixed to $I = 9/2$. For reasons of comparison the classical result is included.

The discrete second-order spectrum $C_2(\omega)$ of $N = 1$ is mirrored in the higher-order cumulant S_4. The equidistant spacing [48, 77] of the S_4 peaks around $|\vec{b}_{\text{ext}}|$ is owed to the Zeeman splitting of the nuclear spins coupled to the central spin via hyperfine coupling. The spectrum contains $(2I+1)^2 = 100$ peaks that are positive on the diagonal

[1] The quantum mechanical simulations were implemented by Nina Fröhling in Ref. [137].

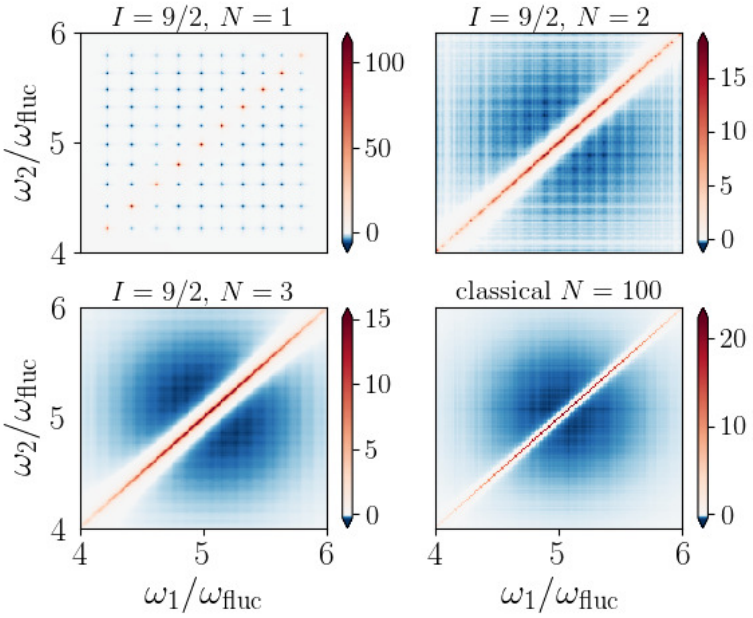

Figure 6.4: $S_4(\omega_1, \omega_2)$ for different bath sizes $N = 1, 2, 3$ for a quantum mechanical calculation with $I = 9/2$. The classical spin bath has size $N = 100$. The external magnetic field is $|\vec{b}_{\mathrm{ext}}| = 5$. Quadrupolar coupling is not included. Plot taken from [137].

and negative for $\omega_1 \neq \omega_2$. Already for $N = 2$ the ensemble average over various a_k leads to a discernibly more continuous spectrum. For $N = 3$ the quantum mechanical spectrum on the lower left panel is qualitatively very similar to its classical counterpart on the lower right panel of Fig. 6.4.

The comparison between the results of both approaches solidifies the conjecture that the classical approach can be used in the limits of large nuclear spins $I \to \infty$ or large spin baths $N \to \infty$.

6.3.3 Influence of the external magnetic field strength on S_4

For a small magnetic field the bispectrum S_4 changes considerably. But the differences displayed in Fig. 6.5 can still be attributed to the same components as for $|\vec{b}_{\mathrm{ext}}| = 5$. In the absence of a magnetic field the contributions on the axes $\omega_{1/2} = 0$, and along the diagonal are emphasized due to the strong spectral weight of the $\delta(\omega)$-peak, cf. Eq. (6.2.1). For a full classical simulation with varying a_k the δ-peak contains slightly less weight than calculated for the FOA [55] but is still dominant.

With increasing magnetic field, the spectral weight shifts from the δ-peak to the Gaussian and the mean of the normal distribution moves depending on the external magnetic strength $\mu(|\vec{b}_{\mathrm{ext}}|)$. For $|\vec{b}_{\mathrm{ext}}| = 1$ the spectrum is depicted in Fig. 6.5. The Gaussian is centred around $\mu(|\vec{b}_{\mathrm{ext}}| = 1) = \omega_{\mathrm{fluc}}\sqrt{3/2}$ and has a variance of $(\omega_{\mathrm{fluc}}/2)^2$. The anti-correlations can be traced back to the second-order correlation functions which are shown in the panel labeled $C_2(\omega_1)C_2(\omega_2)\omega_{\mathrm{fluc}}^2$. C_2 is also responsible for the distinct form of S_4. The fourth-order correlations are depicted in the lower left panel. C_4 mostly contributes to the diagonal and weakly along the axes $\omega_1 = 0$ and $\omega_2 = 0$. The weak

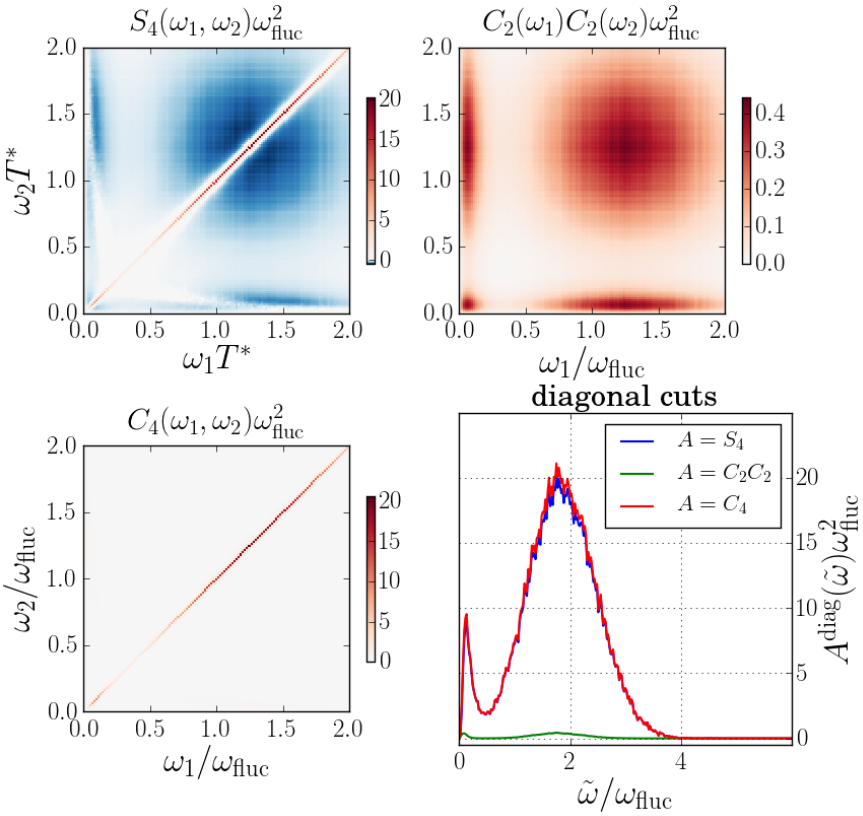

Figure 6.5: $S_4(\omega_1,\omega_2)\omega_{\text{fluc}}^2$ as well as its components $C_4(\omega_1,\omega_2)\omega_{\text{fluc}}^2$ and $C_2(\omega_1)C_2(\omega_2)\omega_{\text{fluc}}^2$ for $|\vec{b}_{\text{ext}}| = 1$. In the bottom right panel the diagonal cut through all three spectra is shown. Data taken from [137].

contributions can be noticed in the S_4-spectrum as an incision to the anti-correlations near the ω_1-axis and ω_2-axis.

To further investigate the part of the spectrum where both, second and fourth-order correlations, come into play, we parametrize the diagonal cut

$$A^{\text{diag}}(\tilde{\omega}) = A(\tilde{\omega}/\sqrt{2}, \tilde{\omega}/\sqrt{2}) \tag{6.3.1}$$

with the dummy variable A representing the spectra $S_4(\tilde{\omega})$, $C_4(\tilde{\omega})$ or $C_2(\tilde{\omega})C_2(\tilde{\omega})$. The diagonal frequency is $\tilde{\omega} = \sqrt{\omega_1^2 + \omega_2^2} = \sqrt{2}\omega_1$. These cuts are depicted in the panel labeled "diagonal cuts". The cut through C_4 mirrors the shape of S_4 along the diagonal. It is given by $\sum_\mu (C_{2,\mu}(\omega_1))^2$ which still follows a Gaussian distribution $\tilde{\omega} \sim \mathcal{N}(\sqrt{2}\mu(|\vec{b}_{\text{ext}}|), 2(\omega_{\text{fluc}}/2)^2)$. The second-order correlation changes the shape of the diagonal cut only marginally.

For different magnetic fields ranging from $|\vec{b}_{\text{ext}}| = 1$ to 20 the diagonal $\omega_1 = \omega_2$ cut through the S_4-spectrum is plotted in Fig. 6.6. For lower magnetic fields the Gaussian has lesser spectral weight since the $\delta(\omega)$-peak is not yet completely decayed. The Gaussian form persists for higher magnetic fields as well as the centering around $\sqrt{2}\mu(|\vec{b}_{\text{ext}}|)$.

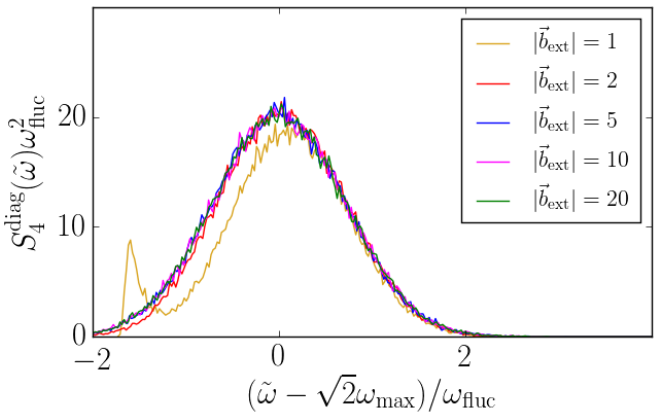

Figure 6.6: $S_4^{\mathrm{diag}}(\tilde{\omega})$ for magnetic fields ranging from $|\vec{b}_{\mathrm{ext}}| = 1$ to 20. The spectra are shifted by $\sqrt{2}\omega_{\mathrm{max}} = \sqrt{2}\mu(|\vec{b}_{\mathrm{ext}}|)$.

6.4 Influence of the quadrupolar interaction on the fourth-order spin noise

Fröhling et al. [93] have shown that the quadrupolar interaction plays an important role in higher-order spin correlations. We investigate the broadening of the S_4-spectrum caused by the quadrupolar interaction and its dependence on the spin bath size N and the quadrupolar interaction strength. After we have adjusted the quadrupolar coupling in such a way that SCA and quantum mechanical results match in Sec. 5.3.4, we investigate how this agreement between the two approaches translates to the fourth-order cumulant.

Since the second-order correlation functions for non-zero magnetic fields show no obvious changes if the quadrupole interaction is included, we turn to the fourth-order cumulant. In Sec. 5.3.4 its influence on the long-time electron spin decay was discussed and compared to a quantum mechanical approach for $|\vec{b}_{\mathrm{ext}}| = 0$. A matching long-time dynamics can be found if the quadrupolar strength Q_{r} is adjusted to compensate for the difference in spin length and spin bath size. Their linear correlation is used to choose the parameters for the fourth-order cumulant. Again, the classical simulation uses $I = 3/2$ to determine the quadrupolar couplings given by Eq. (5.2.29b).

In Fig. 6.7 the fourth-order cumulant is shown for $I = 3/2, 7/2, 9/2$ as the result of a quantum mechanical simulation and supplemented by a classical approach. The most notable contribution of the quadrupolar interaction is the broadening of the correlation orthogonal to the diagonal. The broadening of the spectrum can be explained in the context of classical configurations. To illustrate the concept, Fig. 6.8 is added. It shows the Fourier transformation of the dynamics found in one configuration $C_{2,\mu}(\omega)$ with and without quadrupolar interaction. Independent of Q_{r} the second-order spin noise $C_2(\omega)$ follows $\mathcal{N}(\mu(|\vec{b}_{\mathrm{ext}}|), \omega_{\mathrm{fluc}}^2/4)$ (black, dashed curve). Without quadrupolar interaction, the spin noise $C_{2,\mu}$ and, therefore, the frequency composition in a single configuration is given by an almost sharp peak (blue curve). But when the quadrupole interaction induces an additional electron dephasing by extending the effective field of the nuclear spin dynamics, it also expands the frequency spectrum in a single configuration (green curve). Therefore, the product $C_{2,\mu}(\omega_1)C_{2,\mu}(\omega_2)$ in Eq. (6.1.1) results also in non-zero

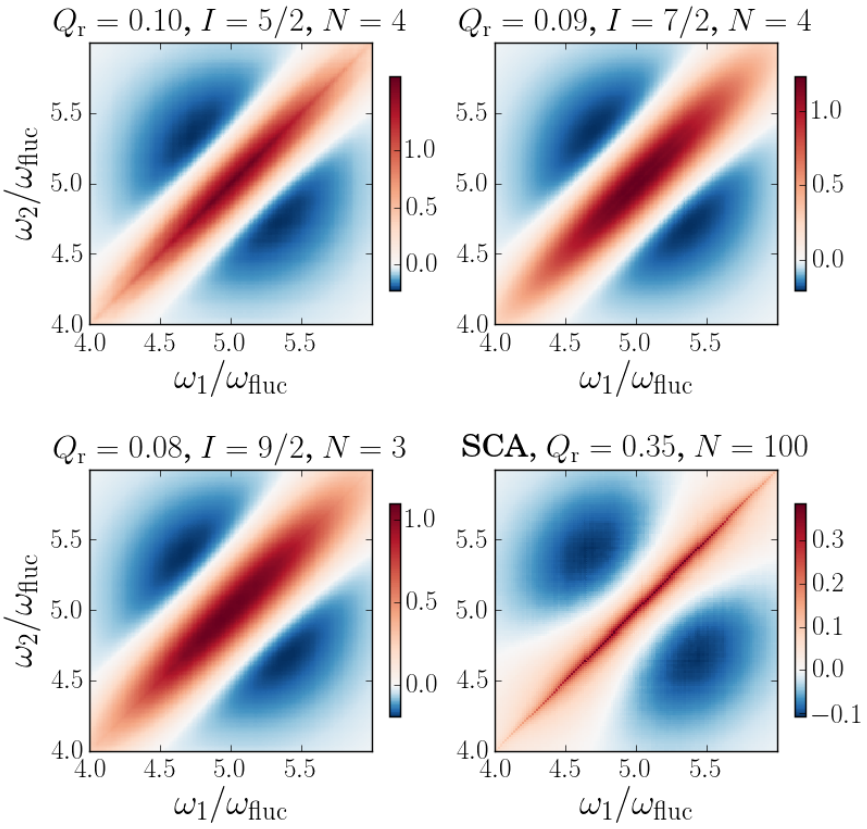

Figure 6.7: $S_4(\omega_1, \omega_2)$ for a quantum mechanical and classical approach including the quadrupolar coupling. The parameters Q_r, N and I are chosen to coincide with those in Fig. 5.6. The data of the quantum mechanical approach is taken from [137].

contributions for $\omega_1 \neq \omega_2$ and the broadening in each configuration translates directly to a broadening of the spectrum.

While all quantum mechanical spectra exhibit approximately the same behavior, the classical spectrum seems to retain more of the heretofore sharp peak on the diagonal and shows weaker broadening. Since the mismatch is not apparent in the shape of $C_2(\omega)$, the observed broadening is related to the fourth-order spin correlation function. To further investigate this effect, we resort to cuts through S_4. The definition of the diagonal cut function is given by Eq. (6.3.1), and the anti-diagonal cut through the center and global maximum of the spectrum $S_4(\omega_{\max}, \omega_{\max})$, with $\omega_{\max} = \mu(|\vec{b}_{\mathrm{ext}}|)$ is defined by

$$S_4^{\mathrm{adiag}}(\tilde{\omega}) = S_4\left(\frac{\tilde{\omega}}{\sqrt{2}} + \omega_{\max}, -\frac{\tilde{\omega}}{\sqrt{2}} + \omega_{\max}\right). \tag{6.4.1}$$

The cut is shifted to be centered around $\omega_{\max}$ with $\tilde{\omega} = 0$ as new origin. The antidiagonal cuts for $C_4(\omega_1, \omega_2)$ and $C_2(\omega_1)C_2(\omega_2)$ are defined analogously as $C_4^{\mathrm{diag}}(\tilde{\omega})$ and $C_2(\tilde{\omega})C_2^{\mathrm{diag}}(\tilde{\omega})$.

Diagonal cuts through the classical spectra at $|\vec{b}_{\mathrm{ext}}| = 5$ are presented in Fig. 6.9. On the diagonal we observe a dip in S_4 for higher Q_r. This feature is directly linked to the broadening in the C_4-spectrum. While cut through $C_2(\omega_1)C_2(\omega_2)$ is independent of the

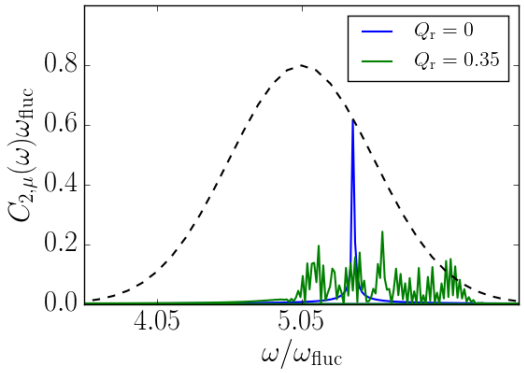

Figure 6.8: Frequency broadening in one configuration with ($Q_r = 0.35$) and without ($Q_r = 0$) quadrupolar interaction. The envelope of the averaged $C_2(\omega)$ is added in black. The scaling of the Fourier transform $\mathcal{F}S_{z,\mu}(\omega)$ is arbitrarily adjusted for better comparability.

quadrupolar interaction, the C_4 part shifts spectral weight from the diagonal to $\omega_1 \neq \omega_2$ parts depending on Q_r. Therefore, its contribution along the diagonal decreases. While both building blocks of S_4 individually retain a Gaussian shape, the difference along the diagonal is influenced by the reduced weight of $C_4^{\text{diag}}(\tilde{\omega})$. For weak quadrupolar interaction, e. g. $Q_r = 0.1$, the spectral weight of the second-order contribution can be neglected compared to those of the fourth-order correlation function. The diagonal cut $S_4^{\text{diag}}(\tilde{\omega})$ through the fourth-order cumulant can then be described by a Gaussian with variance $2(\omega_{\text{fluc}}/2)^2$. But the quadrupolar interaction has a second effect on the fourth-order correlation function C_4. The variance of the Gaussian antidiagonal C_4-cut decreases with increasing Q_r, see Fig. 6.9 on the right. The shrinking variance together with the reduction of amplitude conserves the spectral weight of the C_4 contributions to S_4.

The antidiagonal cuts through the S_4-spectrum as well as the components of the second and fourth-order are depicted for a varying quadrupole coupling constants in Fig. 6.10. As it was the case with the diagonal cuts, antidiagonal cuts through $C_2(\omega_1)C_2(\omega_2)$ are described by a Gaussian [55, 76]. The $C_2(\omega_1)C_2(\omega_2)$ is symmetric around $\omega_{\max}$ and independent of Q_r. The antidiagonal cut through the C_4-spectrum reveals the influence of the quadrupolar interaction. For small Q_r the curve exhibits a cusp which could be fitted by a power law, while the shape transitions to a Gaussian shape for stronger quadrupole coupling. To connect the quadrupolar coupling to the shape of the cut, Fig. 6.10 is augmented by a full width half maximum $\Omega_{1/2}$ measurement of the C_4 cut. For small Q_r the full width half maximum increases roughly linear up to $Q_r \approx 0.4$ and flattens out for $Q_r \gtrsim 0.7$. As an upper bound we assume $\Omega_{1/2}/\omega_{\text{fluc}} = 0.15$. At $Q_r = 0$ the shape of the C_4 curve should follow a δ-peak but is limited to a finite width due to the measuring time T_m.

The scaling behavior between classical approach and quantum mechanical approach that is observed for C_2 does not hold for the higher-order cumulants. However, qualitatively similar behavior is observed in the broadening behavior of the antidiagonal cut. For the quantum mechanical results see Ref. [137]. Partially, we can attribute the mismatch to the difference in bath size or, to be more precise, to the difference of the ratio between quadrupolar coupling strength affecting a single nuclear spin and the nuclear Zeeman strength. Due to the increase in computational effort with the increase of the external magnetic field strength, we vary the the nuclear bath size in the classical approach. For a fixed external magnetic field of $|\vec{b}_{\text{ext}}| = 5$ and a nuclear interaction strength of $\zeta = 0.00125$, the diagonal and antidiagonal cuts through the S_4-spectrum are presented

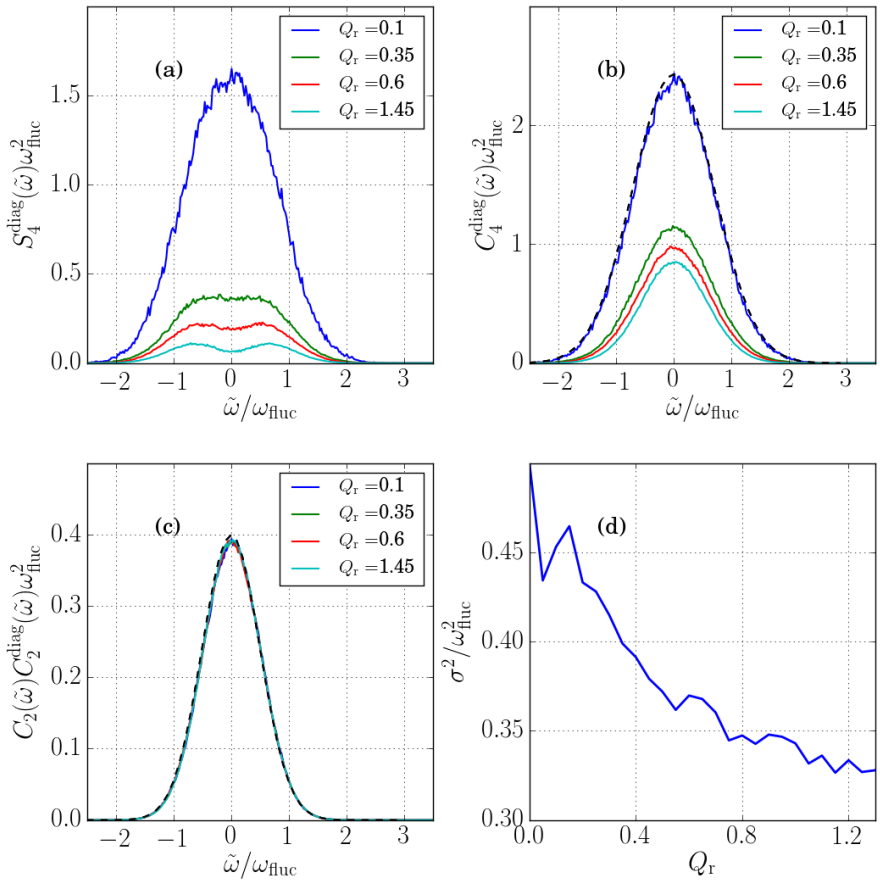

Figure 6.9: Diagonal cuts $\omega_1 = \omega_2$ for the spectrum $S_4^{\mathrm{diag}}(\tilde{\omega})$, as well as its components for different quadrupolar coupling strength Q_r. The Gaussian envelope $\mathcal{N}(0, \omega_{\mathrm{fluc}}^2/2)$ and $\mathcal{N}(0, \omega_{\mathrm{fluc}}^2/4)$ was added in dashed black lines for the C_4 and C_2C_2 cut, respectively. The variance of Gaussians fitted to C_4^{diag} is plotted in panel (d).

in Fig. 6.11 for different N to connect to the quantum mechanical simulation presented in Ref. [137].

The difference between the result for $N = 100$ and those for smaller nuclear spin baths can be understood in the context of the time scales that affect a single nuclear spin. For small magnetic fields the quadrupolar interaction leads to an energy splitting dependent on q_k and the Zeeman interaction can be considered as a perturbation. Once the quadrupolar interaction far exceeds the Zeeman interaction strength, spin-flip scattering processes between the quadrupolar energy doublets are suppressed and no further broadening can be observed. The electron spin dynamics becomes independent of Q_r. For large magnetic fields the quadrupolar interaction acts as a perturbation to the Zeeman interaction.

While in a physically realistic system the distribution and the value of the q_k is dependent on the local strain tensor, we simplified the quadrupolar coupling by using a more phenomenological approach. The parameter Q_r was fitted to experiments [75, 91, 92] by numerically simulating the second-order spin correlation function [81]. This still neglects the question of the value for q_k for a single nuclear spin. By the definition of the quadrupolar coupling Eq. (3.1.32), the expectation value of a quadrupolar coupling

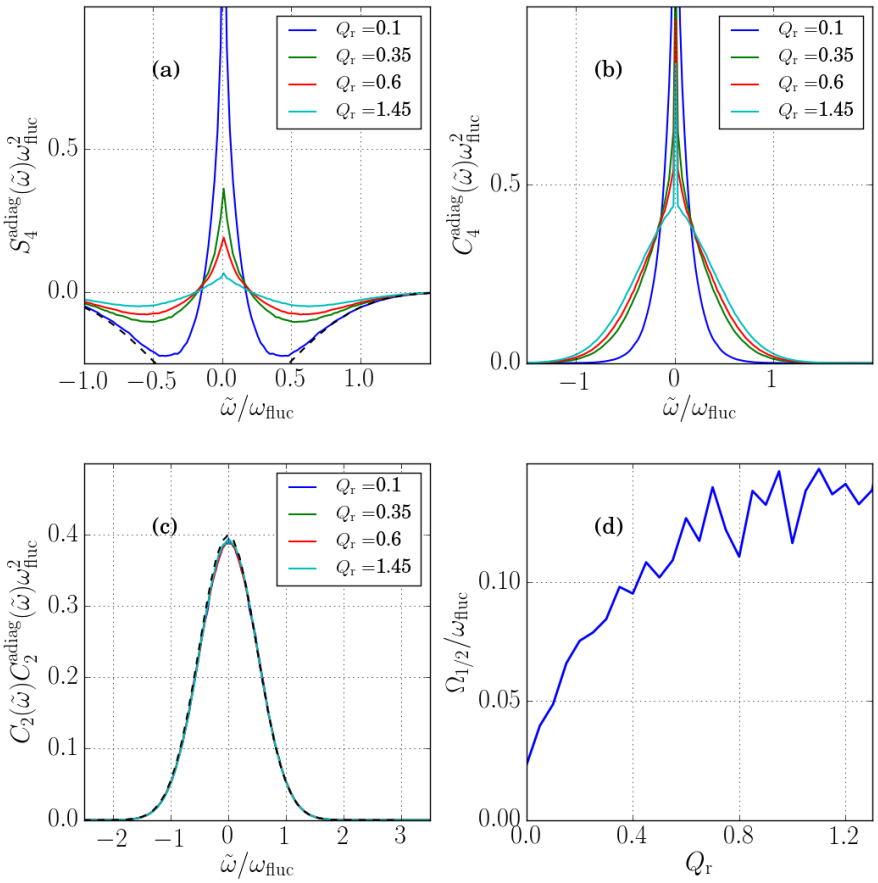

Figure 6.10: Antidiagonal cuts $\omega_1 + \omega_2 = 2\omega_{\max}$, $S_4^{\mathrm{adiag}}(\tilde{\omega})$ for the same data as in Fig. 6.9 under variation of Q_r. The full width half maximum $\Omega_{1/2}$ of C_4 in relation to the quadrupolar coupling strength Q_r was added. The Gaussian envelope $\mathcal{N}(0, \omega_{\mathrm{fluc}}^2/4)$ is marked in dashed black lines in the S_4 and C_2C_2 cut.

constant under the assumption of equal hyperfine coupling constants is $\langle q_k \rangle \sim \frac{Q_r}{\sqrt{N}}$. This leads to a stronger effect of the quadrupolar coupling with less nuclear spins involved. For a constant full width half maximum $\Omega_{1/2}$, the parameter Q_r has to be adjusted to take the bath size into account. In Fig. 6.11 (a) the enhanced influence of the quadrupolar interaction for small numbers of nuclear spins is visible in the loss of spectral weight at $\tilde{\omega} = 0$. The same effect could be observed in Fig. 6.9 for large Q_r and $N = 100$. The antidiagonal cut, see panel (b), reveals the transition from an exponential shape to a Gaussian shape which also goes hand in hand with an increase of the quadrupolar coupling constant q_k. For the quantum mechanical simulation the size of the nuclear spin bath is limited by that of the Hilbert space $\dim(\mathcal{H}) = 2(2I+1)^2$. Therefore, it is preferable to adjust the external magnetic field to show the dependence of the antidiagonal cut of S_4 on the ratio between nuclear Zeeman and quadrupolar coupling strength (plot found in Ref. [137]). That a similar transition from the Gaussian shape of the antidiagonal cut to the exponential decaying shape can be observed for a quantum mechanical simulation under variation of the external magnetic field is shown in Fröhling et al. [137]. For a high magnetic field of $|\vec{b}_{\mathrm{ext}}| = 200$ the quantum mechanical result assumes an exponential shape even for three $I = 9/2$ nuclear spins.

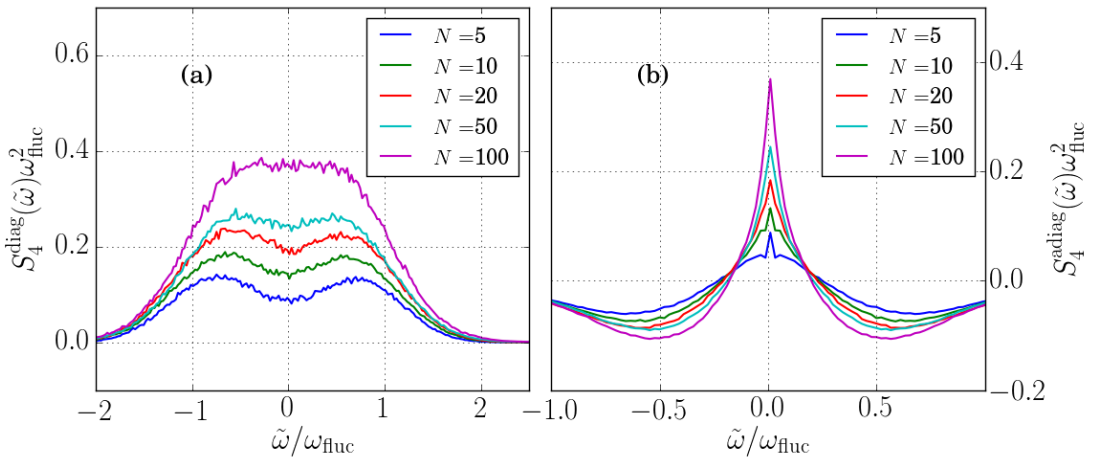

Figure 6.11: Diagonal and antidiagonal cuts through the S_4-spectrum for different bath sizes N for $Q_\mathrm{r} = 0.35$ and $|\vec{b}_\mathrm{ext}| = 5$.

When the dynamics is dominated by the Zeeman energy, the quadrupolar interaction can be interpreted as a perturbation to the dynamics. This lines up with observations of the fourth-order spin correlation function in the time domain [78, 91–93], where high magnetic fields induce an exponential time decay $T_2 \propto \mathcal{O}(\mu\mathrm{s})$.

6.4.1 Fourth-order spin noise in the crossover regime

Up until now the choice of the parameters $|\vec{b}_\mathrm{ext}|$, Q_r and hyperfine interaction determined one dominating energy, which usually is the Zeeman energy. Here, we turn to the crossover regime where the Zeeman energy is of the order of the hyperfine energy ω_fluc. Then the electron spin dynamics is equally influenced by the external magnetic field of $|\vec{b}_\mathrm{ext}| = 1$ and the Overhauser field.

If we also apply a quadrupolar interaction with $Q_\mathrm{r} = 0.35$, the contribution of the nuclear-electric quadrupolar interaction $\langle q_k' \rangle |(\vec{n}_k \vec{I}_k')\vec{n}_k| \leq 1.2 \cdot 10^{-3}$ to the effective field on the nuclear spin is approximately equal to that of the nuclear Zeeman $\zeta|\vec{b}_\mathrm{ext}| = 1.25 \cdot 10^{-3}$ for $N = 100$. Both are of the order of magnitude of 10^{-3} and one order of magnitude smaller than the Knight field.

In Fig. 6.12 we compare the classical results with a quantum mechanical calculation of the S_4-spectrum for the smallest possible nuclear bath size $N = 1$. The parameter values $Q_\mathrm{r} = 0.08$ and $I = 9/2$ were used. Note that for $N = 1$ the quadrupolar coupling is strong compared to the Zeeman energy. Even though the influence of the measurement on the result was neglected, the quantum mechanical result in Fig. 6.12 is near identical to those of a strong and continuous measurement presented in Ref. [94] for a nuclear spin bath size of $N = 1$. The quantum mechanical S_4-spectrum already hints at its classical limit with its broadened C_4-contributions along the diagonal and the weak contributions to the positive S_4-spectrum near the ω_1-axis and ω_2-axis. The classical S_4-spectrum shows the same broadening due to quadrupolar interaction, albeit in a continuous spectrum.

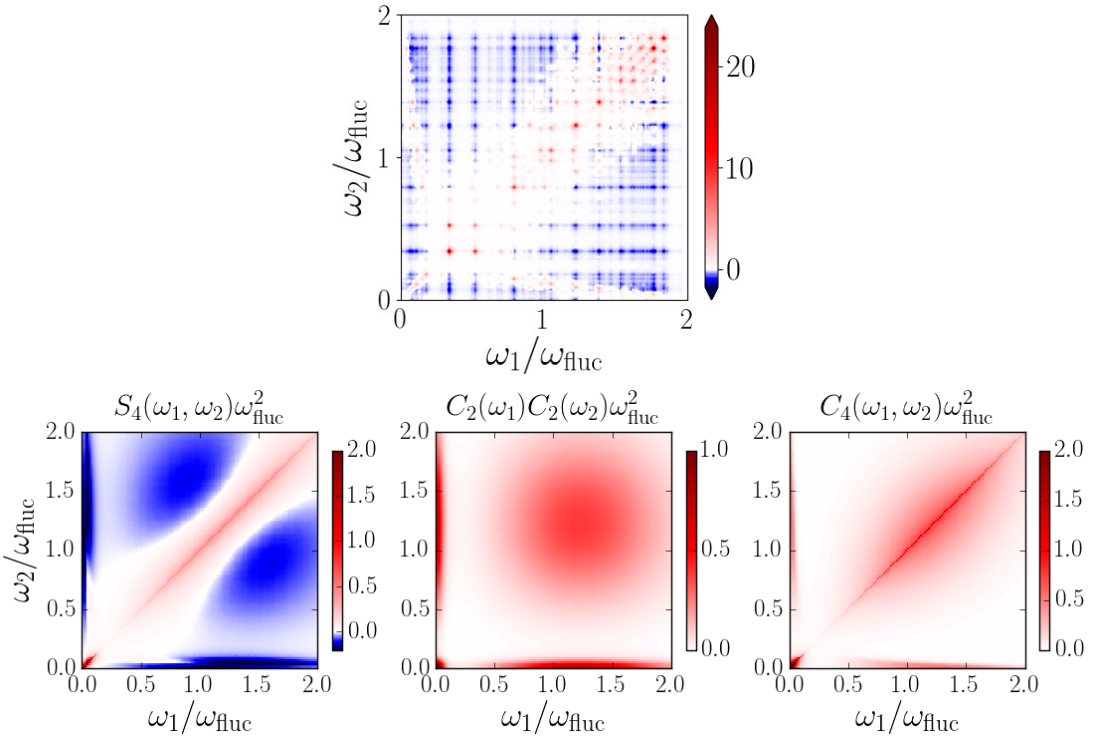

Figure 6.12: Comparison between a quantum mechanical simulation with $N = 1$, $I = 9/2$ and $Q_{\mathrm{r}} = 0.08$ on top and a classical simulation with $N = 100$ and $Q_{\mathrm{r}} = 0.35$ in the bottom line. For the SCA the spectrum of the components $C_2(\omega_1)C_2(\omega_2)$ and $C_4(\omega_1,\omega_2)$ was added. The external magnetic field is $|\vec{b}_{\mathrm{ext}}| = 1$. The plot containing the quantum mechanical result was already published in Ref. [137].

6.5 Chapter conclusion

In the preceding sections we devised a semiclassical expression for the fourth-order correlation function. This higher-order spectrum quantifies the correlation between two frequencies while subtracting the Gaussian contributions originating from lower-order correlation functions. The bispectrum $S_4(\omega_1,\omega_2)$ as a cut through the cumulant $\tilde{S}_4(\omega_1,-\omega_1,\omega_2,-\omega_2)$ can be divided in two parts: $C_4(\omega_1,\omega_2)$, which leads to correlation in the spectrum, and $C_2(\omega_1)C_2(\omega_2)$, which is responsible for the occurring anti-correlations. For magnetic fields which exceed $|\vec{b}_{\mathrm{ext}}| > 1$ the correlations are concentrated on the diagonal and are encompassed by a multivariate Gaussian with a diagonal covariance matrix. The spectrum is centered around $\mu(|\vec{b}_{\mathrm{ext}}|)$, cf. Eq. (6.2.3).

We showed that a good agreement between semiclassical and quantum mechanical simulations is found if the quadrupolar interaction is disregarded. The classical approach acts as a limit to the quantum mechanical result either for a large nuclear spin bath N or for a large spin length I.

The second-order correlation function decays quickly on the time scale of T^* in the presence of a magnetic field. Long-time effects stemming for example from quadrupolar interaction can, therefore, not be observed in C_2. Fourth-order correlation functions provide an approach to make these previously hidden interactions visible. In the fre-

quency correlations of the bispectrum, the influence of the quadrupolar interaction makes itself felt as a broadening of the C_4-contributions along the diagonal. We found that the full width half maximum is proportional to the quadrupolar interaction strength Q_r. While this broadening effect is consistent with the observations in the quantum mechanical case [137], it exhibits a different curve shape at the parameters acquired by generating congruent, second-order correlation functions $C_2(t)$. The matching process performed in Sec. 5.3.4 does not translate to S_4 with quadrupolar interaction. We linked the shape of the antidiagonal cut to the ratio between effective fields originating from the nuclear Zeeman interaction and the quadrupolar interaction. The smaller bath size of the quantum mechanical simulation leads to a stronger coupling constant q_k which exerts a larger influence on an individual $\vec{I}_k$. The same connection is found in the SCA through a variation of Q_r or N at a fixed $|\vec{b}_\mathrm{ext}|$.

Since spin-noise spectroscopy facilitates minimally invasive experimental measurements [95, 174], they can be seen as the complement to pump-probe spectroscopy where the spin system is driven away from equilibrium. The investigation of higher-order spin correlation functions goes hand in hand with spin-noise spectroscopy and opens the door to a better understanding of many phenomena of the spin dynamics in a QD. As an exemplary interaction, we chose the quadrupolar interaction, whose effects in the time domain were already experimentally documented in Refs. [91–93] by measuring the fourth-order correlator $\langle S_z(t_1)S_z(t_1+t_2)S_z(t_1)S_z\rangle$ and theoretically described by Fröhling et al. [93].

Chapter 7

Mode locking in a pulsed quantum dot

We aim to describe a single electron charged QD subjected to periodic laser pulses and located in an externally applied magnetic field. The time scales of the system vary greatly: the time duration of the pulses ($\sim 1.5\,\mathrm{ps}$), the trion decay ($\sim 0.4\,\mathrm{ns}$) and the repetition time of the pulse (13.2 ns) [33, 35, 177]. The mode-locking occurs on a time scale of seconds up to minutes [33].

We have already derived and discussed the spin dynamics of an unpumped system in the SCA in Sec. 5. Those results are still an essential building block of the semiclassical simulation. But additionally, we need a theoretical description of the pump pulses and the subsequent trion decay. For the pulses per se a quantum mechanical approach suffices since they can be assumed as instantaneous compared to the other relevant time scales. The nuclear spin dynamics is assumed frozen during the pulse. This reasoning is not valid for the trion decay for which a semiclassical approach – equivalent to the quantum mechanical, commonly used Lindblad approach [178] – can be found. The quadrupolar interaction is neglected in this chapter, $H_\mathrm{Q} = 0$.

The simulation of a periodic pulse sequence on a QD in the hybrid quantum-classical approach is initialized by N_C classical configurations with randomly oriented N nuclear spins and a central spin. At $t = 0$ the first pulse arrives. The nuclear spins are frozen and the electron spin in each configuration is represented as a density matrix. The transformation of the pulse is applied. After translating the now pulsed electron spin state back to a semiclassical vector representation, the electron spin dephasing between two consecutive pulses is described by a set of coupled equations of motion. We string together the repeating parts of pulse and semiclassical spin dynamics and calculate the expectation values as an average over all configurations.

In addition to the simulation, we derive analytical resonance conditions for the Overhauser field in a pulsed steady state under the assumption of frozen nuclear spins.

The contents of this chapter was already published in Jäschke et al. [89].

7.1 Pump laser pulses

The σ^+-pulse initiates a transition between the electron state $|\uparrow\rangle$ and the trion state $|\uparrow\downarrow\Uparrow\rangle$. The trion-up state is abbreviated as $|\uparrow\downarrow\Uparrow\rangle =: |\mathrm{T}\rangle$. Since the other trion state $|\uparrow\downarrow\Downarrow\rangle$ cannot be excited by a σ^+-pulse, the system for the pulses is reduced to a 3×3 problem. We chose the spin eigenbasis along the z-axis. Furthermore, we assume that the time scale of the pulse is much shorter than that of all other dynamics given by the Hamiltonian Eq. (3.1.13) as well as the trion decay. Therefore, the pump pulse, assumed to be instantaneous, is described by a unitary transformation.

Starting from a laser pulse of finite length in time, the Hamiltonian for the pulse consists of the level occupations and the transition from $|\uparrow\rangle$ to the trion state $|\mathrm{T}\rangle$

$$H_\mathrm{P} = \epsilon_\mathrm{T}|\mathrm{T}\rangle\langle\mathrm{T}| + \Omega(t)\left(\mathrm{e}^{\mathrm{i}\epsilon_\mathrm{P}t} + \mathrm{e}^{-\mathrm{i}\epsilon_\mathrm{P}t}\right)\left(|\mathrm{T}\rangle\langle\uparrow| + |\uparrow\rangle\langle\mathrm{T}|\right). \tag{7.1.1}$$

The characteristic frequency of the laser pump pulse is ϵ_P and the envelope of the amplitude of the laser pulse is $\Omega(t)$. ϵ_T denotes the difference between the electron and the trion energy. Via a rotating wave approximation with the unitary transformation U_I into the interaction picture

$$U_\mathrm{I} = |\uparrow\rangle\langle\uparrow| + |\downarrow\rangle\langle\downarrow| + \exp(\mathrm{i}\epsilon_\mathrm{T}t)|\mathrm{T}\rangle\langle\mathrm{T}| \tag{7.1.2}$$

the light-matter interaction can be rewritten as

$$H_\mathrm{P} \approx H_\mathrm{P}^\mathrm{RWA} = \epsilon_\mathrm{T}|\mathrm{T}\rangle\langle\mathrm{T}| + \Omega(t)\left(\mathrm{e}^{-\mathrm{i}\epsilon_\mathrm{P}t}|\mathrm{T}\rangle\langle\uparrow| + \mathrm{e}^{+\mathrm{i}\epsilon_\mathrm{P}t}|\uparrow\rangle\langle\mathrm{T}|\right). \tag{7.1.3}$$

A second rotating wave approximation into the rotating frame of the excitation laser renders the effect of the laser dependent on its envelope $\Omega(t)$ only

$$\begin{aligned}\tilde{H}_\mathrm{P}^\mathrm{RWA} &= U_{\epsilon_\mathrm{P}}(H_\mathrm{P}^\mathrm{RWA} - \epsilon_\mathrm{P}|\mathrm{T}\rangle\langle\mathrm{T}|)U_{\epsilon_\mathrm{P}}^\dagger \\ &= (\epsilon_\mathrm{T} - \epsilon_\mathrm{P})\,|\mathrm{T}\rangle\langle\mathrm{T}| + \Omega(t)\left(|\mathrm{T}\rangle\langle\uparrow| + |\uparrow\rangle\langle\mathrm{T}|\right)\end{aligned} \tag{7.1.4}$$

with

$$U_{\epsilon_\mathrm{P}} = |\uparrow\rangle\langle\uparrow| + |\downarrow\rangle\langle\downarrow| + \exp(\mathrm{i}\epsilon_\mathrm{P}t)|\mathrm{T}\rangle\langle\mathrm{T}|. \tag{7.1.5}$$

The prefactor $\epsilon_\mathrm{T} - \epsilon_\mathrm{P}$ is defined as the detuning δ, the deviation of the pump pulse from the trion excitation energy. In this work we only take perfectly resonant laser pulses $\delta = 0$ into account. For an in-depth consideration of the detuned or non-instantaneous laser pulses on the dynamics, see e. g. Yugova [121] or others [64, 179–182]. The effect of a series of non-instantaneous pulses on a QD in a quantum mechanical approach is discussed by Kleinjohann et al. [63].

Since we are not interested in the time evolution during the pulse but rather in the final state of the system after the pulse, we integrate over the entire time of the pulse

$$U(t_\mathrm{final}) = \mathcal{T}\left[\exp\left(\mathrm{i}\int_0^{t_\mathrm{final}} \mathrm{d}t' \tilde{H}_\mathrm{P}^\mathrm{RWA}(t')\right)\right] = \exp\left[\mathrm{i}\frac{F}{2}\left(|\uparrow\rangle\langle\mathrm{T}| + |\mathrm{T}\rangle\langle\uparrow|\right)\right]. \tag{7.1.6}$$

For the resonant case $\delta = 0$, the time ordering operator $\mathcal{T}$ can be neglected since the relation $[\tilde{H}_\mathrm{P}^\mathrm{RWA}(t), \tilde{H}_\mathrm{P}^\mathrm{RWA}(t')] = 0$ holds at all times. The integral in the time-evolution operator is replaced by the pulse area $F := 2\int_{-\infty}^{\infty}\Omega(t')\mathrm{d}t'$ which is dependent on the

duration of the pulse and its intensity. For instantaneous pulses the pulse shape is irrelevant. The unitary transformation operator T_F is

$$T_F = \cos\left(\frac{F}{2}\right)\left(|\uparrow\rangle\langle\uparrow| + |\mathrm{T}\rangle\langle\mathrm{T}|\right) + \mathrm{i}\sin\left(\frac{F}{2}\right)\left(|\uparrow\rangle\langle\mathrm{T}| + |\mathrm{T}\rangle\langle\uparrow|\right) + |\downarrow\rangle\langle\downarrow|. \tag{7.1.7}$$

The pulse operator is applied to the electronic subsystem

$$\tilde{\rho}_\mu^{\mathrm{ap}} = \left(U_{\epsilon_\mathrm{P}}^\dagger T_F U_{\epsilon_\mathrm{P}}\right) \rho_\mu^{\mathrm{bp}} \left(U_{\epsilon_\mathrm{P}}^\dagger T_F U_{\epsilon_\mathrm{P}}\right)^\dagger . \tag{7.1.8}$$

where the density matrix ρ_μ^{bp} of the system before the pulse is translated to that after the pulse $\tilde{\rho}_\mu^{\mathrm{ap}}$. Since the nuclear spins are considered as frozen during the pulse, the transformation can be applied in each configuration μ independent of its nuclear bath configuration.

7.1.1 Transition between classical simulation and quantum mechanical density matrix

In Eq. (7.1.8) a translation from classical electron spin vector to quantum mechanical density matrix is required. The gap between those two is closed by interpreting the semiclassical spin vector $\vec{S}$ as an expectation value of a quantum mechanical spin 1/2 in each configuration μ

$$S_{i,\mu} = \mathrm{Tr}\left[\frac{1}{2}\rho_\mu \sigma_i\right] \tag{7.1.9}$$

where σ_i is the Pauli spin matrix for $i = x, y, z$. Note that because of the statistical nature of the pulses the spin vector has no constant length. A purely classical interpretation where only the average over all configurations is equivalent to an expectation value is therefore impossible.

Considering the requirements that the density matrix is a positive semi-definite, Hermitian operator of trace 1, the density matrix ρ_μ^{bp} of the electronic subsystem corresponding to a semiclassical vector of length $|\vec{S}| = 1/2$

$$\rho_\mu^{\mathrm{bp}} = \begin{pmatrix} \frac{1}{2} + S_{z,\mu}^{\mathrm{bp}} & S_{x,\mu}^{\mathrm{bp}} - \mathrm{i}S_{y,\mu}^{\mathrm{bp}} & 0 \\ S_{x,\mu}^{\mathrm{bp}} + \mathrm{i}S_{y,\mu}^{\mathrm{bp}} & \frac{1}{2} - S_{z,\mu}^{\mathrm{bp}} & 0 \\ 0 & 0 & 0 \end{pmatrix} \tag{7.1.10}$$

can be related to the vector components $S_{i,\mu}^{\mathrm{bp}}$. The density matrix represents the electron spin alignment in a single configuration μ immediately before the pulse. Before the pulse a 2×2 matrix is sufficient to describe the electron spin. The dimension is extended to include the yet unoccupied trion $|\mathrm{T}\rangle$-state.

7.1.2 Transformation of a density operator by a laser pulse

The transformation of the density matrix and the resulting expectation values for the electron spin and trion components shall be investigated for the general case of an instantaneous pulse with an arbitrary pulse area F, see also [121, 179–181].

For convenience the reverse transformation in Eq. (7.1.8) is neglected. This is possible due to the fact that the transformation, given by U_{ϵ_P}, only acts on the trion state while in the density matrix before the pulse Eq. (7.1.10) we assume that the trion state is completely decayed. Therefore, while the density matrix $\tilde{\rho}_\mu^{\mathrm{ap}}$ does not have to equal

$$\begin{aligned}\rho_\mu^{\mathrm{ap}} &= T_F \rho_\mu^{\mathrm{bp}} T_F^\dagger \\ &= \begin{pmatrix} \cos^2\left(\frac{F}{2}\right)\rho^{\mathrm{bp}}_{\uparrow\uparrow,\mu} & \cos\left(\frac{F}{2}\right)\rho^{\mathrm{bp}}_{\uparrow\downarrow,\mu} & -\mathrm{i}\sin\left(\frac{F}{2}\right)\cos\left(\frac{F}{2}\right)\rho^{\mathrm{bp}}_{\uparrow\uparrow,\mu} \\ \cos\left(\frac{F}{2}\right)\rho^{\mathrm{bp}}_{\downarrow\uparrow,\mu} & \rho^{\mathrm{bp}}_{\downarrow\downarrow,\mu} & -\mathrm{i}\sin\left(\frac{F}{2}\right)\rho^{\mathrm{bp}}_{\downarrow\uparrow,\mu} \\ \mathrm{i}\sin\left(\frac{F}{2}\right)\cos\left(\frac{F}{2}\right)\rho^{\mathrm{bp}}_{\uparrow\uparrow,\mu} & \mathrm{i}\sin\left(\frac{F}{2}\right)\rho^{\mathrm{bp}}_{\uparrow\downarrow,\mu} & \sin^2\left(\frac{F}{2}\right)\rho^{\mathrm{bp}}_{\uparrow\uparrow,\mu} \end{pmatrix},\end{aligned} \tag{7.1.11}$$

the expectation values Eq. (7.1.9) of $\tilde{\rho}_\mu^{\mathrm{ap}}$ and ρ_μ^{ap} still agree. The matrix elements $\rho^{\mathrm{bp}}_{\sigma\sigma',\mu}$ can be taken from Eq. (7.1.10) with σ denoting the spin state. The expectation values $S^{\mathrm{ap}}_{i,\mu}$ and $P_{\mathrm{T},\mu}$ after the pulse using Eq. (7.1.11) and Eq. (7.1.9) are

$$S^{\mathrm{ap}}_{x,\mu} = \cos\left(\frac{F}{2}\right) S^{\mathrm{bp}}_{x,\mu} \tag{7.1.12a}$$

$$S^{\mathrm{ap}}_{y,\mu} = \cos\left(\frac{F}{2}\right) S^{\mathrm{bp}}_{y,\mu} \tag{7.1.12b}$$

$$S^{\mathrm{ap}}_{z,\mu} = \frac{1}{2}\left[\left(S^{\mathrm{bp}}_{z,\mu} - \frac{1}{2}\right) + \cos^2\left(\frac{F}{2}\right)\left(S^{\mathrm{bp}}_{z,\mu} + \frac{1}{2}\right)\right] \tag{7.1.12c}$$

$$P_{\mathrm{T},\mu} = \sin^2\left(\frac{F}{2}\right)\left(S^{\mathrm{bp}}_{z,\mu} + \frac{1}{2}\right). \tag{7.1.12d}$$

The maximal effect of a pulse is reached if the pulse area is $F = \pi$, which empties the $|\uparrow\rangle$-state completely and excites the maximum possible trion state of $P_{\mathrm{T},\mu} = 1$. For a pulse area of $F = 2\pi$, the pulse has no effect due to $T_F = \mathbb{1}$.

A more in-depth look shall be dedicated to the resonant π-pulses

$$T_\pi = \mathrm{i}|\mathrm{T}\rangle\langle\uparrow| + \mathrm{i}|\uparrow\rangle\langle\mathrm{T}| + |\downarrow\rangle\langle\downarrow|, \tag{7.1.13}$$

since they are the ideal pulse to excite a trion state. In this case $\cos(F/2) = 0$ and therefore most matrix entries in Eq. (7.1.11) vanish which reduces the matrix to

$$\rho_\mu^{\mathrm{ap}} = \begin{pmatrix} 0 & 0 & 0 \\ 0 & \frac{1}{2} - S^{\mathrm{bp}}_{z,\mu} & S^{\mathrm{bp}}_{y,\mu} - \mathrm{i}S^{\mathrm{bp}}_{x,\mu} \\ 0 & S^{\mathrm{bp}}_{y,\mu} + \mathrm{i}S^{\mathrm{bp}}_{x,\mu} & \frac{1}{2} + S^{\mathrm{bp}}_{z,\mu} \end{pmatrix}. \tag{7.1.14}$$

After a π-pulse the x- and y-component of the electron spin vanish and the initial electron spin is always aligned in negative z-direction after the pulse

$$\vec{S}^{\mathrm{ap}}_\mu(0) = \frac{1}{2}\left(S^{\mathrm{bp}}_{z,\mu} - \frac{1}{2}\right)\vec{e}_z. \tag{7.1.15}$$

The maximal spin polarization is reached for a spin alignment in the negative z-direction before the pulse. For greater values of S^{bp}_z, the polarization decreases and vanishes for $\vec{S}^{\mathrm{bp}} = 1/2\vec{\mathrm{e}}_z$. Since the trion

$$P_{\mathrm{T},\mu}(0) = \left(S^{\mathrm{bp}}_{z,\mu} + \frac{1}{2}\right) \tag{7.1.16}$$

is excited from the $|\uparrow\rangle$-state, the trion occupation depends on the z-alignment of the central spin before the pulse.

Other pulses are discussed in literature which are independent of the spin alignment before the pulse [60]. Those pulses align the electron spin in the z-direction without changing the spin length or exciting a trion state. Another way to tackle the pulse is described in Ref. [65] where the spin length is kept invariant by rotating the spin in the z-direction $\vec{S}^{\mathrm{ap}} = |\vec{S}^{\mathrm{bp}}|\vec{\mathrm{e}}_z$. The other possibility, discussed ibid., takes the quantum mechanical nature of a pulse into account which only allows for the knowledge of the exact polarization in one direction $\vec{S}^{\mathrm{ap}} = (X, Y, 1/2)^{\mathrm{T}}$ with $X, Y \sim \mathcal{N}(0, 1/4)$.

7.1.3 Quantum mechanical Lindblad approach

The laser pump pulse excites an electron state to a trion state which decays back into the $|\uparrow\rangle$-state emitting a photon. A master equation for the trion decay in Lindblad form [178, 183] is derived.

The density operator Eq. (5.2.30) has to be extended to include the excitation of the trion state $|\mathrm{T}\rangle$. For σ^+ polarized light the addition of this one state is sufficient since $|\uparrow\downarrow\Downarrow\rangle$ is never excited. The electronic subspace can be described by a 3×3 matrix given by the eigenstates $|\uparrow\rangle$, $|\downarrow\rangle$ and $|\mathrm{T}\rangle$. The entire Hilbert space including the nuclear bath with N spins of length I has the dimension $D = \dim(\mathcal{H}) = 3(2I+1)^N$.

The fact that the density matrix features a mixed Ising basis, in z-direction for the electron spin and parallel to the external magnetic field for the nuclear spin bath, can be neglected. This is due to the difference in energy scales for the nuclear spins and electron spins. The time scales of nuclear Zeeman energy, coupling to the Knight field and quadrupolar interaction far surpass the short time of the trion decay and Larmor precession of the electron spin [33]. Therefore, the trion decay is modeled for a frozen Overhauser field configuration $\alpha = (m, m')$. This reduces the system $T^* H_{\mathrm{CSM}}$ to that of electron and trion spin dynamics $H_{\mathrm{S}}(\alpha) = \vec{b}_{\mathrm{ext}}\vec{S} + \Delta H(\alpha)$ in a static field given by the external magnetic field and the configuration dependent frozen Overhauser field.

The photon emission which accompanies the trion decay necessitates the inclusion of an environment to the system H_{S}. The complete description of the energy dissipation in this environment would require the explicit form of reservoir correlation functions. To circumvent unnecessary complications the Born-Markov approximation is applied: The environment is large compared to the system and is not significantly altered by the interaction. Therefore, the density matrix is a product state $\rho_{\mathrm{tot}} \approx \rho_{\mathrm{S}}(t) \otimes \rho_{\mathrm{E}}$ of the system $\rho_{\mathrm{S}}(t)$ and the static environment ρ_{E}. Moreover, we have to assume that the bath correlation time is much shorter than the time scale for the evolution of the system. Intuitively, this means that the environment "forgets" its past faster than the system progresses. Resulting from this approximation, the Markovian description of an open quantum system for the reduced density matrix ρ_{S} is given by the Lindblad equation

$$\dot{\rho}_{\mathrm{S}} = -\mathrm{i}[H_{\mathrm{S}}, \rho_{\mathrm{S}}] - \gamma(s_2 s_1 \rho_{\mathrm{S}} + \rho_{\mathrm{S}} s_2 s_1 - 2 s_1 \rho_{\mathrm{S}} s_2). \tag{7.1.17}$$

The unitary dynamics of a closed system is given by the von-Neumann equation which encompasses the first summand. The coupling to the environment is encoded in the non-unitary trion decay governed by the decay rate γ which has the dimension of an

inverse time. The transition operators between trion and electron state, s_1 and s_2, are given by the projectors $s_1 := |\uparrow\rangle\langle \mathrm{T}|$ and $s_2 := |\mathrm{T}\rangle\langle\uparrow|$.

The Lindblad equation can formally be solved by flattening the density matrix to a vector $\vec{\rho}_\mathrm{S} = (\rho_{11}, ..., \rho_{1n}, ..., \rho_{n1}, ..., \rho_{nn})^\mathrm{T}$ and mapping the projectors with the Kronecker product from the matrix product $A\rho B \to (B^\mathrm{T} \otimes A)\vec{\rho}$. This leads to the form

$$\dot{\vec{\rho}}_\mathrm{S} = \mathcal{L}\vec{\rho}_\mathrm{S} = \left[\mathrm{i}(H_\mathrm{S} \otimes \mathbb{1} - \mathbb{1} \otimes H_\mathrm{S}) - \gamma\left(s_2 s_1 \otimes \mathbb{1} + \mathbb{1} \otimes s_2 s_1 - 2 s_1 \otimes s_1\right)\right] \vec{\rho}_\mathrm{S} \tag{7.1.18}$$

which can be solved by

$$\rho_\mathrm{S}(t) = \mathrm{e}^{\mathcal{L}t}\rho_\mathrm{S}(0). \tag{7.1.19}$$

The advantages of a FOA become even more obvious in this mapping procedure which increases the matrix size to $(\dim\mathcal{H})^2$. An exact treatment would see the 9×9 dimensional, mapped Hamiltonian $H_\mathrm{S} \otimes \mathbb{1}$ replaced by the full Hamiltonian matrix of dimension $D^2 \times D^2$ leading to a computationally unsolvable problem for a large nuclear spin bath. This severely limits the number of nuclear spins [61, 63, 184] in the case of inhomogeneous coupling. In the frozen nuclear approximation, independent Lindblad equations for each nuclear bath configuration α are solved instead. The Liouvillians $\mathcal{L}_\alpha$ vary only by a constant, configuration dependent Overhauser field $\Delta H(\alpha)$, therefore, changing only the von-Neumann part of the superoperator. The starting density vector $\rho_{\mathrm{S},\alpha}(t = 0)$ has to be extracted from the simulation result of the previous pulse period, see Sec. 7.1.2. The solution in each nuclear configuration

$$\rho_{\mathrm{S},\alpha}(t) = \mathrm{e}^{\mathcal{L}_\alpha(t)}\rho_{\mathrm{S},\alpha}(0) \tag{7.1.20}$$

only requires the diagonalization of a 9×9 Liouville matrix.

7.1.4 Extending the equations of motion by a classical Lindblad formalism

While the coupled classical equations of motion Eqs. (5.2.27) describe a unitary time evolution which leaves the spin length invariant, the Liouvillian is a non-unitary operator. In an external magnetic field, this leads to a build-up of polarization caused by the pulse and consecutive trion decay. In quantum mechanics this fact is accounted for by the transition from an initially pure to a mixed electron state which is reflected in the semiclassical simulation by the variation of the length of the electron spin vector. The polarization gain through pulsing may vary from configuration to configuration.

In the FOA the trion decay and electron spin dynamics is given by Eq. (7.1.18). The static magnetic field allows for a reduction to nine coupled linear differential equations for each density matrix element. One differential equation is eliminated through the conservation of the trace. Furthermore, the time dynamics of the density matrix elements for the transition between electron and trion states decouple from the rest. Those off-diagonal trion matrix elements decay exponentially with the trion. This enables further downsizing of the differential equation system by four equations. The remaining

differential equations of the density matrix ρ_{S} are

$$\dot{\rho}_{\uparrow\uparrow} = \frac{\mathrm{i}\omega_x - \omega_y}{2}\rho_{\uparrow\downarrow} - \frac{\mathrm{i}\omega_x + \omega_y}{2}\rho_{\downarrow\uparrow} + 2\gamma\rho_{\mathrm{TT}} \tag{7.1.21a}$$

$$\dot{\rho}_{\uparrow\downarrow} = \frac{\mathrm{i}\omega_x + \omega_y}{2}\rho_{\uparrow\uparrow} - \mathrm{i}\omega_z\rho_{\uparrow\downarrow} - \frac{\mathrm{i}\omega_x + \omega_y}{2}\rho_{\downarrow\downarrow} \tag{7.1.21b}$$

$$\dot{\rho}_{\downarrow\uparrow} = \frac{-\mathrm{i}\omega_x + \omega_y}{2}\rho_{\uparrow\uparrow} + \mathrm{i}\omega_z\rho_{\downarrow\uparrow} + \frac{\mathrm{i}\omega_x + \omega_y}{2}\rho_{\downarrow\downarrow} \tag{7.1.21c}$$

$$\dot{\rho}_{\downarrow\downarrow} = \frac{-\mathrm{i}\omega_x + \omega_y}{2}\rho_{\uparrow\downarrow} + \frac{\mathrm{i}\omega_x + \omega_y}{2}\rho_{\downarrow\uparrow} \tag{7.1.21d}$$

$$\dot{\rho}_{\mathrm{TT}} = -2\gamma\rho_{\mathrm{TT}}, \tag{7.1.21e}$$

where $\omega_i T^* = b_{\mathrm{ext},i} + b_{\mathrm{N},i,\mu}$ with $i = x, y, z$ are the constant effective frequencies of a classical configuration μ. The Eqs. (7.1.21) are inserted in the first derivative in time of the electron spin expectation value or trion occupation probability given by

$$\frac{d}{dt}\langle O\rangle_\mu = \mathrm{i}\mathrm{Tr}\left[\rho_{\mathrm{S}}(t)[H_{\mathrm{S}}, O]\right] - \gamma\mathrm{Tr}\left[\Delta\rho_L O\right]. \tag{7.1.22}$$

O is a local placeholder variable in the electronic subspace and

$$\Delta\rho_L = |\mathrm{T}\rangle\langle\mathrm{T}|\rho_{\mathrm{S}}(t) + \rho_{\mathrm{S}}(t)|\mathrm{T}\rangle\langle\mathrm{T}| - 2|\uparrow\rangle\langle\uparrow|P_{\mathrm{T},\mu}(t). \tag{7.1.23}$$

The trion occupation probability $P_{\mathrm{T},\mu}(t) = \langle\mathrm{T}|\rho_{\mathrm{S}}(t)|\mathrm{T}\rangle$ is directly accessible through Eq. (7.1.21e)

$$\frac{d}{dt}P_{\mathrm{T},\mu}(t) = -2\gamma P_{\mathrm{T},\mu}(t). \tag{7.1.24}$$

with the analytic solution

$$P_{\mathrm{T},\mu}(t) = P_{\mathrm{T},\mu}(0)e^{-2\gamma t}. \tag{7.1.25}$$

The trion occupation at $t = 0$ is given by the laser pump pulse Eq. (7.1.12d). The equation of motion for the electron expectation value is also faithfully reproduced by the ansatz

$$\frac{d}{dt}\left\langle\vec{S}\right\rangle_\mu = \vec{\omega}\times\left\langle\vec{S}\right\rangle_\mu + \gamma P_{\mathrm{T},\mu}(t)\vec{\mathrm{e}}_z, \tag{7.1.26}$$

with $\vec{\omega}T^*$ being an effective field. Through the correspondence principle the expectation value agrees with that of the semiclassical variable Eq. (5.2.27). Inserting Eq. (7.1.25) into Eq. (7.1.26) gives the final electronic equation of motion for the period that bridges the time between two pulses

$$\frac{\mathrm{d}}{\mathrm{d}t}\vec{S}_\mu(t) = \frac{1}{T^*}\left(\vec{b}_{\mathrm{N},\mu} + \vec{b}_{\mathrm{ext}}\right)\times\vec{S}_\mu(t) + \gamma P_{\mathrm{T},\mu}(0)\vec{\mathrm{e}}_z e^{-2\gamma t}. \tag{7.1.27}$$

The time t is measured relative to the last pulse. A rescaling of the classical vector to length unity as discussed in Sec. 5.2.3 changes the $\gamma P_{\mathrm{T},\mu}(0)\vec{\mathrm{e}}_z e^{-2\gamma t}$ to $\gamma/S P_{\mathrm{T},\mu}(0)\vec{\mathrm{e}}_z e^{-2\gamma t}$. In the SCA we replace the constant Overhauser field $\vec{b}_{\mathrm{N},\mu}$ by $\vec{b}_{\mathrm{N},\mu}(t)$.

The addition to the central spin dynamics is easy to grasp: The vector product still describes the electronic spin precession in the effective field $\vec{b} = \vec{b}_{\mathrm{N}} + \vec{b}_{\mathrm{ext}}$. Therefore, in Fig. 7.1 the dynamics of the electron is shown in the rotating frame of the Larmor precession. The negative S_z^{ap}-part given by $|\downarrow\rangle$ which is unaffected by the laser pulse stays constant in this frame while the trion decays back with the rate 2γ into the electron $|\uparrow\rangle$-state which in the classical simulation is represented by the positive S_z-component. Since the trion always decays in positive z-direction, the recently decayed trion part (green) is always differently aligned compared to the now rotating $|\downarrow\rangle$-part. This leads to a changing length of the electron spin vector over the time of the trion decay. As soon as the trion is decayed $P_{\mathrm{T}} = 0$ the classical spin vector length stays constant. The change of the vector length of the spin length hints to the statistical nature of the photon absorption which can be found in the density matrix description. This affirms the fact that the purely classical interpretation of a spin vector has to be relinquished for the central spin - due to the pulse and trion decay - even within a single configuration.

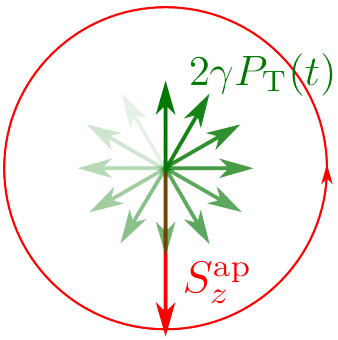

Figure 7.1: Schematic of the trion decay in the rotating frame of the electron spin.

For a large magnetic field where the Larmor precession period is of the order of magnitude of the trion decay time or faster, the $|\uparrow\rangle$-state is assumed to average to nearly zero in the rotating frame. The unpumped $|\downarrow\rangle$-component then leads to an effective polarization in the system.

7.2 Analytic solution in the frozen Overhauser field approximation

Even with the additional complication imposed by the inclusion of the trion decay, an analytical solution for the electron spin dynamics in a periodically pulsed system can be derived by the standard workhorse FOA. Combined with initial conditions dictated by the pulse, restrictions for the Overhauser field distribution in a non-equilibrium steady state are found.

7.2.1 Central spin dynamics with trion decay

The solution for Eq. (7.1.27) in the FOA without the source term is already known and given by Eq. (5.2.34). When including the trion decay term, the homogeneous part of the solution no longer directly includes the initial spin $\vec{S}_0$. Instead, the three-component vector $\vec{A}$, which depends on conditions set by the pulses, replaces $\vec{S}_0$

$$\vec{S}_{\mathrm{hom}} = (\vec{A}\vec{n})\vec{n} + [\vec{A} - (\vec{A}\vec{n})\vec{n}]\cos(\omega_{\mathrm{L}}t) + \vec{n} \times [\vec{A} - (\vec{A}\vec{n})\vec{n}]\sin(\omega_{\mathrm{L}}t). \tag{7.2.1}$$

The inhomogeneous solution has the form

$$\vec{S}_{\mathrm{in}} = \vec{C}e^{-2\gamma t}. \tag{7.2.2}$$

The vector $\vec{C}$

$$-P_{\mathrm{T}}(0)\vec{\mathrm{e}}_z = 2\vec{C} + \frac{\vec{\omega}}{\gamma} \times \vec{C} \tag{7.2.3}$$

depends on the effective frequency $\vec{\omega} = (\vec{b}_{\mathrm{ext}} + \vec{b}_{\mathrm{N}})/T^*$ as well as the trion occupation $P_{\mathrm{T}}(0)$. With the definition of a rotation matrix $\underline{\underline{M}}$ for the cross product $\underline{\underline{M}}\vec{v} = \vec{n} \times \vec{v}$ the solution for $\vec{C}$ is

$$\vec{C} = -\frac{P_{\mathrm{T}}(0)}{2}\left[\mathbb{1} + \frac{\omega_L}{2\gamma}\underline{\underline{M}}\right]^{-1}\vec{e}_z. \tag{7.2.4}$$

The total solution comprises $\vec{S}(t) = \vec{S}_{\mathrm{hom}}(t) + \vec{S}_{\mathrm{in}}(t)$ in which the initial condition determines the vector

$$\vec{A} = \vec{S}(0) - \vec{C}, \tag{7.2.5}$$

where the initial spin alignment after the pulse $\vec{S}(0)$ can be gleaned from Eqs. (7.1.12). Since $P_{\mathrm{T}}(0)$ is positive for all pulse areas, $\vec{C}$ has a negative sign and $|\vec{S}(0)|$ increases with the decaying trion.

For a strong external field applied in x-direction $\vec{b}_{\mathrm{ext}} = b_{\mathrm{ext}}\vec{\mathrm{e}}_x$ the following $\vec{C}$ results:

$$\vec{C} = -\frac{P_{\mathrm{T}}(0)}{2}\frac{\overline{\gamma}}{\overline{\gamma}^2 + \omega_{\mathrm{L}}^2}\left(\omega_{\mathrm{L}}\vec{\mathrm{e}}_y + \overline{\gamma}\vec{\mathrm{e}}_z\right) \tag{7.2.6}$$

with $2\gamma = \overline{\gamma}$. This leads to the general solution for a frozen effective field with trion decay

$$\vec{S}(t) = \begin{pmatrix} A_x \\ -A_z\sin(\omega_{\mathrm{L}}t) + A_y\cos(\omega_{\mathrm{L}}t) - \dfrac{\overline{\gamma}\omega_{\mathrm{L}}}{\overline{\gamma}^2 + \omega_{\mathrm{L}}^2}\dfrac{P_{\mathrm{T}}(0)}{2}\mathrm{e}^{-\overline{\gamma}t} \\ A_y\sin(\omega_{\mathrm{L}}t) + A_z\cos(\omega_{\mathrm{L}}t) - \dfrac{\overline{\gamma}^2}{\overline{\gamma}^2 + \omega_{\mathrm{L}}^2}\dfrac{P_{\mathrm{T}}(0)}{2}\mathrm{e}^{-\overline{\gamma}t} \end{pmatrix}. \tag{7.2.7}$$

The parameters A_i with $i = x, y, z$ depend on the pulse area and the state of the central spin before the pulse.

7.2.2 Resonance Conditions

The electron spin dynamics under the influence of a periodic sequence of laser pump pulses is described in the approximative approach of a frozen nuclear spin bath. This assumption is usually not justified since the feedback of the Knight field is an integral part for the energy conservation in the dynamics between two consecutive pulses. Especially for long periods of time this omission of the nuclear spin dynamics is problematic since the hyperfine interaction leads to a rearrangement of the Overhauser field distribution. This is why we only gain information about the steady state but not about the build-up of the same with this method.

A revival effect for the electron spin even without the influence of the nuclear spin bath is uncovered. The nuclear spin dynamics is not determined exactly. Instead, restrictions for the Overhauser field are found in the steady state. A simple toy model shows the

interplay between those nuclear resonance conditions of the nuclear spin bath and the electron spin dynamics.

Again, the dynamics of the nuclear spins is assumed frozen on the time scale T_R compared to that of the much faster electron spins. As for additional simplifications: Only the Overhauser field parallel to the external magnetic field is taken into account. The perpendicular components are regarded as small perturbations in relation to the much larger external magnetic field. The pulses discussed are always perfectly resonant π-pulses.

The effect of the pulses is described by Eqs. (7.1.15) and (7.1.16) which serve as initial conditions for the analytic solution Eq. (7.2.7)

$$\vec{S}(t) = \begin{pmatrix} 0 \\ -A_z \sin(\omega_\mathrm{L} t) + A_y \cos(\omega_\mathrm{L} t) - A_y \mathrm{e}^{-\overline{\gamma} t} \\ A_y \sin(\omega_\mathrm{L} t) + A_z \cos(\omega_\mathrm{L} t) - A_y \frac{\overline{\gamma}}{\omega_\mathrm{L}} \mathrm{e}^{-\overline{\gamma} t} \end{pmatrix}. \tag{7.2.8}$$

The prefactors are given by

$$A_y = \frac{\omega_\mathrm{L} \overline{\gamma}}{\overline{\gamma}^2 + \omega_\mathrm{L}^2} \frac{2S_z^\mathrm{bp} + 1}{4} \tag{7.2.9a}$$

$$A_z = \frac{\overline{\gamma}^2}{\overline{\gamma}^2 + \omega_\mathrm{L}^2} \frac{2S_z^\mathrm{bp} + 1}{4} + \frac{2S_z^\mathrm{bp} - 1}{4} \tag{7.2.9b}$$

and depend only on the system parameter $\overline{\gamma}$, the constant Larmor frequency ω_L as well as the electron spin component in z-direction before the pulse S_z^bp.

For the steady state assumption two additional conditions come into play: (1) the Floquet periodicity condition

$$\vec{S}(n T_\mathrm{R}) = S_z^\mathrm{bp} \vec{\mathrm{e}}_z \quad n \in \mathbb{N} \tag{7.2.10}$$

which in the case of the π-pulse reduces to a non-zero entry only for the z-component of the central spin and (2) a nuclear spin dynamics that stays constant in the time average over a repetition rate T_R

$$\left\langle T^* \frac{\mathrm{d}}{\mathrm{d}t} \vec{I}_k \right\rangle_{T_\mathrm{R}} = \langle a_k \vec{S} \times \vec{I}_k \rangle_{T_\mathrm{R}} = 0. \tag{7.2.11}$$

For the slow nuclear spin dynamics this rather complicated condition can be factorized and the nuclear spin stays constant from pulse to pulse if the average feedback through the Knight field [64] vanishes over the same period T_R

$$\langle \vec{S} \rangle_{T_\mathrm{R}} = \frac{1}{T_\mathrm{R}} \int_0^{T_\mathrm{R}} \vec{S}(t) \mathrm{d}t = 0. \tag{7.2.12}$$

This condition holds independent of the distribution of the coupling constants a_k. Since the effective magnetic field is applied in x-direction, the electron spin component along this axis stays constant after the pulse. For the π-pulse this means it remains at zero value.

From Eq. (7.2.12) we obtain

$$\langle \vec{S} \rangle_{T_\mathrm{R}} = \frac{1}{T_\mathrm{R}\omega_\mathrm{L}} \begin{pmatrix} \text{const.} \\ A_z \left[\cos(\omega_\mathrm{L} T_\mathrm{R}) - 1\right] + A_y \sin(\omega_\mathrm{L} T_\mathrm{R}) + A_y \dfrac{\omega_\mathrm{L}}{\overline{\gamma}} \left[\exp(-\overline{\gamma} T_\mathrm{R}) - 1\right] \\ -A_y \left[\cos(\omega_\mathrm{L} T_\mathrm{R}) - 1\right] + A_z \sin(\omega_\mathrm{L} T_\mathrm{R}) + A_y \left[\exp(-\overline{\gamma} T_\mathrm{R}) - 1\right] \end{pmatrix}. \tag{7.2.13}$$

All terms with $\exp(-\overline{\gamma} T_\mathrm{R})$ are neglected because it is assumed that the trion is long decayed before the next pulse $T_\mathrm{R} \gg 1/\overline{\gamma}$. The periodicity condition Eq. (7.2.10) returns the equality $S_z(T_\mathrm{R}) = S_z^\mathrm{bp}$. The x- and y-components of the electron spin before the pulse only depend on S_z^bp. Solving the equation of the S_z-component for S_z^bp yields

$$\vec{S}(T_\mathrm{R}) = S_z^\mathrm{bp} \vec{\mathrm{e}}_z = \frac{1}{2B} \left[\overline{\gamma}\omega_\mathrm{L} \sin(\omega_\mathrm{L} T_\mathrm{R}) - \omega_\mathrm{L}^2 \cos(\omega_\mathrm{L} T_\mathrm{R})\right] \vec{\mathrm{e}}_z \tag{7.2.14}$$

with

$$B = (\omega_\mathrm{L}^2 + \overline{\gamma}^2)(2 - \cos(\omega_\mathrm{L} T_\mathrm{R})) - \overline{\gamma}\omega_\mathrm{L} \sin(\omega_\mathrm{L} T_\mathrm{R}) - \overline{\gamma}^2 \cos(\omega_\mathrm{L} T_\mathrm{R})$$

with S_z^bp inserted in $S_y(T_\mathrm{R})$ and $S_x(T_\mathrm{R})$. The same approximation for $T_\mathrm{R}\overline{\gamma} \to \infty$ as before applies. Utilizing the information gained from the Floquet condition S_z^bp is plugged in Eq. (7.2.13)

$$\langle S_z(T_\mathrm{R}) \rangle_{T_\mathrm{R}} = \frac{1}{2BT_\mathrm{R}} \left(\overline{\gamma}(1 - \cos(\omega_\mathrm{L} T_\mathrm{R})) - \omega_\mathrm{L} \sin(\omega_\mathrm{L} T_\mathrm{R})\right). \tag{7.2.15}$$

The averaged Knight field is proportional to $1/\omega_\mathrm{L}$ leading to a weaker influence on the nuclear spins for a fast electron spin dynamics. The condition $\langle S_z(T_\mathrm{R}) \rangle_{T_\mathrm{R}} = 0$ of a vanishing Knight field in the steady state is met when the effective Larmor frequency obeys one of the following classes of resonance conditions:

$$\omega_\mathrm{L} T_\mathrm{R} = 2\pi n \qquad \text{with} \quad n \in \mathbb{Z} \tag{7.2.16}$$

or

$$\omega_\mathrm{L} T_\mathrm{R} = 2\mathrm{arctan}\left(\frac{\omega_\mathrm{L}}{\overline{\gamma}}\right) + 2\pi n \qquad \text{with} \quad n \in \mathbb{Z}. \tag{7.2.17}$$

The resonance conditions dictate the positions of peaks in the Overhauser field distribution $\omega_\mathrm{L} = |\vec{b}_\mathrm{ext} + \vec{b}_N|/T^*$. The even resonance condition (7.2.16), is well known in literature [33, 34] and also supported theoretically by Refs. [60, 64, 65, 185]. This resonance condition is only dependent on the external magnetic field and the pulse repetition rate and is, therefore, also observed in models which neglect the excitation of a trion state and its subsequent decay. The second resonance condition (7.2.17) is only observed if a trion decay is included since the ratio $\omega_\mathrm{L}/\overline{\gamma}$ generates an additional phase shift. Because the principal determination $\arctan \in (-\frac{\pi}{2}, \frac{\pi}{2})$ is monotonically increasing and $|\vec{b}_\mathrm{ext}| \gg |\vec{b}_\mathrm{N}|$, the transcendent equation (7.2.17) can be approximated by $2\mathrm{arctan}\left(\frac{|\vec{b}_\mathrm{ext}|}{\overline{\gamma} T^*}\right)$. For large magnetic fields $\omega_\mathrm{L} \gg \overline{\gamma}$ the second resonance condition is further simplified to $\omega_\mathrm{L} T_\mathrm{R} = (2n+1)\pi$ which is called the odd resonance condition for its odd multiples of π. For small magnetic fields the arctangent contribution decreases and the frequencies determined by the second resonance condition are brought closer

to those of Eq. (7.2.16). Both resonance conditions have also been observed in purely quantum mechanical simulations [61–63].

The restrictions of the Overhauser field distribution translate to the electron spin dynamics. The even resonance condition (7.2.16) forces the electron spin to carry out an integer number of full rotations from the negative spin alignment $S_z^{\mathrm{bp},1} = -1/2$ after the pulse to the same position right before the next pulse. For this case the pulse has no effect on the electronic state and does not excite a trion.

The odd resonance condition also leads to a spin orientation along the z-axis albeit positive direction $S_z^{\mathrm{bp},2} = 1/6$. The π-pulse flips the central spin to a spin alignment in negative z-direction $S_z^{\mathrm{ap},2} = -1/6$. As before the laser pulse conserves the spin length. Under the influence of a π-pulse, the vector length stays constant only for those two alignments of the electron spin vector before the pulse.

7.2.3 Electron spin revival in an unpolarized, pulsed system

Pump-probe experiments are usually conducted at $\sim 6\,\mathrm{K}$ [33] which corresponds to an energy scale considerably larger than that of the hyperfine interaction. In this high-temperature limit the Overhauser field is unpolarized in the equilibrium before pulses are applied and the classical nuclear spin vectors are uniformly distributed on the unit sphere. This leads to a Gaussian $b_{\mathrm{N},i} \sim \mathcal{N}(0, 1/4)$ for the Overhauser field distribution in all spatial directions $i = x, y, z$ due to the central limit theorem [55].
Before we turn our attention to the electron dynamics of a pulsed quantum dot under the influence of nuclei-induced frequency focusing, the electron dynamics in a still unpolarized bath is investigated briefly.

For an estimate of the purely electronic behavior in a pulsed system the amplitude before and after the pulse are estimated in the limit of large magnetic fields $\frac{\omega_{\mathrm{L}}}{\bar{\gamma}} \gg 1$. The equation (7.2.14) can be reduced to

$$S_z^{\mathrm{bp}}(\omega_{\mathrm{L}}) \approx -\frac{1}{2}\frac{\cos(\omega_{\mathrm{L}} T_{\mathrm{R}})}{(2 - \cos(\omega_{\mathrm{L}} T_{\mathrm{R}}))} \tag{7.2.18}$$

and the z-component after the pulse follows with Eq. (7.1.15) for π-pulses [61, 64]

$$S_z^{\mathrm{ap}}(\omega_{\mathrm{L}}) \approx -\frac{1}{2}\frac{1}{2 - \cos(\omega_{\mathrm{L}} T_{\mathrm{R}})}. \tag{7.2.19}$$

Even in the absence of any mode-locking effect, an electron spin polarization can be observed [61]. The nuclear spin dynamics on the time scale of a few pulses is considered frozen and the precession of the electron spin is given by the frequency $\omega_{\mathrm{L}} = |\vec{b}_{\mathrm{ext}} + \vec{b}_{\mathrm{N}}|/T^*$. The expectation value for Eq. (7.2.18)

$$\langle S_z^{\mathrm{bp}} \rangle = \int_{-\infty}^{\infty} f(\omega_{\mathrm{L}}) S_z^{\mathrm{bp}}(\omega_{\mathrm{L}}) \mathrm{d}\omega_{\mathrm{L}} \tag{7.2.20}$$

is calculated as an integral over the density $f(\omega_{\mathrm{L}})$ which constitutes the frequency distribution. $f(\omega_{\mathrm{L}})$ is a Gaussian with shifted mean $|\vec{b}_{\mathrm{ext}}|/T^*$ and $\sigma^2 = (\omega_{\mathrm{fluc}}/2)^2$. $S_z^{\mathrm{bp}}(\omega_{\mathrm{L}})$ is periodic with $2\pi/T_{\mathrm{R}}$ in frequency. The integral is divided into parts regarding

this periodicity and approximated by a step function

$$\begin{aligned}\langle S_z^{\mathrm{bp}}\rangle &\approx \sum_{n=-\infty}^{\infty} f\left(n\frac{2\pi}{T_\mathrm{R}}\right) \int_{n\frac{2\pi}{T_\mathrm{R}}}^{(n+1)\frac{2\pi}{T_\mathrm{R}}} S_z^{\mathrm{bp}}(\omega_\mathrm{L})\mathrm{d}\omega_\mathrm{L} \\ &= \underbrace{\left[\frac{2\pi}{T_\mathrm{R}}\sum_{n=-\infty}^{\infty} f\left(n\frac{2\pi}{T_\mathrm{R}}\right)\right]}_{=1}\left[\frac{T_\mathrm{R}}{2\pi}\int_0^{\frac{2\pi}{T_\mathrm{R}}} S_z^{\mathrm{bp}}(\omega_\mathrm{L})\mathrm{d}\omega_\mathrm{L}\right].\end{aligned} \tag{7.2.21}$$

In the last step, we took the definition for periodic functions $S_z^{\mathrm{bp}}(\omega_\mathrm{L}) = S_z^{\mathrm{bp}}(\omega_\mathrm{L} + 2\pi n/T_\mathrm{R})$ and the normalization condition of a density into account. Finally, we arrive at

$$\langle S_z^{\mathrm{bp}}\rangle = \frac{T_\mathrm{R}}{2\pi}\int_0^{2\pi/T_\mathrm{R}} \frac{1}{2}\frac{-\cos(\omega_\mathrm{L}T_\mathrm{R})}{(2-\cos(\omega_\mathrm{L}T_\mathrm{R}))}\mathrm{d}\omega_\mathrm{L} = \frac{1}{2} - \frac{1}{\sqrt{3}} \approx -0.077 \tag{7.2.22}$$

for the purely electronic revival and

$$\langle S_z^{\mathrm{ap}}\rangle = \frac{T_\mathrm{R}}{2\pi}\int_0^{2\pi/T_\mathrm{R}} \frac{1}{2}\frac{-1}{(2-\cos(\omega_\mathrm{L}T_\mathrm{R}))}\mathrm{d}\omega_\mathrm{L} = -\frac{1}{2\sqrt{3}} \approx -0.289 \tag{7.2.23}$$

for the average electronic polarization after the pulse. We call revival, that occurs when the frequency distribution is Gaussian, the electronic revival.

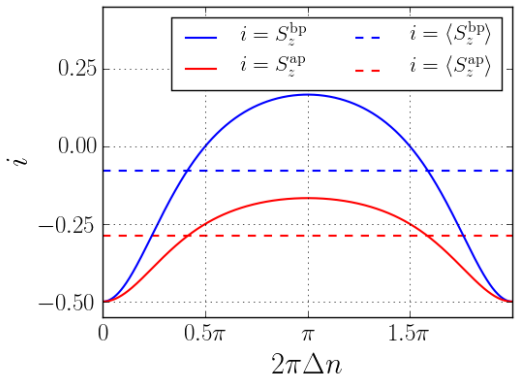

Figure 7.2: The dependence of S_z^{bp} and S_z^{ap} on partially executed rotations in T_R are depicted. The dashed line represents the estimated average of the same quantities over multiple configurations with $\langle S_z^{\mathrm{bp}}\rangle \approx -0.077$ and $\langle S_z^{\mathrm{ap}}\rangle \approx -0.289$.

The alignment of the electron spin before and after the pulse depending on incomplete rotations $2\pi\Delta n$ with $\Delta n \in \mathbb{R}$ in a pulse repetition time $\omega_\mathrm{L}T_\mathrm{R} = (n+\Delta n)2\pi$ is depicted in Fig. 7.2. In the purely electronic steady state all frequencies $\omega_\mathrm{L}/\omega_\mathrm{fluc} = |\vec{b}_\mathrm{ext} + \vec{b}_\mathrm{N}|$ contribute to the dynamics. However, the pulse gives preference to frequencies which leads to a negative alignment before the pulse. This is reflected by the fact that the amplitude of $\vec{S}$ is maximal for $\Delta n = 0$ and, therefore, contributes most to the configuration averages $\langle S_z^{\mathrm{bp}}\rangle$ and $\langle S_z^{\mathrm{ap}}\rangle$. Other frequencies deviating from $\omega_\mathrm{L}T_\mathrm{R} = 2\pi n$ are suppressed.

The build-up of the electronic revival is described by Kleinjohann et al. [63]. The semi-classical derivation is conducted in an analogous manner. We first consult Eq. (7.2.8). Since the π-pulse only leaves a S_z-component, the electron spin dynamics can be written as

$$S_{z,\mu}(t) = S_{z,\mu}^{\mathrm{ap}}\cos(\omega_\mathrm{L}t) \tag{7.2.24}$$

in the limit of $|\vec{b}_{\mathrm{ext}}| \gg \gamma T^*$. The initial $S_z^{\mathrm{ap}}(0)$ is $-1/4$. For consecutive pulses Eq. (7.1.15) up to the N_{P}-th pulse the electron spin revival in one configuration μ is

$$S_{z,\mu}^{\mathrm{bp}}(T_{\mathrm{R}}, N_{\mathrm{P}}) = -\sum_{p=1}^{N_{\mathrm{P}}} \frac{1}{2^{p+1}} \cos^p(\omega_{\mathrm{L}} T_{\mathrm{R}}) \tag{7.2.25}$$

with ω_{L} given by the individual, frozen Overhauser field in a configuration. The configuration average is replaced by the integral over all frequencies

$$\langle S_z^{\mathrm{bp}}(T_{\mathrm{R}}, N_{\mathrm{P}})\rangle = \frac{T_{\mathrm{R}}}{2\pi} \int_0^{\frac{2\pi}{T_{\mathrm{R}}}} S_{z,\mu}^{\mathrm{bp}}(T_{\mathrm{R}}, N_{\mathrm{P}}) \mathrm{d}\omega_{\mathrm{L}}. \tag{7.2.26}$$

Note that only integrals with even exponents of the cosine contribute. Therefore, the series is

$$\langle S_z^{\mathrm{bp}}(T_{\mathrm{R}}, N_{\mathrm{P}})\rangle = -\sum_{p=1}^{N_{\mathrm{P}}/2} \frac{1}{2^{4p+1}} \frac{(2p)!}{(p!)^2}. \tag{7.2.27}$$

The increase of the revival amplitude occurs every second pulse. In the limit of large N_{P} the result of Eq. (7.2.22) can be retrieved. For the amplitude after the pulse the same approach is applied. Here only odd pulse numbers contribute the final series

$$\langle S_z^{\mathrm{ap}}(T_{\mathrm{R}}, (N_{\mathrm{P}}-1))\rangle = -\frac{1}{4} - \frac{1}{2} \sum_{p=1}^{N_{\mathrm{P}}/2} \frac{1}{2^{4p+1}} \frac{(2p)!}{(p!)^2} \tag{7.2.28}$$

with the limit at $N_{\mathrm{P}} \to \infty$ of $-\frac{1}{2\sqrt{3}}$ as shown in Eq. (7.2.23).

The electron spin amplitude after the pulse and before the pulse stays constant for one pulse and alternately increase with the number of pulses applied.

7.2.4 Mode-locked electron spin

The focus of investigation in this section is the influence of the frozen Overhauser field, following a non-equilibrium steady state distribution, on the electron spin dynamics.

An infinitely long periodic pulse sequence imprints some of its characteristics such as information about T_{R} on the Gaussian distribution of the initially unpolarized Overhauser field. We expect that peaks, whose position corresponds to the resonance conditions, emerge from the Gaussian Overhauser field distribution in the direction of the external magnetic field. Therefore, the weight of each peak is derived from the Gaussian. In the non-equilibrium steady state, we assume perfectly sharp peaks at the positions predicted by the resonance conditions (7.2.16) and (7.2.17). In this simple model both resonance conditions contribute equally. The Overhauser field distribution for $i = x, y, z$ is given by

$$p_y(b_{\mathrm{N},i}) = p_z(b_{\mathrm{N},i}) = \mathcal{F}(b_{\mathrm{N},i}), \tag{7.2.29a}$$

$$p_x(b_{\mathrm{N},x}) = \sum_n \mathcal{F}(b_{\mathrm{N},x}) \left[\delta(b_{\mathrm{N},x} - b_{\mathrm{e},n}) + \delta(b_{\mathrm{N},x} - b_{\mathrm{o},n})\right], \tag{7.2.29b}$$

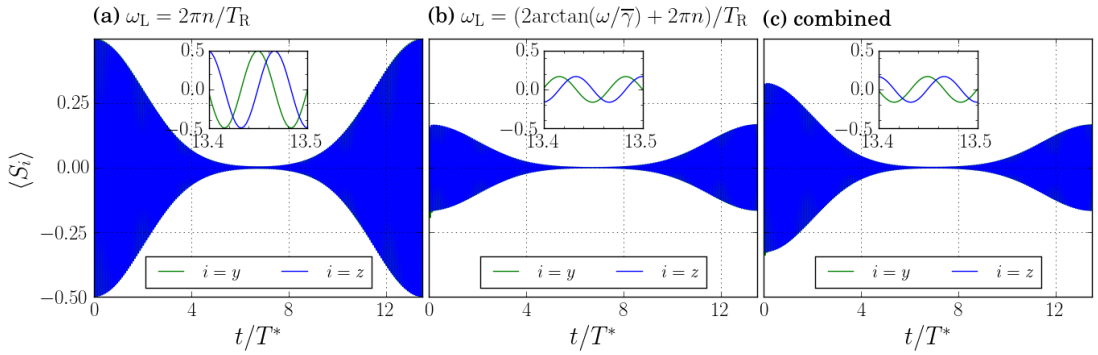

Figure 7.3: Toy model for the central spin dynamics. $S_z(t)$ and $S_y(t)$ during one pulse repetition time $t \in [N_P T_R, (N_P + 1)T_R]$ for the even (a) and the odd resonance condition (b). Panel (c) depicts the combination of both weighted with the Gaussian envelope of the Overhauser field $b_{N,x} \sim \mathcal{N}(0, 1/4)$. The insets show the electron spin dynamics immediately before the next pulse.

where

$$\mathcal{F}(b_{N,i}) = \frac{1}{\sqrt{2\pi\sigma^2}} \exp\left(-\frac{b_{N,i}^2}{2\sigma^2}\right) \text{ for } i = x, y, z \tag{7.2.30}$$

with a variance $\sigma^2 = 1/4$ and $\delta(b)$ is the Dirac δ-function. The effective field $b_{e,n}$ $[b_{o,n}]$ is derived from the condition (7.2.16) [(7.2.17)].

For a statistical evaluation we connect the number of configurations with the same Overhauser field to the weight given by the Gaussian. In each configuration the electron spin dynamics $S_{z,\mu}(t)$ is provided using Eq. (7.2.8) before the statistical average for $\langle S_z(t) \rangle$ between two pulses is calculated, see Eq. (5.2.33).

In Fig. 7.3 the external magnetic field is chosen to be about 2 T and the repetition rate is given by $T_R = 13.5\, T^*$. Here, the electron spin executes about 200 Larmor precessions in the period T_R. For the strong magnetic field the approximation of $b_{o,n} \approx (2n+1)\pi T^*/T_R$ holds.

For the even resonance condition, featured in panel (a), the electron spin is fully aligned in negative z-direction after and before the pulse. The maximum spin length is conserved and, therefore, the spin polarization transferred to the next pulse period. This behavior is synonymous with the laser pulse having no effect.

The electron spin dynamics in panel (b) belongs to the odd resonance conditions. After the pulse the electron spin is also aligned in the negative z-direction, however, the absolute value of $\vec{S}_\mu$ is reduced to 1/6, cf. Eq. (7.1.15). The spin length again is retained but the polarization before the next pulse is inverted.

While the central spin dynamics of both classes of resonance conditions possess a perfect revival, the superposition of the two, as shown in panel (c), does not. After the pulse the electron spin configurations of even and odd resonant Overhauser fields are aligned in the same direction and an amplitude of $\langle S_z^{ap} \rangle = -1/3$ is reached. Before the next pulse the amplitude is reduced to $\langle S_z^{bp} \rangle = -1/6$ due to the spin vectors of each sub-class pointing in opposite directions.

In the context of this toy model no predictions can be made about the weighting ratio

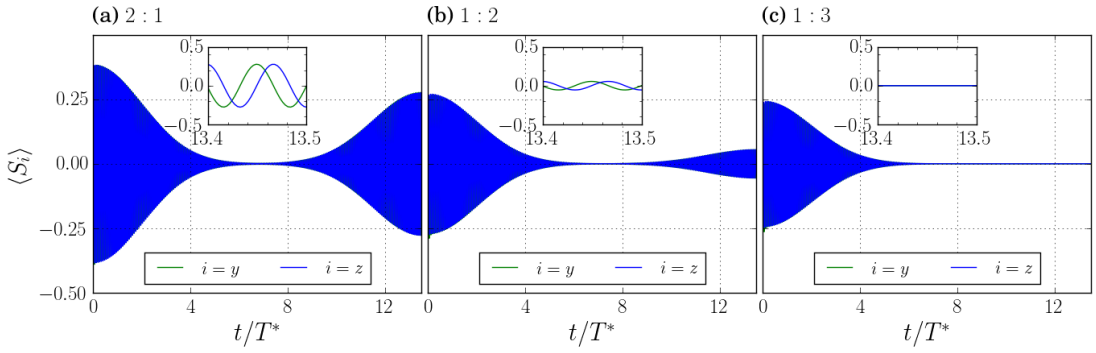

Figure 7.4: Toy model of $S_z(t)$ and $S_y(t)$ with $t \in [N_\mathrm{P} T_\mathrm{R}, (N_\mathrm{P}+1)T_\mathrm{R}]$ for the different ratios between even and odd resonance conditions. The insets shows the electron spin dynamics immediately before the next pulse.

of even and odd resonance peaks. However, with a different ratio of the two sub-classes the revival can be influenced, cf. Fig. 7.4. If the even resonances dominate, as seen in panel (a), the amplitude after the pulse as well as the revival increases. In the limiting case of even to odd weighting ratio 1:0, only the Overhauser field peaks given by the even resonance conditions remain as was discussed in Petrov et al. [60]. For a larger contribution of the odd class of resonance conditions, the polarization is diminished, cf. panel (b), and reaches its minimum at 1:3 where the revival is suppressed completely, see panel (c).

7.3 Full semiclassical simulations

This section encompasses the results of the numerical semiclassical simulations. We first set the stage by discussing the makeup of the pulse sequence and its parameters. Then basic features like the dependence on the number of pulses, the external magnetic field and the pulse repetition rate are the focus of our investigation. Further simulations show the influence of the spin dynamics under the variation of bath size N, pulse area F and the trion decay rate γ. But also, the change in dynamics for an off-resonance external magnetic field or a rescaling of the time constant T^* is observed. Last but not least the influence of the nuclear Zeeman and the variation of the hyperfine coupling constant distribution $p(a)$ is discussed. We briefly compare the new insights with recent experimental results presented in Ref. [89].

7.3.1 Recipe for the numerical simulation of a pulse sequence

After the components of the numerical simulation were discussed in previous sections, let us combine the individual parts to a pulse sequence.

At $t = 0$ the nuclear spin bath is unpolarized. This translates to N_C classical configurations where each configuration features N classical nuclear spin vectors and a central spin vector which are equally distributed over a Bloch sphere. Each configuration is labeled by μ. The first pulse is applied at $t = 0$. During this time period the nuclear spins are considered frozen and are not affected by the pulse. The quantum mechanical

expectation value of the central spin as well as the expectation value of the excited trion state is dictated by Eqs. (7.1.12)., The pulse is applied independently in each configuration, see Fig. 7.5. This leads to a decreasing electron spin length in a single configuration. The value $\vec{S}_\mu^{\mathrm{ap}}$ is the initial condition for the time period T_R at $t = N_\mathrm{P} T_\mathrm{R}$ which is governed by the system of coupled equations of motion given by Eqs. (7.1.27) and (5.2.27b). The quadrupolar interaction is not taken into account. The recipe for the numerical solution via RK4 was presented in Sec. 5.2.6.

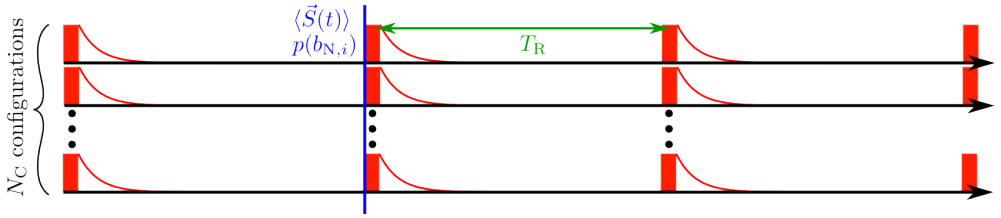

Figure 7.5: Schematics of a pulse sequence. Each black line represents an independent semiclassical configuration. In red the pulse and the trion decay are depicted. The blue lines indicate where the ensemble averaging for the electron spin dynamics is performed and the histogram of the Overhauser field distribution is created.

For a pulse sequence multiple building blocks of length T_R are put in a row. At predetermined pulse numbers N_P the quantities of interest, like the expectation value of the electron spin dynamics $\langle \vec{S}(t) \rangle$ and the Overhauser field distribution $p_i(b_{\mathrm{N},i})$, are calculated as an average or histogram over all configurations μ immediately before the pulse at $t = N_\mathrm{P} T_\mathrm{R}$.

7.3.2 Parameters of the pulse sequence

The subject of investigation are the electron spin dynamics $\langle S_z \rangle$ and the Overhauser field distribution $p_i(b_{\mathrm{N},i})$ with $i = x, y, z$ under periodical, optical excitation. The aim of this investigation is a qualitative understanding of the spin dynamics observed in experiments. The parameters are chosen to approximately reflect the experimental setup given by Greilich et al. [33] and stay the same for the following sections unless stated otherwise. In previous comparisons between theory and experiment [49] T^* has been found to be $T^* \approx 1\,\mathrm{ns}$.

The standard set of parameters for the SCA was presented in Sec. 5.3.2. Each of the $N = 100$ nuclear spins has a spin length $I = 1/2$. The electron spin vector with an effective spin $S = 1/2$ can decrease in length from the maximal absolute value of $1/2$. The $\langle S_z \rangle$ and $p_i(b_{\mathrm{N},i})$ are determined as the mean value of the electron spin dynamics and the histogram of all Overhauser fields of $N_\mathrm{C} = 10^5$ independent classical configurations, respectively. The differential equations are solved using a Runge-Kutta fourth-order method.

The electron spin interaction with the external magnetic field is 800 times stronger than that of the nuclear spins. Therefore, the ratio of the Zeeman interaction is given by $\zeta = \frac{g_\mathrm{N}\mu_\mathrm{N}}{g_\mathrm{e}\mu_\mathrm{B}} = 1/800$. The repetition time T_R between the pulses is 13.2 ns in experiment [33]. For the sake of convenience, we set it to $T_\mathrm{R} = 13.5\,T^*$ in the simulations. The trion decay rate is $\gamma = 10\,\frac{1}{T^*}$.

The parameter K' is used to indicate if the external magnetic field fulfills the even resonance condition (7.2.16)

$$K' = K + \Delta K = \frac{|\vec{b}_{\mathrm{ext}}|}{2\pi} \frac{T_{\mathrm{R}}}{T^*} \tag{7.3.1}$$

with $\Delta K \in [0, 1)$ and $K \in \mathbb{Z}$. If $\Delta K = 0$ then the external magnetic field leads to an even number of full electron spin precessions in T_{R}. Otherwise, ΔK returns the fraction of the rotation that is off-resonance. The arbitrary real number ΔK can be used as simple means to account for different g-factors of individual quantum dots and the associated deviations from the resonance conditions. As the default parameter for the external magnetic field, we chose $|\vec{B}_{\mathrm{ext}}| \approx 2\,\mathrm{T}$. Since we usually demand a resonant external magnetic field as an additional condition, this value is represented by $K = 200$. The dimensionless external magnetic field is $|\vec{b}_{\mathrm{ext}}(K = 200)| \approx 93$. The external magnetic field is applied in Voigt geometry with $\vec{b}_{\mathrm{ext}} = |\vec{b}_{\mathrm{ext}}|\vec{\mathrm{e}}_x$.

The Larmor precession of the electron spin for $K = 200$ is much faster than the previously in Sec. 5.3.3 discussed dynamics in an external magnetic field of $|\vec{b}_{\mathrm{ext}}| = 10$ which corresponds to approximately 200 mT. The step width is adjusted to $\sim 0.001T^*$ to resolve the dynamics for an external magnetic field with $K = 200$.

The so-called box model is used [45, 60, 146] to investigate basic features of the spin dynamics subjected to a pulse sequence. Setting all coupling constants to $a_k = a = 1/\sqrt{N}$ allows us to collapse all N nuclear equations of motion to a single differential equation of the total nuclear spin $\vec{M} = \sum_k \vec{I}_k$. Weighting $\vec{M}$ with the universal coupling constant a reveals the Overhauser field dynamics directly. The computational resources needed for a simulation are reduced by approximately a factor N. When the hyperfine coupling constant distribution $p(a)$ is the focus of investigations the distributions $p_{r_0}(a)$ from Sec. 3.2 are used. The parameter ξ is set to allow for two- and three-dimensional QDs. The cut-off ratio is varied between 1.0 and 2.0.

The starting point for each simulation in this chapter is a completely unpolarized electron spin and nuclear spin bath. The first pulse is applied immediately at $t = 0$. Unless stated otherwise, the total number of pulses is $N_{\mathrm{P}} = 20\,000$.

7.3.3 Influence of the number of pulses

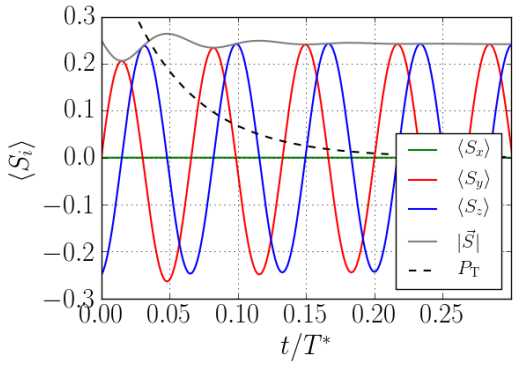

Figure 7.6: Precession of the electron spin y- and z-component in the external magnetic field as well as constant x-component and its absolute value. The analytical solution of the trion state is added as a dashed line.

In the case of a strong external magnetic field the electron spin dynamics is dominated by the Larmor precession. Since the laser pulse aligns the electron spin in negative

z-direction, only the components orthogonal to the external magnetic field contribute. The x-component stays approximately constant at $\langle S_x \rangle = 0$. The short-time dynamics during the trion decay is depicted in Fig. 7.6.

Starting from an unpolarized electron spin the laser pulse at $t = 0$ generates a polarization in z-direction. Eq. (7.1.15) quantifies this polarization as $\langle S_z \rangle = -0.25$ since the $|\uparrow\rangle$-state is depleted. The electron components perpendicular to the external magnetic field begin to precess after the pulse and the trion state P_T decays on a time scale of $0.1 - 0.2T^*$. The trion decay changes the spin length as illustrated the grey line for the absolute value of the electron spin vector. Since the trion state decays into the $|\uparrow\rangle$-state, the absolute value increases where $\langle S_z \rangle$ is positive. Only after the trion is decayed stays the spin length constant.

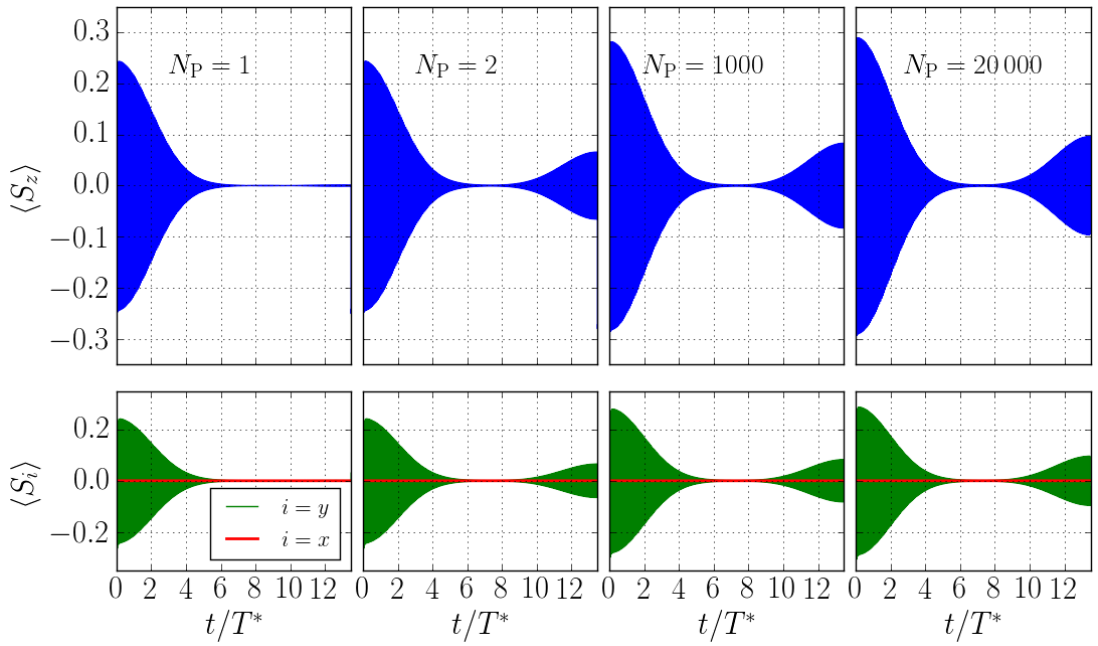

Figure 7.7: Upper row: S_z-expectation value of central spin dynamics on the time scale of one $T_\mathrm{R} = 13.5\,T^*$ between two consecutive pulses for an increasing number of pulses in the box model. The simulation is conducted for $N = 100$ nuclear spins and $N_\mathrm{C} = 100\,000$ configurations. The nuclear Zeeman strength is $\zeta = 1/800$ and the external magnetic field is defined by the resonance condition $K = 200$ which leads to $|\vec{b}_\mathrm{ext}| = \frac{2\pi 200 T^*}{13.5\,T^*} \approx 93$ corresponding to approximately 2 T. Lower row: $\langle S_x \rangle$ and $\langle S_y \rangle$ for the same parameters.

For larger time scales the hyperfine interaction comes into play. In the upper panels of Fig. 7.7 the electron spin dynamics in z-direction for different pulse numbers N_P is depicted. Unlike in the previous detail plot of the trion decay, the Larmor precession is too fast to be resolved on the time scale of T_R. After each pulse $\langle S_z \rangle$ dephases on the time scale T^*. Here, no revival is observed and in the second time period T_R the starting value is given by $\langle S_z \rangle \approx -0.25$, cf. Eq. (7.2.19). However, the behavior compared to the first pulse period changes before the third pulse where $\langle S_z \rangle$ now features a revival of the approximate magnitude 0.06 as described by Eq. (7.2.27). The envelope of the revival mirrors that of the dephasing after the pulse. The electron spin revival always is connected to frequency focusing. On the time scale of only a few pulses this synchronization of the electron spin precession modes to the pulse repetition time T_R

is linked to the effect of the pump pulses only, cf. Sec. 7.2.3.

After the initial sharp increase, the revival amplitude grows with the number of pulses. Since the amplitude of the spin after the pulse depends on S_z^{bp}, cf. Eq. (7.1.15), for π-pulses, it also increases. The amplitude after the pulse converges to $\langle S_z^{\mathrm{ap}} \rangle = -1/3$ and likewise the value before the pulse converges to the predicted $\langle S_z^{\mathrm{bp}} \rangle = -1/6$. The corresponding spin dynamics for the x- and y-components of the central spin are found in the lower panels of Fig. 7.7. $\langle S_y \rangle$ features the same behavior as the S_z-component albeit with a phase shift in the Larmor precession. $\langle S_x \rangle$ is suppressed by the laser pulse and since the external magnetic field of $\sim 2\,\mathrm{T}$ leads to a Larmor precession much faster than the hyperfine interaction the spin component is approximately conserved. Therefore, it does not contribute to the revival that is plotted in Fig. 7.8. The revival $\langle S_y^{\mathrm{bp}} \rangle$ is diminished for an increasing number of pulses. This agrees well with the prediction of the toy model, see Fig. 7.3, where in the steady state the central spin is aligned in the z-direction before the pulse. But it also means that after 20 000 pulses the steady state is not yet reached for this choice of parameters. Since $\langle S_x \rangle$ is approximately constant, it is sufficient to investigate $\langle S_z \rangle$ and the absolute value of the revival.

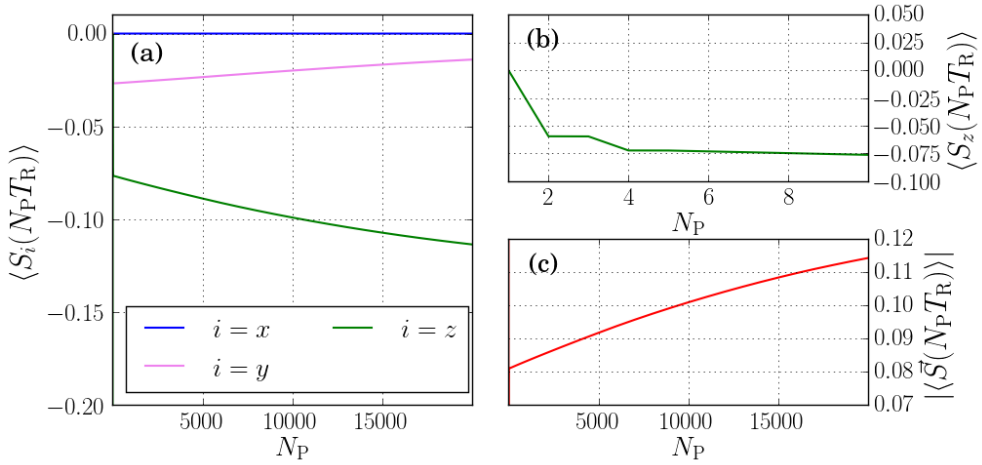

Figure 7.8: Revival of the central spin immediately before the pulse. Panel (a): components of the electron spin immediately before the pulse. Panel (b): detail of the S_z-component for a few pulses. Panel (c): absolute value of the revival amplitude.

The revival on the time scale of only a few pulses, cf. Fig. 7.8 panel (b), shows the revival amplitude of S_z increases every second pulse due to the electronic revival as described in Ref. [63]. After four pulses the electronic steady state of $\langle S_z \rangle = -0.077$ is approximately reached.

After the rapid increase of revival amplitude of the electron spin on the time scale of a few pulses all further increase is linked to the development of non-equilibrium Overhauser field distributions. The Overhauser field distributions in all spatial directions $(p_x(b_{\mathrm{N},x}), p_y(b_{\mathrm{N},y}), p_z(b_{\mathrm{N},z}))$ for the box model are depicted in Fig. 7.9. At $t = 0$ the Overhauser field is unpolarized which due to the central limit theorem leads to a Gaussian distribution. It is centered around 0 and its variance in each direction is given by $1/4$.

Under the influence of periodic laser pump pulses, the components perpendicular to the external magnetic field do not change their initial Gaussian shape. But the distribution

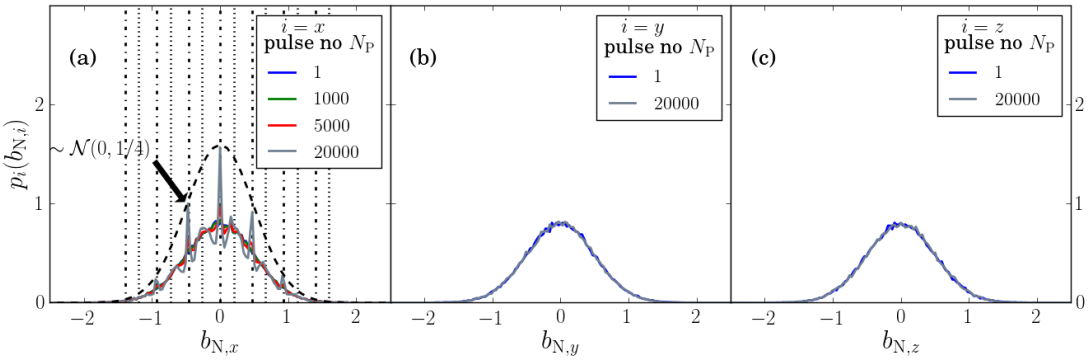

Figure 7.9: Overhauser field distributions $p_i(b_{\mathrm{N},i})$ in all spatial directions $i = x, y, z$. At $t = 0$ the Overhauser field is unpolarized, translating to a Gaussian distribution $b_{\mathrm{N},i} \sim \mathcal{N}(0, 1/4)$ in all directions. The vertical lines in panel (a) indicate the even (dash-dotted) and odd (dotted) resonance conditions defined by the equations (7.2.16) and (7.2.17). The panels (b) and (c) show the Overhauser field distribution orthogonal to the external magnetic field after 1 pulse and 20 000 pulses.

$p_x(b_{\mathrm{N},x})$ develops a new shape. While the envelope of the distribution retains its Gaussian shape, peaks begin to emerge. The distance between neighboring peaks is given by $\Delta b_{\mathrm{N},x} = \pi T^*/T_{\mathrm{R}}$. As the peaks become more distinct with time, we can identify the position of the peaks by the resonance conditions (7.2.16) and (7.2.17). A guide to the eye for the even and odd conditions is added to the plot as vertical dashed-dotted and dotted lines. The peaked Overhauser field distribution reduces the possible frequencies of the electron spin dynamics which is the reason for the additional increase in revival. This selection of only a few frequencies or modes via a re-alignment of the nuclear spins is called mode-locking and leads to electron spin coherence due to nuclei-induced frequency focusing [33]. Despite the strong approximation of a frozen Overhauser field, the analytical predictions fit remarkably well to the result of the full numerical simulation. The measured deviations form the analytical predictions are as small as $1 - 2\,\%$ and never exceed $9\,\%$.

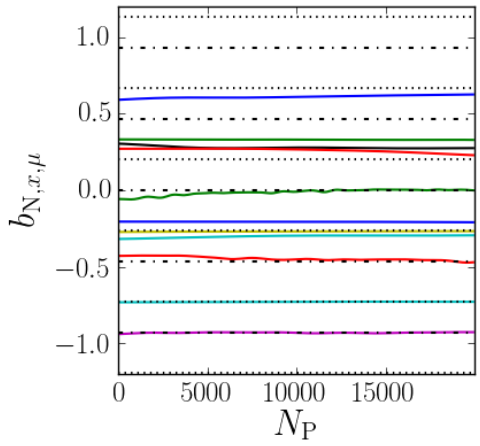

Figure 7.10: Exemplary convergence of the Overhauser field in a single configuration μ (colored lines) to the even (dash-dotted) and odd (dotted) resonance conditions.

Another behavior, that catches the eye, is the different build-up speed of the two peak classes. Since no analytical prediction is on hand, we have a look at a few random configurations μ and track the development of their Overhauser field value $b_{\mathrm{N},x,\mu}$ once per

T_R. The individual Overhauser fields in Fig. 7.10 show different convergence depending on their starting value. Both resonance conditions act as attractive fixpoints for the Overhauser field. If the initial value of $b_{\mathrm{N},x,\mu}$ is on a resonance condition, it stays constant for this value. If $b_{\mathrm{N},x,\mu}$ is closer to the even resonance condition, the Overhauser field converges to the resonance condition in under 10 000 pulses. This can be observed, for example, for the green line at $b_{\mathrm{N},x} = 0$ or the red line at $b_{\mathrm{N},x} \approx -0.5$ which both start with a deviation from the resonance condition at $t = 0$. For the remaining, initial values of the Overhauser field that deviate from the odd resonance condition, the convergence to the dotted lines progresses much slower. The more the configurations deviate from the resonance conditions, the slower the Overhauser field attains its steady state. In the picture of the ensemble distribution the slower convergence of the configurations with odd resonance conditions leads to broader peaks for (7.2.17) and fast developing, sharp peaks for (7.2.16).

Since the Overhauser field distributions $p_y(b_{\mathrm{N},y})$ and $p_z(b_{\mathrm{N},z})$ do not change over time, only the Overhauser field distribution $p_x(b_{\mathrm{N},x})$ parallel to the external magnetic field is taken into account for subsequent investigations.

7.3.4 Influence of the external magnetic field

In pump-probe experiments a strong external magnetic field [88] serves a dual purpose: (i) the coherent oscillation in the external magnetic field dominates the electron spin dynamics. The electron spin precession is necessary for the generation of polarization via the pulse. (ii) the long-time dephasing stemming from the fluctuations of the Overhauser field is suppressed.

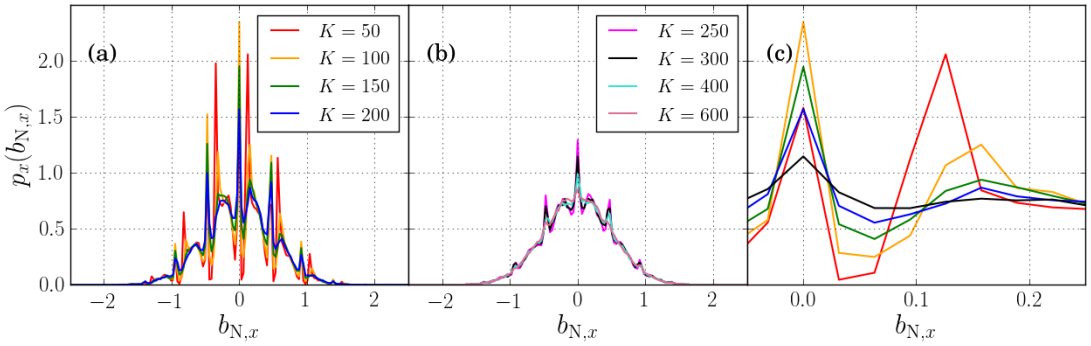

Figure 7.11: Overhauser field distribution in the direction of the magnetic field after 20 000 pulses for different magnetic field strengths given by K: $|\vec{b}_\mathrm{ext}| = \frac{2\pi K T^*}{T_\mathrm{R}}$. Panel (a) and (b) show the entire distribution while panel (c) highlights the shift of the odd peaks given by $\omega_\mathrm{L}/\overline{\gamma}$ for the data from panel (a) and $K = 300$, see Eq. (7.2.17).

The influence of the external magnetic field on the peak structure of the Overhauser field is depicted in Fig. 7.11. The Overhauser field distribution in the direction of the external magnetic field $p_x(b_{\mathrm{N},x})$ is plotted for different magnetic fields in resonance given by $K = 50$, 100, 150 and 200 in panel (a) and $K = 250$, 300, 400 and 600 in panel (b) representing magnetic field strength ranging from approximately 0.5 T for $K = 50$ up to 6 T for $K = 600$. Panel (c) shows one even peak of the Overhauser field distribution at $b_{\mathrm{N},x} = 0$ and the corresponding odd peak in detail. Only results from panel (a)

and $p_x(b_{\mathrm{N},x})$ for $K = 300$ are shown. The odd peak shifts depending on the external magnetic field.

In all panels the even peaks related to Eq. (7.2.16) do not change position and are independent of the external magnetic field. In panel (a) the peaks following the odd resonance condition Eq. (7.2.17) shift towards $(2n+1)\pi/T_{\mathrm{R}}$ for increasing $|\vec{b}_{\mathrm{ext}}|$ since $2\mathrm{arctan}(|\vec{b}_{\mathrm{ext}}|/(\overline{\gamma}T^*)) \to \pi$. For higher magnetic fields, see panel (b) the positions of the odd resonance peaks do not visibly change further.

However, while the peak positions are the same in panel (b), the speed of the build-up is not. Larger magnetic fields lead to a slower build-up than weaker fields. For 6 T the peaks are barely visible after 20 000 pulses. The speed of the build-up is inverse to the external magnetic field due to the $(1/\omega_{\mathrm{L}})$ dependency of the averaged Knight field, cf. Eq. (7.2.15). An inverse dependence between speed-up and external magnetic field strength was discussed by Glazov et al. [64]. In quantum mechanical calculations [61] the mode locking rate has been found proportional to $|\vec{b}_{\mathrm{ext}}|^{-2}$.

For $K = 50$ the Overhauser field shows one significant difference compared with the larger magnetic fields: the even resonance peaks have less weight compared to the odd peaks. The odd peaks are also much sharper in contrast to the odd peaks of higher magnetic fields. Those features cannot be predicted by the resonance conditions. For an external magnetic field lower than $|\vec{b}_{\mathrm{ext}}(K = 50)|$, we approach the regime where the Larmor precession for an external magnetic field is not significantly faster than the dynamics induced by the hyperfine interaction. Therefore, the analytical prediction for the position of the Overhauser field peaks does not work for small magnetic fields since the FOA [55] is no longer valid [49, 75, 76].

7.3.5 Electron spin revival depending on the external magnetic field

We discussed the influence of the magnetic field strength on the nuclear spin dynamics in the previous section. However, only the electron spin dynamics is measured in pump-probe experiments, see Fig. 2.4. Here, the behavior of the electron spin revival amplitude in the context of their Overhauser field distribution is discussed.

In Fig. 7.12 the revival amplitude $|\langle\vec{S}(T_{\mathrm{R}}N_{\mathrm{P}})\rangle|$ and $\langle S_z(T_{\mathrm{R}}N_{\mathrm{P}})\rangle$ are presented for varying magnetic field strength in the upper and lower panels, respectively. Magnetic fields from $\sim 0.25\,\mathrm{T}$ up to 1.5 T, which correspond to $K = 25$ and $K = 150$, are on the left-hand side, larger magnetic fields up to 6 T on the right-hand side. Independent of the magnetic field strength each revival amplitude increases from $\langle S_z\rangle = 0$ to a finite value for $N_{\mathrm{P}} < 10$. This purely electronic revival was discussed in Sec. 7.2.3. The toy model provides good predictions for higher magnetic fields, especially for the magnetic fields used in pump-probe experiments which are between 2 T or higher [33, 63, 89]. The electronic revival is $S_z^{\mathrm{bp}} = -0.077$ for all magnetic fields $K \geq 100$, see Fig. 7.12 (d), which corresponds to $|\vec{B}_{\mathrm{ext}}| \geq 1\,\mathrm{T}$, cf. Eq. (7.2.22).

After the purely electronic steady state is reached $N_{\mathrm{P}} < 10$, the revival amplitude increases monotonously for high magnetic fields, see panel (b), and decreases monotonously for its corresponding $\langle S_z\rangle$ in (d) of Fig. 7.12. The two classes of resonance conditions predict the spin alignment in each configuration. $\vec{S}_\mu$ is aligned in the negative z-direction before the pulse for the even resonance condition. This resonance condition

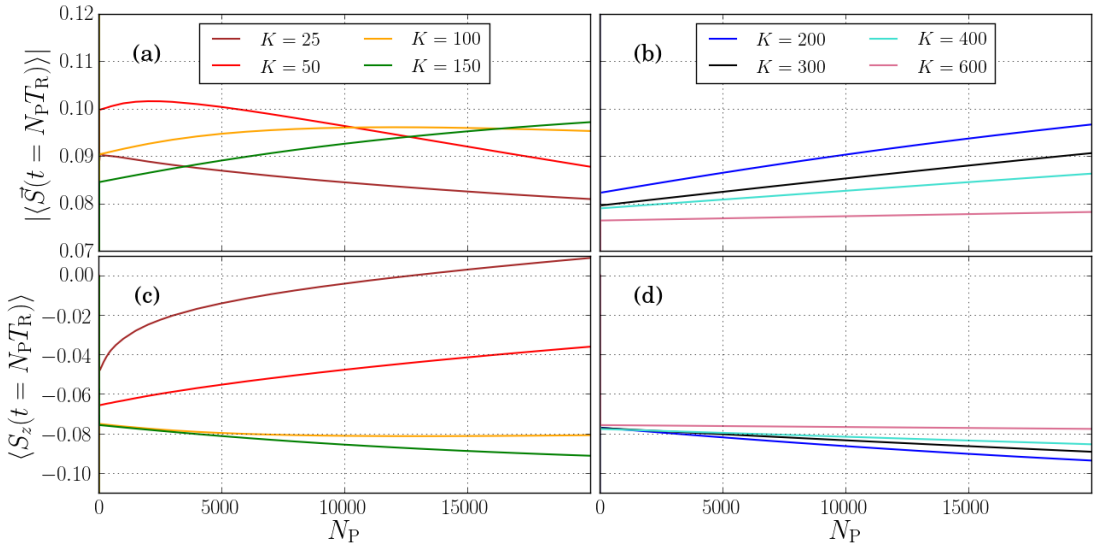

Figure 7.12: Revival amplitude of the electron spin. Upper panels: absolute value of the electron spin before the pulse $|\langle\vec{S}(T_\mathrm{R}N_\mathrm{P})\rangle|$ and lower panels: $S_z(T_\mathrm{R}N_\mathrm{P})$. The external magnetic field is $(2\pi KT^*/T_\mathrm{R})\vec{e}_x$.

corresponds to an integer number of precessions in T_R starting from $-|\vec{S}_\mu^\mathrm{ap}|\vec{e}_z$ after the pulse. The electron spin amplitude in one configuration with a frequency given by (7.2.16) is not diminished by the pulses and is $S_{z,\mu} = -1/2$. For the odd resonance condition, the spin orientation before the pulse is also in z-direction, albeit positive. Here, the electron spin amplitude approximates its steady state amplitude $S_{z,\mu} = 1/6$ in one configuration. Since the peaks of the Overhauser field distribution following the even resonance condition develop faster, see Fig. 7.11 for $K > 100$, the negative revival $\langle S_z\rangle$ increases. Due to the fact that the build-up speed of the peaked Overhauser field distribution is linked to the external magnetic field strength, $|\vec{b}_\mathrm{ext}|$ also influences the long-time build-up of the revival amplitude. For example, for $K = 600$ the revival amplitude is only further increased by ~ 0.002 after $N_\mathrm{P} = 10$, whereas the difference between $\langle S_z^\mathrm{bp}\rangle$ at $N_\mathrm{P} = 10$ and $N_\mathrm{P} = 20\,000$ assumes the value of ~ 0.03 for $K = 200$. This means a longer pulse sequence is needed to get a revival amplitude, similar to that of $K = 200$, for the stronger magnetic field of $K = 600$. The still almost linear slope of the electron spin revival amplitude in Fig. 7.12 (b) as well as the shape of $p_x(\vec{b}_{\mathrm{N},x})$ in Fig. 7.11 indicates that the non-equilibrium steady state is not yet reached. For large magnetic fields $K > 100$, $\langle S_z^\mathrm{bp}\rangle$ is expected to converge to $-1/6$ with an increasing number of pulses. The value is predicted by the toy model for an assumed equal weighting of the even and odd Overhauser field peaks. Slower convergence with increasing external magnetic field strength is also observed in quantum mechanical calculations, see Ref. [63].

For lower magnetic fields the revival amplitude is subject to much faster changes due to faster development of the Overhauser field Eq. (7.2.15). But even in this regime no convergence is yet observed and a larger number of pulses is necessary to reach the steady state. Also, $|\langle\vec{S}\rangle|$ does not increase monotonously for magnetic fields $K < 150$. This can be partially understood in the context of the toy model through the spectral weight of the peaks. As seen in Fig. 7.11 for $K = 100$ but especially for $K = 50$, the

weight in the odd peaks increases compared to that of the even peaks. The revival decreases. For the ratio of 1 : 3 between even and odd Overhauser field peaks the revival would vanish completely. The weight of the peaks cannot be determined from the analytical calculations. Another effect, the toy model does not predict, is the spin polarization in y-direction for $K < 150$. For the $|\vec{b}_{\mathrm{ext}}(K = 50)|$, but especially for the even smaller $|\vec{b}_{\mathrm{ext}}(K = 25)|$, the modulus of the S_z-component and the absolute value of the electron spin vector assume different values. Since the π-pulse only depends on S_z^{bp}, a non-zero component S_y that remains immediately before the pulse cannot be transferred to the next pulse period. The averaged spin amplitude $|\langle \vec{S}^{\mathrm{ap}} \rangle|$ after the pulse decreases. If the S_y is the dominating contribution to the revival amplitude, we can assume that $S_z^{\mathrm{bp}} \approx 0$ and $S_z^{\mathrm{ap}} \approx -1/4$. For external magnetic fields, whose Larmor precession frequency is on the time scale of the trion decay, the trion decay causes an additional decrease in polarization. The trion decay leads to a contribution to the electron spin polarization in positive z-direction while the trion decays. Therefore, both contributions interact destructively for a slowly rotating central spin and the spin polarization decreases further.

7.3.6 Spin dynamics depending on the pulse repetition time

Besides the external magnetic field, the pulse repetition time T_{R} is an integral part of both resonance conditions. We investigate the spin dynamics dependent on T_{R}. For comparable results $|\vec{b}_{\mathrm{ext}}| \approx 93.08$ corresponding to 2 T is kept constant and in resonance. The parameter K has to be adjusted accordingly to $K = \lfloor \frac{200}{13.5T^*} T_{\mathrm{R}} \rfloor$. To observe mode locking, T_{R} has to be larger than the hyperfine dephasing time.

In Fig. 7.13 the dependency of the Overhauser field distribution $p_x(b_{\mathrm{N},x})$ and the absolute value of the electron spin revival $|\langle \vec{S}(N_{\mathrm{P}} T_{\mathrm{R}}) \rangle|$ on the repetition time T_{R} are presented. The position of the peaks in the Overhauser field distribution in panel (a) are predicted correctly by the resonance conditions (7.2.16) and (7.2.17). No definitive point can be made about the rate of the build-up depending on $p_x(b_{\mathrm{N},x})$ alone. Adding the electron spin revival in panel (b) to the picture, it becomes obvious that the speed of the mode locking increases with T_{R} since the electron has more time per pulse to influence the nuclear spins.

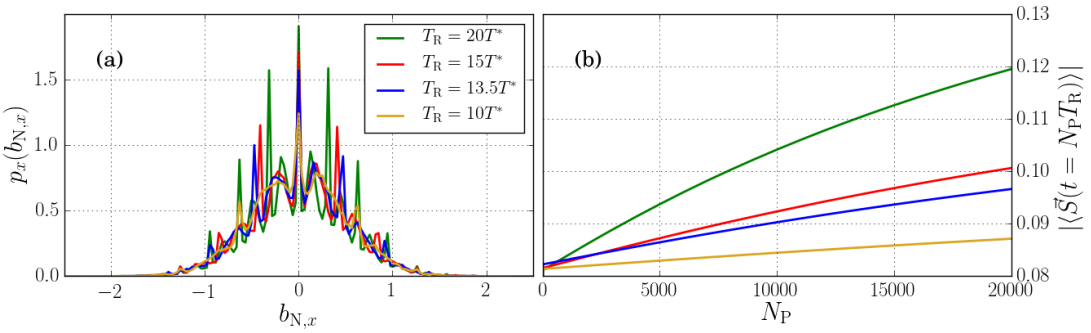

Figure 7.13: Panel (a): Overhauser field distributions depending on the pulse repetition time T_{R}. Panel (b): revival amplitude $|\langle \vec{S} \rangle|$ depending on T_{R}.

The electronic revival is universal for all T_{R} as predicted by Eq. (7.2.22). The faster

speed of the nuclei-induced frequency focusing process can be explained by revisiting Fig. 7.10 which exemplary shows the convergence to the resonance conditions in individual configurations. For a longer T_R the distance between the resonance conditions is smaller $\Delta\omega_\mathrm{L} = 2\pi/T_\mathrm{R}$. For the same rate of convergence the steady state is reached earlier even if we take absolute times into account instead of the number of pulses. The build-up of the Overhauser field is faster.

7.3.7 Dependence on the decay rate

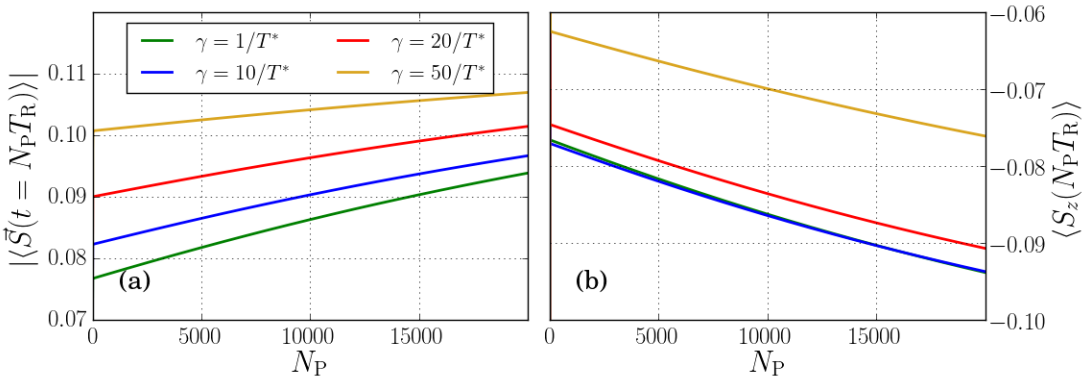

Figure 7.14: Revival of the absolute value of the electron spin and the S_z-component before the pulse.

Although the trion decay rate γ is not an adjustable quantity in experiment [35], it influences the electron spin dynamics, see Eq. (7.2.8). In this section, we investigate the influence of γ on this spin dynamics. The revival amplitude as well as the z-component of the central spin are depicted in Fig. 7.14. Larger decay rates lead to shorter decay time $\tau_\mathrm{T} = 1/\gamma$. It seems counterintuitive at first glance that the electron spin revival amplitude is larger for a faster trion decay as seen in the left panel of Fig. 7.14.

In the non-equilibrium steady state the electron spin dynamics is periodic in the pulse repetition time T_R. It does not necessarily imply that S_y is always zero before the pulse. This assumption is affirmed, if we include the information about the revival of S_z presented in panel (b). While for small γ the relation $|\langle\vec{S}(N_\mathrm{P}T_\mathrm{R})\rangle| = |\langle S_z(N_\mathrm{P}T_\mathrm{R})\rangle|$ approximately holds, the z-component contributes only a fraction to the absolute value for a faster trion decay. The missing part has to be attributed to the S_y-component since the pulse sets S_x to zero, and it stays constant during T_R except for small fluctuations. For a decay rate of $\gamma = 50$, the quantity $\overline{\gamma} = 2\gamma = 100/T^*$ is in the order of magnitude of the Larmor precession $|\vec{b}_\mathrm{ext}| = 93.1$ and the approximation $\overline{\gamma} \approx \omega_\mathrm{L}$ is justified. With this new simplification, we proceed similar to Sec. 7.2.3 and integrate over the spectrum. The result is an electronic revival in the z-direction of $S_z^\mathrm{bp} = -0.063$. For the y-direction the additional step of plugging S_z^bp into Eq. (7.2.8) has to be taken. The result is $S_y^\mathrm{bp} = -0.078$ and the resulting absolute value assuming $S_x^\mathrm{bp} = 0$ is $|\vec{S}^\mathrm{bp}| = 0.100$. The predictions agree with the simulation.

To reveal the origin of the changed electron behavior, the electron spin dynamics is depicted for one period T_R after 20 000 pulses in Fig. 7.15. After the pulse the electron amplitude is smaller the larger γ, cf. panel (a). This is intuitive to grasp: At $\Delta t = 0$

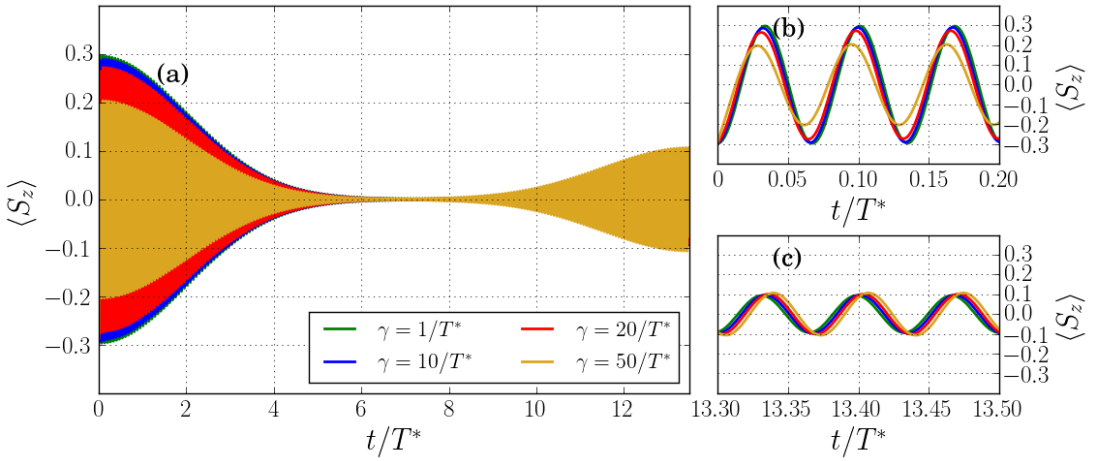

Figure 7.15: Electron spin dynamics after the 20 000 pulses over the time period T_R in panel (a). Panel (b) and (c) show the short-time dynamics immediately after and before the pulse.

after the pulse, the electron spin is aligned in negative z-direction and the trion is excited. If γ is fast compared to the Larmor precession, the trion is decayed before the electron has executed one rotation. During most of the decay time, the electron spin vector is aligned in negative z-direction while the trion adds a positive S_z contribution. Those two mechanisms cancel each other out and $\langle \vec{S}^\mathrm{ap} \rangle$ decreases. For the limit of $\gamma \to \infty$ the trion decays instantly. The pulse has no effect and $\langle \vec{S}^\mathrm{ap} \rangle = 0$.

In the panels (b) and (c) of Fig. 7.15 the short-time dynamics after and before the pulse is shown. They reveal the reason for the behavior of the revival amplitudes. The trion decay induces a phase shift Φ [180, 186, 187]. If the trion decays slowly compared to $1/\omega_\mathrm{L}$, the decaying trion part is distributed "more equally" on the two electron states during a Larmor precession and the phase shift is small. For a fast decay the sum of $\gamma P_\mathrm{T} \mathrm{e}^{-2\gamma t} \vec{\mathrm{e}}_z$ from the source term, Eq. (7.1.27), and a rotating electron spin vector with mostly negative components S_y and S_z leads to a significant phase shift. This phase shift can be quantified [180, 186, 187] by simplifying Eq. (7.2.8)

$$S_z(t) \approx A_y \sin(\omega_\mathrm{L} t) + A_z \cos(\omega_\mathrm{L} t) = \sqrt{A_y^2 + A_z^2} \cos\left[\omega_\mathrm{L} t + \frac{\pi}{2} + \arctan\left(\frac{A_z}{A_y}\right)\right] \tag{7.3.2}$$

with

$$\frac{A_z}{A_y} = \frac{\overline{\gamma}}{\omega_\mathrm{L}} - \frac{2S_z^\mathrm{bp} - 1}{2S_z^\mathrm{bp} + 1} \left(\frac{\overline{\gamma}}{\omega_\mathrm{L}} + \frac{\omega_\mathrm{L}}{\overline{\gamma}}\right).$$

For $\overline{\gamma} \ll \omega_\mathrm{L}$ the phase shift is π and the electron spin dynamics can be approximated by $-\cos(\omega_\mathrm{L} t)$. For ω_L and $\overline{\gamma}$ of the same order of magnitude the phase shift retains its dependence on S_z^bp with

$$\Phi = \frac{\pi}{2} + \arctan\left(1 + 2\frac{2S_z^\mathrm{bp} - 1}{2S_z^\mathrm{bp} + 1}\right). \tag{7.3.3}$$

This can lead to a non-zero S_y before the pulse not only in each configuration but also in the expectation value.

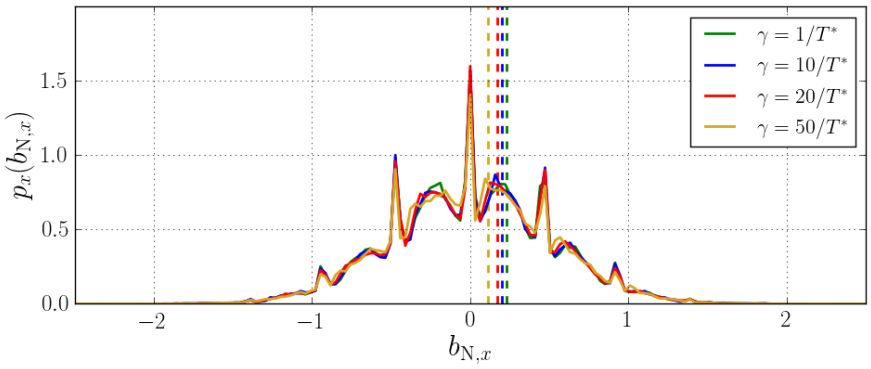

Figure 7.16: $p_x(b_{\mathrm{N},x})$ for different trion decay rates. The vertical lines indicate the first mode given by the resonance condition (7.2.17).

The histograms of the Overhauser field are depicted in Fig. 7.16. All $p_x(b_{\mathrm{N},x})$ seem equally advanced and no trion decay rate favors a faster build-up. The even resonance condition is unaffected by the trion decay rate. The peaks predicted by the odd resonance condition (7.2.17) are shifted or deformed for large γ. But the shift, indicated by the dashed vertical lines, is not as pronounced as it is for the variation of the external magnetic field strength.

7.3.8 Scaling behavior with the bath size

The pulse sequences are investigated up to $N_{\mathrm{P}} = 20\,000$ pulses with a laser repetition time $T_{\mathrm{R}} \approx 13.5\,\mathrm{ns}$. This corresponds to a total of $N_{\mathrm{P}} T_{\mathrm{R}} \sim 0.27\,\mathrm{ms}$ for the whole pulse sequence. However, in experiments [33] the measurement time can last from seconds up to 20 min. This leads to $7.4 \cdot 10^7$ pulses per second for $T_{\mathrm{R}} = 13.5\,\mathrm{ns}$. With the currently employed SCA scheme, including the simplification of the box model, those times are not achievable due to computational constraints. The discrepancy to experimental setups can be bridged exploiting the scaling behavior of the dynamics with the number of nuclear spins.

In Fig. 7.17 each panel contains snapshots of Overhauser field distributions along the external magnetic field $p_x(b_{N,x})$ at different numbers of pulses N_{P} for varying numbers of nuclear spins N. The constant quantity in each panel is the ratio $\nu_{\mathrm{P}} = N_{\mathrm{P}}/N$ which is given in ascending order from left to right as $\nu_{\mathrm{P}} = 20$, 200 and 2000.

In each panel the Overhauser field distribution $p_x(b_{N,x})$ is universal. This indicates that a larger spin bath leads to a slower time evolution of $p_x(b_{N,x})$. Since the nuclear spins in the box model all precess with the same frequency, they do not change alignment to each other. The only exchange of polarization is with the electron spin via the hyperfine interaction. This is linked to the two effective fields of the hyperfine interaction and their dependence on the coupling constant $a := a_k \sim \sqrt{3/N}\,\forall\, k$: the Knight field $a\vec{S} = \sqrt{3/N}\vec{S}$ and the Overhauser field $a\sum_k \vec{I}_k = \sqrt{3/N}\sum_k \vec{I}_k$. Through the Knight field, the electron spin dynamics is directly coupled to the nuclear spin dynamics which then is fed back to the electron spin via the Overhauser field. Both fields contain a dependence on the coupling constant $a = \sqrt{3/N}$ which causes the build-up to scale directly with the bath size $a^2 \sim 1/N$.

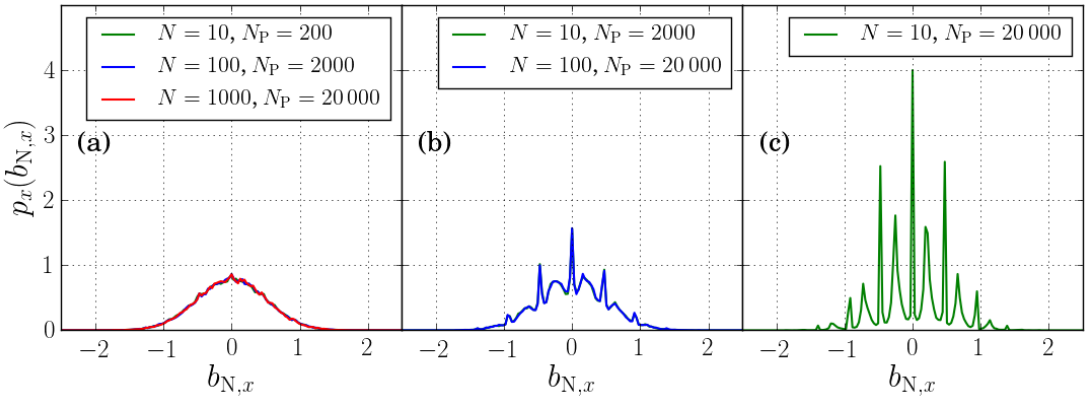

Figure 7.17: Overhauser field distributions at different numbers of pulses for systems with different bath sizes. The time evolution of $p_x(b_{\mathrm{N},x})$ in (a) features the ratio $\nu_\mathrm{P} = N_\mathrm{P}/N = 20$, in panel (b) and (c) $\nu_\mathrm{P} = 200$ and 2000, respectively.

The time-dependent build-up of the mode locking in experimental setups can be predicted by the simulation of smaller systems and by exploiting the scaling property outlined above. At all times the results for $N = 10$ are followed faithfully by its counterparts with larger N. We can, therefore, assume that this trend carries on for a more realistic case of $N = 10^5$ where more laser pulses have to be applied to compensate for the build-up speed. For $N = 10$ and $N_\mathrm{P} = 20\,000$ the Overhauser field distribution still features a Gaussian envelope, while resonance peaks of both resonance conditions are sharper compared to $\nu_\mathrm{P} = 200$. The Overhauser field $p_x(b_{\mathrm{N},x})$ for $N = 10$ will then be equivalent to the result for $N = 10^5$ after $N_\mathrm{P} = 2 \cdot 10^8$ pulses. The corresponding time $t = 2.7\,\mathrm{s}$ is in the order of magnitude of the times occurring in experiments.

However, the steady state is still not reached at $\nu_\mathrm{P} = 2000$ as can be seen in Fig. 7.18 where the revival amplitude of $|\langle\vec{S}\rangle|$ plotted. The same behavior observed for the Overhauser field distribution translates to the revival. If the time scale is rescaled with the nuclear spin bath size, then all curves are superposable. Since no convergence is observed even for $N = 10$, a longer pulses sequence would be necessary to reach the steady state revival. Increasing the number of pulses by a factor of $10 - 100$ provides a more accurate estimate for the nuclei-induced frequency focusing time in experiment [33].

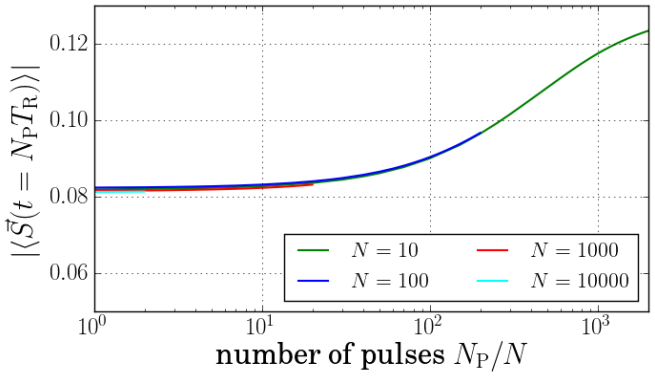

Figure 7.18: Revival amplitude of the absolute value of the electron spin with different nuclear bath sizes depending on the ratio N_P/N.

Exploiting the scaling behavior further, we chose a bath size of $N = 10$ to reach the steady state. The number of pulses applied is $N_\mathrm{P} = 5 \cdot 10^5$. The result is shown in Fig. 7.19. However, one has to be aware that the analytical steady state with infinitesimally sharp peaks is neither feasible in experiment nor in a numerical simulation. Therefore, the peak width of the Overhauser field distribution is finite here and the revival of $\langle S_z \rangle$, as well as the amplitude after the pulse, turn out smaller than predicted. We assume that the steady state is reached after $N_\mathrm{P}/N = 20\,000$ when $\langle S_z \rangle$ and $\langle S_y \rangle$ converge to their final value. Applying the scaling behavior to the curve, the estimated non-equilibrium stead state for $N = 100$ and a realistic $N = 10\,000$ is reached after $N_\mathrm{P} = 2 \cdot 10^7$ and $N_\mathrm{P} = 2 \cdot 10^9$, respectively.

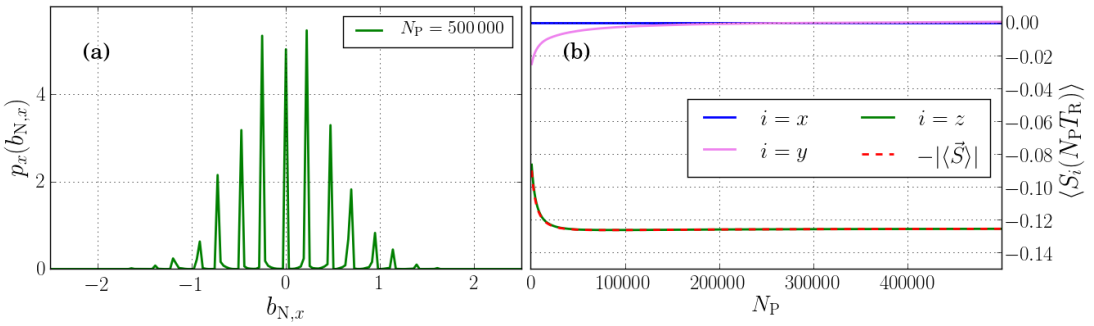

Figure 7.19: Overhauser field distribution and revival amplitude for a pulse sequence of 500 000 pulses with $N = 10$. The steady state is reached after $\nu_\mathrm{P} = N_\mathrm{P}/N = 20\,000$.

7.3.9 Pump efficiency depending on the pulse area

It was shown in experiments [35, 188] that the Faraday rotation amplitude is connected to the area of the laser pulse. The theoretically calculated spin dynamics of a pulse sequence for different pulse areas F is presented in Fig. 7.20. In panel (a) the histogram of the Overhauser field distribution after $N_\mathrm{P} = 20\,000$ pulses is plotted. Panel (b) and (c) show the electron spin amplitude immediately before and after the pulse. After only one pulse the π-pulse leads to the largest amplitude after the optical excitation. With an increasing number of pulses $N_\mathrm{P} > 5$, the electron spin amplitude after the pulse for $F = 1.2\pi$ and $F = \pi$ show approximately the same time evolution.

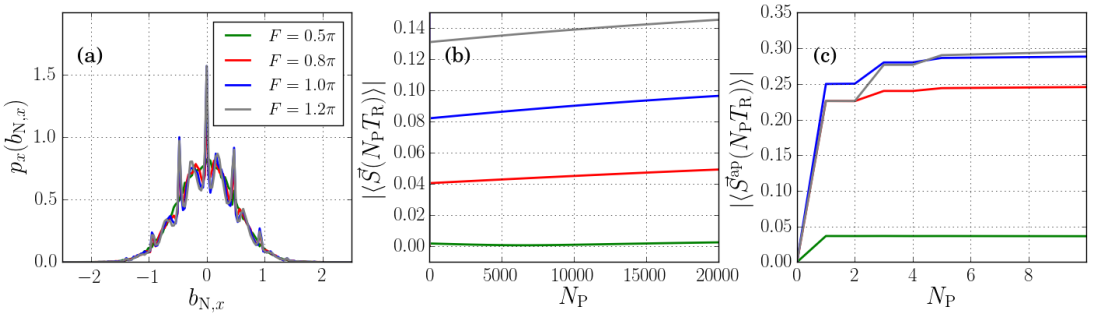

Figure 7.20: Panel (a): Overhauser field distributions depending on the pulse area F. Panel (b): revival amplitude $|\langle \vec{S} \rangle|$ depending on F. Panel (c) the electron spin amplitude after the pulse for up to 10 pulses.

In the distribution function $p_x(b_{\mathrm{N},x})$ the position of the peaks is invariant under a change of the pulse area. However, no distinct peaks are observable if F deviates strongly from π as it is the case for $F = 0.5\pi$. For the smaller deviations of $\Delta F = \pm 0.2\pi$ the distribution matches that of $F = \pi$.

The differences between the chosen pulse area become more obvious in panel (b). As expected, the revival amplitude is smaller than that of the π-pulse for $F < \pi$. For $F = 0.5\pi$ the revival vanishes almost completely. However, what catches the eye most is the revival increase of $F = 1.2\pi$ compared to $F = \pi$. For the same spin alignment before the pulse S_z^{bp} the pulse with $F = 0.8\pi$ and $F = 1.2\pi$ lead to the same absolute value in each spatial direction after the pulse. While the x-component of the electron spin is constant during T_{R} and vanishes with $\cos(1.2\pi/2)S_x^{\mathrm{bp}} = \cos(0.8\pi/2)S_x^{\mathrm{bp}} \approx 0.309 S_x^{\mathrm{bp}}$ in either case, the S_y-component plays an important role for the electron spin amplitude $|\vec{S}| \approx \sqrt{S_y^2 + S_z^2}$. The difference can be found in the sign of S_x and S_y. For $0 < F < \pi$ the S_y before the pulse is shrunk and forwarded to the next pulse but for $\pi < F < 2\pi$ it is also flipped, see Eq. (7.1.12). This leads to a refocusing effect every second pulse in each configuration.

Since the model for the pulses is too simplistic, it cannot make quantitative predictions. But it can explain a few features also observed in experiment [1]. The pulse area is proportional to the pump power. In experiments it is assumed that the maximum signal after the pulse is measured for a pulse area of π. With increasing pump power the Faraday rotation signal after the pulse decreases after it reached a maximum whereas the revival amplitude increases further and even surpasses the amplitude after the pulse.

Although a pump pulse with $F = 2\pi$ adds a flip of the x and y spin component to the dynamics, the result is the same as for $F = 0$: no frequency focusing is achieved and the spin expectation value remains at $\langle \vec{S} \rangle = 0$. For $2\pi < F < 4\pi$ the presented dynamics is mirrored and the results repeat with a 4π periodicity of F. However, in experiment it was observed that the Faraday rotation amplitude does not descend to zero for $F = 2\pi$ [35]. To replicate those features a more sophisticated approach to pump pulses has to be chosen, e. g. incorporating pulses of finite duration [63], different shape [121, 189] or also include detuning [179, 182, 189].

7.3.10 Influence of an off-resonance, external magnetic field

Up until now, we assumed that the externally applied magnetic field fulfills the resonance condition $\frac{2\pi K T^*}{T_{\mathrm{R}}}$ with $K \in \mathbb{Z}$. However, an individual QD might deviate from this perfect resonance due to a variation of the g-factor g_{e} [33]. The adjusted parameter $K' = K + \Delta K$ defined in Eq. (7.3.1) takes into account the difference from the integer resonance condition by including the parameter $\Delta K \in \mathbb{R}$.

Figure 7.21 shows $p_x(b_{N,x})$ for different ΔK. Independent of the deviation from the resonance condition, the Gaussian envelope retains its variance of 1/4 and remains centered around $b_{\mathrm{N},x} = 0$. Beneath the envelope the peaks shift to new positions which satisfy the resonance conditions (7.2.16) and (7.2.17). Their displacement $2\pi\Delta K$ is subtracted in the right panel with $\bar{b}_{\mathrm{N},x} = b_{\mathrm{N},x} + 2\pi\Delta K T^*/T_{\mathrm{R}}$. Now the peak positions

[1] Private communications and experimental data from Faraday rotation and ellipticity for increasing pump power from E. Evers.

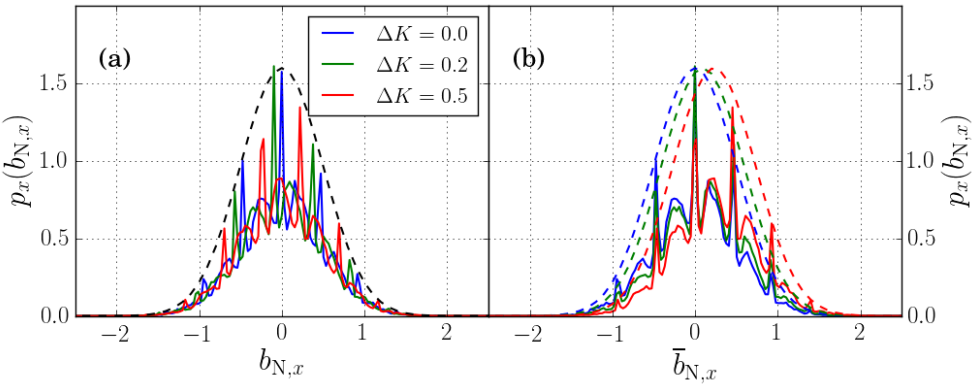

Figure 7.21: Overhauser field distribution $p_x(b_{\mathrm{N},x})$ after 20 000 pulses for deviations from the resonance given by $K = 200$ in panel (a). Overhauser field distribution $p_x(b_{\mathrm{N},x})$ shifted by $2\pi\Delta K T^*/T_\mathrm{R}$. The Gaussian envelope of the shifted $p_x(b_{\mathrm{N},x})$ is marked by dashed lines.

of all ΔK match but the Overhauser field distribution becomes asymmetric with respect to the origin due to the enhanced weight of the peaks to the right side. The weight of the peaks is determined by the also shifted Gaussian envelope function centered at $b_{\mathrm{N},x} = 2\pi\Delta K T^*/T_\mathrm{R}$.

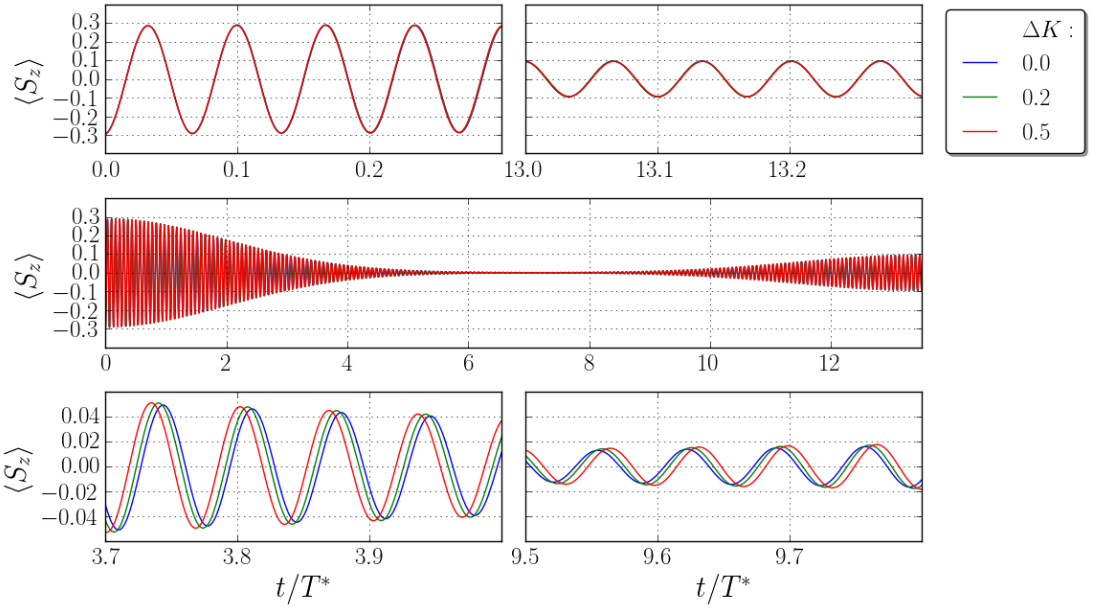

Figure 7.22: Electron spin dynamics after 20 000 pulses depending on ΔK. Upper panels: self-focusing immediately before and after the pulse. Middle panel: dynamics for one pulse period T_R. The Larmor precession cannot be resolved. Lower panel: frequency shift at intermediate times.

The adjusted peak positions compensate for the non-resonant settings in T_R and $\vec{b}_\mathrm{ext}$ since the sum of the external magnetic field and the Overhauser field have to fulfill Eqs. (7.2.16) and (7.2.17). This is backed by the notion [33] that the central spin is self-focusing under periodic laser pulsing. In Fig. 7.22 the z-component of the electron spin is depicted after 20 000 pulses. The entire time evolution of the spin expectation value

over T_R is shown in the middle panel. The Larmor precession cannot be well resolved on this time scale and only the Gaussian envelope of the dephasing and the revival is visible. No difference between the three ΔK is noticeable in panel (b). The same applies to the dynamics directly after and before the pulse, shown in the top panels. However, for intermediate times shown in the bottom panels $\langle S_z(t)\rangle$ a dephasing is visible due to the shifted, prevalent frequencies given by $p_x(b_{\mathrm{N},x})$. The dephasing observed during 3.7 to 4.0 T^* is inverse to that of 9.5 to 9.8 and vanishes once T_R is reached.

7.3.11 Simple preview to quantum dot ensembles

The g-factors do not only vary over an ensemble of QDs, but multiple parameters can also influence the dephasing. First and foremost among them are the hyperfine coupling constants a_k which define the time scale T^* [55]. We account for the difference between individual QDs by introducing a modified dephasing time

$$T_\eta^* = \eta T^*. \tag{7.3.4}$$

The parameter η is chosen in relation to a fictitious reference QD with a $\eta = 1.0$. It depends, for example, on the growth process or the distribution of radii of the QDs and is purely phenomenological in this context. In a realistic system the dephasing is also connected to interactions between QDs. Experimentally, the interplay in an ensemble was investigated in Ref. [188] and a more sophisticated, theoretical approach is dedicated to describing the correlation between QDs in Ref. [182]. Note that the rescaling of the dimensionless external magnetic field still depends on $T^* \approx 1\,\mathrm{ns}$ since the pulse repetition rate is the same for all QDs.

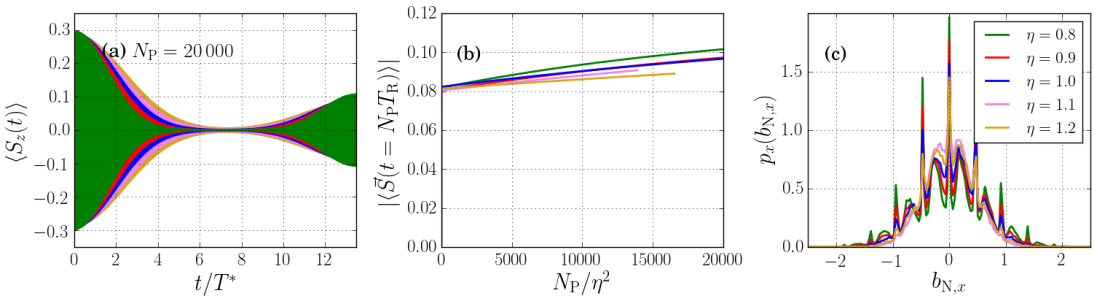

Figure 7.23: Spin dynamics for a variation of $T_\eta^* = \eta T^*$. Panel (a): electron spin dynamics $\langle S_z\rangle$ after the 20 000 pulses. Panel (b): revival amplitude $|\langle \vec{S}\rangle|$. Panel (c): Overhauser field distribution in x-direction.

We investigate a variation of η between 0.8 and 1.2 in Fig. 7.23 such that $\langle T_\eta^*\rangle = T^*$. After 20 000 pulses the central spin dynamics in z-direction is depicted in panel (a). For larger η the dephasing time is slower than for T^*. The adjusted dephasing time is mirrored in the Gaussian envelope of the revival. A stronger revival is observed for smaller η. The convergence to the steady state is faster, since a smaller rescaling factor η increases the strength of the hyperfine interaction. This is partially attributed to the feedback mechanism between the Overhauser field and the Knight field. In panel (b) the revival amplitude is plotted against the number of pulses N_P/η^2 to account for the leading effect of η. The revival curves are brought closer to each other, thus verifying the underlying feedback mechanism. However, the curves for different η do not converge.

These deviations may be ascribed to the fact that the ratio T_R/T_η^* is not kept constant. In panel (c) we see that all η share the same peak positions. The difference lies in the build-up speed of the distribution. For larger T_η^* the peaks are not as distinctive as they are for smaller η. This fact can be linked to the electron spin dynamics shown in panel (b).

In an ensemble of resonantly pumped QDs the electron spin dynamics for different η is approximately in-phase and interferes constructively. Therefore, simple phenomenological predictions for the total dephasing depending on the parameter η can be made based on the results obtained for a single QD.

7.3.12 Influence of the nuclear Zeeman effect

Like the trion decay time, the nuclear Zeeman effect is a non-adjustable quantity in experiment. As discussed in Sec. 5.3.2, the parameter ζ, determining the relative strength of the nuclear Zeeman to the electronic Zeeman, assumes a value between $\zeta = 1/1062$ and $\zeta = 1/597$ for ^{75}As and ^{71}Ga, respectively.

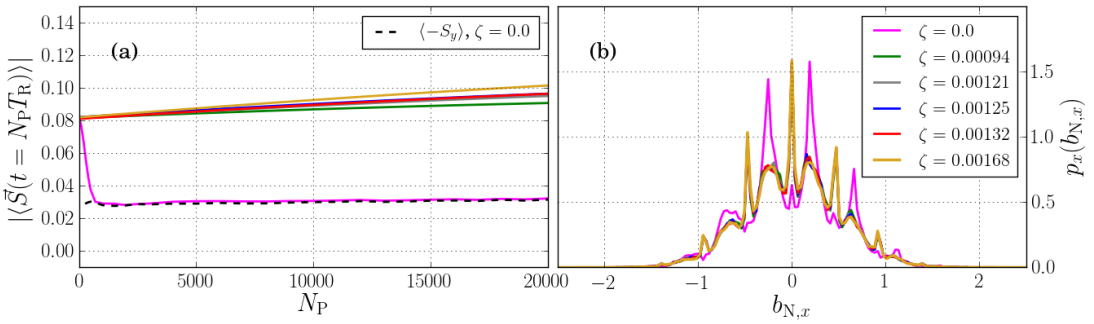

Figure 7.24: Panel(a): Histogram of the Overhauser field in x-direction for a varying ζ. Panel (b): Electron spin amplitude for different ζ. The y-component of the electron spin revival is added for $\zeta = 0$ in a dashed black line.

In Fig. 7.24 the results of simulations for different ζ based on the isotopes of a In(Gas)As QD and for $\zeta = 0$ are plotted. The electron spin revival is presented in panel (a). The initial revival is universal for all curves since its origin is purely electronic. Afterwards, approximately the same behavior is observed for realistic $\zeta > 0$. The build-up of the revival amplitude correlates with the nuclear Zeeman term and $\zeta = 1/597 \approx 0.00168$ features the largest revival. A vastly different behavior occurs for $\zeta = 0$ after some 100 pulses when the nuclear spin dynamics comes into play. The revival amplitude decreases on the time scale of only a few pulses and evens out at 0.03. For $\zeta = 0$ the largest contribution to the revival amplitude is the y-component of the electron spin – added as a dashed black line in Fig. 7.24 (a) – as opposed to the S_z-value for the other cases where $\zeta \neq 0$. Therefore, neglecting the nuclear Zeeman interaction leads to a phase shift of $\pi/2$.

The corresponding Overhauser field distributions $p_x(b_{\mathrm{N},x})$ to the electron spin dynamics in panel (a) of Fig. 7.24 is found in panel (b) of the same plot. All Overhauser field distributions feature a Gaussian envelope. Also, the position of the peaks remains the same. The weight of the peaks, however, changes drastically depending on whether the Zeeman interaction is incorporated or switched off. The peak weights to each other

differ only marginally for the Zeeman energy ratios of the isotopes. But for $\zeta = 0$ the weights transition almost completely to the sub-set of peaks defined by the trion decay dependent on resonance condition (7.2.17).

The correlation between revival and Overhauser field distribution was already shortly discussed in the context of the toy model in Sec. 7.2.4. In the toy model we started out with a given shape of $p_x(b_{\mathrm{N},x})$. We assumed the presence of δ-peaks at both resonance conditions (7.2.16) and (7.2.17) and choose a spectral weight ratio between the Gaussian envelope of the two sub-classes of the resonance conditions. If the envelope of Eq. (7.2.17) has thrice the amplitude compared to that of the even resonance conditions, see Fig. 7.4, the spin polarizations of configurations with frequencies given by the even and odd resonance conditions interfere destructively. The spin expectation value at the time of the pulse is zero. For deviations from this ratio, a non-zero revival amplitude can be observed. For a weight imbalance of $1 : a$ between even to odd sub-set with $a > 3$, the electron spin expectation value is aligned in positive z-direction in the toy model. Therefore, the remarkable decrease of the spin revival is linked to the Overhauser field distribution. The remaining, finite value can be explained by the ratio between the two sub-sets of peaks slightly deviating from $1 : 3$ and by the broadening of the peaks.

While the toy model assumes a given Overhauser field distribution and derives an electron spin revival amplitude, it requires a priori knowledge of $p_x(b_{\mathrm{N},x})$. It cannot reveal the deeper reason for the spectral weight balance between the peak heights of the two sub-classes. This simplistic approach also fails to predict the correct phase shift of the electron spin between different ζ. Unlike for quantum mechanical approaches [62, 63], no transfer of spectral weight between the two sub-sets of resonance conditions was observed for variations of $\zeta > 0$ and K.

7.3.13 Influence of the hyperfine coupling distribution function $p(a)$

So far, we exclusively used the box model with $a_k = a \forall k$. Now, the focal point of the investigation is the influence of the hyperfine coupling distribution $p(a)$ on the electron spin dynamics and the Overhauser field distribution $p_x(b_{\mathrm{N},x})$. $p_{r_0}(a)$ presented in Sec. 3.2 is used. For $\xi = 2$ the distribution is equivalent to exponential coupling constants $a_k \sim \exp(-\lambda u)$ with $\lambda = r_0^2$ and $u \sim \mathcal{U}(0,1)$ which is often used in literature, see e. g. [38, 48, 129]. For a three-dimensional QD the coupling constants are given by $a_k \sim \exp(-r_0^2 u^{2/3})$.

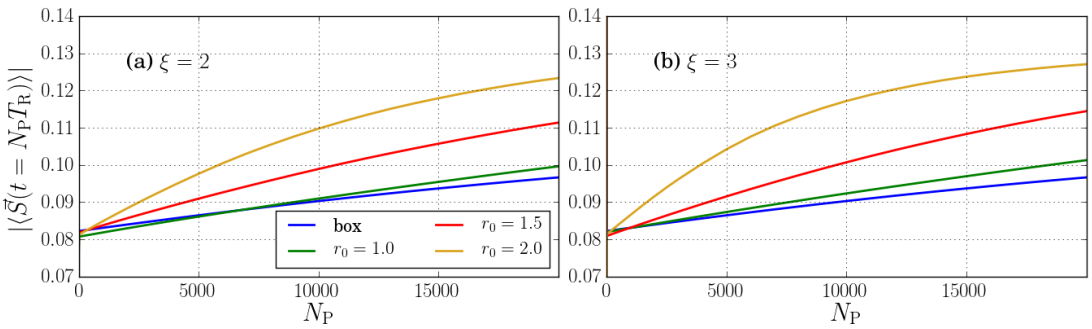

Figure 7.25: Revival build-up of the electron spin for different cut-off parameters r_0. Panel (a) two-dimensional QD $\xi = 2$ and (b) $\xi = 3$.

While the short-time electron spin dynamics of the order of one T_R reveals no significant changes, the differences become more apparent when the revival is in focus. The time evolution of the revival amplitude over 20 000 pulses is depicted in Fig. 7.25. The curve for the box model is added for reasons of comparison. The cut-off parameters $r_0 = 1.0$, 1.5 and 2.0 are chosen. The revival for the box model shows the least increase over the course of 20 000 pulses compared to $p_{r_0}(a)$ for a two-dimensional QD, as depicted in Fig. 7.25 (a). From the various options for the r_0-parameter, those with a higher cut-off lead to a faster revival growth. This observation is universal and independent of ξ as can be seen via comparison with panel (b) which shows the data for $\xi = 3$. The revival increase is faster for $\xi = 3$ than for $\xi = 2$.

The coupling constants enter quadratically into the time evolution of the Overhauser field

$$T^* \frac{\mathrm{d}}{\mathrm{d}t}\vec{b}_N = \sum_k a_k^2 \vec{S} \times \vec{I}_k + \zeta \vec{b}_\mathrm{ext} \times \vec{b}_N. \tag{7.3.5}$$

If the hyperfine coupling constant distribution favors a few larger a_k, the dynamics is dominated by a reduced number of nuclear spins. Therefore, it shows comparable behavior to the N scaling in the box model presented in Sec. 7.3.8 with additional distribution specific corrections. We took the sum over all coupling constants a_S as an indicator for the influence of the distribution $p_{r_0}(a)$ on the long-time behavior, cf. Sec. 3.2: A reduction of nuclear spins shows the same qualitative behavior as an increase in the cut-off parameter. Both reduce the number of nuclear spins that couple effectively to the electron spin. As a result, the build-up of the Overhauser field distribution and the revival are faster. A similar effect has been observed for dynamics of an unpulsed system for $|\vec{b}_\mathrm{ext}| = 0$ in Fig. 5.3. By adjusting the parameter r_0 a comparable long-time behavior of $C_2(t)$ could be found even for different bath sizes N.

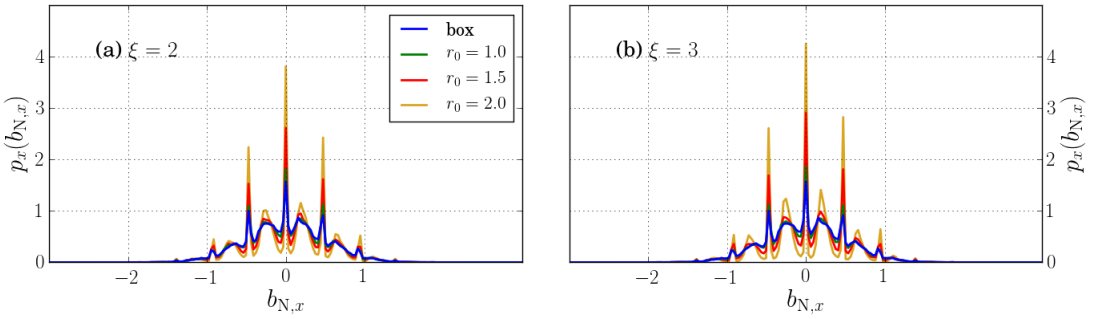

Figure 7.26: Overhauser field distribution after $N_\mathrm{P} = 20\,000$ for different r_0 corresponding to Fig. 7.25. The data is presented for two- and three-dimensional QDs in panel (a) with $\xi = 2$ and in (b) with $\xi = 3$.

The faster build-up of the revival amplitude is translated to that of the Overhauser field distribution shown in Fig. 7.26. Again, the data for $\xi = 2$ and $\xi = 3$ are compared to the box model in panel (a) and (b). The Overhauser field distribution along the external magnetic field $p_x(b_{\mathrm{N},x})$ is presented after 20 000 pulses. All distributions feature their peaks at the same positions given by the two classes of resonance conditions inside the Gaussian envelope. Those peaks become sharper over time, and we assume that the steady states of the pulsed system are the same for $N_\mathrm{P} \to \infty$. However, the build-up of $p_x(b_{\mathrm{N},x})$ advances at different speeds. As with the revival build-up of the electron spin,

lower r_0 lead to a slower development of the Overhauser field distribution and a lower ξ also results in a reduced build-up speed. For the ξ-variation this can be traced back to the histograms of the coupling constants, cf. Fig. 3.3, where $\xi = 3$ also leads to a greater spread of the coupling constant distribution than $\xi = 2$. Therefore, the effective number of nuclear spins can also be assumed as further reduced for $\xi = 3$.

7.3.14 Scaling behavior with the bath size for arbitrary a_k distributions

In the previous section we showed that while the time evolution approaches the same steady state independent of $p(a)$, the build-up speeds of revival and Overhauser field distribution are determined by the hyperfine coupling constant distribution. Another factor related to the coupling constants that influenced the build-up speed is the number of nuclear spins which acts as a rescaling factor to an individual a_k. In the box model this scaling property translates directly into the scaling behavior of the build-up. We show that a qualitatively similar behavior is observed for an arbitrary distribution function $p(a)$. In this case the scaling behavior is even more desirable because the simplification applied in the box model, which allows us to condense the dynamics of all nuclear spins into those of a single total spin, does not hold anymore. When each spin has to be simulated individually for $a_k \sim p(a)$ the computation time is proportional to $N \cdot N_\mathrm{P}$. Then a reduction from e. g. $N = 100$ to $N = 10$, which still faithfully represents the spin dynamics, leads to a significant speed-up of the numerical analysis.

The scaling of the Overhauser field distribution for $p_{r_0=1.5}(a)$ defined in Eq. (3.2.2) with $r_0 = 1.5$ is depicted in Fig. 7.27. Both $\xi = 2$ and $\xi = 3$ are presented on the left and right side, respectively. To show the scaling behavior the bath sizes of $N = 100$ and $N = 10$ were contrasted in the combinations $(N, N_\mathrm{P}) = (100, 20\,000), (10, 2000)$, $(10, 20\,000)$. The defining constant of the scaling was $\nu_\mathrm{P} = N_\mathrm{P}/N$ in the box model. For distinct a_k the result for $(10, 3000)$ for $\xi = 2$ as well as for $\xi = 3$ match the Overhauser field of $(100, 20\,000)$ better. All nuclear spins rotate synchronized in the box model. In contrast to this, each nuclear spin has an individual precession speed for the general case of $a_k \sim p(a)$. This addition to the dynamics necessitates the introduction of the correction function $f(p(a), N)$ defining a new scaling variable $x_\mathrm{P} = \nu_\mathrm{P} f(p(a), N)$. The unknown function $f(p(a), N)$ accounts for the correction to the scaling behavior of the box model. It depends on the hyperfine coupling constant distribution as well as the nuclear spin bath size. Since the same $p_x(b_{\mathrm{N},x})$ leads to the same x_P, we estimate the ratio $f(p_{1.5}(a), 100)/f(p_{1.5}(a), 10) = 3/2$ for both $\xi = 2$ and $\xi = 3$ based on the data in Fig. 7.27. A larger number of pulses is needed to achieve the same speed-up displayed by the box model. This implies that $f(p(a), N_\mathrm{A}) < f(p(a), N_\mathrm{B})$ if $N_\mathrm{A} < N_\mathrm{B}$.

The scaling behavior exhibited by the box model is found in all classical simulations for arbitrary hyperfine coupling constant distributions, albeit with an additional correction factor. The argument presented above allows us to utilize the bath size as a simulation parameter of the classical model to either reduce computation time or predict the dynamics of longer pulse sequences.

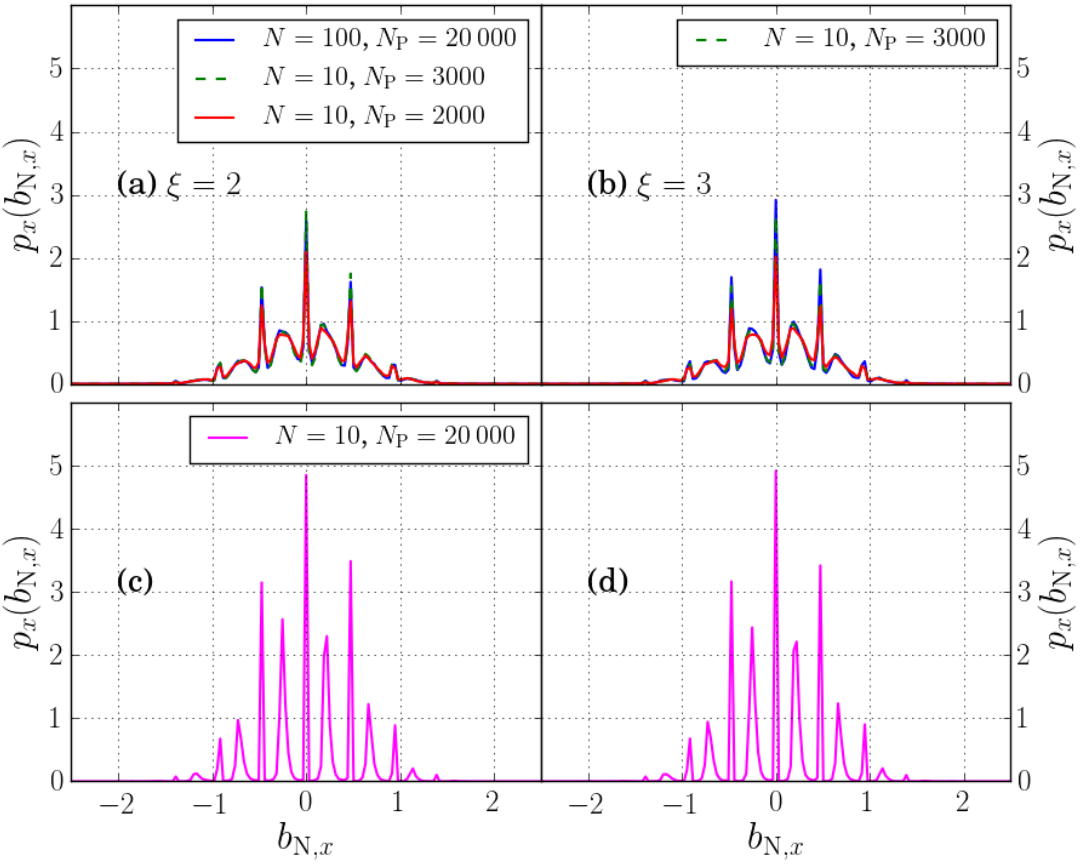

Figure 7.27: Scaling behavior for different hyperfine coupling constant distributions $p_{r_0}(a)$ for $\xi = 2$ and $\xi = 3$ according to Eq. (3.2.2) with $r_0 = 1.5$. Panel (a) and (b) show the comparison between the calculations with $N = 100$ and $N_\mathrm{P} = 20\,000$ with those of $N = 10$ after $N_\mathrm{P} = 2000$ for $\xi = 2$ on the left and for $\xi = 3$ on the right. The combination $(N, N_\mathrm{P}) = (100, 20\,000)$ coincides with approximately $(10, 3000)$ for $\xi = 2$ and for $\xi = 3$ instead of the tuple $(10, 2000)$ recorded for the box model. The last two panels (c) and (d) show the distribution that can be reached with $(N, N_\mathrm{P}) = (10, 20\,000)$ for $\xi = 2$ in (c) and for $\xi = 3$ in (d).

7.4 Comparison with the experimental results

In order to check whether our theoretical findings of the two classes of resonance conditions are a realistic prediction, we turn our attention to experiments. The experimental results of pump-probe experiments on semiconductor QDs presented in Fig. 7.28 have previously been published in Ref. [89]. The time evolution of the electron spins in panel (a) is recorded as proportional to the Faraday rotation signal after the periodic pulsing with repetition period $T_\mathrm{R} = 13.2\,\mathrm{ns}$ has stopped at $t = 0$. Its Fourier transform in panel (b) reveals the frequency dependence of the spin dynamics for the two presented external magnetic fields $|\vec{B}_\mathrm{ext}| = 2\,\mathrm{T}$ and $4\,\mathrm{T}$.

The electron spin dynamics in Fig. 7.28 (a) shows a re-occurring revival in the interval of T_R for both magnetic field strength. The fast spin precession in the time domain is barely resolved for $2\,\mathrm{T}$ on the time scale of multiple T_R and is not resolved for $4\,\mathrm{T}$. The Faraday rotation signals for the two magnetic field strengths also differ in intensity as well as in the revival amplitude over time. For the higher magnetic field the first

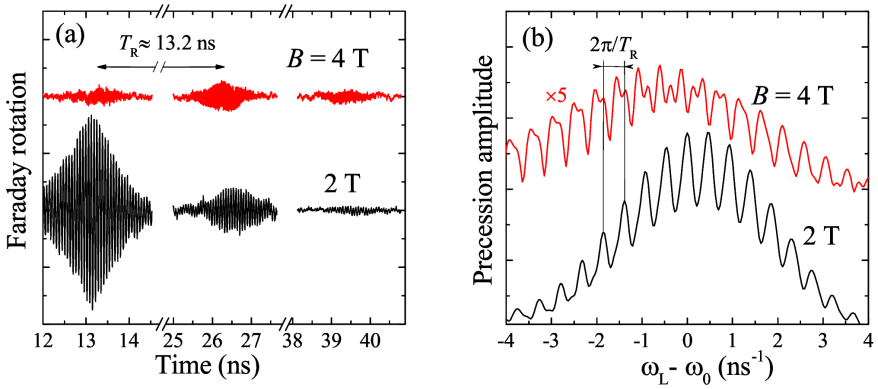

Figure 7.28: In panel (a) the Faraday rotation signal which is proportional to the electron spin dynamics is depicted for $|\vec{B}_{\text{ext}}| = 2\,\text{T}$ and $4\,\text{T}$. The data is recorded after the pumping pulse sequence with pulse repetition time $T_\text{R} = 13.2\,\text{ns}$ was switched off at $t = 0$. Panel (b) shows the Fourier transform of the electron spin dynamics shifted by the Larmor precession frequency of the external magnetic field. The plots are taken from [89].

revival amplitude after the last pulse is weaker than the directly following revival burst. The revival amplitude decays over the duration of a few T_R for both field strengths. The precession amplitudes in panel (b) show a roughly Gaussian envelope centered on the frequency given by the external magnetic field. As a substructure broadened peaks occur with a distance given by $2\pi/T_\text{R}$. For $|\vec{B}_{\text{ext}}| = 2\,\text{T}$ the spacing of those peaks is even. For $|\vec{B}_{\text{ext}}| = 4\,\text{T}$ a second set of side peaks can be observed in between the more prominent peaks. The distance between those additional peaks is also $2\pi/T_\text{R}$.

The even resonance conditions have been known for a long time [33, 88] and the precession frequencies peaks, defined by Eq. (7.2.16), are visible at both external magnetic field strengths in Fig. 7.28 (b). The smaller side peaks, occurring only at $|\vec{B}_{\text{ext}}| = 4\,\text{T}$, indicate the existence of additional modes. While we can claim no quantitative agreement between the experimentally measured spectral positions of the additional modes and those predicted by Eq. (7.2.17), the shape of the precession amplitude spectrum is also noticeable in the Faraday rotation signal in time in panel (a). The weak mode-locked amplitude for $|\vec{B}_{\text{ext}}| = 4\,\text{T}$ at $t = 13.2\,\text{ns}$ can be traced back to the additional modes. We have shown that superimposing modes with frequencies defined by (7.2.16) and (7.2.17) diminishes the first revival amplitude after the pulse. This is due to the fact that the phase difference between the modes of the two classes of resonance conditions is an odd multiple of π at this time. The positive interference of the modes leads to re-emerging, second revival at $t = 2T_\text{R}$ after the last pulse.

The occurrence of the additional modes seems to be linked to the external magnetic field in the experiment. This correlation cannot be reproduced in the presented semiclassical model. However, quantum mechanical approaches [62, 63] were able to verify this interplay via an additional resonance condition for the nuclear spins which depends on the nuclear g-factor and $\vec{B}_{\text{ext}}$. Further deviations from the experimental results are expected due to the limited number of nuclear spins and pump pulses in the semiclassical approach. While we assume that the experiments reach the steady state, the theoretically calculated amplitude does not yet converge after 20 000 pulses. Here, we either have to exploit the scaling behavior of the system for smaller spin baths or apply different algorithms [58, 63, 65]. Furthermore, the current approach neglects interactions such

as the nuclear dipole-dipole interaction [32] or the quadrupolar interaction [75, 81, 83]. Both can lead to an additional broadening of the peaks. We also have to take into account that we restrict our investigations to a single QD while the experiments are usually conducted on a QD ensemble. This way any ensemble effects are not taken into account [182].

7.5 Chapter conclusion

We complemented the semiclassical approach presented in Chap. 5 by a description of the trion decay and pump pulses which enabled us to perform a simulation of a periodically pulsed QD. From this new set of coupled equations of motion, we derived two resonance conditions in the FOA: $\omega_{\mathrm{L}} T_{\mathrm{R}} = 2\pi n$ which only depends on the repetition rate of the pulses and the external magnetic field and $\omega_{\mathrm{L}} T_{\mathrm{R}} = 2\arctan(\omega_{\mathrm{L}}/\overline{\gamma}) + 2\pi n$. Beyond the dependencies of the first resonance condition, the second condition is also subject to the trion decay rate. This result has far-reaching influence on the shape of the non-equilibrium Overhauser field distribution function and the electron spin revival before the next pulse. The analytical predictions are valid especially in the limit of large magnetic fields.

In semiclassical simulations we demonstrated that the nuclei-induced frequency focusing effect manifests itself in the build-up of the Overhauser field distribution along the external magnetic field. From the previously unpolarized, Gaussian distribution emerge peaks whose position corresponds to the theoretically predicted resonance conditions. For large magnetic fields the distance between two such peaks is given by π/T_{R}. The electron spin revival, that occurs on the time scale of only a few pulses, can be attributed purely to the effect the pulse has on the spin vector. Later increase of the revival amplitude is connected to the frequency focusing due to the realignment of the nuclear spins.

The parameters, that occur in the resonance conditions, T_{R} and the trion decay rate γ, were investigated. The variation of T_{R} influences the distance between the resonance peaks in the spectrum and thereby also the build-up speed of revival and $p_x(b_{\mathrm{N},x})$. A larger time delay between pulses leads to a faster spin revival build-up per pulse. The trion decay rate only influences the odd resonance conditions and induces a phase shift in the electron spin dynamics. This fact translates to a larger revival amplitude for the electron spin but leaves the build-up speed of the Overhauser field distribution unaffected. Compared to changes in the external magnetic field, the variation of γ has only a small effect on the position of the odd peaks. The trion decay rate is a constant in experiment and the inequality $\gamma \ll \omega_{\mathrm{L}}$ holds.

We conducted a simplistic investigation on the influence of ensemble effects on the dynamics in a single QD, such as variation of the electron g-factor or change of the characteristic time scale T^*. The behavior displayed shortly before and after the pulse reveals the self-focusing nature of the electron spin dynamics even in the face of a non-resonant external magnetic field. That the electron spin dynamics is independent of the characteristics of an individual QD is owed to an adjusted Overhauser field distribution in which the peak positions are shifted to accommodate the resonance conditions. Different coupling constants in each QD can lead to different dephasing times given by a rescaled T^*. Therefore, a stronger hyperfine coupling induces a faster

dephasing after a pulse but also results in a faster nuclei-induced frequency focusing. The electron spin revival and the Overhauser field distribution become more pronounced earlier in the pulse sequence. Due to their self-focusing quality the superposition of electron dynamics of different QDs still leads to congruent central spin behavior in the ensemble. The theoretical results about the dynamics in one QD can therefore be used to glean information about the ensemble properties.

The influence of the nuclear Zeeman interaction is parametrized by ζ which is the ratio between nuclear and electron Zeeman energy. For parameters, that model the g-factors found in a In(Ga)As QD faithfully, the dynamics of electron spin and nuclear spins varies only slightly. The behavior changes fundamentally for $\zeta = 0$ where the peaks described by the odd resonance condition stand out and the revival amplitude decreases after an electronic revival.

If a distribution of the hyperfine coupling constants is introduced, then we had to relinquish the computational time won by the box model. A differential equation had to be solved for each individual nuclear spin instead of one for the total nuclear spin. Basic features like the increase in electron spin revival with the progress in mode locking observed in the Overhauser field distribution remain. However, the time, in which the system converges to the non-equilibrium steady state, depends on the distribution of the hyperfine coupling constants. If $p(a)$ features a broad spread, then the convergence is faster.

A variation of the bath size can be used to approximate the build-up time of the Overhauser field in experiment for realistic numbers of nuclear spins and extrapolate the steady state while reducing the computational effort. We found that in the box model the scaling with the bath size follows the ratio $\nu_P = N_\mathrm{P}/N$. Similar dependencies are also found for more intricate distributions of coupling constants $p(a)$, albeit, to a weaker extend. This makes the reduction of the nuclear spin bath size less efficient.

The even resonance conditions are easily identifiable in experiment and have been reported in many experimental studies. But there are indicators that the precession modes defined by Eq. (7.2.17) are also present in experiment: While the revival amplitude decreases exponentially after the last pulse, the first revival after the last pulse is additionally damped. For the external magnetic field strength, where this behavior in the revival has been reported, the spectrum also features small side peaks next to the frequencies given by Eq. (7.2.16). But while both peak classes are always present in the SCA, it only occurs at select external magnetic field strength in experiment. This correlation between the external magnetic field strength and the ratio of the two resonance conditions cannot be reproduced by the SCA.

Chapter 8

Spin dynamics in a mode-locked system

After an extended period of laser pulses, which can last up to several minutes [33], we assume that the steady state of the system is reached. The non-equilibrium steady state distribution of the Overhauser field is determined by Eqs. (7.2.29) and (7.2.30). However, since the Overhauser field distribution is not directly measurable in experiments, it is difficult to validate the theoretical predictions made in the previous chapter through comparison alone. The nuclear spin distribution becomes accessible by studying the electron spin fluctuations via spin-noise spectroscopy [66, 69–71]. This technique provides a non-perturbative way to detect fluctuations of the polarization plane of the probe pulse by exploiting the Kerr effect, if the beam is reflected, or utilizing the Faraday rotation, if the probe beam is transmitted through the sample.

In experiments the electron spin dynamics is often not measured in between laser pulses but rather in between sequences of pump pulses. We investigate the electron spin dynamics and the time evolution of the Overhauser field distribution after the pump pulses have stopped and the system is under the influence of nuclei-induced frequency focussing. We show how the electron spin-noise spectrum grants insight into the dynamics of the nuclear spin bath. The knowledge about the non-equilibrium steady state of the pulsed system gained in the last chapter is used as a point of reference for the initial condition in this investigation.

The contents of this chapter was presented in Ref. [190].

8.1 Generation of the Overhauser field distribution

The starting point for most simulations presented in this chapter is the steady state Overhauser field distribution described in Sec. 7.2.4. Since the non-equilibrium steady state was not yet reached in the simulations conducted in the previous chapter, the initial conditions have to be generated. For a given classical configuration the Overhauser field $b_{\mathrm{o/e},n}$ has to obey either the resonance condition Eqs. (7.2.16) or (7.2.17), see also Eq. (7.2.29). For the box model the Overhauser field is set in one go as $a\vec{M}_\mu = \left(b_{\mathrm{o/e},n}, b_{\mathrm{N},y}, b_{\mathrm{N},z}\right)^T$ with a the coupling constant for all nuclear spins and the total

nuclear spin $\vec{M} = \sum_k \vec{I}_k$. The components orthogonal to the external magnetic field $b_{\mathrm{N},y}$ and $b_{\mathrm{N},z}$ follow the Gaussian, given in Eq. (7.2.30).

For a given distribution of the hyperfine coupling constants $a_k \sim p(a)$, the following algorithm is used to determine the non-equilibrium steady state Overhauser field distribution: The number of configurations with a certain Overhauser field in x-direction $b_{\mathrm{o/e},n}$ is determined by the spectral weight given by the Gaussian envelope Eq. (7.2.30). For the initial step a random nuclear spin vector $\vec{I}_1$ is drawn from the unit sphere and assigned to a coupling constant $a_1 \sim p(a)$. The first auxiliary Overhauser field is $\vec{b}_{\mathrm{N},1} = a_1\vec{I}_1$. For all subsequent steps $\vec{I}_k$ is again randomly generated. The spin vector is accepted if the deviation from the desired analytical Overhauser field in x-direction decreases and rejected otherwise. The applied condition is

$$\left|b_{\mathrm{N},k-1,x} - b_{\mathrm{o/e},n}\right| > \left|b_{\mathrm{N},k,x} - b_{\mathrm{o/e},n}\right| \tag{8.1.1}$$

with the preliminary Overhauser field up to the k-th nuclear spin $\vec{b}_{\mathrm{N},k} = \sum_{j=1}^{k} a_j\vec{I}_j$ and the target Overhauser field $b_{\mathrm{o/e},n}$ of one configuration in x-direction. The y- and z-components follow a Gaussian due to the central limit theorem if the nuclear spin bath size is large enough.

In theory the algorithm gets more precise, the more nuclear spins are incorporated. However, the rejection rate of $\vec{I}_j$ also grows with an increasing number of nuclear spins and, therefore, the computation time has to be limited by restricting the precision

$$|\Delta b_{\mathrm{N},x}| = \left|\left(\sum_k a_k I_{k,x}\right) - b_{\mathrm{o/e},n}\right| < 10^{-3}. \tag{8.1.2}$$

The analytical result of infinitesimally sharp Overhauser field peaks cannot be reached this way and the Overhauser field distribution as a histogram over all classical configurations features a small but finite peak width. While the deviations from ideal δ peaks can be ascribed to restrictions of the generation method, in experiments perfect frequency focusing is also an overly optimistic assumption due to different nuclear spin relaxation mechanisms or fluctuations in the pumping laser.

If the number of nuclear spins is large enough and the precision of $|\Delta b_{\mathrm{N},x}|$ is reached before all nuclear spins are accepted, then the peak shape is given as a uniform distribution inside the boundaries $\pm|\Delta b_{\mathrm{N},x}|$. But while this case always occurs for $N = 100$, the number of configurations that are allotted to a certain resonance peak varies over the Overhauser field distribution. This noise to the distribution can also affect calculations for which it serves as an initial condition.

If no perfect frequency focusing is assumed – either by not reaching the steady state or an already partially decayed Overhauser field distribution – the peaks in $p_x(b_{\mathrm{N},x})$ are broadened. In this case the distribution is binned around the peaks and rejection sampling is used in each bin.

8.2 Spin dynamics after the pumping

We compare the spin dynamics after $N_{\mathrm{P}} = 20\,000$ with one starting from a generated non-equilibrium steady state. In the first case, we choose the data presented in

Sec. 7.3.13 with the hyperfine coupling constant distribution $p_{r_0}(a)$ with $r_0 = 1.5$ and $\xi = 3$ as the initial $p(\vec{b}_\mathrm{N})$ at $t = 0$. In the second case, we generate a non-equilibrium steady-state Overhauser field distribution as described in Sec. 8.1. Those two Overhauser field distributions differ in their peak width. The peaks after 20 000 pulses are much broader than the peaks in the non-equilibrium steady state. We show that the degree of mode locking is directly linked to the dephasing time of the electron spin. The electron spin dynamics is presented in Sec. 8.2.1 and the change of the Overhauser field distribution in time is investigated in 8.2.2.

8.2.1 Electron spin dynamics immediately after the pumping

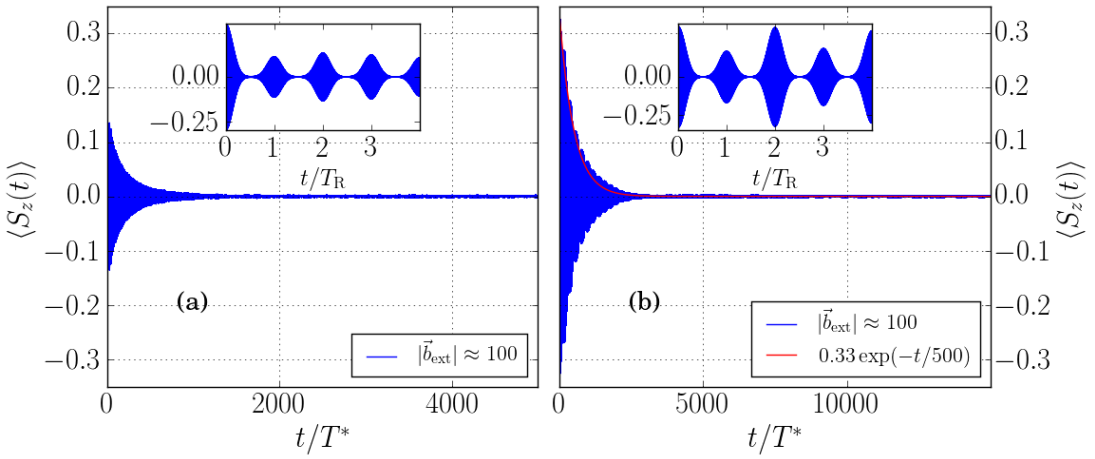

Figure 8.1: Electron spin dynamics immediately after the last pulse at $t = 0$. The inset shows the spin dynamics on the time scale of a few T_R. Panel (a): at $t = 0$ the result from previous simulations for $N_\mathrm{C} = 20\,000$, cf. Fig. 7.26, is used. The a_k distribution is $p_{r_0}(a)$ with $r = 1.5$ and $\xi = 3$. Panel (b): at $t = 0$ the system is in the non-equilibrium steady state and the Overhauser field distribution is given by Eq. (7.2.29).

In Fig. 8.1 (a) we utilize the results from the previous chapter concerning the Overhauser field distribution and the alignment of the electron spin after $N_\mathrm{C} = 20\,000$ pulses, see Sec. 7.3.13. The electron spin precessions occur on a time scale of $10^{-2}T^*$ and, therefore, cannot be resolved in this figure. The electron spin revival in the inset occurs periodically with the previous pump pulse period T_R. On the time scale of $1000T_\mathrm{R} \approx 10\,000T^*$ the long-time decay of the electron spin is shown. After approximately $t/T^* \approx 1500$ its envelope function converges to zero. The time of the decay can be linked to the finite width of the peaks in the Overhauser field distribution $p_x(b_{\mathrm{N},x})$.

To further investigate the correlation between the dephasing time of the revival and the peak width of the Overhauser field, we turn to the assumed non-equilibrium steady state distribution of the Overhauser field. Then the initial distribution $p_x(b_{\mathrm{N},x})$, which features two different peak shapes for the resonance classes defined by Eq. (7.2.16) and (7.2.17), is replaced with a weighted Dirac comb (7.2.29) where both resonance classes contribute equally. This assumption for the Overhauser field distribution in the long-time limit of a pulsed system was substantiated by the scaling argument presented in Sec. 7.3.8 and 7.3.14.

The initial $p(\vec{b}_\mathrm{N})$ for the data presented in Fig. 8.1 (b) is generated by the algorithm

in Sec. 8.1. The parameters of the previous chapter are retained. The magnetic field is applied in resonance with $K = 200$ and the period of the prior pump pulse sequence is $T_\mathrm{R} = 13.5\,T^*$. The nuclear spin bath size is $N = 100$. The inset in Fig. 8.1 (b) shows the electron spin dynamics on a time scale of a few T_R. At every time distance of T_R an electron spin revival is observed. The revivals are a clear indicator for nuclei-induced spin precession frequency focusing. The alternating revival strength can be attributed to the interplay of the even and odd resonance frequencies. In the pulsed sequence, configurations with even frequencies fully align the electron spin along the negative z-direction. Those, which follow the odd resonance condition, lead to $\vec{S}_\mathrm{odd} = \vec{e}_z/6$ for pumping with σ^+ polarized light. The expectation value is a configuration average and features a reduced amplitude for the first revival after the last pulse and an increase of the revival amplitude at the second T_R where the negative spin alignment of both resonance classes boosts the spin amplitude. For every second T_R this dynamics repeats. This alternating behavior of the electron spin dynamics cannot be observed for broader peaks like in Fig. 8.1.

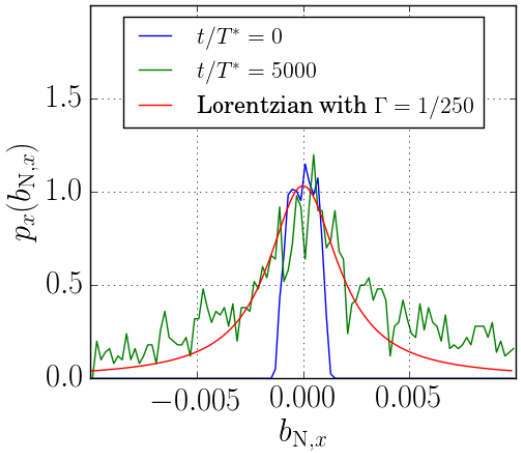

Figure 8.2: Exemplary change of the peak shape from an indicator shaped peak to a Lorentzian peak. The red line adds a Lorentzian curve with width Γ extracted from the decay in Fig. 8.1 (b).

The decay of the electron spin revival proceeds slower than before in Fig. 8.1 due to the narrower peaks of the Overhauser field distribution. In Fig. 8.1 (b) the electron spin is completely decayed after $t/T^* \approx 5000$. This shows that a stronger mode locking, i.e. sharper peaks in $p_x(b_{\mathrm{N},x})$, extends the spin dephasing time in a QD. The shape of the enveloping electron spin decay is to be examined on the basis of the peak at $b_{\mathrm{N},x} = b_{e,0} = 0$. It is depicted in Fig. 8.2. Due to the generation process the shape at $t/T^* = 0$ is rectangular with its width given by the accepted precision of $\pm|\Delta b_{\mathrm{N},x}| \sim 10^{-3}$. The "edges" of this peak are not stable and decay due to interaction with the electron spin. The resulting shape is approximated by a Lorentzian

$$L(x) = \frac{1}{\pi}\frac{\Gamma/2}{(x-x_0)^2 + (\Gamma/2)^2} \tag{8.2.1}$$

with mean $x_0 = b_{o/e,n} = 0$ and a width parameter Γ. A $\Gamma \approx 0.004$ ties in with the exponential decay $\langle S_z(t)\rangle \sim \exp(-t/T_\mathrm{D})$ observed in Fig. 8.1 (b) over a time of $T_\mathrm{D} = 2T^*/\Gamma \approx 500\,T^*$. The limitations of the accuracy of the Overhauser field peak $\pm|\Delta b_{\mathrm{N},x}| \sim 10^{-3}$ translate to the decay time T_D which cannot exceed $1/|\Delta b_{\mathrm{N},x}|$.

If either the shape of the decay or the shape of the Overhauser field peak is known, the other can be derived via Fourier transformation. The exponential decay was added as a red solid line in Fig. 8.1 (b) and matches well with the red Lorentzian in Fig. 8.2. If

the peak shape deviates from the Lorentzian, the envelope of the electron spin beats in the time domain would also adjust. For example, Gaussian peaks result in a Gaussian envelope of the electron spin decay.

8.2.2 Overhauser field distribution after pulsing

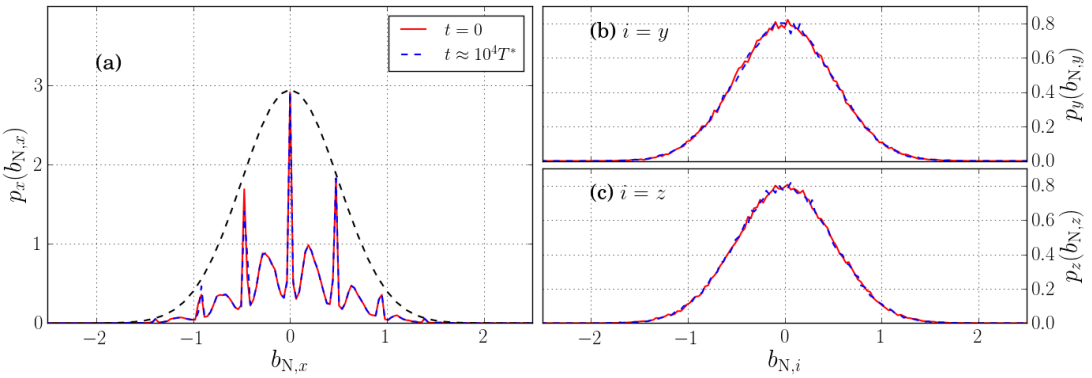

Figure 8.3: The Overhauser field distribution at $t = 0$ and after $t = 2\,000 T_\mathrm{R} \approx 10^4\, T^*$ along the external magnetic field in panel (a) and orthogonal to it in panel (b) and (c). The starting point at $t = 0$ is the data from Sec. 7.3.13 after $N_\mathrm{P} = 20\,000$ also used in Fig. 8.1. No further pulses are applied. The Gaussian envelope is added in black dashed lines in panel (a).

Analogous to the previous section the change of the Overhauser field distribution is investigated for two starting points: $p(\vec{b}_\mathrm{N})$ after a pulse sequence of $N_\mathrm{P} = 20\,000$ pulses and the assumed steady state distribution in Eq. (7.2.29). The Overhauser field distribution and its time evolution, belonging to the electron spin dynamics in Fig. 8.1 (a) after $N_\mathrm{P} = 20\,000$ pulses, are presented in Fig. 8.3. Panel (a) contains $p_x(b_{\mathrm{N},x})$ along the external magnetic field and panel (b) and (c) its orthogonal components. The Gaussian envelope is added in black panel (a). After the time period of an additional $t_\mathrm{fin} = 2\,000\, T_\mathrm{R} \approx 3 \cdot 10^4\, T^*$, the Overhauser field distribution is measured again in all spatial directions. The results are plotted as dashed blue lines.

While the electron spin relaxes to zero on much shorter time scales than t_fin depending on the initial Overhauser field distribution, $p(\vec{b}_\mathrm{N})$ itself changes only marginally and the peak structure is preserved over the period of a few thousand T_R.

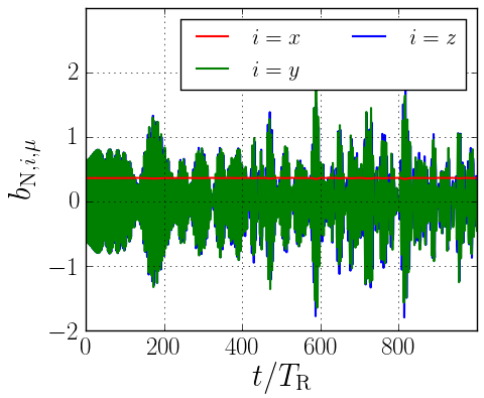

Figure 8.4: Time evolution of all spatial directions of the Overhauser field exemplary for one configuration μ after a pulse sequence with $N_\mathrm{P} = 20\,000$.

To better understand this behavior, an exemplary time dynamics of the Overhauser field in one classical configuration $b_{\mathrm{N},i,\mu}$ over multiple T_R is tracked in Fig. 8.4. $b_{\mathrm{N},i,\mu}$ is recorded in each direction $i = x, y, z$ once in every T_R at $t = nT_\mathrm{R}$. It is noticeable that the Overhauser field value in x-direction is subject to little change while the contributions orthogonal to the external magnetic field fluctuate significantly. The fluctuations of $b_{\mathrm{N},y,\mu}$ and $b_{\mathrm{N},z,\mu}$ have no effect on the Gaussian Overhauser field distribution in y- and z-direction.

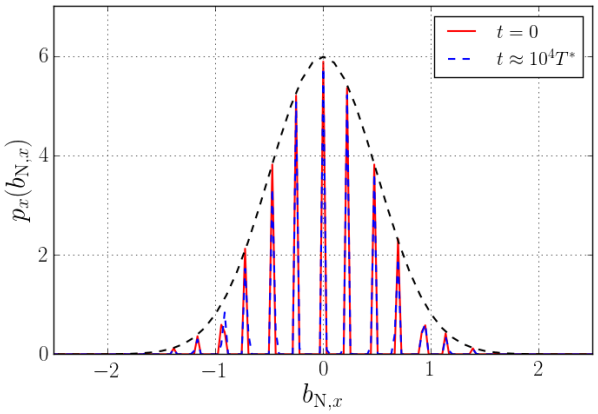

Figure 8.5: Overhauser field distributions in the x-direction starting from the non-equilibrium steady state of the periodically pulsed system given by Eq. (7.2.29) at $t = 0$.

Very similar behavior is observed in Fig. 8.5 where the initial $p_x(b_{\mathrm{N},x})$ is given by the non-equilibrium steady state distribution (7.2.29). A slight loss in peak heights is noticeable over $10^4\, T^*$. This decay is induced by the distribution of the hyperfine coupling constants a_k [54, 55, 127, 130] and is small due to the conservation of the x-component of the total spin

$$\vec{F} = \vec{S} + \sum_k \vec{I}_k \tag{8.2.2}$$

parallel to the external magnetic field. For $N = 100$ the total nuclear spin $\vec{M} = \sum_k \vec{I}_k \propto \sqrt{N}$ is a good approximation for $\vec{F}$ and, therefore,

$$\langle F_x \rangle \approx \langle M_x \rangle = \text{const.} \tag{8.2.3}$$

holds. The influence of electron spin dynamics on the nuclear spins can be neglected on the time scales of t_fin. The conserved $p_{M_x}(M_x)$ corresponding to the Overhauser field in Fig. 8.3 and Fig. 8.5 are shown in Fig. 8.6 in panel (a) and (b). The time evolution of the distribution of the total nuclear spin in the box model is added in panel (c).

For the nuclear spin distribution related to the Overhauser field in Fig. 8.3 after $N_\mathrm{P} = 20\,000$, no nuclear spin polarization is visible in Fig. 8.6 (a). Instead, it shows a still Gaussian nuclear spin distribution. The peaked structure observed in the Overhauser field distribution can be traced back solely to the weighting of the individual nuclear spins with coupling constants $a_k \sim p_{r_0=1.5}(a)$. The total nuclear spin distribution in Fig. 8.6 (b) shows broadened peaks. The collapse of these peaks to a δ-peak is due to hyperfine coupling constant distribution. If equal coupling constants are used, those broadened peaks transition into sharp peaks, as seen in panel (c). The Overhauser field

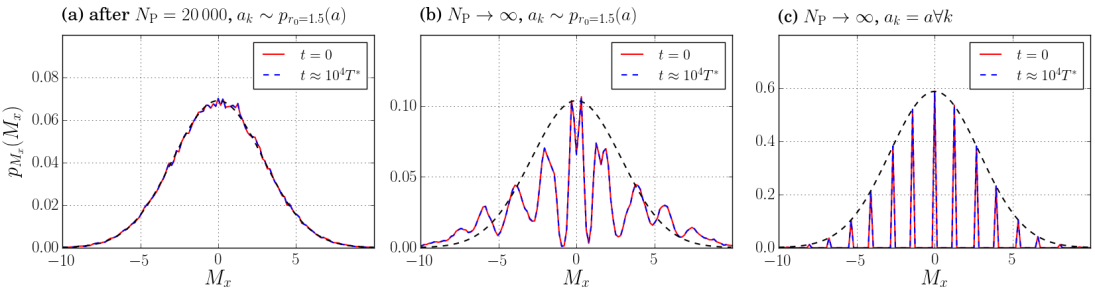

Figure 8.6: Distribution of the total nuclear spin $\vec{M}$ in x-direction for an Overhauser field starting at the non-equilibrium steady state of the pulsed system after $N_P \to \infty$ at $t = 0$ and after $1000\,T_R$ in darkness. In panel (a) the hyperfine coupling constants a_k follow $p_{r_0}(a)$ with $r_0 = 1.5$ and $\xi = 3$. The data from Fig. 8.3 after a pulse sequence with $N_P = 20\,000$ is used. In panel (b) and (c) the distribution in Eq. (7.2.29) is the starting point. In panel (b) the a_k are distributed according to $p_{r_0=1.5}(a)$ with $r_0 = 1.5$ and $\xi = 3$. In panel (c) the box model is used. A rescaled Gaussian with the variance of $N \cdot (|\vec{I}_k|^2/3)$ is added. $I = 1/2$ and the bath size of $N = 100$ are used.

distribution can directly be recovered by rescaling the M_x-axis with $a = \sqrt{3/N}$. All distributions are framed by the envelope given by the Gaussian $\mathcal{N}(0, N \cdot (|\vec{I}_k|^2/3))$ with a nuclear spin length of $I = 1/2$ and a bath size $N = 100$.

It is important to note that while the Overhauser field shows little change on the time scale of the simulation, its long-time decay is facilitated by a finite spread of a_k while the total nuclear spin polarization $\langle M_x \rangle$ is still approximately conserved.

The fact that the Overhauser field distribution remains stable for probably at least a few milliseconds is particularly interesting with respect to experiments. After leaving a mode-locked system several minutes in darkness, Greilich et al. reported an instant re-emergence of the revival when the laser pulses were applied again [33]. This strongly suggests that the information imprinted on the system by the previous laser sequence remains intact in the distribution of the Overhauser field.

8.3 Restarting the pulses

We want to verify the fast re-emergence of the revival in the numerical simulations. After some time in darkness, the Overhauser field distribution is still conserved and described by the distribution given by Eq. (7.2.29). The electron spin is unpolarized. The first π-pulse arrives at $t = 0$. A short pulse sequence of only a few pump pulses shall be reapplied.

The electron spin dynamics is depicted in Fig. 8.7. Starting from $S_z = 0$, the instantaneous π-pulse leads to a half polarization at $t = 0$ which decays on a time scale of T^*. The revival – unlike for those with a Gaussian Overhauser field distribution – is finite after the first pulse. The influence of the electronic revival build-up is evident in the shifted, two-step increment of the amplitude after the pulse and the spin revival. But the increase in each step is larger compared to that of the electronic revival alone cf. Eq. (7.2.27). Therefore, the revival build-up is much faster.

Within about five pulses the maximum revival amplitude is already reached. Electron

dynamics does not change anymore and repeats every T_R. The non-equilibrium steady state of the pulsed system is recovered again. This shows that information about previous pulsing was stored in Overhauser field and can be recovered by the electron spin dynamics.

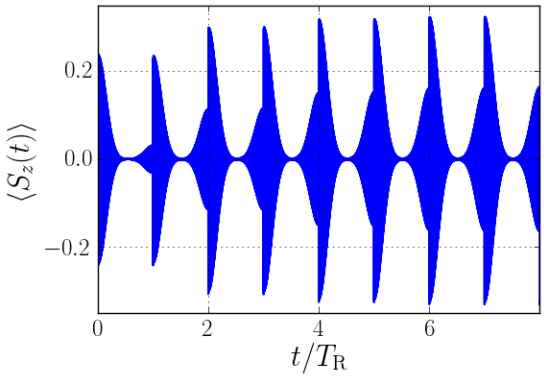

Figure 8.7: Electron spin dynamics in a mode-locked system. The first pulse arrives at $t = 0$ on an unpolarized spin.

8.4 Electron spin noise in a mode-locked system

After pulsing at $t' = 0$, the Overhauser field distribution is given by Eq. (7.2.29) instead of the Gaussian equilibrium distribution. Here, the initial electron spin alignment in each classical configuration is correlated to the value of the Overhauser field in this configuration. The negatively aligned spin vector belonging to the resonance condition (7.2.16) has a greater absolute value than a $\vec{S}_\mu$ related to (7.2.17). This leads to a finite electron spin expectation value of $\langle S_z(t' = 0)\rangle = -1/3$ after the last pulse. Due to this non-equilibrium situation, the second-order spin correlator $\langle S_z(t+t')S_z(t')\rangle$ cannot be reduced to $\langle S_z(t)S_z\rangle$. Then, the spin-noise spectrum, which still depends on the absolute time t', reads

$$C_{2,t'}(\omega) = \int_{-\infty}^{\infty} \mathrm{e}^{-\mathrm{i}\omega t}\langle S_z(t+t')S_z(t')\rangle \mathrm{d}t. \tag{8.4.1}$$

We have proven in previous sections that the time scales of the electron spin dynamics and the Overhauser field dynamics differ by several orders of magnitude in time. The electron spin dephases on the time scale T_D related to the finite width of Overhauser field peaks while the time scale of the nuclear spin relaxation $T_{1,\mathrm{N}}$ exceeds T_D. The inequality

$$T_\mathrm{D} \ll t' \ll T_{1,\mathrm{N}} \tag{8.4.2}$$

is assumed where $T_{1,\mathrm{N}}$ can last up to tens of minutes [191, 192]. Therefore, correlations between the Overhauser field value in x-direction and the electron spin vector can be neglected for $t' \gg T_\mathrm{D}$. The electron spin is approximately dephased after $t = 4000\,T^*$ after the pump train, cf. Fig. 8.1. After $t' > 1000T_\mathrm{R} \approx 10\,000T^*$, we consider the system in a quasi-steady state for a given t'. The correlation function $\langle S_z(t+t')S_z(t')\rangle$ and the spin-noise spectrum $C_{2,t'}(\omega)$ are independent of the time t'.

The electron spin dynamics of the correlator as a function of the time t is also solved by the coupled equations of motion used for the expectation value Eq. (5.2.27a) and Eq. (5.2.27b). The trion decay plays no role anymore at $t' \gg T_\mathrm{D}$ and $P_\mathrm{T} = 0$ holds. The initial Overhauser field distribution is given by (7.2.29) and the electron spin correlation function is $\langle S_i(t')S_i(t')\rangle = 1/4$ for all spatial directions $i = x, y, z$. All cross-correlations vanish $\langle S_y(t')S_z(t')\rangle = \langle S_x(t')S_z(t')\rangle = 0$.

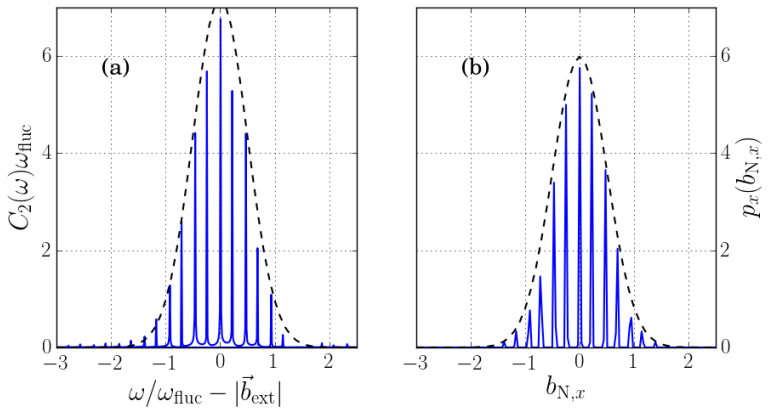

Figure 8.8: (a) Spin-noise spectrum calculated from $\langle S_z(t+t')S_z(t')\rangle$ for a starting point of $t' = 1000T_\mathrm{R} \approx 10\,000T^*$. The initial $\langle\vec{S}\rangle$ is unpolarized. (b) The Overhauser field distribution is taken from Fig. 8.5 at $t' \approx 10\,000T^*$.

In Fig. 8.8 the spin-noise spectrum in panel (a) is compared to the Overhauser field distribution in panel (b). Like the non-equilibrium Overhauser field distribution, the spin-noise spectrum $C_{2,t'}(\omega)$ also features peaks inside a Gaussian envelope of the same variance. Its mean value is shifted by the Larmor frequency $|\vec{b}_\mathrm{ext}|/T^*$. The electron spin precession frequencies meet the resonance conditions Eqs. (7.2.16) or (7.2.17). While $p_x(b_{\mathrm{N},x})$ is normed to unity, the integral of the spin-noise spectrum over ω is $\pi/2$ cf. (4.2.6). This explains the difference in peak heights.

Both, the slow-time evolution of Overhauser field and the near independence of the electron spin dynamics from t', indicate a very slow nuclear spin relaxation which also makes the assumption of a static nuclear field in spin-noise investigations viable cf. Ref. [76]. This premise is also applied in Ref. [193, 194] to discuss electron spin noise under the effect of dynamical nuclear polarization. In the FOA the Overhauser field can be directly derived from the central spin dynamics via

$$C_{2,t'}(\omega) \propto p_x\left(\omega - b_{\mathrm{ext},x}/T^*\right). \tag{8.4.3}$$

As Fig. 8.8 shows this relation also applies for a mode-locked system and information about the nuclear spins can be accessed via the spin-noise spectrum. Small discrepancies between the shape of the distributions in panel (a) and (b) can be attributed to neglecting the nuclear spin dynamics as well as numerical noise due to a finite measurement time.

8.5 Phenomenological relaxation of the Overhauser field

While the Overhauser field decay is not observable on the time scales of the simulation, in a real system several processes contribute to a slow relaxation of the Overhauser field distribution. Since interactions like the dipole-dipole interaction between nuclear spins on a time scale of 100 µs [55, 122] or quadrupolar splittings [33, 195, 196] are not included explicitly in the model (3.1.13), we employ a phenomenological approach introduced in Ref. [190]. The relaxation of the nuclear spin distribution is derived analytically via a kinetic differential equation. For reasons of simplicity we use a box model to translate p_{M_x} into the Overhauser field distribution. The electron spin-noise spectrum is obtained via Fourier transform from the result of the semiclassical equations of motion (5.2.27) and satisfies Eq. (8.4.3).

A basic assumption of the phenomenological approach is that the longitudinal nuclear spin relaxation time $T_{1,\mathrm{N}}$ is much larger than the time scales associated with the electron spin dynamics. Therefore, the Overhauser field distribution is constant for t while the correlation function $\langle S_z(t'+t)S_z(t')\rangle$ is calculated via Eq. (5.2.27). For $t' \gg T_\mathrm{D}$ the electron spin is long decayed and assumed unpolarized at a time interval starting at t', cf. Fig. 8.1 (b). $t'=0$ marks the time when the pulsing ends.

The underlying mechanism for the time evolution of a nuclear spin distribution are spin-flips. Starting from the total nuclear spin in x-direction M_x, a spin-flip either increases or decreases M_x over the time t'. All processes with $|\Delta M_x| > 1$ are neglected here since they do not qualitatively affect the outcome. Albeit, it is possible that the dipole-dipole interaction leads to a $\Delta M_x = \pm 2$. The rate equation for the time-dependent nuclear spin distribution $p_{M_x}(M_x;t')$ is

$$\begin{aligned}\frac{\mathrm{d}p_{M_x}(M_x;t')}{\mathrm{d}t'} &= W_\downarrow(M_x+1)p_{M_x}(M_x+1;t') \\ &+ W_\uparrow(M_x-1)p_{M_x}(M_x-1;t') \\ &- \left[W_\downarrow(M_x)+W_\uparrow(M_x)\right]p_{M_x}(M_x;t').\end{aligned} \tag{8.5.1}$$

$W_\uparrow T^*$ is the probability that a nuclear spin-flip increases the total nuclear spin M_x by 1 in T^* and $W_\downarrow T^*$ is the probability for receiving a total nuclear spin of $M_x - 1$. The rate $W_\downarrow(M_x)$ is given by the W_1, the rate of single spin-flips, and the number of spins in the spin-up state

$$\binom{1}{N/2+M_x} = N/2 + M_x. \tag{8.5.2}$$

The rates for both possible spin-flips can be rewritten as

$$W_\uparrow(M_x) = W_1(N/2 - M_x), \tag{8.5.3a}$$
$$W_\downarrow(M_x) = W_1(N/2 + M_x). \tag{8.5.3b}$$

This leads to the equation

$$\begin{aligned}\frac{\mathrm{d}p_{M_x}(M_x;t')}{\mathrm{d}t'} = \frac{W_1}{2}\big\{ & N\left[p_{M_x}(M_x+1;t') + p_{M_x}(M_x-1;t') - 2p_{M_x}(M_x;t')\right] \\ & + 2\left[p_{M_x}(M_x+1;t') + p_{M_x}(M_x-1;t')\right] \\ & + 2M_x\left[p_{M_x}(M_x+1;t') - p_{M_x}(M_x-1;t')\right]\big\}.\end{aligned} \tag{8.5.4}$$

Since $1 \ll |M_x| \ll N$ holds for realistic systems the discrete M_x is replaced by a continuous variable. The change of M_x by a small step of 1 leads to first and second derivations of $p_{M_x}(M_x)$ defined by difference quotients:

$$\lim_{1\ll|M_x|} \left[p_{M_x}(M_x+1;t') + p_{M_x}(M_x-1;t') - 2p_{M_x}(M_x;t')\right] = \frac{\partial^2 p_{M_x}(M_x;t')}{\partial M_x^2} \quad (8.5.5a)$$

$$\lim_{1\ll|M_x|} \left[p_{M_x}(M_x+1;t') + p_{M_x}(M_x-1;t')\right] = 2p_{M_x}(M_x;t') \quad (8.5.5b)$$

$$\lim_{1\ll|M_x|} \left[p_{M_x}(M_x+1;t') - p_{M_x}(M_x-1;t')\right] = 2\frac{\partial p_{M_x}(M_x;t')}{\partial M_x}. \quad (8.5.5c)$$

The rate equation (8.5.1) transitions into the differential equation

$$\frac{\partial p_{M_x}(M_x;t')}{\partial t'} = \frac{1}{T_{1,\mathrm{N}}}\frac{\partial}{\partial M_x}\left[M_x p_{M_x}(M_x;t') + \frac{M^2}{3}\frac{\partial}{\partial M_x}p_{M_x}(M_x;t')\right] \quad (8.5.6)$$

with the square of the total spin of the nuclei $M^2 = |\vec{I}_k^2|N$. The longitudinal relaxation time $T_{1,\mathrm{N}} = 1/(2W_1)$ governs the relaxation of the mean nuclear spin $\overline{M}_x(t') = \int M_x p_{M_x}(M_x;t')\mathrm{d}M_x$ which follows an exponential decay

$$\frac{\partial \overline{M}_x}{\partial t'} = -\frac{\overline{M}_x(t')}{T_{1N}}. \quad (8.5.7)$$

As a side condition the nuclear spin distribution is also normalized

$$\int p_{M_x}(M_x)\mathrm{d}M_x = 1 \quad (8.5.8)$$

at any time. The non-equilibrium steady state solution of Eq. (8.5.6) converges to the Gaussian distribution function of an unpolarized nuclear spin bath

$$p_{M_x}(M_x) = \frac{1}{2}\sqrt{\frac{6}{\pi M^2}}\exp\left(-\frac{3M_x^2}{2M^2}\right) \quad (8.5.9)$$

for long times. Its variance is independent of t'

$$\int p_{M_x}(M_x)M_x^2\mathrm{d}M_x = M^2/3. \quad (8.5.10)$$

The non-changing Gaussian envelope is added as a dashed line in Fig. 8.6 panel (c) which contains the nuclear spin distribution for $t' = 0$ for the box model.

We want to investigate the time dependency of the Overhauser field distribution analytically depending on $t'/T_{1,\mathrm{N}}$ as well as the corresponding electron spin noise. In the box model the time evolution of the Overhauser field is directly derived from the time evolution of the nuclear spin distribution by multiplying a constant prefactor a. The Overhauser field distribution immediately after a long pulse train is given by Eq. (7.2.29). At $t' = 0$ the peaks are broadened and approximated by a Gaussian distribution with the variance $\sigma_{\mathrm{P}}^2 = 10^{-4}$

$$\delta(x) \to \frac{1}{\sqrt{2\pi\sigma_{\mathrm{P}}^2}}\exp\left(-\frac{x^2}{2\sigma_{\mathrm{P}}^2}\right). \quad (8.5.11)$$

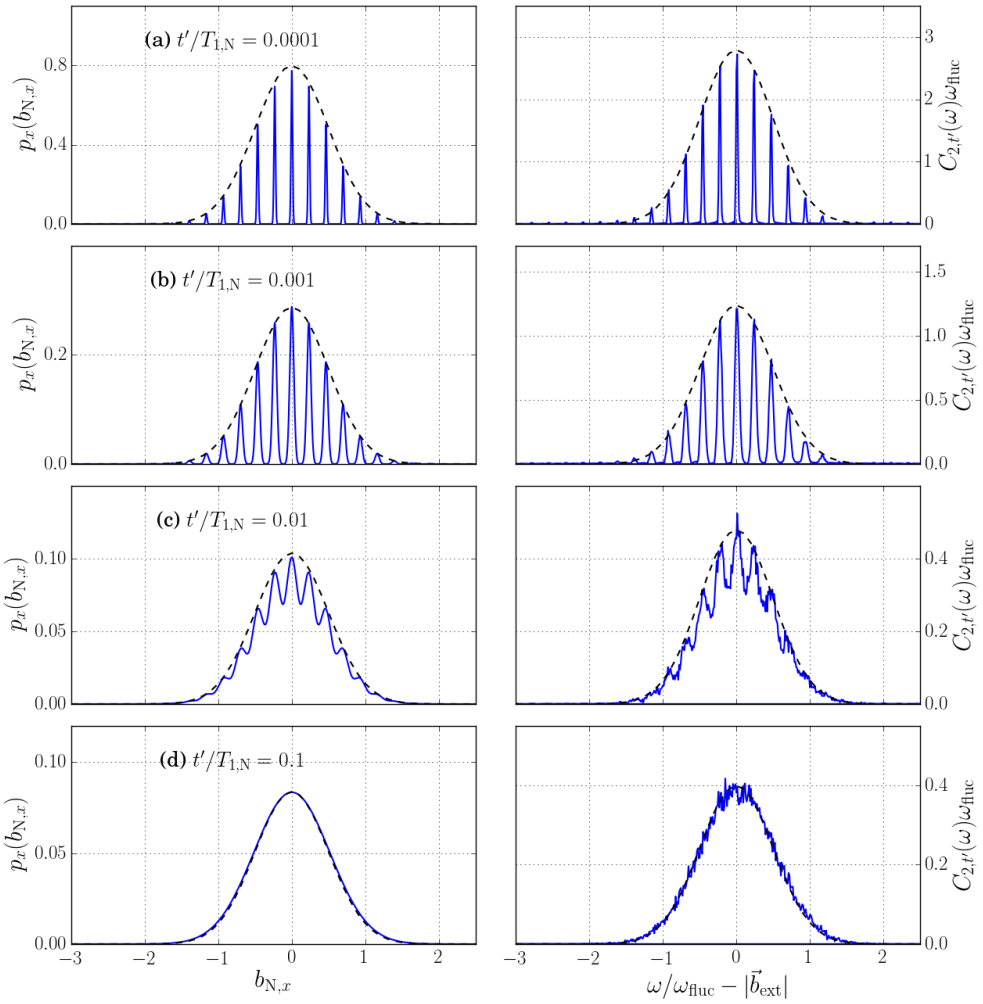

Figure 8.9: The Overhauser field distribution along the external magnetic field for different times $t'/T_{1,\mathrm{N}}$ depending on the nuclear spin relaxation time $T_{1,\mathrm{N}}$ in the left panels. The $p_x(b_{\mathrm{N},x})$ are a result of the phenomenological equation (8.5.6). On the right side the corresponding electron spin-noise spectra shifted by the frequency of the external magnetic field are sbown.

The positions of the peaks are chosen to be multiples of π/T_{R} in agreement with the large magnetic field limit of Eq. (7.2.17).

The ansatz to solve the differential equation (8.5.6) analytically consists of applying a Fourier transformation to both the time t' and the nuclear spin variable M_x. This reduces Eq. (8.5.6) to a differential equation of first order which can be solved by using separation of variables. The solution is dependent on the ratio $t'/T_{1,\mathrm{N}}$. The relaxation of the Overhauser field distribution is calculated for $t'/T_{1,\mathrm{N}} = 10^{-4}$, 10^{-3}, 10^{-2} and 10^{-1}. $p_x(b_{\mathrm{N},x})$ is shown on the left side in Fig. 8.9. On the right-hand side the corresponding spin-noise spectrum is presented. For each time $t'/T_{1,\mathrm{N}}$ a set of classical configurations following the Overhauser field distribution is generated. Then the electron spin dynamics in the time domain $\langle S_z(t'+t)S_z(t')\rangle$ is determined using the full numerical simulations of (5.2.27). The Fourier transformation over the duration of multiple T_{R} is $C_{2,t'}(\omega)$.

The nuclear spin distribution and the derived Overhauser field distribution in the box

model show a relaxation to the Gaussian distribution of an unpolarized bath in Fig. 8.9 (d). The almost sharp peaked structure at $t'/T_{1,\mathrm{N}} = 0.0001$ in panel (a) broadens at first to still distinct peaks at $t'/T_{1,\mathrm{N}} = 0.001$ in panel (b) and then to overlapping peaks in Fig. 8.9 (c).

The electron spin-noise spectrum on the right-hand side of Fig. 8.9 is shifted by the Larmor precession frequency given by $|\vec{b}_{\mathrm{ext}}|$. The shifted $C_{2,t'}(\omega)$ follow their Overhauser field distributions counterpart apart from normalization. It shows clearly that $C_2(\omega)$ reveals the nuclear spin dynamics and can be used to determine the time constant of the nuclear spin relaxation $T_{1,\mathrm{N}}$ through comparison with experimental data.

8.6 Chapter conclusion

This chapter is dedicated to the spin dynamics in a QD that is subjected to an extended pump pulse protocol. Since only the electron dynamics is experimentally accessible, attention was especially directed at the electron spin-noise spectrum. We demonstrated that electron spin noise provides a tool to derive the Overhauser field distribution under the conditions of the nuclei-induced frequency focusing effect.

The non-equilibrium steady state discussed in Chap. 7 served as a starting point for the simulation. Two hyperfine coupling constant distributions were used in the numerical simulations, equal coupling constants and $a_k \sim p_{r_0}(a)$ with $\xi = 3$ and $r_0 = 1.5$. Independent of $p(a)$, the Overhauser field distribution is given by a set of δ-peaks at the resonance conditions weighted by a Gaussian while the distribution of the total nuclear spin features broadened peaks for a spread in a_k. We showed that the electron spin dephasing is directly linked to the shape and width of the peaks in the Overhauser field distribution $p_x(b_{\mathrm{N},x})$. The total nuclear spin distribution is stable due to angular momentum component conservation in the electron-nuclear spin system. The hyperfine coupling constant distribution facilitates a slow decay of the Overhauser field distribution. The relaxation to the equilibrium Gaussian cannot be reproduced in this simulation due to the long-time scale. The theoretical result of a very long relaxation time goes well with experimental observations that the system quickly retains its frequency focused electron spin dynamics even after several minutes in darkness.

In experiments the pump pulse sequence is interrupted at different times and the spin noise is measured. The electron spin noise follows the Overhauser field distribution closely. This protocol can also be used to gauge the progress of the focusing process since the electron spin signal decays on a time scale that is given by the width of the δ-peaks.

Since a numerical simulation of the Overhauser field distribution decaying to the equilibrium Gaussian in the long-time limit is not feasible in the current approach, we resorted to a kinetic equation. The derivation of the phenomenological Overhauser field decay includes all spin-flips of $\Delta M = \pm 1$ independent of origin. The slow nuclear spin relaxation which is the result of this differential equation can also be recovered in the electron spin fluctuations. The relaxation process is governed by the nuclear spin relaxation time $T_{1,\mathrm{N}}$ which can be acquired through comparison with experiments. Since a large magnetic field suppresses spin-flips, the time scale $T_{1,\mathrm{N}}$, which is inverse to the rate of flipping single spins, is increased under those conditions. Possible contributing

interactions to the long-time relaxation of the Overhauser field distribution next to the hyperfine interaction are the quadrupolar interaction or the dipole-dipole interaction.

Chapter 9

Conclusion

The spin dynamics in a singly charged semiconductor QD occupies center stage in this thesis. Hereby, special focus lies on the understanding of pump-probe experiments. We devised a semiclassical description of the periodically pulsed QD which also includes the trion decay. The electron spin decoherence can partially be suppressed due to the realignment of the nuclear spins in the direction of the external magnetic field. We derived two mode-locking resonance conditions. It is possible to extract the non-equilibrium steady-state Overhauser field distribution from the electron spin-noise spectrum under the conditions of the nuclei-induced frequency focusing effect. Indicators for additional precession modes defined by the second, trion decay-dependent resonance condition have been found in recent experiments [63, 89].
We showed that higher-order spin-noise spectroscopy can provide an alternative to pump-probe measurements when investigating the spin dynamics in a singly charged semiconductor QD. This is made possible because they make higher-order correlation functions accessible. The fourth-order spin-noise correlation function reveals the influence of the nuclear-electric quadrupolar interaction in a QD even in the presence of a large magnetic field. Therefore, it provides additional information compared to second-order noise and second-order correlation functions.

To pave the way for the numerical simulations, we first presented the central spin model [37] to account for the hyperfine interaction between the electron spin and the nuclear spins as well as the nuclear and electron Zeeman interaction. The model was extended upon to include the nuclear-electric quadrupolar interaction. We discussed different choices of the distribution function [49] based on the shape of the QD. The definition of the correlation functions is another prerequisite for the simulations. We defined the second- and fourth-order correlation functions and the corresponding spin noise.

A semiclassical approach was chosen as the method for all simulations. While the Hilbert space dimension grows exponentially with the nuclear spin bath size, the computational effort in a SCA increases linearly with N at most. Therefore, the SCA combines the advantages of large nuclear spin baths sizes with access to long time scales. We derived a set of classical Euler-Lagrange differential equations of motion via the path integral formalism and saddle-point approximation [54]. A configuration average over all classical configurations replaces the quantum mechanical trace. Benchmark results of the second-order correlation function against quantum mechanical approaches showed that

the SCA is an appropriate tool to tackle the spin dynamics in a QD. We also used the second-order correlation function to connect the quadrupolar interaction strength used in the SCA to the parameters of the quantum mechanical calculation.

The cumulant $S_4(\omega_1, \omega_2)$ consists of two components: the fourth-order correlation function $C_4(\omega_1, \omega_2)$ and the squared second-order spin noise $C_2(\omega_1)C_2(\omega_2)$. $C_4(\omega_1, \omega_2)$ only contributes to the diagonal $\omega_1 = \omega_2$ in the CSM without quadrupolar interaction. It adds positively to the bispectrum. The anti-correlations are a result of the two-dimensional Gaussian of $C_2(\omega_1)C_2(\omega_2)$. If only hyperfine interaction and Zeeman interaction contribute, then the quantum mechanical and the classical bispectrum agree well for either the limit of large nuclear spin bath sizes N or large spin lengths I. In both cases the discrete eigenvalue spectrum approaches a continuous distribution. Including the quadrupolar interaction leads to a broadening of the C_4-spectrum orthogonal to $\omega_1 = \omega_2$. The width of this broadening is proportional to the quadrupolar coupling strength Q_r. The antidiagonal cut ($\omega_1 + \omega_2 = \text{const.}$) through the bispectrum reveals the transition from a Gaussian to a shape, which decreases exponentially on both sides of the diagonal. We found that the shape of the bispectrum is linked to the ratio of the effective field of the nuclear Zeeman interaction to that of the quadrupolar interaction on an individual nuclear spin. Due to the smaller nuclear spin bath in the quantum mechanical approach, the quantitative agreement derived for $C_2(t)$ does not translate to the bispectrum with $Q_\mathrm{r} \neq 0$. The qualitative agreement between the SCA and the quantum mechanical approach, however, holds. In experiment, the shape of the bispectrum can be used to extract the average quadrupolar interaction strength of a sample.

We introduced a semiclassical description of the spin dynamics in a QD under a periodic laser pulse train. The equations of motion were extended to include the trion decay. Under the assumption of a frozen Overhauser field, two classes of resonance conditions for the non-equilibrium steady state were derived: $\omega_\mathrm{L} T_\mathrm{R} = 2\pi n$ and $\omega_\mathrm{L} T_\mathrm{R} = 2\pi n + 2\arctan(\omega_\mathrm{L}/\overline{\gamma})$. The first condition corresponds to an integer number of precessions in the pulse repetition time. The second resonance condition results in an additional phase shift depending on the trion decay rate and the external magnetic field. Assuming the limit of large external magnetic fields, we analytically linked the Overhauser field distribution to the electron spin revival amplitude in a simple toy model. Employing a full semiclassical simulation, we demonstrated that the electron spin revival observed in experiments is associated with mode-locking effects. The revival of the electron spin on the time scale of only a small number of pulses ($N_\mathrm{P} < 10$) can be solely attributed to the synchronizing effect of the laser pulses on the electron spin dynamics. Nuclei-induced frequency focusing, which occurs on a much longer time scale, increases the electron spin revival further and leads to the build-up of a non-equilibrium Overhauser field distribution. While the envelope of this distribution remains Gaussian, two classes of peaks emerge from the initial distribution. The peak positions in our simulations correspond to the two classes of the derived resonance conditions.

We showed that the electron spin-noise spectrum provides a way to access the underlying Overhauser field distribution under the condition of nuclei-induced frequency focusing. Starting from the non-equilibrium Overhauser field distribution of a periodically pulsed QD, the decay of the electron spin revival after the end of pulsing was investigated. We linked the time and envelope of the decay to the shape and width of the peaks in the Overhauser field distribution. The Overhauser field distribution is stable even

after the electron spin is long decayed due to the conservation of angular moment components. The Overhauser field distribution can be accessed via the electron spin-noise spectrum. The long relaxation time of the nuclear spins $T_{1,\mathrm{N}}$ can be exploited to recover the information about the electron spin dynamics imprinted on the Overhauser field distribution even after minutes in darkness. However, the duration of $T_{1,\mathrm{N}}$ prevents the investigation of the long-time limit of the Overhauser field relaxation within our theoretical approach. Since the numerical simulation is too computationally expensive, we resorted to a kinetic equation which phenomenologically includes all mechanisms that lead to a single spin-flip. The Overhauser field relaxes from the peaked distribution function to the Gaussian of an unpolarized nuclear spin bath. The relaxation process is also traced in the electron spin noise. Its time scale $T_{1,\mathrm{N}}$ can be determined e. g. through comparison with a spin-noise spectroscopy measurement.

We gained interesting new insights about the spin dynamics in a singly charged semiconductor QD. Those results pave the way for further investigations. The first step to expand upon the current model is through a more detailed description of the quadrupolar interaction. This mainly concerns the choice of a non-zero asymmetry parameter η_{Q} and of a more realistic distribution of the q_k based on the strain tensor [197]. A more detailed modeling of the strain in a QD can be desirable, especially if long-time effects like the mode-locking effects in pump-probe experiments are investigated. The next step could be the inclusion of the dipole-dipole interaction. Both induce an additional spin dephasing and we assume that taking them into account leads to a more realistic representation of the spin dynamics in a periodically pulsed system. Another area in which the SCA has already proven its usefulness is the simulation of the interaction between the QDs. While a good phenomenological description has been found in Ref. [182], the microscopic origin of this interaction is still unknown.

Bibliography

[1] C. H. Bennett. Logical reversibility of computation. *IBM Journal of Research and Development*, 17(6):525–532, 1973.

[2] Y. I. Manin. Classical computing, quantum computing, and Shor's factoring algorithm. In *Séminaire bourbaki : volume 1998/99, exposés 850-864*, number 266 in Astérisque, pages 375–404. Société mathématique de France, 2000. talk:862.

[3] S. Wiesner. Conjugate coding. *SIGACT News*, 15(1):78–88, 1983.

[4] T. D. Ladd, F. Jelezko, R. Laflamme, Y. Nakamura, C. Monroe, and J. L. O'Brien. Quantum computers. *Nature*, 464:45 – 53, 2010. Review Article.

[5] S. Lloyd. Ultimate physical limits to computation. *Nature*, 406(6799):1047–1054, 2000.

[6] C. H. Bennett and D. P. DiVincenzo. Quantum information and computation. *Nature*, 404:247 – 255, 2000. Review Article.

[7] I. Žutić, J. Fabian, and S. Das Sarma. Spintronics: Fundamentals and applications. *Rev. Mod. Phys.*, 76:323–410, 2004.

[8] A. Gaita-Ariño, F. Luis, S. Hill, and E. Coronado. Molecular spins for quantum computation. *Nature Chemistry*, 11(4):301–309, 2019.

[9] J. M. Zadrozny, J. Niklas, O. G. Poluektov, and D. E. Freedman. Multiple quantum coherences from hyperfine transitions in a vanadium(iv) complex. *Journal of the American Chemical Society*, 136(45):15841–15844, 2014.

[10] V. Havlícek, A. D. Córcoles, K. Temme, A. W. Harrow, A. Kandala, J. M. Chow, and J. M. Gambetta. Supervised learning with quantum-enhanced feature spaces. *Nature*, 567(7747):209–212, 2019.

[11] J. Biamonte, P. Wittek, N. Pancotti, P. Rebentrost, N. Wiebe, and S. Lloyd. Quantum machine learning. *Nature*, 549:195 – 202, 2017.

[12] S. Bravyi, D. Gosset, and R. König. Quantum advantage with shallow circuits. *Science*, 362(6412):308–311, 2018.

[13] P. Shor. Polynomial-time algorithms for prime factorization and discrete logarithms on a quantum computer. *SIAM Journal on Computing*, 26(5):1484–1509, 1997.

[14] L. M. K. Vandersypen, M. Steffen, G. Breyta, C. S. Yannoni, M. H. Sherwood, and I. L. Chuang. Experimental realization of Shor's quantum factoring algorithm using nuclear magnetic resonance. *Nature*, 414(6866):883–887, 2001.

[15] L. K. Grover. A fast quantum mechanical algorithm for database search. In *Annual ACM symposium on theory of computing*, pages 212–219. ACM, 1996.

[16] L. K. Grover. Quantum mechanics helps in searching for a needle in a haystack. *Phys. Rev. Lett.*, 79:325–328, 1997.

[17] R. P. Feynman. Simulating physics with computers. *International Journal of Theoretical Physics*, 21(6):467–488, 1982.

[18] Ju. I. Manin. *Vychislimoe i nevychislimoe*. "Sovet. Radio", Moscow, 1980. Kibernetika. [Cybernetics].

[19] D. P. DiVincenzo. The physical implementation of quantum computation. *Fortschritte der Physik*, 48(9-11):771–783, 2000.

[20] D. Loss and D. P. DiVincenzo. Quantum computation with quantum dots. *Phys. Rev. A*, 57:120–126, 1998.

[21] E. Knill, R. Laflamme, and G. J. Milburn. A scheme for efficient quantum computation with linear optics. *Nature*, 409(6816):46–52, 2001.

[22] S. L. Braunstein and P. van Loock. Quantum information with continuous variables. *Rev. Mod. Phys.*, 77:513–577, 2005.

[23] X.-L. Wang, Y.-H. Luo, H.-L. Huang, M.-C. Chen, Z.-E. Su, C. Liu, C. Chen, W. Li, Y.-Q. Fang, X. Jiang, J. Zhang, L. Li, N.-L. Liu, C.-Y. Lu, and J.-W. Pan. 18-qubit entanglement with six photons' three degrees of freedom. *Phys. Rev. Lett.*, 120:260502, 2018.

[24] T. C. Ralph, A. Gilchrist, G. J. Milburn, W. J. Munro, and S. Glancy. Quantum computation with optical coherent states. *Phys. Rev. A*, 68:042319, 2003.

[25] Y. Nakamura, Yu. A. Pashkin, and J. S. Tsai. Coherent control of macroscopic quantum states in a single-Cooper-pair box. *Nature*, 398(6730):786–788, 1999.

[26] J. M. Martinis, S. Nam, J. Aumentado, and C. Urbina. Rabi oscillations in a large Josephson-junction qubit. *Phys. Rev. Lett.*, 89:117901, 2002.

[27] D. Vion, A. Aassime, A. Cottet, P. Joyez, H. Pothier, C. Urbina, D. Esteve, and M. H. Devoret. Manipulating the quantum state of an electrical circuit. *Science*, 296(5569):886–889, 2002.

[28] M. Ansmann, H. Wang, R. C. Bialczak, M. Hofheinz, E. Lucero, M. Neeley, A. D. O'Connell, D. Sank, M. Weides, J. Wenner, A. N. Cleland, and J. M. Martinis. Violation of Bell's inequality in Josephson phase qubits. *Nature*, 461:504 – 506, 2009.

[29] D. J. Wineland, C. Monroe, W. M. Itano, D. Leibfried, B. E. King, and D. M. Meekhof. Experimental issues in coherent quantum-state manipulation of trapped atomic ions. *Journal of research of the National Institute of Standards and Technology*, 103(3):259–328, 1998.

[30] R. Blatt and D. Wineland. Entangled states of trapped atomic ions. *Nature*, 453:1008 – 1015, 2008.

[31] J. P. Home, D. Hanneke, J. D. Jost, J. M. Amini, D. Leibfried, and D. J. Wineland. Complete methods set for scalable ion trap quantum information processing. *Science*, 325(5945):1227–1230, 2009.

[32] R. Hanson, L. P. Kouwenhoven, J. R. Petta, S. Tarucha, and L. M. K. Vandersypen. Spins in few-electron quantum dots. *Rev. Mod. Phys.*, 79:1217–1265, 2007.

[33] A. Greilich, A. Shabaev, D. R. Yakovlev, Al. L. Efros, I. A. Yugova, D. Reuter, A. D. Wieck, and M. Bayer. Nuclei-induced frequency focusing of electron spin coherence. *Science*, 317:1896, 2007.

[34] A. Greilich, M. Wiemann, F. G. G. Hernandez, D. R. Yakovlev, I. A. Yugova, M. Bayer, A. Shabaev, Al. L. Efros, D. Reuter, and A. D. Wieck. Robust manipulation of electron spin coherence in an ensemble of singly charged quantum dots. *Phys. Rev. B*, 75:233301, 2007.

[35] A. Greilich, R. Oulton, E. A. Zhukov, I. A. Yugova, D. R. Yakovlev, M. Bayer, A. Shabaev, Al. L. Efros, I. A. Merkulov, V. Stavarache, D. Reuter, and A. Wieck. Optical control of spin coherence in singly charged (In,Ga)As/GaAs quantum dots. *Phys. Rev. Lett.*, 96:227401, 2006.

[36] M. Bayer. All for one and one for all. *Science*, 364(6435):30–31, 2019.

[37] M. Gaudin. Diagonalisation d'une classe d'hamiltoniens de spin. *J. Physique*, 37:1087, 1976.

[38] M. Bortz and J. Stolze. Exact dynamics in the inhomogeneous central-spin model. *Phys. Rev. B*, 76:014304, 2007.

[39] M. Bortz and J. Stolze. Spin and entanglement dynamics in the central-spin model with homogeneous couplings. *Journal of Statistical Mechanics: Theory and Experiment*, 2007(06):P06018, 2007.

[40] M. Bortz, S. Eggert, C. Schneider, R. Stübner, and J. Stolze. Dynamics and decoherence in the central spin model using exact methods. *Phys. Rev. B*, 82:161308, 2010.

[41] A. Faribault and D. Schuricht. Spin decoherence due to a randomly fluctuating spin bath. *Phys. Rev. B*, 88:085323, 2013.

[42] A. Faribault and D. Schuricht. Integrability-based analysis of the hyperfine-interaction-induced decoherence in quantum dots. *Phys. Rev. Lett.*, 110:040405, 2013.

[43] S. Ryabchenko and Y. Semenov. Localized electron states determined by spin correlations in a paramagnetic semiconductor. *Soviet Physics, Solid State (English translation of Fizika Tverdogo Tela), 26(11), 2011-2015 (1984)*, 26:2011–2015, 1984.

[44] O. Krebs, B. Eble, A. Lemaître, P. Voisin, B. Urbaszek, T. Amand, and X. Marie. Hyperfine interaction in InAs/GaAs self-assembled quantum dots: dynamical nuc-

lear polarization versus spin relaxation. *Comptes Rendus Physique*, 9(8):874–884, 2008.

[45] G. G. Kozlov. Exactly solvable spin dynamics of an electron coupled to a large number of nuclei; the electron-nuclear spin echo in a quantum dot. *Journal of Experimental and Theoretical Physics*, 105(4):803–815, 2007.

[46] G. G. Kozlov. The limiting nuclear polarization in a quantum dot under optical electron-spin orientation and applicability of the box-model of the electron-nuclear dynamics. *arXiv e-prints*, page arXiv:0801.1391, 2008.

[47] A. V. Khaetskii, D. Loss, and L. Glazman. Electron spin decoherence in quantum dots due to interaction with nuclei. *Phys. Rev. Lett.*, 88(18):186802, 2002.

[48] J. Schliemann, A. Khaetskii, and D. Loss. Electron spin dynamics in quantum dots and related nanostructures due to hyperfine interaction with nuclei. *Journal of Physics: Condensed Matter*, 15(50):R1809, 2003.

[49] J. Hackmann and F. B. Anders. Spin noise in the anisotropic central spin model. *Phys. Rev. B*, 89:045317, 2014.

[50] W. M. Witzel and S. Das Sarma. Quantum theory for electron spin decoherence induced by nuclear spin dynamics in semiconductor quantum computer architectures: Spectral diffusion of localized electron spins in the nuclear solid-state environment. *Phys. Rev. B*, 74:035322, 2006.

[51] W. M. Witzel, M. S. Carroll, Ł. Cywiński, and S. Das Sarma. Quantum decoherence of the central spin in a sparse system of dipolar coupled spins. *Phys. Rev. B*, 86:035452, 2012.

[52] D. Stanek, C. Raas, and G. S. Uhrig. Dynamics and decoherence in the central spin model in the low-field limit. *Phys. Rev. B*, 88:155305, 2013.

[53] D. Stanek, C. Raas, and G. S. Uhrig. From quantum-mechanical to classical dynamics in the central-spin model. *Phys. Rev. B*, 90:064301, 2014.

[54] G. Chen, D. L. Bergman, and L. Balents. Semiclassical dynamics and long-time asymptotics of the central-spin problem in a quantum dot. *Phys. Rev. B*, 76:045312, 2007.

[55] I. A. Merkulov, Al. L. Efros, and M. Rosen. Electron spin relaxation by nuclei in semiconductor quantum dots. *Phys. Rev. B*, 65:205309, 2002.

[56] S. I. Erlingsson and Y. V. Nazarov. Hyperfine-mediated transitions between a Zeeman split doublet in GaAs quantum dots: The role of the internal field. *Phys. Rev. B*, 66:155327, 2002.

[57] K. A. Al-Hassanieh, V. V. Dobrovitski, E. Dagotto, and B. N. Harmon. Numerical modeling of the central spin problem using the spin-coherent-state p representation. *Phys. Rev. Lett.*, 97:037204, 2006.

[58] B. Fauseweh, P. Schering, J. Hüdepohl, and G. S. Uhrig. Efficient algorithms for the dynamics of large and infinite classical central spin models. *Phys. Rev. B*, 96:054415, 2017.

[59] G. S. Uhrig. Keeping a quantum bit alive by optimized π-pulse sequences. *Phys. Rev. Lett.*, 98:100504, 2007.

[60] M. Yu. Petrov and S. V. Yakovlev. Comparison of quantum-mechanical and semiclassical approaches for an analysis of spin dynamics in quantum dots. *Journal of Experimental and Theoretical Physics*, 115(2):326–336, 2012.

[61] W. Beugeling, G. S. Uhrig, and F. B. Anders. Quantum model for mode locking in pulsed semiconductor quantum dots. *Phys. Rev. B*, 94:245308, 2016.

[62] W. Beugeling, G. S. Uhrig, and F. B. Anders. Influence of the nuclear Zeeman effect on mode locking in pulsed semiconductor quantum dots. *Phys. Rev. B*, 96:115303, 2017.

[63] I. Kleinjohann, E. Evers, P. Schering, A. Greilich, G. S. Uhrig, M. Bayer, and F. B. Anders. Magnetic field dependence of the electron spin revival amplitude in periodically pulsed quantum dots. *Phys. Rev. B*, 98:155318, 2018.

[64] M. M. Glazov, I. A. Yugova, and Al. L. Efros. Electron spin synchronization induced by optical nuclear magnetic resonance feedback. *Phys. Rev. B*, 85:041303, 2012.

[65] P. Schering, J. Hüdepohl, G. S. Uhrig, and B. Fauseweh. Nuclear frequency focusing in periodically pulsed semiconductor quantum dots described by infinite classical central spin models. *Phys. Rev. B*, 98:024305, 2018.

[66] E. B. Aleksandrov and V.S. Zapasskii. Magnetic resonance in the Faraday-rotation noise spectrum. *JETP*, 54:64, 1981.

[67] V. S. Zapasskii. Spin-noise spectroscopy: from proof of principle to applications. *Adv. Opt. Photon.*, 5(2):131–168, 2013.

[68] N. A. Sinitsyn and Y. V. Pershin. The theory of spin noise spectroscopy: a review. *Reports on Progress in Physics*, 79(10):106501, 2016.

[69] S. A. Crooker, D. G. Rickel, A. V. Balatsky, and D. L. Smith. Spectroscopy of spontaneous spin noise as a probe of spin dynamics and magnetic resonance. *Nature*, 431:49, 2004.

[70] M. Oestreich, M. Römer, R. J. Haug, and D. Hägele. Spin noise spectroscopy in GaAs. *Phys. Rev. Lett.*, 95(21):216603, 2005.

[71] S. A. Crooker, L. Cheng, and D. L. Smith. Spin noise of conduction electrons in n-type bulk GaAs. *Phys. Rev. B*, 79:035208, 2009.

[72] F. Berski, J. Hübner, M. Oestreich, A. Ludwig, A. D. Wieck, and M. Glazov. Interplay of electron and nuclear spin noise in n-type GaAs. *Phys. Rev. Lett.*, 115:176601, 2015.

[73] S. A. Crooker, J. Brandt, C. Sandfort, A. Greilich, D. R. Yakovlev, D. Reuter, A. D. Wieck, and M. Bayer. Spin noise of electrons and holes in self-assembled quantum dots. *Phys. Rev. Lett.*, 104:036601, 2010.

[74] J. Hübner, F. Berski, R. Dahbashi, and M. Oestreich. The rise of spin noise spectroscopy in semiconductors: From acoustic to GHz frequencies. *physica status solidi (b)*, 251:1824–1838, 2014.

[75] Ph. Glasenapp, D. S. Smirnov, A. Greilich, J. Hackmann, M. M. Glazov, F. B. Anders, and M. Bayer. Spin noise of electrons and holes in (In,Ga)As quantum dots: Experiment and theory. *Phys. Rev. B*, 93:205429, 2016.

[76] M. M. Glazov and E. L. Ivchenko. Spin noise in quantum dot ensembles. *Phys. Rev. B*, 86:115308, 2012.

[77] N. Fröhling, F. B. Anders, and M. M. Glazov. Nuclear spin noise in the central spin model. *Phys. Rev. B*, 97:195311, 2018.

[78] A. Bechtold, D. Rauch, F. Li, T. Simmet, P. Ardelt, A. Regler, K. Muller, N. A. Sinitsyn, and J. J. Finley. Three-stage decoherence dynamics of an electron spin qubit in an optically active quantum dot. *Nat Phys*, 11:1005, 2015.

[79] G. S. Uhrig, J. Hackmann, D. Stanek, J. Stolze, and F. B. Anders. Conservation laws protect dynamic spin correlations from decay: Limited role of integrability in the central spin model. *Phys. Rev. B*, 90:060301, 2014.

[80] Y. Li, N. Sinitsyn, D. L. Smith, D. Reuter, A. D. Wieck, D. R. Yakovlev, M. Bayer, and S. A. Crooker. Intrinsic spin fluctuations reveal the dynamical response function of holes coupled to nuclear spin baths in (In,Ga)As quantum dots. *Phys. Rev. Lett.*, 108:186603, 2012.

[81] J. Hackmann, Ph. Glasenapp, A. Greilich, M. Bayer, and F. B. Anders. Influence of the nuclear electric quadrupolar interaction on the coherence time of hole and electron spins confined in semiconductor quantum dots. *Phys. Rev. Lett.*, 115:207401, 2015.

[82] N. Wu, N. Fröhling, X. Xing, J. Hackmann, A. Nanduri, F. B. Anders, and H. Rabitz. Decoherence of a single spin coupled to an interacting spin bath. *Phys. Rev. B*, 93:035430, 2016.

[83] N. A. Sinitsyn, Y. Li, S. A. Crooker, A. Saxena, and D. L. Smith. Role of nuclear quadrupole coupling on decoherence and relaxation of central spins in quantum dots. *Phys. Rev. Lett.*, 109:166605, 2012.

[84] Ph. Glasenapp, N. A. Sinitsyn, L. Yang, D. G. Rickel, D. Roy, A. Greilich, M. Bayer, and S. A. Crooker. Spin noise spectroscopy beyond thermal equilibrium and linear response. *Phys. Rev. Lett.*, 113:156601, 2014.

[85] M. Poggio, H. J. Mamin, C. L. Degen, M. H. Sherwood, and D. Rugar. Nuclear double resonance between statistical spin polarizations. *Phys. Rev. Lett.*, 102:087604, 2009.

[86] C. L. Degen, M. Poggio, H. J. Mamin, and D. Rugar. Role of spin noise in the detection of nanoscale ensembles of nuclear spins. *Phys. Rev. Lett.*, 99:250601, 2007.

[87] D. K. Young, J. A. Gupta, E. Johnston-Halperin, R. Epstein, Y. Kato, and D. D. Awschalom. Optical, electrical and magnetic manipulation of spins in semiconductors. *Semiconductor Science and Technology*, 17(4):275, 2002.

[88] A. Greilich, D. R. Yakovlev, A. Shabaev, Al. L. Efros, I. A. Yugova, R. Oulton, V. Stavarache, D. Reuter, A. Wieck, and M. Bayer. Mode locking of electron spin coherences in singly charged quantum dots. *Science*, 313(5785):341–345, 2006.

[89] N. Jäschke, A. Fischer, E. Evers, V. V. Belykh, A. Greilich, M. Bayer, and F. B. Anders. Nonequilibrium nuclear spin distribution function in quantum dots subject to periodic pulses. *Phys. Rev. B*, 96:205419, 2017.

[90] S. Varwig, E. Evers, A. Greilich, D. R. Yakovlev, D. Reuter, A. D. Wieck, T. Meier, A. Zrenner, and M. Bayer. Advanced optical manipulation of carrier spins in (In,Ga)As quantum dots. *Applied Physics B*, 122(1):17, 2016.

[91] D. Press, K. De Greve, P. L. McMahon, T. D. Ladd, B. Friess, C. Schneider, M. Kamp, S. Höfling, A. Forchel, and Y. Yamamoto. Ultrafast optical spin echo in a single quantum dot. *Nat. Photon.*, 4:367 – 370, 2010.

[92] A. Bechtold, F. Li, K. Müller, T. Simmet, P.-L. Ardelt, J. J. Finley, and N. A. Sinitsyn. Quantum effects in higher-order correlators of a quantum-dot spin qubit. *Phys. Rev. Lett.*, 117:027402, 2016.

[93] N. Fröhling and F. B. Anders. Long-time coherence in fourth-order spin correlation functions. *Phys. Rev. B*, 96:045441, 2017.

[94] D. Hägele and F. Schefczik. Higher-order moments, cumulants, and spectra of continuous quantum noise measurements. *Phys. Rev. B*, 98:205143, 2018.

[95] F. Li, S. A. Crooker, and N. A. Sinitsyn. Higher-order spin-noise spectroscopy of atomic spins in fluctuating external fields. *Phys. Rev. A*, 93:033814, 2016.

[96] F. Li and N. A. Sinitsyn. Universality in higher order spin noise spectroscopy. *Phys. Rev. Lett.*, 116:026601, 2016.

[97] E. Evers, V. V. Belykh, N. E. Kopteva, I. A. Yugova, A. Greilich, D. R. Yakovlev, D. Reuter, A. D. Wieck, and M. Bayer. Decay and revival of electron spin polarization in an ensemble of (In,Ga)As quantum dots. *Phys. Rev. B*, 98:075309, 2018.

[98] D. Gammon, E. S. Snow, B. V. Shanabrook, D. S. Katzer, and D. Park. Homogeneous linewidths in the optical spectrum of a single gallium arsenide quantum dot. *Science*, 273(5271):87–90, 1996.

[99] A. Zrenner, L. V. Butov, M. Hagn, G. Abstreiter, G. Böhm, and G. Weimann. Quantum dots formed by interface fluctuations in AlAs/GaAs coupled quantum well structures. *Phys. Rev. Lett.*, 72:3382–3385, 1994.

[100] A. Babinski, J. Borysiuk, S. Kret, M. Czyz, A. Golnik, S. Raymond, and Z. Wasilewski. Natural quantum dots in the InAs/GaAs wetting layer. *Appl. Phys. Lett.*, 92, 2008.

[101] V. B. Verma and J. J. Coleman. High density patterned quantum dot arrays fabricated by electron beam lithography and wet chemical etching. *Appl. Phys. Lett.*, 93(11):111117, 2008.

[102] O. Schilling, A. Forchel, and M. Lebedev. Deep etched InGaAs/InP quantum dots with strong lateral confinement effects. *Superlattices and Microstructures*, 16(3):261 – 264, 1994.

[103] L. Goldstein, F. Glas, J. Y. Marzin, M. N. Charasse, and G. Le Roux. Growth by molecular beam epitaxy and characterization of InAs/GaAs strained layer superlattices. *Appl. Phys. Lett.*, 47(10):1099–1101, 1985.

[104] S. Franchi. Chapter 1 - Molecular beam epitaxy: fundamentals, historical background and future prospects. In M. Henini, editor, *Molecular beam epitaxy*, pages 1 – 46. Elsevier, Oxford, 2013.

[105] J. Wu and P. Jin. Self-assembly of InAs quantum dots on GaAs(001) by molecular beam epitaxy. *Frontiers of Physics*, 10(1):7–58, 2015.

[106] Semiconductors on NSM. `http://www.ioffe.ru/SVA/NSM/Semicond/index.html`. Accessed: 2019-05-10.

[107] I. N. Stranski and L. Krastanow. Zur Theorie der orientierten Ausscheidung von Ionenkristallen aufeinander. *Monatshefte für Chemie und verwandte Teile anderer Wissenschaften*, 71(1):351–364, 1937.

[108] M. Colocci, F. Bogani, L. Carraresi, R. Mattolini, A. Bosacchi, S. Franchi, P. Frigeri, M. Rosa-Clot, and S. Taddei. Growth patterns of self-assembled InAs quantum dots near the two-dimensional to three-dimensional transition. *Appl. Phys. Lett.*, 70(23):3140–3142, 1997.

[109] S. Sauvage, P. Boucaud, F. H. Julien, J.-M. Gérard, and V. Thierry-Mieg. Intraband absorption in n-doped InAs/GaAs quantum dots. *Appl. Phys. Lett.*, 71(19):2785–2787, 1997.

[110] S. Huang, S. J. Kim, R. Levy, X. Q. Pan, and R. S. Goldman. Mechanisms of InAs/GaAs quantum dot formation during annealing of In islands. *Appl. Phys. Lett.*, 103(13):132104, 2013.

[111] P. M. Lam, J. Wu, S. Hatch, D. Kim, M. Tang, H. Liu, J. Wilson, and R. Allison. Effect of rapid thermal annealing on InAs/GaAs quantum dot solar cells. *IET Optoelectronics*, 9:65 – 68, 2014.

[112] S. Bietti, L. Esposito, A. Fedorov, A. Ballabio, A. Martinelli, and S. Sanguinetti. Characterization and effect of thermal annealing on InAs quantum dots grown by droplet epitaxy on GaAs(111)A substrates. *Nanoscale Res Lett*, 10(1):930–930, 2015.

[113] A. O. Kosogov, P. Werner, U. Gösele, N. Ledentsov, D. Bimberg, V. M. Ustinov, A. Yu. Egorov, A. Zhukov, P. S. Kop'ev, N. Bert, and Zh. I. Alferov. Structural and optical properties of InAs-GaAs quantum dots subjected to high temperature annealing. *Appl. Phys. Lett.*, 69:3072–3074, 1996.

[114] B. Urbaszek, X. Marie, T. Amand, O. Krebs, P. Voisin, P. Maletinsky, A. Högele, and A. Imamoglu. Nuclear spin physics in quantum dots: An optical investigation. *Rev. Mod. Phys.*, 85:79–133, 2013.

[115] F. Meier and B. P. Zakharchenya, editors. *Optical orientation*. Modern problems in condensed matter sciences. Elsevier Science Pub. Co, 1984.

[116] E. L. Ivchenko. *Optical spectroscopy of semiconductor nanostructures*. Alpha Science, 2005.

[117] M. I. Dyakonov and A. V. Khaetskii. Spin hall effect. In M. I. Dyakonov, editor, *Spin physics in semiconductors*, volume 157 of *Springer Series in Solid-State Sciences*, pages 211–243. Springer Berlin Heidelberg, 2008.

[118] S. Cortez, O. Krebs, S. Laurent, M. Senes, X. Marie, P. Voisin, R. Ferreira, G. Bastard, J-M. Gérard, and T. Amand. Optically driven mpin memory in n-doped InAs-GaAs quantum dots. *Phys. Rev. Lett.*, 89:207401, 2002.

[119] M. S. Kuznetsova, K. Flisinski, I. Ya. Gerlovin, M. Yu. Petrov, I. V. Ignatiev, S. Yu. Verbin, D. R. Yakovlev, D. Reuter, A. D. Wieck, and M. Bayer. Nuclear magnetic resonances in (In,Ga)As/GaAs quantum dots studied by resonant optical pumping. *Phys. Rev. B*, 89:125304, 2014.

[120] M. M. Glazov. Coherent spin dynamics of electrons and excitons in nanostructures (a review). *Physics of the Solid State*, 54(1):1–27, 2012.

[121] I. A. Yugova, M. M. Glazov, E. L. Ivchenko, and Al. L. Efros. Pump-probe Faraday rotation and ellipticity in an ensemble of singly charged quantum dots. *Phys. Rev. B*, 80:104436, 2009.

[122] P. A. Abragam and A. Abragam. *The principles of nuclear magnetism.* Comparative pathobiology - Studies in the postmodern theory of education. Clarendon Press, 1961.

[123] M. M. Glazov. *Electron and nuclear spin dynamics in semiconductor nanostructures.* Oxford science publications. Oxford University Press, 2018.

[124] E. Fermi. Über die magnetischen Momente der Atomkerne. *Zeitschrift für Physik*, 60(5):320–333, 1930.

[125] C. Testelin, F. Bernardot, B. Eble, and M. Chamarro. Hole-spin dephasing time associated with hyperfine interaction in quantum dots. *Phys. Rev. B*, 79:195440, 2009.

[126] D. Paget, G. Lampel, B. Sapoval, and V. I. Safarov. Low field electron-nuclear spin coupling in gallium arsenide under optical pumping conditions. *Phys. Rev. B*, 15:5780–5796, 1977.

[127] W. A. Coish and D. Loss. Hyperfine interaction in a quantum dot: Non-Markovian electron spin dynamics. *Phys. Rev. B*, 70:195340, 2004.

[128] A. Khaetskii, D. Loss, and L. Glazman. Electron spin evolution induced by interaction with nuclei in a quantum dot. *Phys. Rev. B*, 67:195329, 2003.

[129] U. Seifert, P. Bleicker, P. Schering, A. Faribault, and G. S. Uhrig. Persisting correlations of a central spin coupled to large spin baths. *Phys. Rev. B*, 94:094308, 2016.

[130] S. I. Erlingsson and Y. V. Nazarov. Evolution of localized electron spin in a nuclear spin environment. *Phys. Rev. B*, 70:205327, 2004.

[131] E. A. Chekhovich, M. Hopkinson, M. S. Skolnick, and A. I. Tartakovskii. Suppression of nuclear spin bath fluctuations in self-assembled quantum dots induced by inhomogeneous strain. *Nature Communications*, 6:6348 – 6355, 2015. Article.

[132] R. V. Pound. Nuclear electric quadrupole interactions in crystals. *Phys. Rev.*, 79:685–702, 1950.

[133] C. P. Slichter. *Principles of magnetic resonance*. Springer Science & Business Media,, Berlin, 1996.

[134] R. I. Dzhioev and V. L. Korenev. Stabilization of the electron-nuclear spin orientation in quantum dots by the nuclear quadrupole interaction. *Phys. Rev. Lett.*, 99:037401, 2007.

[135] C. Bulutay. Quadrupolar spectra of nuclear spins in strained $In_xGa_{1-x}As$ quantum dots. *Phys. Rev. B*, 85:115313, 2012.

[136] A. Högele, M. Kroner, C. Latta, M. Claassen, I. Carusotto, C. Bulutay, and A. Imamoglu. Dynamic nuclear spin polarization in the resonant laser excitation of an InGaAs quantum dot. *Phys. Rev. Lett.*, 108:197403, 2012.

[137] N. Fröhling, N. Jäschke, and F. B. Anders. Fourth-order spin correlation function in the extended central spin model. *Phys. Rev. B*, 99:155305, 2019.

[138] T. Auer, R. Oulton, D. R. Yakovlev, S. Verbin, R. Cherbunin, D. Reuter, and A. Wieck. Measurement of the Knight field and local nuclear dipole-dipole field in an InGaAs/GaAs quantum dot ensemble. *Phys. Rev. B*, 80, 2009.

[139] C. W. Lai, P. Maletinsky, A. Badolato, and A. Imamoglu. Knight-field-enabled nuclear spin polarization in single quantum dots. *Phys. Rev. Lett.*, 96:167403, 2006.

[140] R. Oulton, A. Greilich, S. Yu. Verbin, R. V. Cherbunin, T. Auer, D. R. Yakovlev, M. Bayer, I. A. Merkulov, V. Stavarache, D. Reuter, and A. D. Wieck. Subsecond spin relaxation times in quantum dots at zero applied magnetic field due to a strong electron-nuclear interaction. *Phys. Rev. Lett.*, 98:107401, 2007.

[141] J. Hackmann. Spin dynamics in doped semiconductor quantum dots. PhD Dissertation, TU Dortmund, 2015.

[142] P.-F. Braun, X. Marie, L. Lombez, B. Urbaszek, T. Amand, P. Renucci, V. K. Kalevich, K. V. Kavokin, O. Krebs, P. Voisin, and Y. Masumoto. Direct observation of the electron spin relaxation induced by nuclei in quantum dots. *Phys. Rev. Lett.*, 94:116601, 2005.

[143] A. C. Johnson, J. R. Petta, J. M. Taylor, A. Yacoby, M. D. Lukin, C. M. Marcus, M. P. Hanson, and A. C. Gossard. Triplet-singlet spin relaxation via nuclei in a double quantum dot. *Nature*, 435(7044):925–928, 2005.

[144] F. H. L. Koppens, J. A. Folk, J. M. Elzerman, R. Hanson, L. H. Willems van Beveren, I. T. Vink, H. P. Tranitz, W. Wegscheider, L. P. Kouwenhoven, and L. M. K. Vandersypen. Control and detection of singlet-triplet mixing in a random nuclear field. *Science*, 309(5739):1346–1350, 2005.

[145] J. Fischer, W. A. Coish, D. V. Bulaev, and D. Loss. Spin decoherence of a heavy hole coupled to nuclear spins in a quantum dot. *Phys. Rev. B*, 78:155329, 2008.

[146] M. Yu. Petrov, G. G. Kozlov, I. V. Ignatiev, R. V. Cherbunin, D. R. Yakovlev, and M. Bayer. Coupled electron-nuclear spin dynamics in quantum dots: A graded box model approach. *Phys. Rev. B*, 80:125318, 2009.

[147] F. Li, A. Saxena, D. Smith, and N. A. Sinitsyn. Higher-order spin noise statistics. *New Journal of Physics*, 15(11):113038, 2013.

[148] T. Arai and B. Goodman. Cumulant expansion and Wick's theorem for spins. Application to the antiferromagnetic ground state. *Phys. Rev.*, 155:514–527, 1967.

[149] R. Steinigeweg and T. Prosen. Burnett coefficients in quantum many-body systems. *Phys. Rev. E*, 87:050103, 2013.

[150] J. N. Zhuang and J. Wang. Conductance fluctuation and shot noise in disordered graphene systems, a perturbation expansion approach. *Journal of Applied Physics*, 114(6):063708, 2013.

[151] M. Endres, M. Cheneau, T. Fukuhara, C. Weitenberg, P. Schauß, C. Gross, L. Mazza, M. C. Bañuls, L. Pollet, I. Bloch, and S. Kuhr. Observation of correlated particle-pole pairs and string order in low-dimensional Mott insulators. *Science*, 334(6053):200–203, 2011.

[152] K. W. Becker and P. Fulde. Ground-state energy of strongly correlated electronic systems. *Zeitschrift für Physik B Condensed Matter*, 72(4):423–427, 1988.

[153] J. M. Mendel. Tutorial on higher-order statistics (spectra) in signal processing and system theory: theoretical results and some applications. *Proceedings of the IEEE*, 79:278–305, 1991.

[154] R. Kubo. Generalized cumulant expansion method. *Journal of the Physical Society of Japan*, 17(7):1100–1120, 1962.

[155] A. Khintchine. Korrelationstheorie der stationären stochastischen Prozesse. *Mathematische Annalen*, 109(1):604–615, 1934.

[156] N. Wiener. Generalized harmonic analysis. *Acta Math.*, 55:117–258, 1930.

[157] L. P. Lindoy and D. E. Manolopoulos. Simple and accurate method for central spin problems. *Phys. Rev. Lett.*, 120:220604, 2018.

[158] A. Auerbach. *Interacting electrons and quantum magnetism.* Springer-Verlag New York, 2 edition, 1994.

[159] E. Fradkin. *Field theories of condensed matter physics.* Cambridge University Press, 2 edition, 2013.

[160] A. Altland and B. D. Simons. *Condensed matter field theory.* Cambridge University Press, 2 edition, 2010.

[161] A. M. Perelomov. Coherent states for arbitrary Lie group. *Comm. Math. Phys.*, 26(3):222–236, 1972.

[162] E. Fradkin and M. Stone. Topological terms in one- and two-dimensional quantum Heisenberg antiferromagnets. *Phys. Rev. B*, 38:7215–7218, 1988.

[163] J. R. Klauder. Path integrals and stationary-phase approximations. *Phys. Rev. D*, 19:2349–2356, 1979.

[164] N. A. Sinitsyn, Y. Li, S. A. Crooker, A. Saxena, and D. L. Smith. Supplementary material: Role of nuclear quadrupole coupling on decoherence and relaxation of central spins in quantum dots. *Phys. Rev. Lett.*, 109:166605, 2012.

[165] George Marsaglia. Choosing a point from the surface of a sphere. *Ann. Math. Statist.*, 43(2):645–646, 1972.

[166] J. C. Butcher. Coefficients for the study of Runge-Kutta integration processes. *Journal of the Australian Mathematical Society*, 3(2):185–201, 1963.

[167] R. Scherer. Herleitung von Runge-Kutta-Verfahren der Ordnung vier mit übersichtlichen Fehlerdarstellungen. *Mathematische Zeitschrift*, 128(4):311–323, 1972.

[168] H. E. Walchli, U. S. Atomic Energy Commission., Isotope Analysis Methods Laboratory., and Oak Ridge National Laboratory. *A Table of nuclear moment data*. Oak Ridge National Laboratory, Oak Ridge, Tenn., 1955.

[169] N. J. Stone. Table of nuclear magnetic dipole and electric quadrupole moments. *Atomic Data and Nuclear Data Tables*, 90(1):75 – 176, 2005.

[170] H. E. Weaver. Magnetic moments of si^{29}, s^{33}, zn^{67}, as^{75}, se^{77}, te^{123}, and te^{125}. *Phys. Rev.*, 89:923–930, 1953.

[171] A. Greilich, S. E. Economou, S. Spatzek, D. R. Yakovlev, D. Reuter, A. D. Wieck, T. L. Reinecke, and M. Bayer. Ultrafast optical rotations of electron spins in quantum dots. *Nature Physics*, 5(4):262–266, 2009.

[172] J. Meija, T. B. Coplen, M. Berglund, W. Brand, P. De Bièvre, M. Gröning, N. Holden, J. Irrgeher, D. R. Loss, T. Walczyk, and T. Prohaska. Isotopic compositions of the elements 2013 (IUPAC technical report). *Pure and Applied Chemistry*, 88:293–306, 2016.

[173] Ł. Cywiński, V. V. Dobrovitski, and S. Das Sarma. Spin echo decay at low magnetic fields in a nuclear spin bath. *Phys. Rev. B*, 82:035315, 2010.

[174] S. Starosielec, R. Fainblat, J. Rudolph, and D. Hägele. Two-dimensional higher order noise spectroscopy up to radio frequencies. *Review of Scientific Instruments*, 81(12):125101, 2010.

[175] Leigh M. Norris, Gerardo A. Paz-Silva, and L. Viola. Qubit noise spectroscopy for non-Gaussian dephasing environments. *Phys. Rev. Lett.*, 116:150503, 2016.

[176] M. S. Kuznetsova, R. V. Cherbunin, I. Ya. Gerlovin, I. V. Ignatiev, S. Yu. Verbin, D. R. Yakovlev, D. Reuter, A. D. Wieck, and M. Bayer. Spin dynamics of quadrupole nuclei in InGaAs quantum dots. *Phys. Rev. B*, 95:155312, 2017.

[177] M. Chamarro, F. Bernardot, and C. Testelin. Spin decoherence and relaxation processes in zero-dimensional semiconductor nanostructures. *Journal of Physics: Condensed Matter*, 19(44):445007, 2007.

[178] H. J. Carmichael. *Statistical methods in quantum optics 1*. Springer-Verlag Berlin Heidelberg, 1 edition, 1999.

[179] M. M. Glazov, I. A. Yugova, S. Spatzek, A. Schwan, S. Varwig, D. R. Yakovlev, D. Reuter, A. D. Wieck, and M. Bayer. Effect of pump-probe detuning on the

Faraday rotation and ellipticity signals of mode-locked spins in (In,Ga)As/GaAs quantum dots. *Phys. Rev. B*, 82:155325, 2010.

[180] I. A. Yugova, M. M. Glazov, D. R. Yakovlev, A. A. Sokolova, and M. Bayer. Coherent spin dynamics of electrons and holes in semiconductor quantum wells and quantum dots under periodical optical excitation: Resonant spin amplification versus spin mode locking. *Phys. Rev. B*, 85:125304, 2012.

[181] S. Spatzek, S. Varwig, M. M. Glazov, I. A. Yugova, A. Schwan, D. R. Yakovlev, D. Reuter, A. D. Wieck, and M. Bayer. Generation and detection of mode-locked spin coherence in (In,Ga)As/GaAs quantum dots by laser pulses of long duration. *Phys. Rev. B*, 84:115309, 2011.

[182] A. Fischer, E. Evers, S. Varwig, A. Greilich, M. Bayer, and F. B. Anders. Signatures of long-range spin-spin interactions in an (In,Ga)As quantum dot ensemble. *Phys. Rev. B*, 98:205308, 2018.

[183] C. Gardiner and P. Zoller. *Quantum noise*. Springer-Verlag Berlin Heidelberg, 3 edition, 2004.

[184] J. Hildmann, E. Kavousanaki, G. Burkard, and H. Ribeiro. Quantum limit for nuclear spin polarization in semiconductor quantum dots. *Phys. Rev. B*, 89:205302, 2014.

[185] V. L. Korenev. Multiple stable states of a periodically driven electron spin in a quantum dot using circularly polarized light. *Phys. Rev. B*, 83:235429, 2011.

[186] E. A. Zhukov, D. R. Yakovlev, M. Bayer, M. M. Glazov, E. L. Ivchenko, G. Karczewski, T. Wojtowicz, and J. Kossut. Spin coherence of a two-dimensional electron gas induced by resonant excitation of trions and excitons in CdTe/(Cd,Mg)Te quantum wells. *Phys. Rev. B*, 76:205310, 2007.

[187] A. Fischer. Semiklassische Simulation zweier schwach gekoppelter Halbleiterquantenpunkte. Master thesis, TU Dortmund, 2017.

[188] S. Spatzek, A. Greilich, Sophia E. Economou, S. Varwig, A. Schwan, D. R. Yakovlev, D. Reuter, A. D. Wieck, T. L. Reinecke, and M. Bayer. Optical control of coherent interactions between electron spins in InGaAs quantum dots. *Phys. Rev. Lett.*, 107:137402, 2011.

[189] D. S. Smirnov and M. M. Glazov. Spin coherence generation and detection in spherical nanocrystals. *Journal of Physics: Condensed Matter*, 24(34):345302, 2012.

[190] N. Jäschke, F. B. Anders, and M. M. Glazov. Electron spin noise under the conditions of nuclei-induced frequency focusing. *Phys. Rev. B*, 98:045307, 2018.

[191] A. K. Hüttel, J. Weber, A. W. Holleitner, D. Weinmann, K. Eberl, and R. Blick. Nuclear spin relaxation probed by a single quantum dot. *Phys. Rev. B*, 69, 2003.

[192] C. Latta, A. Srivastava, and A. Imamoğlu. Hyperfine interaction-dominated dynamics of nuclear spins in self-assembled InGaAs quantum dots. *Phys. Rev. Lett.*, 107:167401, 2011.

[193] D. S. Smirnov. Spin noise of localized electrons interacting with optically cooled nuclei. *Phys. Rev. B*, 91:205301, 2015.

[194] I. I. Ryzhov, G. G. Kozlov, D. S. Smirnov, M. M. Glazov, Y. P. Efimov, S. A. Eliseev, V. A. Lovtcius, V. V. Petrov, K. V. Kavokin, A. V. Kavokin, and V. S. Zapasskii. Spin noise explores local magnetic fields in a semiconductor. *Sci. Rep.*, 6:21062, 2016.

[195] D. Paget, T. Amand, and J.-P. Korb. Light-induced nuclear quadrupolar relaxation in semiconductors. *Phys. Rev. B*, 77:245201, 2008.

[196] D. S. Smirnov, Ph. Glasenapp, M. Bergen, M. M. Glazov, D. Reuter, A. D. Wieck, M. Bayer, and A. Greilich. Nonequilibrium spin noise in a quantum dot ensemble. *Phys. Rev. B*, 95:241408, 2017.

[197] P. S. Sokolov, M. Yu. Petrov, T. Mehrtens, K. Müller-Caspary, A. Rosenauer, D. Reuter, and A. D. Wieck. Reconstruction of nuclear quadrupole interaction in (In,Ga)As/GaAs quantum dots observed by transmission electron microscopy. *Phys. Rev. B*, 93:045301, 2016.

Acknowledgements

I thank my advisor Prof. Frithjof B. Anders for his support throughout the last four years but especially for the valuable feedback on this final part of the journey. I also want to express my gratitude to my second advisor Prof. Mikhail M. Glazov not only for the great scientific cooperation but also for taking the time to help newcomers from Germany and even show them some of the many sights of Saint Petersburg.
Special thanks also goes to Iris Kleinjohann, Andreas Fischer, Christian Wischnewski and Nina Fröhling for proofreading my thesis and to Eiko Evers for breaking down experimental intricacies for a theorist to understand.
I also want to thank my colleagues in Dortmund for the pleasant working environment, especially my office mates, Nina and Andreas, for helping to guarantee a never-ending supply of tea. Further, I would like to thank my colleagues in Saint Petersburg for always making me feel welcome and at home during my stays in Russia.
I thank my family for their unwavering support. At last but not least I want to thank my friends, especially René Grzeszick, for helping and reminding me that there is also life outside work.